UNIVERSITÄT
BERN

Excitation-Energy- and Field-driven Ultrafast Charge Processes in Organic Semiconductors

von

Cedric Hoffmann

aus

Gera, Deutschland

Dissertation im Studiengang
Chemie und Molekulare Wissenschaften

Universität Bern

Gutachterin: Prof. Dr. Natalie Banerji

Zweitgutachterin: Prof. Dr. Tracey Clarke

Oktober 2025

Danksagung

Diese Arbeit wurde am Departement für Chemie, Biochemie und Pharmazie der Universität Bern unter Leitung von Professor Natalie Banerji verfasst. Hiermit möchte ich den Menschen, die mich in den letzten Jahren begleitet und unterstützt haben meine Anerkennung und Dankbarkeit aussprechen.

Ein grosser Dank gilt meiner Professorin Dr. Natalie Banerji, die mir die Ultrafast-Spektroskopie nahebrachte und so mein Verständnis physikalischer Zusammenhänge entscheidend erweiterte, sowie für ihre langjährige Begleitung und Betreuung meiner Arbeit. Ein ebensolcher Dank gebührt Dr. Demetra Tsokkou und Dr. Julien Réhault für die Weitergabe ihres unerschöpflichen Wissens und ihren Erfahrungen und Fähigkeiten im Umgang mit den komplexesten Fragestellungen und Problemen. An dieser Stelle möchte ich ebenfalls der gesamten *FemtoMat*-Gruppe für die tolle gemeinsame Zeit und den regen fachlichen und privaten Austausch untereinander danken. Auch möchte ich mich bei Jakob Wolansky von der Technischen Universität Dresden, sowie bei Manasi Pranav und Dr. Atul Shukla von der Universität Potsdam für die grossartige Zusammenarbeit bedanken, welche massgeblich zu dieser Arbeit beigetragen haben. Neben Manasi Pranav und Dr. Atul Shukla gilt mein Dank ebenso Prof. Dr. Dieter Neher, welcher mich herzlichst an der Universität Potsdam begrüsste und mich für die Zeit meines Forschungsaufenthaltes in seine wundervolle Arbeitsgruppe aufnahm.

Des Weiteren bin ich der *Rhenania* und den *Northern Bears* unendlich dankbar mich in ihre Reihen aufgenommen zu haben und für die grossartigen Erlebnisse, die ich mit euch haben durfte. Durch euch fand ich Anschluss fernab der alten Heimat und über Zeit wurdet ihr wie eine zweite Familie für mich, die mir Rückhalt gibt und auf die ich mich immer und zu jeder Zeit in jeder Lebenslage verlassen kann, erscheint sie auch noch so ausweglos. Mittlerweile empfinde ich eine starke Verbundenheit zu diesem Land, insbesondere dem Kanton Bern, in einer Art und Weise, dass mir ein Leben an einem anderen Ort völlig unvorstellbar scheint. Auch daran seid ihr massgeblich beteiligt und ich kann meine Dankbarkeit euch gegenüber kaum in Worte fassen endlich das Gefühl zu haben, angekommen zu sein.

Auch meiner Familie gilt mein allergrösster Dank, dass sie mir stets mit Rat und Tat zur Seite standen. Ihr habt mich durch jede Phase meines Lebens begleitet, habt jede meiner Entscheidungen unterstützt und immer an mich geglaubt, was mir den Weg bis hierhin überhaupt erst ermöglicht hat. An Liam: Ich bin unendlich dankbar, dass es dich gibt. Du hast mich zum glücklichsten Menschen auf Erden gemacht und ich geniesse jede freie Minute, die ich mit dir verbringen kann. Ich wünsche dir nur das Allerbeste für die Zukunft und mögen all deine Träume und Wünsche in Erfüllung gehen. Für dich wird es immer einen Platz an meiner Seite und in meinem Herzen geben, hab dich lieb.

Selbständigkeitserklärung

Author:	Cedric Hoffmann
Titel der Arbeit:	Excitation-Energy- and Field-driven Ultrafast Charge Processes in Organic Semiconductors
Studiengang:	PhD of Science in Chemie und Molekulare Wissenschaften
Leiter der Arbeit:	Prof. Dr. Natalie Banerji

Ich erkläre hiermit, dass ich diese Arbeit selbständig verfasst und keine anderen als die angegebenen Quellen benutzt habe. Alle Stellen, die wörtlich oder sinngemäss aus Quellen entnommen wurden, habe ich als solche gekennzeichnet. Mir ist bekannt, dass andernfalls der Senat gemäss Artikel 36 Absatz 1 Buchstabe r des Gesetzes über die Universität vom 5. September 1996 und Artikel 69 des Universitätsstatuts vom 7. Juni 2011 zum Entzug des Doktortitels berechtigt ist.

Für die Zwecke der Begutachtung und der Überprüfung der Einhaltung der Selbständigkeitserklärung bzw. der Reglemente betreffend Plagiate erteile ich der Universität Bern das Recht, die dazu erforderlichen Personendaten zu bearbeiten und Nutzungshandlungen vorzunehmen, insbesondere die Doktorarbeit zu vervielfältigen und dauerhaft in einer Datenbank zu speichern sowie diese zur Überprüfung von Arbeiten Dritter zu verwenden oder hierzu zur Verfügung zu stellen.

Worb, den 07.10.2025

Cedric Hoffmann

Abstract

This work investigates how excitation energy, internal electric fields and device architecture control ultrafast charge formation, separation and extraction in organic semiconductors. The thesis contrasts a vacuum-deposited single-component small-molecule system, DCV2-5T, with a solution-processed donor–acceptor blend, PM6:Y6. Transient absorption spectroscopy tracks excited-state populations, electro-modulated differential absorption quantifies field-assisted separation and extraction, and optical-pump terahertz-probe spectroscopy evaluates photoconductivity and carrier localisation. Higher photon energy accelerates the initial formation of charges in both systems, yet long-lived charge populations emerge only when early extraction competes successfully with recombination. In DCV2-5T, the dominant bottleneck is extraction in the absence of a donor–acceptor interface rather than charge-generation kinetics. Introducing transport layers increases quantum efficiency but produces slower initial extraction that limits initial photoresponse, relevant for photodiode operation. External reverse bias improves extraction and exposes recombination and localisation as direct competitors to charge collection. In PM6:Y6, durable charge populations arise when excitation accesses delocalised Y6 aggregates at early times. Direct excitation of aggregated Y6 yields the most stable carriers, whereas populations originating from less connected regions show stronger field response. The thesis establishes extraction-limited behaviour in the single-component system and identifies aggregate connectivity with access to delocalised acceptor states as the decisive lever in the blended system.

Table of Contents

Abbreviations

A	Acceptor
Abs	Absorption
AFM	Atomic Force Microscopy
AL	Active Layer
BHJ	Bulk Heterojunction
BPAPF	9,9-bis[4-(N,N-bis-biphenyl-4-ylamino)phenyl]-9H-fluorene
BPhen	Bathophenanthroline
BS	Beam Splitter
BTO	2,2'-((2Z,2'Z)-((12,13-bis(2-(2-(2-methoxyethoxy)ethoxy)ethyl)-3,9-diundecyl-12,13-dihydro-[1,2,5]thiadiazolo[3,4-e]thieno[2'',3'':4',5']thieno[2',3':4,5]pyrrolo[3,2-g]thieno[2',3':4,5]thieno[3,2-b]indole-2,10-diyl)bis(methanylylidene))bis(5,6-difluoro-3-oxo-2,3-dihydro-1H-indene-2,1-diylidene))dimalononitrile
C/C	Core/Core Interactions
C/T	Core/Terminal Interactions
CCA	Charge-Charge Annihilation
CCD	Charge-Coupled Device
cf.	conferatur, compare
$CHCl_3$	Chloroform
CT	Interfacial Charge Transfer
CTx/ICT	Intramolecular Charge Transfer
D	Donor

D°	Detectivity
D*	Specific Detectivity
DCV2-5T	2,2'-[3'',4''-dimethyl-2,2':5',2'':5'',2''':5''',2''''-quinquethien-5,5''''-diylbis(methane-1-yl-1-ylidine)]dimalononitrile
DET	Dexter Energy Transfer
DFG	Difference-Frequency Generation
DN400/650	DCV2-5T without TL and with electrodes, excited at 400/650 nm
DOS	Density of States
DS400/650	DCV2-5T with TL and electrodes, excited at 400/650 nm
e.g.	exempli gratia, for example
EA	Electroabsorption
EDA	Electromodulated Differential Absorption
EEA	Exciton-Exciton Annihilation
EOS	Electro-Optic Sampling
EQE	External Quantum Efficiency
ESA	Excited-State Absorption
ETL	Electron Transport Layer
FC	Free Charges
FF	Fill Factor
Flu	Fluorescence
FN400/650	DCV2-5T without TL and electrodes, excited at 400/650 nm
FRET	Förster Resonance Energy Transfer
fs	Femtosecond

FS400/650	DCV2-5T with TL and without electrodes, excited at 400/650 nm
FWM	Four-Wave Mixing
GSB	Ground State Bleach
GVD	Group Velocity Dispersion
HOMO	Highest Occupied Molecular Orbital
HTL	Hole Transport Layer
i.a.	inter alia, among other things
i.e.	id est, that is
IC	Internal Conversion
IQE	Internal Quantum Efficiency
ISC	Intersystem Crossing
ITO	Indium Tin Oxide
LCAO	Linear Combination of Atomic Orbitals
LUMO	Lowest Unoccupied Molecular Orbital
MCR	Multivariate Curve Resolution
n	Negative
NEP	Noise Equivalent Power
NFA	Non-Fullerene Acceptor
NIR	Near-Infrared
nl	Nonlinear
OD	Optical Density
OPA	Optical Parametric Amplifier
OPD	Organic Photodiode

OPV/OSC	Organic Photovoltaic/Solar Cell
p	Positive
PBDB-T	Poly[[4,8-bis[5-(2-ethylhexyl)-2-thienyl]benzo[1,2-*b*:4,5-*b*']dithiophene-2,6-diyl]-2,5-thiophenediyl[5,7-bis(2-ethylhexyl)-4,8-dioxo-4*H*,8*H*-benzo[1,2-*c*:4,5-*c*']dithiophene-1,3-diyl]]
PCE	Power Conversion Efficiency
PDINN	2,9-Bis[3-[[3-(dimethylamino)propyl]amino]propyl]-anthra[2,1,9-def:6,5,10-d'e'f']diisoquinoline-1,3,8,10(2H,9H)-tetrone)
PD	Photodiode
PEDOT:PSS	Poly(3,4-ethylenedioxythiophene) polystyrene sulfonate
Phos	Phosphorescence
PIA	Photoinduced Absorption
PM6	Poly[(2,6-(4,8-bis(5-(2-ethylhexyl-3-fluoro)thiophen-2-yl)-benzo[1,2-b:4,5-b']dithiophene))-alt-(5,5-(1',3'-di-2-thienyl-5',7'-bis(2-ethylhexyl)benzo[1',2'-c:4',5'-c']dithiophene-4,8-dione)]
pol	Polariser
PV	Photovoltaic
QE	Quantum Efficiency
R	Responsivity
RMS	Root Mean Square
RT	Room Temperature (293.15K)
SC	Separated Charges
SE	Stimulated Emission
SPM	Self-Phase Modulation

T/T	Terminal/Terminal Interactions
TA	Transient Absorption
TAT	Triplet Energy Transfer
TCQ	Triplet-Charge Quenching
TL	Transport Layer
TTA	Triplet-Triplet Annihilation
UV	Ultraviolet
VIS	Visible
VR	Vibrational Relaxation
Y6	2,2'-((2Z,2'Z)-((12,13-bis(2-ethylhexyl)-3,9-diundecyl-12,13-dihydro-[1,2,5]thiadiazolo[3,4-e]thieno[2",3'':4',5']thieno[2',3':4,5]pyrrolo [3,2-g]thieno[2',3':4,5]thieno[3,2-b]indole-2,10-diyl)bis(methanylyl-idene))bis(5,6-difluoro-3-oxo-2,3-dihydro-1H-indene-2,1-diylidene)) dimalononitrile
YAG	Yttrium Aluminium Garnet
ZnTe	Zinc Telluride
λ/2-plate	Zero-Order Half-Wave Plate
λ/4-plate	Zero-Order Quarter-Wave Plate

Chapter 1

Introduction

Organic semiconductors are increasingly recognised as promising materials for optoelectronic applications including organic photovoltaics (OPVs) and organic photodiodes (OPDs). While traditional inorganic photovoltaics currently exhibit higher power conversion efficiencies (PCEs), OPVs offer specific advantages such as being thin, lightweight, flexible and easy to process. These characteristics enable them to be easily integrated into a wide range of applications, starting from indoor use in self-powered 'Internet of Things' (IoT) devices, via outdoor and camping materials, wearables, textiles and portable electronics, all the way to integration in agricultural power plants (agrivoltaics) and building materials like windowpanes.[1-8]

The performance of OPV and OPD devices arise from ultrafast photoinduced processes that convert photoexcitations into mobile charges. This thesis asks how excitation wavelengths, electric fields and nanostructure together govern those earliest steps and how that control differs between a neat small molecule and a state-of-the-art donor–acceptor blend. The study focuses on vacuum-deposited DCV2-5T and solution-processed PM6:Y6. It uses transient absorption spectroscopy to follow populations, electromodulated differential absorption spectroscopy to probe field-assisted separation and extraction and optical-pump THz-probe spectroscopy to resolve mobility and localisation of carriers. The theoretical background, recent literature and specific aims are presented in chapter 2, methods and technical details are given in chapter 3, chapters 4–6 present the results for the two material systems and chapter 7 summarises the main findings and gives an outlook for further research.

Chapter 2

Photophysical Processes in Optoelectronic Materials

2.1. Semiconductors

A semiconducting material has an electrical conductivity that lies between those of insulators and conductors. The energy or bandgap (E_g) characterises the energetic behaviour of the material and typically ranges from 0.5 eV to 3 eV.[9] It is the distance between the valence band and conduction band, where at a temperature of 0 K the valence band is completely occupied with electrons and the conduction band completely empty. Promoting an electron from the valence band into the conduction band needs additional thermal energy. This bands are described by band theory. The tight-binding model is commonly used for crystalline systems and states, that electrons initially bound to the individual atoms in localised atomic orbitals. Orbitals of the neighbouring atoms overlap when brought close together in a lattice, which causes the atomic energy levels to split and leads to a formation of conduction and valence bands. In crystalline semiconductors with a high delocalisation the bands can be occupied by delocalised conducting electrons. For other systems like organic semiconductors, atomic orbitals are combined into molecular orbitals, where electrons are described by wavefunctions and bands are formed by molecular orbitals.[10-12]

Delocalisation takes place on a shorter length scale, with electron pairs being delocalised via the conjugated π-system. This π-system originates from the molecular orbital (MO) theory by linear combination of atomic orbitals (LCAO). Every atom has its corresponding number of electrons which are arranged in electron shells (energy levels) around the atomic core, whereby the position (quantum state) of every electron is described by (the probability amplitude of) a specific wavefunction $\psi(r, \theta, \phi)$ which originates from the solution of the time-independent Schrödinger equation for a hydrogen atom.[11]

$$\psi(r, \theta, \phi) = R_{n,l}(r) \cdot Y_{l,m_l}(\theta, \phi) \tag{2-1}$$

The radial part $R_{n,l}(r)$ describes the radial distance r of the electron from the nucleus with $r > 0$. The angular part $Y_{l,m_l}(\theta, \phi)$ describes the angular distribution of the polar angle θ with $\theta \in [0, \pi]$ and the azimuthal angle ϕ with $\phi \in [0, 2\pi)$. Furthermore, the

principal quantum number n represents the electron shell, the azimuthal quantum number l the shape (the letter) of the orbital and the magnetic quantum number m_l the orbital orientation in space. Taking the square of the wavefunction $\psi(r,\theta,\phi)$ results in

$$P(r,\theta,\phi) = |\psi(r,\theta,\phi)|^2 = \left|R_{n,l}(r)\right|^2 \cdot \left|Y_{l,m_l}(\theta,\phi)\right|^2 \qquad (2\text{-}2)$$

where $P(r,\theta,\phi)$ is the probability density for finding an electron at a specific point (r,θ,ϕ) in space.[13]

Only electrons from the outer shell, the valence electrons, are relevant for the formation of so-called covalent bonds. These covalent bonds are needed to form molecules from atoms. These atoms aim for a complete filled outer shell and thus achieve noble gas configuration in order to form stable bonds. Except for the first shell (with only two electrons), almost all main-group elements (mainly of the second period) strive for eight valence electrons, i.e. they follow the octet rule. To form new molecular orbitals, atoms tend to form mixed, so-called hybrid orbitals. For instance, carbon has an electronic configuration $1s^2 2s^2 2p^2$ with six electrons in two shells and four valence electrons in the outer shell. In ethene every carbon has a steric number of three, that means it forms three localised σ-bonds by overlapping, two $C-H$ and one $C-C$. Therefore, each carbon is sp^2-hybridised leaving one p-orbital each unhybridised. These unhybridised p-orbitals are oriented perpendicular to the plane of the molecule and overlapping side-by-side under formation of the π-bond $(C=C)$. This π-bond is delocalised over the two carbon atoms. By extending this to a longer chain or molecular 'backbone' with alternating single and double bounds, a conjugated π-system is formed, which most organic semiconductors are based on. Therefore, the orbitals are described in relation to the molecule, resulting in a highest occupied molecular orbital (HOMO) being used as the equivalent for the valence band and lowest unoccupied molecular orbital (LUMO) as the equivalent for the conduction band with delocalisation on a shorter length scale than for crystalline inorganics. While the valence-electron view is a useful chemical model, modern electronic-structure methods treat all electrons explicitly or via effective core potentials [11,14-16]

2.2. Singlet Excitons

2.2.1. Exciton Formation

Excitons are the initial excited states in organic semiconductors and the origin of charge generation. It is therefore a basic requirement to understand what excitons are, how they are formed and how they behave during the charge generation process. An exciton is a quasiparticle representing the neutral excited state of a bound electron–hole pair that is attracted by Coulomb forces. During photoexcitation, a photon gets absorbed promoting an electron from the HOMO to the LUMO of the molecule, leaving a hole in its former position. This exciton formation occurs on an ultrafast timescale within tens of femtoseconds (fs). Besides Wannier-Mott excitons, which are common for inorganic semiconductors, exhibit a large excitonic radius and can move freely through the lattice, excitons in organic semiconductors are mainly of the Frenkel type, as they exhibit low dielectric constants and localised wave functions. Frenkel excitons are tightly bound to their specific atom or molecule with a corresponding radius and a high exciton binding energy E_b between 0.1 eV and 0.1 eV. E_b is given by the approximation

$$E_b \approx \frac{q^2}{4\pi \cdot \varepsilon_0 \cdot \varepsilon_r \cdot a} \tag{2-3}$$

with a as the effective electron–hole separation distance. The formation of excitons depends on the efficiency of photon absorption and is influenced by several interrelated factors such as the characteristics of excited states and electronic transitions, the transition dipole moment, the overlap of molecular wavefunctions and the Beer-Lambert law.[16,17]

Molecules exhibit discrete energy levels, whereby the state with the lowest energy is referred to as the ground state S_0, where electrons occupy the most stable molecular orbitals. By absorbing a photon, a molecule can transition to a higher energetic, excited state S_n. The efficiency of this process depends on the probability of the transition and on the energy matching between the incident photon and the energy gap between S_0 and S_n. Conversely, this means that the energy gap between ground state and excited state determines the wavelength of the absorbed light, which corresponds to the

resonance of the transition. Typically, this excited state is short-lived, as the molecule tends to return to the ground state by emitting energy. In organics, excitons are described as the transition from S_0 to S_1, with higher transitions being referred to as excess-energy excitons or non-thermalised excitons.[18,19] Unless specified otherwise, 'exciton' in this work refers to the singlet excited state S_1, while a higher-lying singlet excited state S_n ($n \geq 2$) is called 'excess-energy exciton' and 'triplet' refers to triplet excited states.

Transition Dipole Moment

The amplitude for a transition induced by an electromagnetic is quantified by the transition dipole moment $\vec{\mu}_{fi}$

$$\vec{\mu}_{fi} = \sum_i \langle \psi_f | q_i \vec{r}_i | \psi_i \rangle = \langle \psi_f | \hat{\mu} | \psi_i \rangle \tag{2-4}$$

from the initial state $|\psi_i\rangle$ to the final state $\langle \psi_f |$ with q_i as the charge of the i-th particle, the position operator $\vec{r}_i$ and the electric dipole moment operator $\hat{\mu}$. Accordingly, the transition dipole moment $\vec{\mu}_{fi}$ is a product of charge and distance and is dependent on the polarisation of the system during the transition between two states. Intermolecular interactions, solvent effects and temperature can affect wavefunction characteristics and $\vec{\mu}_{fi}$. This can also impact absorption properties of the materials, as the transition dipole moment $\vec{\mu}_{fi}$ is related to the absorption coefficient α_{abs} by the approximation

$$\alpha_{abs} \propto \left| \vec{\mu}_{fi} \right|^2 \tag{2-5}$$

where the absorption coefficient α_{abs} is defined via

$$I = I_0 \cdot e^{-\alpha_{abs} \cdot l} \tag{2-6}$$

where I_0 is the incident light intensity, I the transmitted light intensity and l the optical path length. α_{abs} quantifies how far light of a certain wavelength can penetrate a material. For the classical Beer-Lamber law, which is suitable for solutions, the absorbance A is expressed in terms of optical density (OD) and determined with

$$A = \log_{10}\left(\frac{I_0}{I}\right) = \varepsilon \cdot c \cdot l \tag{2-7}$$

where ε is the molar extinction coefficient and c the molar concentration. Also, the absorption coefficient α_{abs} can be determined via the Beer-Lambert law in conjunction with equation (2-6)

$$A = \frac{\alpha_{abs} \cdot l}{\ln 10} \tag{2-8}$$

and is suitable for films and solids. A larger transition dipole moment $\vec{\mu}_{fi}$ indicates a stronger interaction with light, resulting in an increased absorption coefficient α_{abs}, which is a fundamental principle of spectroscopy.[13,20,21]

Oscillator Strength

The oscillator strength f_{if} quantifies the probability of an optical transition between $|\psi_i\rangle$ and $\langle\psi_f|$ and is directly related the transition dipole moment $\vec{\mu}_{fi}$. In OPVs, the spectral distribution of f_{if} governs the absorption coefficient α_{abs} and thus the absorptance of the active layer A_α under a defined illumination. Together with the IQE, this determines the photogeneration rate and limits the achievable short-circuit current density J_{SC}.[22]

Using Fermi's Golden Rule, f_{if} can be described with

$$f_{if} = \frac{2m_e \cdot \omega_{if}}{3\hbar \cdot q^2} \cdot \left|\vec{\mu}_{fi}\right|^2 = \frac{8\pi^2 \cdot m_e \cdot \nu}{3h \cdot q^2} \cdot \left|\vec{\mu}_{fi}\right|^2 \tag{2-9}$$

where m_e is the mass of an electron, ω_{if} the resonance angular frequency corresponding to the energy difference between the two states, $\hbar$ the reduced Planck constant, h the Planck constant and ν the transition frequency. The oscillator strength f_{if} is strongly influenced by the transition dipole moment $\vec{\mu}_{fi}$, as it grows proportional to its square. A large f_{if} means that the transition is more likely to occur.[23]

Dynamic Polarisability

Not only the oscillator strength f_{if} but also the dynamic polarisability $\alpha(\omega)$ is directly related to the transition dipole moment $\vec{\mu}_{fi}$. Polarisability represents the ability to induce electric dipole moments in a material. While static polarisability describes the response of molecules to static electromagnetic fields, the dynamic polarisability $\alpha(\omega)$ addresses interactions with an oscillating electromagnetic field. Since light is an electromagnetic wave, which is defined as a dynamically changing electromagnetic field, dynamic polarisability is important for optical behaviour and properties of molecules and therefore crucial for understanding and analysing of photophysical processes.[23]

When an external oscillating electric field $F(t)$ with

$$F(t) = F_0 \cdot e^{-i\omega t} \tag{2-10}$$

interacts with a system, a time-dependent dipole moment $p(t)$ is induced, which is quantified as the relation between $F(t)$ and $\alpha(\omega)$ with

$$p(t) = \alpha(\omega) \cdot F(t) \tag{2-11}$$

Since polarisability is not necessarily identical in all directions, for anisotropic systems a more generalized approach is used with

$$p_i(t) = \sum_j \alpha_{ij}(\omega) \cdot F_j(t) \tag{2-12}$$

for the dipole moment in the *i*-th direction caused by an electric field in the *j*-th direction. To determine the dynamic polarisability $\alpha(\omega)$, the sum-over-states formula is used, considering all possible electronic transitions between S_0 and S_n

$$\alpha(\omega) = \frac{1}{\hbar} \sum_f \left(\frac{\langle \psi_f | \hat{\mu} | \psi_i \rangle^2}{\omega_{fi} - \omega - i \cdot \gamma_{fi}} + \frac{\langle \psi_f | \hat{\mu} | \psi_i \rangle^2}{\omega_{fi} + \omega + i \cdot \gamma_{fi}} \right) \tag{2-13}$$

with the resonance angular frequency ω_{fi}, the angular frequency of the external field ω, which represents the frequency of light that interacts with the material, the damping

factor γ_{fi} as the lifetime of ψ_f and the transition dipole moment $\vec{\mu}_{fi}$, which contributes to $\alpha(\omega)$ by the square. Thus, a strong transition dipole moment not only increases the oscillator strength f_{if}, but also leads to enhanced polarisability at frequencies near resonance. This is observable as intense absorption features in the optical spectrum, while the real part of the polarisability $Re[\alpha(\omega)]$ contributes to the refractive index and generally increases the absorption near resonance, the imaginary part $Im[\alpha(\omega)]$ is directly related to the absorption coefficient and leads to a peak formation in the absorption spectra of the material. Consequently, materials with a high f_{if} often exhibit more efficient light absorption and therefore a higher exciton formation ability at and around the resonance frequency. Since the resonance frequency reflects the optical bandgap of the material, the absorption and exciton formation efficiency can be tuned toward the desired absorption region by designing the gap between HOMO and LUMO accordingly.[23-25]

Bandgap Optimisation

The importance of manipulating the bandgap of OPV materials arises from the composition of the solar spectrum, as it does not provide a uniform wavelength distribution. With a wider bandgap, the absorption is more focused on shorter wavelength, while a smaller bandgap enables absorption at higher wavelengths. By aligning the absorption profile of the material with the solar spectrum, the exciton generation efficiency can be maximised. As natural sunlight is highly variable due to environmental, geographical and seasonal influences, the AM1.5 spectrum was globally standardised for solar cell research. It originates from the AM0 spectrum which represents the average solar radiation in space. The 'air mass' (AM) represents the thickness of the atmosphere and is defined via the Kasten & Young equation with

$$AM = \frac{1}{\cos\theta + 0.50572 \cdot (96.07995° - \theta)^{-1.6364}} \approx \frac{1}{\cos\theta} \qquad (2\text{-}14)$$

where AM is the reciprocal cosine of the solar zenith angle θ and can be specified with the empiric correction factor, which becomes important for larger angles. A solar zenith angle of 48.2 ° and thus AM1.5 was defined as the most accurate representation

of the average sunlight conditions during an entire day. While AM1.5D considers only direct radiation, AM1.5G also includes diffuse radiation and represents the solar spectrum most closely.[26,27]

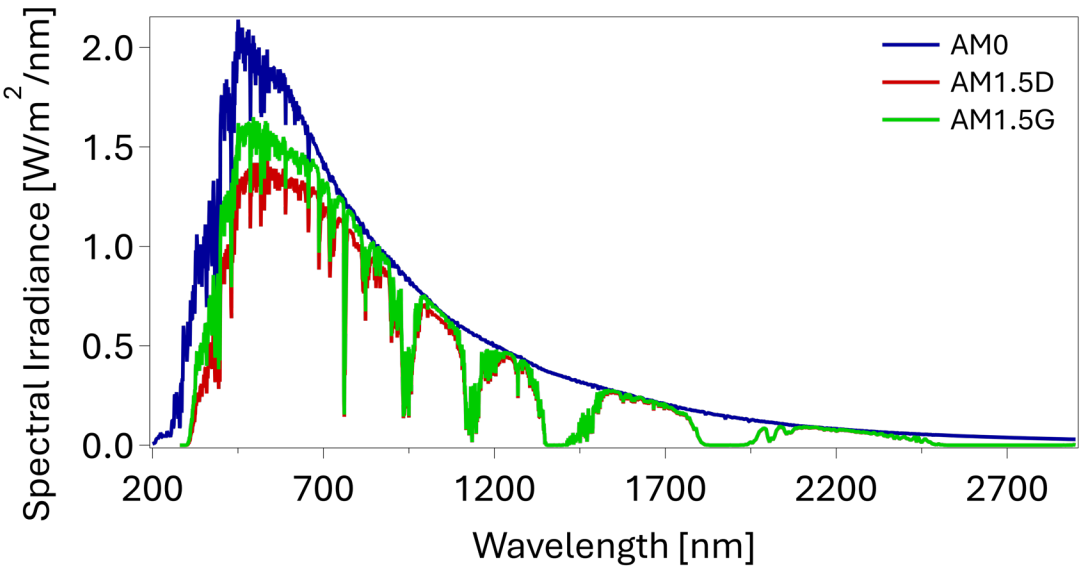

Figure 2-1: Standardisations of the solar spectrum; extraterrestrial (AM0), direct normal (AM1.5D) and global horizontal (AM1.5G) irradiance spectrum.[28]

Density of States

While single molecules exhibit clear energy levels for HOMO and LUMO, it becomes more complex in solid state films. Here, the concept of density of states (DOS) is crucial for understanding their electronic behaviour. Organic molecules usually aggregate to form solids. The occurring interactions among them lead to energetic variations, resulting in a range of energy states for both HOMO and LUMO, rather than discrete molecular orbitals. This broadening can be either homogeneous or inhomogeneous. Inhomogeneous broadening arises from static energetic disorder across local environments, while homogeneous broadening stems from dynamic processes such as electron–phonon coupling and finite excited-state lifetimes.[29]

DOS describes the number of electronic states at a particular energy level that electrons are allowed to occupy. DOS is not a quantity that is fixed by nature, but it often exhibits a Gaussian distribution for organic semiconductors and can be

manipulated to influence charge mobility, recombination dynamics, the broadness of absorption bands and thus significantly improve device performance. A common method for describing the DOS of an organic semiconductor is the Gaussian DOS model with

$$g(E) = \frac{N}{\sqrt{2\pi \cdot \sigma}} \cdot \exp\left(-\frac{(E - E_o)^2}{2\sigma^2}\right) \tag{2-15}$$

where $g(E)$ represents the DOS at energy E, E_o as the central energy around which the states are distributed, N as the total number of states and the standard deviation of DOS σ (energetic disorder), which reflects the width of the distribution and thus the degree of energetic disorder. Inhomogeneous broadening of the DOS typically arises from energetic disorder, coming from variations in molecular packing and local environments. Homogeneous broadening, however, arises from aggregation, which modifies excitonic coupling and redistributes oscillator strength, shifting the spectra. While a broadening leads to a destabilisation of the DOS, a narrower DOS has a stabilising effect as it improves charge transport and reduces recombination.[30,31]

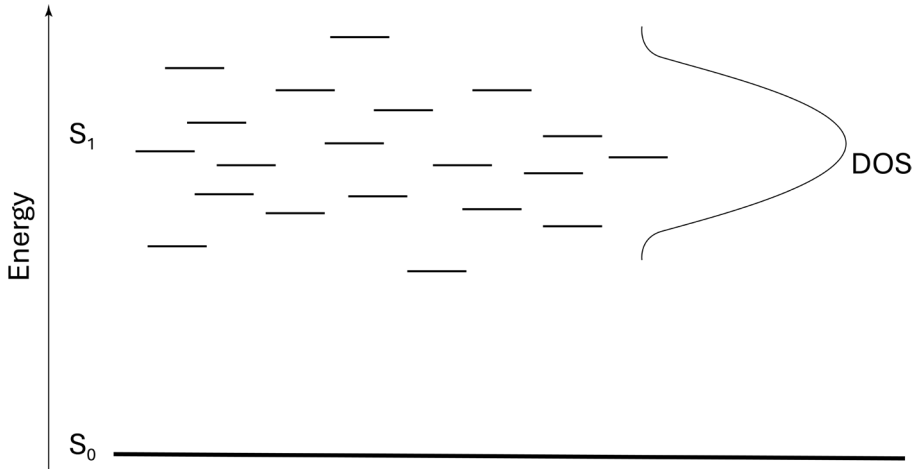

Figure 2-2: Schematic illustration of the density of states (DOS).

Multiphoton Absorption

Multiphoton absorption is a nonlinear interaction involving the simultaneous absorption of two or more photons for a direct electronic transition from S_0 to S_n. While two-photon absorption (TPA) is the most prominent, the simultaneous absorption of three or more photons has a low probability and needs extreme light intensities to occur, making them negligible in OPVs. TPA depends to the square of the intensity of the incident photons and becomes significant at high excitation densities.[32]

The probability for a single-photon absorption is described by the absorption cross-section σ. σ represents the effective area that a molecule presents to incident photons, which will cause a transition from S_0 to S_n. For this single-photon processes, the absorption rate $R(t)$ per molecule is

$$R(t) = \frac{\sigma(t) \cdot I(t)}{\hbar \cdot \omega} \tag{2-16}$$

with the incident photon intensity I and the photon energy $\hbar\omega$.

For TPA, the relevant parameter is the two-photon absorption coefficient $\sigma^{(2)}$ that characterises the molecular strength of the TPA process and modifies σ with

$$\sigma(t) = \sigma^{(2)} \cdot I(t) \tag{2-17}$$

leading to a nonlinear TPA rate $R_{TPA}(t)$ of

$$R_{TPA}(t) = \frac{\sigma I(t)}{\hbar\omega} = \frac{\sigma^{(2)} I(t)^2}{\hbar\omega} \tag{2-18}$$

indicating that while $\sigma^{(2)}$ is independent of intensity, the effective absorption rate $R_{TPA}(t)$ scales quadratically with intensity $I(t)$.[32,33]

2.2.2. Exciton Diffusion

In most cases, excitons are generated within the bulk of the D or A domains rather than directly at the D–A interface. Due to their localised, tightly bound nature, excitons cannot dissociate spontaneously into charges. Consequently, they must diffuse towards an interface, where they can lead to formation of charge–transfer states either by electron or hole transfer. Due to their relatively large binding energy up to 1.4 eV and their short lifetime of less than 1 ns, the distance and velocity of exciton diffusion is an important factor before recombination or trapping occurs. This turns exciton diffusion into a critical step for efficient OPVs.[11,34]

Transfer Mechanisms

Exciton diffusion in organic semiconductors typically occurs via an incoherent hopping mechanism, in which an energy transfer occurs from an excited molecule to a molecule in the ground state. This means that no physical separation between electron and hole takes place, rather only the excitation energy is transferred. This can occur via the two primary energy transfer mechanisms, the Förster Resonance Energy Transfer (FRET) and the Dexter Energy Transfer (DET). The FRET is a long-range, non-radiative dipole-dipole coupling mechanism with an interaction radius of 1–10 nm and is the dominant mechanism for singlet exciton transfer in OPV materials. FRET depends on the distance between the excited molecule (donor chromophore) and its neighbouring molecule in the ground state (acceptor chromophore), how well their spectral properties align, how likely it is that the donor chromophore emit energy and how their dipole moments are oriented relative to each other. Its efficiency decreases rapidly, being inversely proportional to the sixth power of the distance. The rate of FRET (k_F) is given by

$$k_F(d) = \frac{1}{\tau_{hop,F}} = \frac{1}{\tau_0} \cdot \left(\frac{R_0}{d}\right)^6 \qquad (2\text{-}19)$$

where k_F is the reciprocal of the exciton hopping lifetime $\tau_{hop,F}$, while τ_{hop} is the product of the donor chromophore lifetime τ_0 and the ratio of the donor–acceptor

distance d to the Förster Radius R_0 to the sixth power. R_0 is defined as the centre-to-centre distance between donor and acceptor at which the efficiency of the energy transfer is equal to 50 %. The Förster Radius R_0 is related to the overlap integral J of the photoluminescence of the donor and the absorption of the acceptor.

$$R_0 \propto \kappa^2 \cdot \phi_{PL} \cdot \frac{J}{n^4} \tag{2-20}$$

Here, R_0 is proportional to the product of the transition dipole orientation factor κ^2, the donor photoluminescence quantum yield ϕ_{PL} and the ratio of J to the fourth power of the refractive index n. In FRED, κ^2 quantifies the relative orientation of the transition dipole moments of the donor chromophore $\vec{\mu}_D$ and the acceptor chromophore $\vec{\mu}_A$ along with the direction vector $\hat{r}$ from donor to acceptor.

$$\kappa^2 = \left(\frac{\vec{\mu}_D \cdot \vec{\mu}_A}{|\vec{\mu}_D| \cdot |\vec{\mu}_A|} - 3 \frac{(\vec{\mu}_D \cdot \hat{r}) \cdot (\vec{\mu}_A \cdot \hat{r})}{|\vec{\mu}_D| \cdot |\vec{\mu}_A|} \right)^2 \tag{2-21}$$

κ^2 strongly affects the efficiency of energy transfer and ranges from 0 to 4, where a perpendicular orientation without coupling is represented by 0, random orientation by 2/3, parallel orientation by 1 and head-to-tail orientation by 4.[35,36]

DET is a short-range mechanism with an interaction radius of up to 1 nm that requires orbital overlap between the neighbouring donor and acceptor molecules. DET is based on a non-radiative electron exchange transfer mechanism. DET is generally less utilised in organic semiconductors. Typically, their spatial distance between the molecules is too wide and their molecular orientations too irregular to enable a sufficient orbital overlap for efficient energy transfer for singlet excitons. Nevertheless, DET is crucial for triplet energy transfer, while FRET relies on dipole-allowed emission and absorption processes, which are ineffective for triplet exciton states due to their spin-forbidden radiative transitions. The Dexter Energy Transfer rate k_D is the reciprocal of the exciton hopping lifetime $\tau_{hop,D}$ and given by

$$k_D = \frac{1}{\tau_{hop,D}} = K \cdot J \cdot e^{-2R/L} \tag{2-22}$$

with the K as prefactor related to the Dexter coupling J (electronic coupling strength), R as the centre-to-centre distance between donor and acceptor molecules and L as the decay length of the orbital overlap.[35-37]

Quantification of Exciton Diffusion

As both FRET and DET define the energy transfer rates between neighbouring molecules, they both influence the exciton diffusion coefficient D, which is a measure for exciton diffusion efficiency.

$$D = \frac{d^2}{6\tau_{hop}} \tag{2-23}$$

Aside from the mechanism of exciton transfer, the lifetime of excitons is also an important parameter when evaluating the exciton diffusion. The exciton lifetime τ is the average time an exciton exists before undergoing any exciton decay pathway. In organic solar cells, the intended pathway for excitons is the formation of charge–transfer (CT) states (cf. section 2.4.1). Besides that, competing processes such as recombination (cf. section 2.2.3) or intersystem crossing (cf. section 2.3) influence the lifetime of excitons and depend strongly on the material, the local environment, the energetic disorder and the excitation density.[38]

The combination of exciton diffusion coefficient D and exciton lifetime τ enables the determination of the exciton diffusion length L_D, which is defined as the average distance an exciton travels from its initial position during its lifetime.

It is based on the Brownian motion by the general form

$$\langle r \rangle^2 = 2n \cdot D \cdot \tau \tag{2-24}$$

with the number of spatial dimensions n and the mean squared displacement $\langle r \rangle^2$, where the n-dimensional exciton diffusion length L_{nD} is defined as the square root of $\langle r \rangle^2$, leading to

$$L_{nD} = \sqrt{2n \cdot D \cdot \tau} \tag{2-25}$$

However, especially in disordered or anisotropic systems exciton diffusion does not follow exact lattices and rather exhibits mixed or anisotropic transport, which is why often the dimension-independent simplification

$$L_D = \sqrt{D \cdot \tau} \tag{2-26}$$

is used. Thus, specifying a particular dimensionality of exciton diffusion can be avoided, as it is often already implicitly considered in the diffusion coefficient D. For PM6:Y6 BHJ (1:1.2) prepared from chloroform solution and subsequently annealed, domain sizes of about 8.3 nm (60 °C), 9.9 nm (80 °C) and 10.11 nm (100 °C) were reported[39]. In unannealed PM6:Y6 films, domain sizes of 7.7 nm[39] or even as small as 1-2 nm[40] were observed. Since exciton diffusion lengths are reported to be 7.5–13 nm for PM6[41,42] and 37–39 nm for Y6[42-44], the observed domain sizes lie in a range that matches these L_{nD}. This is beneficial as it allows excitons to efficiently reach the D–A interface before recombining, thereby supporting effective charge generation.[35,45,46]

Diffusion Pathways

In organic semiconductors the hopping of excitons takes place via two energetically different pathways. Immediately after photoexcitation, downhill migration takes place within the DOS. Excitons hop towards lower-energy sites, a process that is energetically favourable ($\Delta E < 0$) and therefore occurs more rapidly and spontaneously. As a result, downhill migration initially dominates. After this initial relaxation phase, excitons become distributed around a lower mean quasi-equilibration energy $\langle E_{eq} \rangle$, given by

$$\langle E_{eq} \rangle = E_o + \langle \varepsilon_{eq} \rangle = E_o - \frac{\sigma^2}{k_B T} \tag{2-27}$$

where $\langle \varepsilon_{eq} \rangle$ represents the mean energy relaxation offset $\langle \varepsilon_{eq} \rangle$ relative to the DOS centre energy E_o. After excitons have accumulated near $\langle E_{eq} \rangle$, further diffusion requires thermally activated hopping. Thermally activated hopping represents the second pathway, involving transitions between energetically similar or slightly higher-

energy sites. It describes the process by which excitons perform uphill hops by utilising available thermal energy from the environment. It is much slower than downhill migration as it requires excitons to overcome energetic barriers. Consequently, uphill hopping only becomes significant once downhill migration stagnates and is limited by the available thermal energy k_BT , which at room temperature (RT, 293.15 K) corresponds to 25.26 meV.[35,36,47]

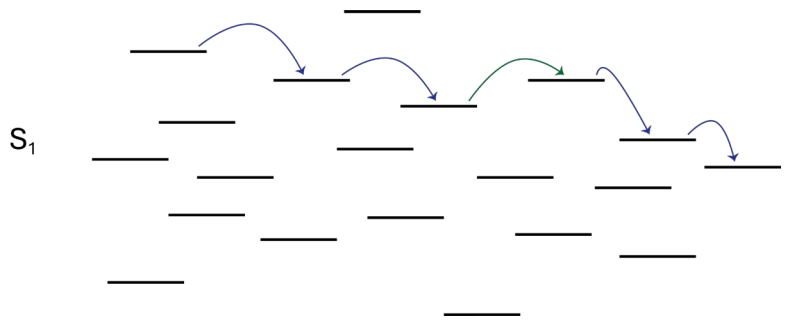

Figure 2-3: Schematic illustration downhill hopping (blue arrows) and thermally activated uphill hopping (green arrow) within the DOS.

Exciton Trapping

During downhill and uphill migration, excitons typically have access to many neighbouring sites within the centre of the DOS, which facilitates continuous diffusion. However, as excitons relax into the lower-energy tail of the DOS, the local density of energetically reachable sites decreases. This increasingly limits the available hopping possibilities in either energetic direction. If no lower-energy site is accessible within the hopping range and if the energetic difference to higher-energy sites exceeds the available thermal energy k_BT, excitons become immobilised. This immobilisation is referred to as exciton trapping and significantly restricts further diffusion.[35]

Trap states are common in organics and arise from a broad DOS caused by energetic and structural disorder. Variations in molecular packing, local structure and local polarisation lead to local energetic minima, favouring the formation of trapping sites. Defects, impurities, grain boundaries and aggregates introduce deep states which cause persistent localisation. Additionally, aggregates can also significantly modify electronic coupling, leading to the formation of energetically deep and spatially

localised trap states. Escaping from trap states is in theory possible via thermally activated hopping and quantum tunnelling. If the trap depth is within k_BT, excitons have a chance to overcome the energetic barrier and proceed with diffusion. Via quantum tunnelling, excitons could escape a trap state by directly transferring between distant sites without the need for intermediate hopping. However, tunnelling requires significant wavefunction overlap, strong coupling and energy resonance between initial and final states, which is less likely to occur in disordered organic semiconductors. Their strong structural and energetic disorder suppresses tunnelling, making thermally activated hopping the dominant mechanism for exciton un-trapping. Nevertheless, uphill migration remains strongly limited by k_BT and becomes drastically less probable with increasing trap depth or lower temperatures. Thus, the presence of traps critically influences exciton dynamics by reducing the diffusion length and increasing recombination, negatively impacting solar cell efficiency.[35,47,48]

Quantum Delocalisation and Reorganisation Energy

Besides classical hopping processes, recent studies revealed that transient quantum delocalisation can significantly enhance exciton mobility. Quantum delocalisation refers to the coherent propagation (identical in energy, phase, polarisation and direction) of the exciton wavefunction across multiple neighbouring molecules within the first few femtoseconds after excitation. This quantum delocalisation is termed 'transient' because the electronic coherence decays within few femtoseconds due to vibronic dephasing and static energetic disorder, before afterwards transport proceeds predominantly by incoherent (Förster-like) hopping or mixed coherent-incoherent transport, depending on coupling and dephasing rates. During transient quantum delocalisation, the exciton does not diffuse via classical hopping. Instead, it propagates as a collective excitonic state through non-local, multi-site energy transfer, which increases the effective exciton diffusion distance. In addition, this short-lived quantum delocalisation has also been reported to reduce exciton trapping by enabling the wavefunction to temporarily bypass localised low-energy sites during the initial diffusion phase.[36,49] Giannini, et al. [36] demonstrated that, in π-conjugated small molecules such as Y6, exciton diffusion rates are significantly enhanced, even though

these quantum delocalisation events persist for less than 10 fs. The extent of this spatial delocalisation can be quantified by the Inverse Participation Ratio (IPR), defined as

$$IPR = \frac{(\sum_i |\psi_i|^2)^2}{\sum_i |\psi_i|^4} \tag{2-28}$$

where ψ_i is the amplitude of the exciton wavefunction at site i. IPR reflects the effective number of sites over which the exciton is coherently delocalised. An IPR of 1 corresponds to complete localisation on a single site, while an IPR of *N* indicates delocalisation across *N* sites.[36,49,50]

The degree of delocalisation is also strongly influenced by the reorganisation energy E_λ. E_λ represents the energy required for structural and vibrational reorganisation of a molecule as an exciton migrates between molecular sites. The reorganisation energy E_λ affects therefore not only the extend of exciton delocalisation but also the efficiency of energy transfer between molecular sites and thus classical exciton hopping. According to FRED, the incoherent exciton-transfer rate k_{EET} is

$$k_{EET} = \frac{2\pi}{\hbar} \cdot |V|^2 \cdot J(\Delta E) \tag{2-29}$$

where V is the electronic coupling between initial and final excitonic states on two sites, ΔE is the energy difference between sites and $J(\Delta E)$ is the donor–acceptor spectral-overlap integral. The reorganisation energy E_λ determines the Stokes shift and linewidths of donor emission and acceptor absorption and thus controls $J(\Delta E)$. A larger E_λ typically decreases the overlap and k_{EET}. Consequently, a lower E_λ is needed for efficient hopping.[51]

Y6 exhibits a reorganisation energy E_λ of approximately 250 meV for excitons[36,52]. This relatively low E_λ enables exciton diffusion via both incoherent hopping and transient quantum delocalisation, which has been associated with experimentally determined diffusion lengths of 37–39 nm[42-44]. This allows excitons in Y6 to travel through typical domain sizes in BHJ, facilitating efficient arrival at D–A interfaces and reducing recombination losses. Furthermore, the low E_λ in Y6 correlates with reduced non-radiative voltage losses and improved V_{OC} in OPVs. In summary, a minimised E_λ

enhances exciton diffusion by enabling both faster incoherent hopping and transient quantum delocalisation. Both mechanisms play a crucial role in determining charge generation efficiency of organic solar cells.[35,49,52]

2.2.3. Exciton Decay

The lifetime of an exciton ends when it undergoes a decay process. In organic photovoltaic materials, the formation of charge–transfer (CT) states is the primary intended decay pathway, where the exciton dissociates and transfers the electron to the acceptor and the hole to the donor. However, this intended pathway is challenged by several mainly monomolecular processes, which are classified into radiative and non-radiative decay channels. The general kinetic rate for a decay channel can be described with the time-depended decay rate $R(t)$ via

$$R(t) = k_{fi} \cdot N(t)^x \tag{2-30}$$

with the general electronic transition rate constant k_{fi}, the exciton population N and with the decay process order x (1 for monomolecular, 2 for bimolecular, 3 for trimolecular). In a time-resolved context, the evolution of the exciton population $N(t)$ for x =1 is given by

$$\frac{dN}{dt} = -R_{mon}(t) = -k_r N(t) - k_{nr} N(t) \tag{2-31}$$

with the radiative recombination rate constant k_r, the non-radiative recombination rate constant k_{nr} and the first-order decay rate $R_{mon}(t)$. Under linear excitation conditions, the time-dependent $R_{mon}(t)$ determines the overall decay rate as only monomolecular pathways are present.[16,53]

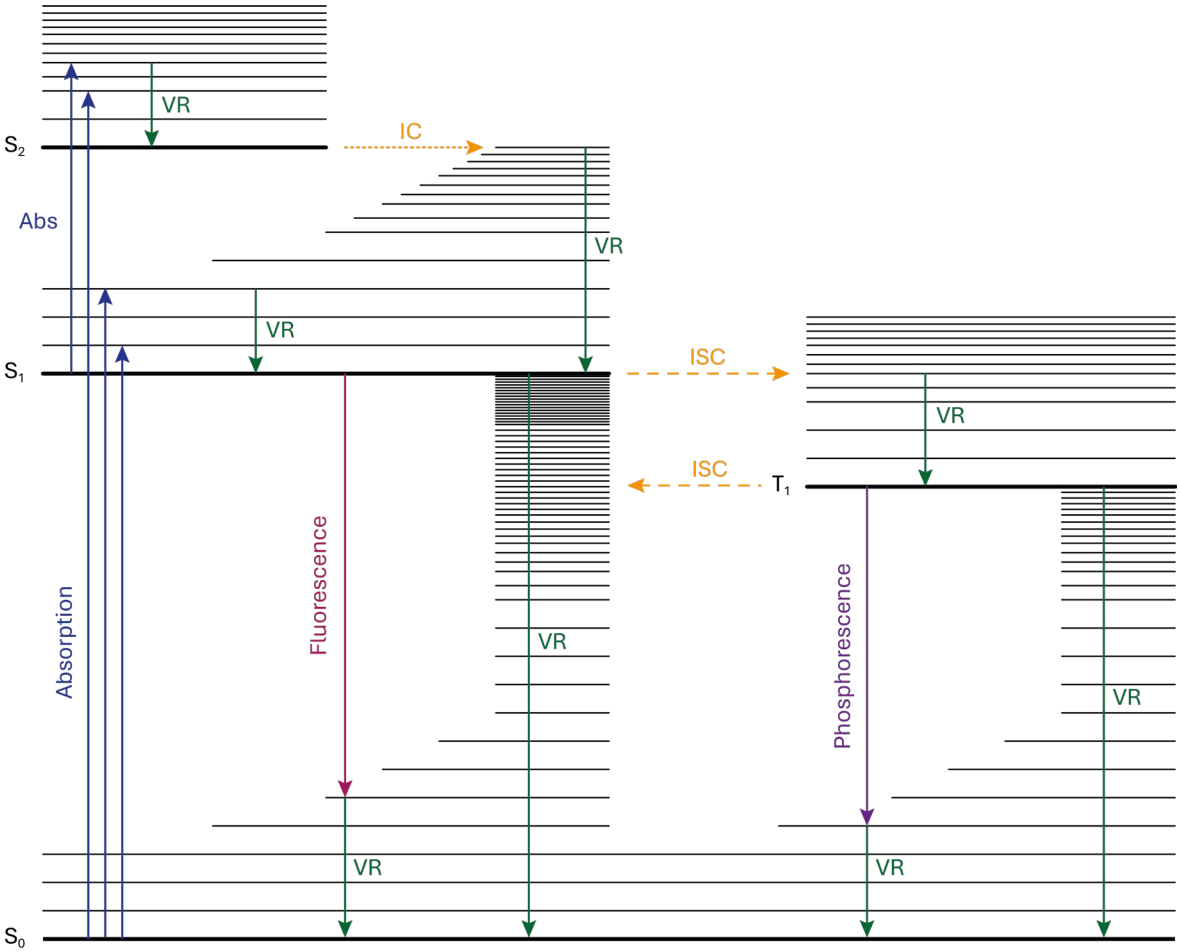

Figure 2-4: Jablonski diagram of singlet (S_n) and triplet (T_n) states with simplified energetic sub-levels and processes such as absorption, radiative decay i.e. fluorescence & phosphorescence, nonradiative decay i.e. vibrational relaxation (VR), internal conversion (IC) and intersystem crossing (ISC).

Unlike linear regimes, where properties such as absorption or decay scale directly with the incident photon density or species population, nonlinear regimes involve additional higher-order interactions. These effects arise because the induced optical polarisation responds nonlinearly to the incident photon density. Nonlinear interactions directly influence generation and recombination dynamics of all excited species, impacting the behaviour of films and devices. These regimes are generally only accessed under laboratory conditions, as the AM1.5G sunlight is far below the intensities typically required for higher-order optical processes.[32]

Spontaneous emission

The radiative recombination of an exciton refers to the process in which an exciton decays by emitting a photon. In organic semiconductors, this process is observed as spontaneous emission, also known as photoluminescence (PL) and can be quantified by the photoluminescence quantum yield ϕ_{PL}

$$\phi_{PL} = \frac{k_r}{k_r + k_{nr}} \tag{2-32}$$

where k_r is the radiative recombination rate constant and k_{nr} is the total non-radiative recombination rate constant. While radiative recombination competes with exciton dissociation in photovoltaics, a higher intrinsic PL yield suppresses non-radiative losses and is thus beneficial for achieving low non-radiative voltage losses, as it was observed for NFAs. While radiative recombination is beneficial in light-emitting devices, it represents an energy loss in photovoltaics, as it reduces the number of excitons available for dissociation. The radiative recombination rate depends primarily on the overlap integral of the electron and hole wavefunctions and the optical transition dipole moment. Thus, higher delocalisation in ordered systems enhances oscillator strength and can increase k_r, while disorder tends to localise excitons, reduce the effective transition dipole and lower k_r.[29,54]

Another important characteristic of radiative recombination is the occurrence of a Stokes shift, whereby the energy of the emitted photon is lower than the energy of the absorbed photon. The Stokes shift arises from relaxation of the exciton to a lower vibrational sublevel in the excited state prior to emission. As a result, the PL emission is redshifted relative to the prior absorption. Also, the spectral overlap between absorption and emission is directly determined by the Stokes shift. A reduced overlap decreases reabsorption losses and thereby enables longer diffusion lengths L_D, making a minimised Stokes shift favourable.[35]

Stimulated emission

Stimulated emission (SE) is a radiative process in which an exciton interacts with an incident photon, decaying to a lower energy level while emitting a second photon that is coherent with the incident one. Unlike spontaneous emission, which occurs randomly in time and space, SE requires the presence of an additional incident photon to occur. The time-dependent SE rate $R_{SE}(t)$ is given by

$$R_{SE}(t) = \sigma_{Sn} \cdot I(t) \cdot N(t) \tag{2-33}$$

with the excited-state cross-section σ_{Sn} and the time-dependent photon intensity $I(t)$ and excited-state population $N(t)$. Although SE is a linear process, its need for a second photon makes it highly dependent on the local photon density. Consequently, SE is negligible under AM1.5G steady-state illumination and only becomes detectable as a negative contribution in transient absorption spectroscopy.[16,55]

Internal Conversion

Internal conversion (IC) describes the non-radiative relaxation of an exciton that occurs due to strong coupling between electronic and vibrational modes. In intra-molecular IC, exciton energy is converted into vibrational energy within the same molecule, rapidly bringing the exciton from higher excited states S_n to lower excited states (e.g. S_1), leading ultimately to vibrational relaxation to the ground state S_0 without emitting a photon. Inter-molecular IC extends this process by transferring vibrational energy to neighbouring molecules. IC becomes more pronounced in materials with high energetic disorder or strong vibronic coupling, but less in materials with higher molecular rigidity and aggregation. Internal conversion can thus significantly shorten exciton lifetime and reduces the probability of reaching a dissociation site. The efficiency of IC is governed by the energy gap law, which states that decreasing the energy gap between the excited state and the ground state leads to an exponential increase in non-radiative decay rates. This relationship can be described using Fermi's Golden Rule. The general relation for all first-order radiative and non-radiative processes is given by the general electronic transition rate k_{fi}

$$k_{fi} = \frac{2\pi}{\hbar} \cdot \rho(E) \cdot \left|H_{fi}\right|^2 \cdot F \quad (2\text{-}34)$$

where $\rho(E)$ is the density of vibrational states at the transition energy, H_{fi} is the electronic coupling matrix element between the initial and final electronic states and F is the Franck-Condon factor quantifying the vibrational overlap integral. In the specific case of internal conversion, the transition rate corresponds to $k_{IC} = k_{fi}$. Accordingly, materials with small exciton binding energies or narrow optical gaps are more vulnerable to fast internal conversion.[16,46,56-58]

Defect-Induced Quenching

Defect-induced quenching is a process that occurs when excitons encounter structural or chemical defects such as impurities, grain boundaries, interfacial defects or morphological flaws. These defects introduce mid-gap states that act as energetic traps, lowering the activation barrier and allowing rapid non-radiative decay via multi-phonon (vibronic) relaxation. In addition, defects create spatial inhomogeneities in the exciton population, limiting the probability of excitons reaching energetically favourable sites for charge transfer. A higher defect density increases the extent of defect-induced quenching. As a result, defects shorten exciton lifetimes and diffusion lengths, leading to lower CT state formation probabilities.[46,58,59]

Exciton–Charge Quenching

Exciton–charge quenching is a non-radiative deactivation of excitons through interaction with free charge carriers in the material. When an exciton diffuses close to a charge carrier, Coulomb interactions can cause exciton quenching without recombination of the charge carrier itself, which remains mobile and continues to contribute to electrical conductivity. This process represents a bimolecular loss channel for excitons, whose rate increases proportionally with the local charge carrier density and therefore becomes more relevant under high excitation densities or in devices where charge carriers can accumulate. The effective quenching radius

depends in addition to Coulombic interactions also on the spatial and energetic distribution of charge–transfer centres. Exciton–charge quenching can be observed in TA at high pump fluence but is typically negligible under AM1.5G operation. This mechanism can affect the formation of CT states by reducing the exciton population prior to dissociation, especially in materials with high defect density, energetic disorder and long exciton diffusion lengths where the probability of encountering free charges increases.[16,35,60,61]

Exciton–Exciton Annihilation

Exciton–exciton annihilation (EEA) is a nonlinear, non-radiative recombination mechanism, in which two excitons interact within a critical interaction radius, leading to the permanent loss of one of the excitons. An exciton gets annihilated by transferring its energy to another, promoting the surviving exciton to a higher excited state S_n. The promoted exciton then undergoes rapid and efficient IC back to the lowest excited state S_1, from which it can continue diffusion. Since two excitons are involved in EEA, the probability of this process (the EEA rate constant k_{EEA}) scales with the square of the exciton population $N(t)$ and is expressed as EEA rate $R_{EEA}(t)$ using equation (2-30).[16,46]

$$R_{EEA}(t) = k_{EEA} \cdot N(t)^2 \tag{2-35}$$

Exciton Decay Dynamics and Diffusion Length

The non-radiative linear decay pathways described above, together with additional non-radiative processes involving triplets (cf. section 2.3), can be kinetically summarised into a total non-radiative decay rate constant k_{nr}, which can be written as

$$k_{nr} = k_{IC} + k_{DIQ} + k_{XQ} + k_{ISC} + \cdots \tag{2-36}$$

with the internal conversion rate k_{IC}, the defect-induced quenching rate k_{DIQ}, the exciton–charge quenching rate k_{XQ} and the intersystem crossing rate k_{ISC}. Combining both the radiative recombination rate constant k_r and the non-radiative decay rate constant k_{nr} results in the first-order total decay rate constant k_{mon} with

$$k_{mon} = k_r + k_{nr} \tag{2-37}$$

which is inversely proportional to the exciton lifetime τ. Taking equation (2-26) into account, τ exhibits a significant influence on the diffusion length L_D, leading to a direct inverse influence of k_{mon} on L_D.

$$L_D = \sqrt{D \cdot \tau} = \sqrt{\frac{D}{k_{mon}}} \tag{2-38}$$

Thus, the total effective decay shortens τ and limits the diffusion length L_D, while the sum of all exciton decay pathways needs to be slower than the exciton diffusion rate to achieve an efficient L_D.[16,46]

Beyond the monomolecular channels, bimolecular and trimolecular processes can be summarised into a common decay rate of k_{bi} and k_{tri} respectively. The general evolution of the exciton population $N(t)$ includes all linear and nonlinear decay pathways and can be expressed by

$$\frac{dN}{dt} = -R_{tot}(t) = -k_{mon}N(t) - k_{bi}N(t)^2 - k_{tri}N(t)^3 \tag{2-39}$$

At low excitation densities (linear regime), the influence of k_{bi} and k_{tri} is negligible, leading to first-order kinetics dominated by k_{mon}. Under high excitation densities, the higher-order terms become significant and introducing nonlinear decay.[16,35,62]

2.3. Triplet Excitons

Triplet excitons in organic photovoltaic systems represent spin-forbidden excited states that typically arise either from singlet states via intersystem crossing (ISC) or from charge recombination pathways. In Y6-based blends such as PM6:Y6, their role is increasingly recognised as a source of energy loss, particularly under open-circuit conditions and their dynamics are influenced by molecular energetics, spin statistics and morphology.[63]

Intersystem Crossing

Intersystem crossing (ISC) is a non-radiative, spin-forbidden transition from the singlet excited state S_1 to the triplet excited state T_1, facilitated by spin–orbit coupling. In organic semiconductors such as Y6, ISC is intrinsically slow due to weak spin–orbit coupling. However, fluorination and other structural features can enhance ISC modestly. In PM6:Y6 blends, ISC occurs primarily in pristine acceptor domains where excitons fail to reach the D–A interface.[63,64]

The reverse process of ISC, known as thermally activated delayed fluorescence (TADF), involves reverse ISC from T_1 back to S_1. While relevant in OLED systems, TADF is absent in OPVs based on NFAs like Y6. The large energy gap between singlet and triplet state exceeds k_BT at RT and prevents efficient TDADF, resulting in long-lived triplet states.[65]

Singlet Fission

Singlet fission (SF) is a spin-allowed bimolecular process in which one singlet exciton splits into two triplet excitons on neighbouring chromophores. SF requires that the energy of a singlet excited state energy is at least twice as that of its corresponding triplet excited state. Therefore, it is energetically inaccessible in the materials studied here as their lowest singlet excited states lie below twice their respective triplet energies. This makes the process exothermically unfavourable and effectively forbidden under any excitation condition.[66]

Triplet Diffusion

Triplets are not strictly localised but can migrate via Dexter-type exchange interactions that requires orbital overlap. These interactions enable triplet energy transfer (TET) over short distances of a few nanometres, especially in ordered molecular domains. In NFA systems such as PM6:Y6, triplet diffusion is mainly limited to the Y6 phase, because a transfer to PM6 is suppressed as the triplet state of Y6 lies energetically below that of PM6. Since triplet diffusion lengths in PM6:Y6 blends are limited by disorder and Dexter coupling, they are theoretically sufficient for triplets to encounter FC or other triplets to enable annihilation processes such as triplet-charge annihilation (TCA) and triplet-triplet annihilation (TTA).[35]

Triplet–Triplet Annihilation

Triplet–Triplet Annihilation (TTA) is analogous to EEA but involves the annihilation of two triplet states instead. When two triplets interact, one triplet gets annihilated while the other one gets promoted to a higher singlet excited state. Like EEA, TTA is a bimolecular nonlinear and non-radiative process which scales with the square of the triplet population and whose rate is expressed by

$$R_{TTA}(t) = k_{TTA} \cdot T(t)^2 \tag{2-40}$$

with the triplet population $T(t)$. TTA can lead to delayed fluorescence if the resulting singlet excited state decays radiatively. In material blends it is possible, that this emitted photon exhibits a higher energy than the initially absorbed photon. In that case, the triplet was generated in the sensitiser and is then transferred via TET to the annihilator which has an energetically higher excited singlet state than the sensitiser. If such triplets then undergo TTA in which the resulting exciton subsequently decays radiatively, this process is referred to as TTA upconversion.[16,67]

Triplet Decay

In NFAs, triplets decay predominantly via IC to the ground state. This decay is spin-forbidden and thus slow up to several microseconds. Phosphorescence is negligible in OPV materials at RT due to the lack of strong spin–orbit coupling. Therefore, any relaxation to the ground state occurs non-radiatively.[65]

Triplet–Charge Quenching

Triplet–charge quenching (TCQ) is a non-radiative bimolecular process in which a triplet interacts with a positive or negative charged carrier. The triplet is quenched by transferring its energy to the charge carrier. TCQ becomes more relevant under strong excitation in systems with coexisting populations of triplets and delocalised charge carriers and were mainly reported in OLED systems.[68]

2.4. Charges

2.4.1. Exciton Dissociation

To generate charges in organic solar cells and photodiodes, dissociation of the excitons is required. When an exciton dissociates, it undergoes separation onto different molecules or molecular units while still being bound by significant Coulombic interactions due to the low dielectric constant of organic materials. This process is also referred to as charge transfer, whereby the photogenerated electron–hole pair populates the charge-transfer (CT) state. The formation of CT states typically occurs when an exciton encounters an interface or electronic discontinuity, allowing electron or hole transfer onto a neighbouring molecule or segment that offers a favourable energetic alignment. The charge transfer process itself typically occurs within 100 ps to 300 fs and is therefore significantly faster than competing exciton decay processes. The formation of charge–transfer states is the initial stage of charge separation and is predominantly governed by energetic alignment, molecular packing, electronic coupling and nuclear reorganisation energy.[46,62,69,70]

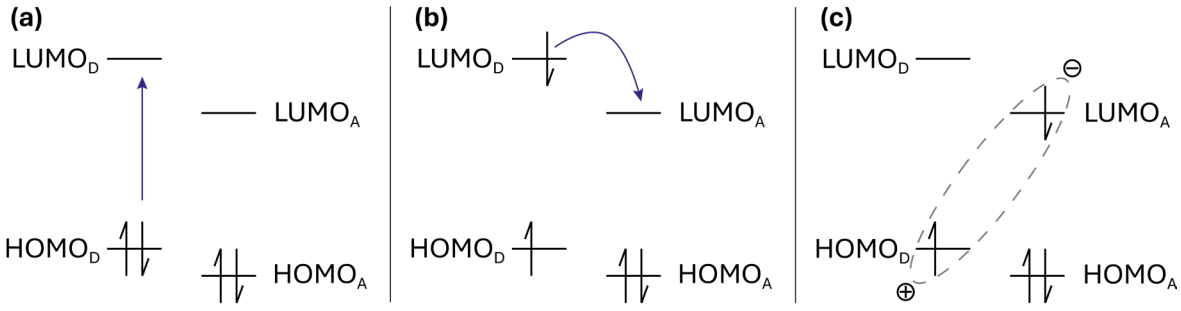

Figure 2-5: Schematic illustration of the orbital occupation at a D–A interface after donor excitation, where (a) shows the formation of an exciton by promoting an electron from HOMO to LUMO within the donor and where (b) shows the electron transfer from the LUMO of the donor to the LUMO of the acceptor, resulting in (c) the formation of a charge-transfer state.

Charge Transfer at Donor–Acceptor Interfaces

In BHJ systems, charge transfer primarily occurs at interfaces between donor and acceptor parts. Excitation of the donor leads to electron transfer to the acceptor at the interface, while excitation of the acceptor leads to hole transfer to the donor. The formation and stability of the CT state is thereby strongly influenced by the energetic

LUMO offset for electron transfer and by the energetic HOMO offset for hole transfer. Interfacial disorder can significantly affect the formation and energetics of CT states. Well-ordered interfaces favour strong electronic coupling and faster charge transfer, whereas disordered interfaces may introduce energetic traps or delay CT formation. In the past, an offset of around 0.3 eV was considered favourable to overcome the exciton binding energy and reorganisation energies, but recent studies revealed, that efficient charge transfer can also occur at significantly lower offsets, especially in NFA blends like PM6:Y6, where the typical effective offset is about 0.1–0.15 eV.[70-73]

Charge transfer with large energy offsets can lead to a loss of available energy, which is reflected in a reduced V_{OC} value in the device. According to Marcus theory, the electron transfer rate is maximised when ΔE balances E_λ, whereas the offset itself is set by the interfacial energetics. However, Marcus theory assumes weak electronic coupling, harmonic parabolic free-energy surfaces and classical high-temperature nuclear motion. These assumptions are not strictly fulfilled in many NFA blends where interfacial states can be partially delocalised and coupling can be moderate. Therefore, Marcus theory should be considered as an approximation.[74,75]

The rate of charge transfer k_{CT} is commonly described by

$$k_{CT} = |V|^2 \cdot \sqrt{\frac{\pi}{\hbar^2 \cdot E_\lambda \cdot k_B \cdot T}} \cdot \exp\left(-\frac{(\Delta E - E_\lambda)^2}{4E_\lambda \cdot k_B T}\right) \tag{2-41}$$

Here, ΔE is defined via

$$\Delta E = \Delta E_{CT} + C \tag{2-42}$$

with the energy difference ΔE_{CT} between the singlet excited state and the CT state and the Coulomb binding energy C. C arises from electrostatic attraction between the oppositely charged particles and represents the required energy for separating an electron–hole pair.[51,62,76]

In systems like organic semiconductors which exhibit rather low dielectric constants ε_r of 2–4[50], the Coulomb binding energy C is stronger due to the relation

$$C = -\frac{q^2}{4\pi \cdot \varepsilon_0 \cdot \varepsilon_r \cdot d_{DA}} \tag{2-43}$$

with the vacuum permittivity ε_0 and the donor–acceptor separation distance d_{DA}.

Organics often show CT-pair binding energies of a few hundred meV at sub-nanometre to nanometre separations which decrease rapidly with increasing separation.[77] The model described by Onsager defines the Coulomb or Onsager radius r_C where the C equals $k_B T$ via

$$r_C = -\frac{q^2}{4\pi \cdot \varepsilon_0 \cdot \varepsilon_r \cdot k_B T} \tag{2-44}$$

which gives a r_C of around 20 nm for a ε_r of around 3 at 300 K, reflecting the simplicity of this model. In real blends effective binding is reduced by interfacial permittivity gradients, hybrid CT–Frenkel character, delocalisation and internal electrostatic fields, which is why separation can proceed efficiently even when $r_C \ll r$.[70,77,78]

Despite small offsets, PM6:Y6 exhibits efficient interfacial transfer and separation. Evidence points to low reorganisation energies of Y-series acceptors and strong interfacial electronic coupling as key factors that lower activation barriers and enable fast transfer with minimal driving force.[44,79] In some systems with small energetic offsets, direct S_0 to CT state excitation can also become possible. While such transitions are negligible in systems with well-separated donor and acceptor orbitals due to their low oscillator strength, strong hybridisation between the local exciton state and the CT state can occur due to small energetic offsets and increase the transition dipole moment through an intensity-borrowing mechanism. This hybridisation enables measurable S_0 to CT absorption and has been observed in systems like PM6:Y6, where the small energetic offset allows strong state mixing. It was shown that direct CT excitation exhibits detectable sub-gap absorption features in the EQE, but weak and several orders of magnitude lower than its allowed π–π* transitions. Thus, direct excitation of CT states remains a minor contribution compared to charge transfer via excitons.[44,64,80-82]

Charge Transfer in Single-Component Systems

Charge transfer can occur within the bulk of a single organic material without requiring a D–A interface. When excitons encounter electronically distinct regions within the material, the formation of charges can occur, which are referred to as 'neat charges' in this work. This process arises from the interaction between donor and acceptor segments within the same molecule, resulting in intramolecular charge–transfer (ICT or CTx) states. An internal D–A structure in the molecule is required for both processes. In neat films of A–D–A structured small molecules such as Y6, CTx states are dominant due to the strong conjugation and delocalisation between donor and acceptor units. The ultrafast charge transfer within single molecules enables the rapid formation of CTx states on sub-picosecond timescales.[76,83-85]

However, intermolecular CT states can also occur, depending on the degree of morphological disorder and packing heterogeneity. Variations in molecular packing, intermolecular interactions and molecular conformations lead to spatial and energetic heterogeneity. The resulting energetic minima can theoretically localise electrons and holes, leading to charge transfer with reduced wavefunction overlap, favouring intermolecular CT states. Additionally, entropic contributions also enhance the dissociation probability of CT states, compared to CTx states. Being located over different molecules allows for much more spatial configurations than it is the case for CTx states, where electron and hole are limited to a single molecule.[86]

CTx states are also spectroscopically observed in blend systems such as PM6:Y6, where local excitations on Y6 may lead to CTx states that coexist with interfacial CT states. Spectral features in the sub-gap region may include contributions from both CT and CTx, especially at interfaces between crystalline Y6 and disordered PM6 domains. CTx states in Y6 regions of PM6:Y6 blends are less likely to directly dissociate into free charges due to their strong Coulombic binding. Instead, these CTx states can act as intermediates by transferring a hole to nearby PM6 units. This results in the formation of an interfacial CT state with a higher probability for dissociation.[70,72,85]

2.4.2. Charge Separation

Charge separation (CS) refers to the process where Coulombically bound charge–transfer states evolve into free charges (FC). Unlike charge transfer, which only involves the redistribution of charges into bound states, CS represents overcoming of Coulombic attraction to obtain spatially and energetically independent FC. Only separated charges can be extracted and contribute to photocurrent.[50]

The transition from CT states to FC typically represents an energetically unfavourable process, as fully separated charges are energetically higher than the bound CT states due to the loss of Coulombic attraction energy. Consequently, the generation of FC from CT states appears thermodynamically unfavourable when only internal energy levels are considered. Nevertheless, efficient CS is commonly observed in neat films and blends due to several factors. One of the key contributions is entropy. When a bound electron–hole pair dissociates, the resulting free charges can occupy a much larger number of spatial configurations compared to CT states. This increase in accessible microstates corresponds to an increase in entropy ΔS, which contributes to the Gibbs free energy via

$$\Delta G = \Delta H - T\Delta S \tag{2-45}$$

where the change in Gibbs free energy ΔG determines if the CS is thermodynamically favourable. Ideally, the enthalpy change ΔH represents the energy required to overcome Coulomb binding energy C. With a sufficient entropy gain, ΔG can even become negative for an uphill process, making CS thermodynamically favourable. However, ΔH is not allways limited to C. In systems where CT states fail to dissociate, additional stabilising contributions can increase the effective ΔH. These may include energetic relaxation of the CT state into deep local minima, structural reorganisation trapping charges or polarisation effects from surrounding molecules that further stabilise the bound CT state. In that case, the energy required to separate the charges increases beyond the Coulombic attraction. If $T\Delta S$ is unable to compensate, ΔG remains positive. Consequently, the CT state becomes thermodynamically trapped, making spontaneous CS either highly inefficient or even suppressed.[50,78,87,88]

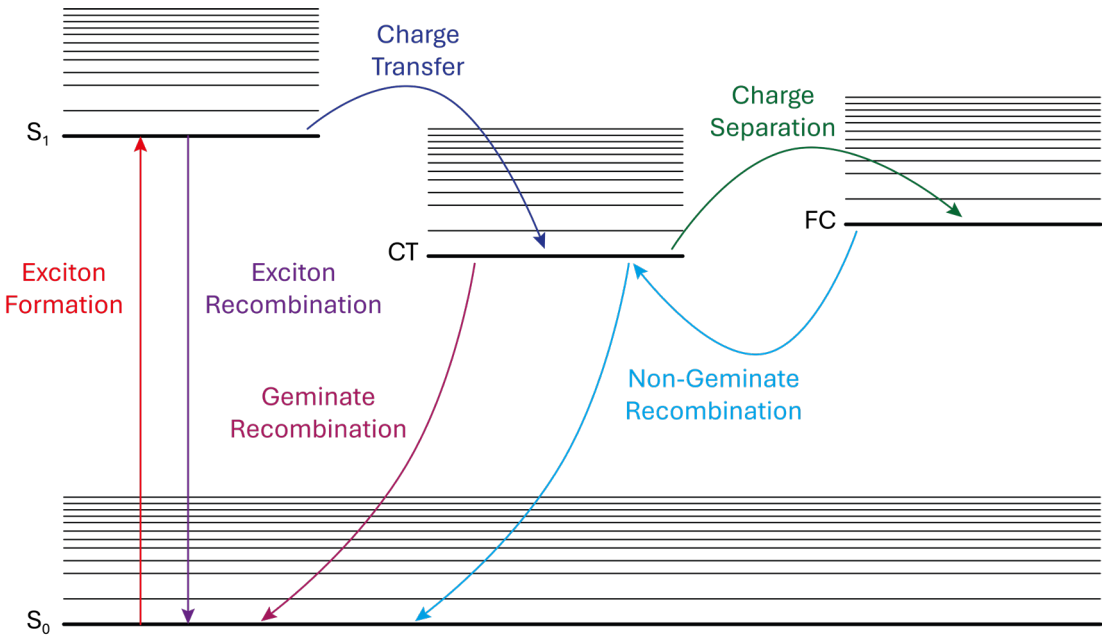

Figure 2-6: Schematic illustration of the ground (S_0), first excited (S_1), charge-transfer (CT) & free-charge (FC) state and the main pathways of exciton formation & recombination, charge transfer, charge separation and geminate & non-geminate recombination during charge generation.

In some systems, especially where donor and acceptor orbitals are strongly coupled across very short distances, quantum mechanical tunnelling may assist charge separation by allowing the electron or hole to overcome the Coulomb barrier without requiring thermal activation or excess energy. However, strong electronic coupling across densely packed interfaces can equally enhance tunnelling-mediated recombination, making it a competitive pathway to CS. Distinguishing tunnelling-assisted separation experimentally from other ultrafast processes remains challenging.[89]

Several key factors influence the efficiency of CT state dissociation. Delocalisation of charges across donor and acceptor units reduces the effective Coulomb interaction C and facilitates CS. If the electron or hole is delocalised across multiple molecules or conjugated domains, their spatial distance increases, which reduces electrostatic attraction. This delocalisation leads to a flatter potential energy distribution and increases the number of available spatial configurations, which contributes to both enthalpic and entropic driving forces for separation. Such effects are particularly pronounced in well-ordered or crystalline regions, where orbital overlap and molecular

packing support extended delocalisation, thereby increasing the probability of spontaneous CS.[50,69]

Another critical factor is the reorganisation energy E_λ. Analogous to exciton diffusion (cf. section 2.2.2 above), the reorganisation energy E_λ for charge separation refers to the energy required for structural and vibrational adjustments as the system evolves from a bound CT state to fully separated charges. Lower reorganisation energies reduce the energetic barrier and facilitate CS. It is also important to note that E_λ depends on the respective process. Exciton migration typically involves only minor changes to molecular geometry. In contrast, CS requires a redistribution of the electronic density, leading to stronger structural relaxation. As a result, E_λ involved in charge separation is typically larger than for exciton migration processes.[79,84]

Also, morphological aspects such as domain size, phase purity and interfacial gradients strongly influence dissociation dynamics. Larger or more crystalline domains can enhance charge delocalisation and reduce energetic disorder, thereby facilitating more efficient CS. Well-defined D–A interfaces maintain energy gradients that assist in separating CT states, while disordered or intermixed regions can enhance localisation and trapping. Although these conditions are favourable for CS, they can a negatively impact earlier processes. In particular, larger domain sizes reduce the total interfacial area available for charge transfer and increase the average distance excitons need to migrate. Consequently, excitons that reach the interface may exhibit less energy, reducing the probability of forming or dissociating CT states.[69,84,87]

A recent publication by Rijal, et al. [90] on PM6:Y6 using time-resolved two-photon photoemission investigates charge separation in PM6:Y6 and discusses the roles of energetic offsets, hot states, entropy, interfacial electrostatics and wavefunction delocalisation. It emphasises that spontaneous and efficient charge separation can occur even under thermodynamically unfavourable conditions if the gain in entropy and spatial delocalisation is sufficiently strong. This was also shown by Price, et al. [91] for single-component systems such as neat Y6, where CS occurs even without a D–A interface. In Y6-based blends, the interfacial electrostatics are dominated by large molecular quadrupole moments that induce energy-level bending over one to two molecular layers and assist separation. Also, the anisotropic molecular packing in Y6

sets the magnitude and sign of these quadrupolar fields and the associated vacuum-level shifts at the interface. This suggests that under certain conditions, intrinsic material properties alone can drive efficient charge separation.[79,92]

Excess Energy

'Hot states' in general are transient electronic or vibronic configurations that carry excess energy relative to the thermalised or lowest-energy states of a system. These states are typically formed directly after the absorption of a photon or a following process such as charge transfer. Due to their increased energy, hot states are not in equilibrium with their surroundings and often exhibit increased mobility, delocalisation or reactivity compared to their lowest-energy states, also described as 'cold states'. In organic photovoltaics, the concept of hot states is especially relevant in the form of hot CT states, which are created at a D–A interface when an exciton dissociates but keeps some of its excess energy. CT states with excess energy can occur if the energy of the singlet excited state exceeds that of the resulting CT sate. The CT state with excess energy can be delocalised across multiple molecules, which reduces the Coulomb interactions and results in a temporary, weakly bound state that benefits CS.[69,81]

CT in high-efficiency donor–acceptor blends has been observed to occur on sub-picosecond timescales, confirming that such processes can take place before full vibrational relaxation. Although this is necessary to be able to form CT states with excess energy, ultrafast dynamics alone do not prove that excess energy also influences CS. Excitons generated directly at D–A interfaces can also undergo similarly fast transfer without requiring hot states to be involved. In systems like PM6:Y6, the energetic offset depends on the origin of the excitation. In organics with low permittivity, the Coulomb binding energy is estimated near 0.4–0.5 eV[50]. For PM6 excitation, the offset between the donor S_1 state and the CT state is approximately 0.3 eV[44], while for Y6 excitation, the offset is considerably smaller with around 0.14–0.17 eV[88].

However, it is important to note that the energetic offset between donor and acceptor in high-efficiency blends such as PM6:Y6 is strongly influenced by the measurement

technique. While cyclic voltammetry and DFT calculations often suggest small or negligible offsets, recent solid-state photoelectron spectroscopy measurements by Bertrandie, et al. [93] reveal a significantly larger D–A ionisation energy difference of approximately 0.5 eV and demonstrated that CS is strongly suppressed when the D–A ionisation energy offset becomes negligible. While excess energy from hot CT states may in some cases support CS, it is not essential in high-performance NFA blends. Besides a substantial energetic offset, entropic gain, interfacial electrostatics and molecular organisation are also recognised as important contributing factors.[70,71,90,93]

Internal Electric Field

Electric fields play a crucial role in facilitating the dissociation of CT states. However, in organic semiconductors, the lack of high equilibrium free-carrier densities and the molecular DOS means that classical depletion-type band bending across the bulk is weak. Instead, energy-level alignment is largely set by interfacial dipoles and local molecular polarisation at contacts or heterojunctions. In devices, the active layer (AL) is embedded between electrodes and often also interlayers (IL). The difference in the electrode work functions creates a macroscopic potential gradient across the device from the electrodes. This gradient is also known as built-in potential V_{bi}, which primarily drops across the AL, defining a built-in field F_{bi}, that significantly impacts the separation of CT states. In the absence of an external bias, the field across the bulk of the active layer equals the built-in field F_{bi}, given by

$$F_{bi} = \frac{V_{bi}}{d} \tag{2-46}$$

where d is the thickness of the active layer. This equation is based on equation (2-47), whereby an idealised, uniform built-in field is assumed.[11,94,95]

In contrast, local electric fields can arise within the AL, even in the absence of electrodes. These fields originate either at D–A interfaces or within neat domains due to the alignment of molecular dipoles and structured charge distributions with quadrupole-like character. Such local fields act over only a few molecular layers, produce vacuum-level steps at interfaces and local energy-level bending, and do not

extend through the bulk of the film. However, local electric fields are generally stronger and more directional at interfaces than in neat domains due to their asymmetry. Introducing interlayers further modulates local electric fields by introducing additional interfacial dipoles. As a result, IL can modify the energy level alignment between the AL and the electrodes. The local electric field F_{loc} is position-dependent and may vary with x . It is given by the general equation for the internal electric field with

$$F(x) = -\frac{dV(x)}{dx} \tag{2-47}$$

where $V(x)$ is the electrostatic potential across the device and $F(x)$ the position-dependent internal electric field.[94-96]

High-performance NFAs with both donor and acceptor groups exhibit polarised intramolecular structures that lead to a push-pull effect, inducing interface dipole steps when donor and acceptor molecules contact. It has been shown that many NFA:polymer blends exhibit a significant vacuum-level shift at the D–A interface due to molecular dipoles formed by polarised donor–acceptor interactions or by permanent dipole moments in push-pull structures. The direction of such dipoles is therefore crucial. A dipole that raises the LUMO of the acceptor relative to the HOMO of the donor promotes CS and suppresses geminate recombination (cf. section 2.4.4).[97]

External Electric Fields

While the internal electric field present under zero applied bias is determined by the device architecture and fixed by design, applying an external field allows dynamic control over the internal potential landscape and can be systematically varied to probe or enhance CS. A forward bias is applied when the positive pole of the voltage source is connected to the anode of the device and the negative pole to the cathode, lowering the internal electric field and counteracting the built-in potential. This reduces the driving force for CS and can increase the probability of recombination. In contrast, a reverse bias increases the internal field by applying the external voltage in the same direction as the built-in field, promoting charge separation and suppressing recombination.[98]

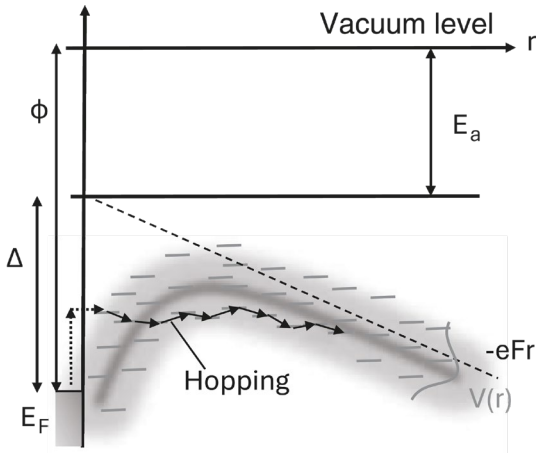

Figure 2-7: Schematic illustration of electron injection from a metallic electrode into an organic semiconductor via hopping, where r is the electrode distance, the dashed line represents the potential energy due to an external electric field F and the grey solid line shows the potential V(r) of the device. Reprinted from [16] with permission © 2015 Wiley-VCH Verlag GmbH.

Under standard conditions, the built-in field F_{bi} in combination with the local field F_{loc} is typically sufficient for CS in high-performance blends. However, modifying the total internal electric field F_{in} with an external bias V_{ex} further influences the dissociation of CT states. In an idealised 1D model, V_{ex} and V_{bi} merge via

$$F_{mac} = \frac{V_{bi} - V_{ex}}{d} \tag{2-48}$$

into the average macroscopic field F_{mac} across the device with the active layer thickness d. The total internal electric field F_{in} may vary with x and can be described with

$$F_{in}(x) = F_{mac} + F_{loc}(x) \tag{2-49}$$

where F_{loc} is position-dependent and F_{mac} is assumed to be uniform across the AL. In any case, the field-dependent behaviour of CS follows the Onsager–Braun model, where the probability of charge dissociation P_{CS} is given by

$$P_{CS}(F_{in}) = \frac{k_{CS}(F_{in})}{k_{CS}(F_{in}) + k_{GR}} = \frac{k_{CS}(F_{in})}{k_{CS}(F_{in}) + \tau_{CT}^{-1}} \tag{2-50}$$

with the rate of field-independent geminate recombination k_{GR}, the CT state lifetime τ_{CT} and the field-dependent dissociation rate $k_{CS}(F_{in})$. In the Onsager–Braun model the geminate e–h pair is treated as two-point charges that diffuse in a homogeneous dielectric under a uniform field where dissociation competes with first order recombination of a CT state with a lifetime τ_{CT}. It omits energetic disorder, interfacial dipoles, quadrupolar fields, morphology and interfacial delocalisation and thus is more for effective device level parameters than for microscopic rates.[62,96]

Within this framework a stronger macroscopic field increases k_{CS} and reduces the CT population, so reverse bias is expected to quench CT PL and enhance charge collection. This was also observed by Pranav, et al. [99] for the low-offset blend PM6:Y5. Under zero or forward bias, CT state photoluminescence (PL) increases, indicating that CT states more likely recombine radiatively than dissociate. Under reverse bias, CT state PL is quenched while CS rises. Therefore, the Coulomb binding of charge–transfer states can be overcome by applying external reverse bias. Further, time-delayed collection field (TDCF, cf. section 3.4) was used to show that on sub-nanosecond timescales a significant fraction of photogenerated e–h pairs recombine at V_{OC} but can be separated into FC under reverse bias conditions. In contrast to reverse bias which facilitates CS, the application of forward bias under illumination interrupts CS, enhances recombination, promotes unwanted charge injection and increases thermal and electrochemical stress on the device. While forward bias can be valuable under low light or short timescales in experiments such as TDCF, in combination with photoexcitation it may cause irreversible degradation of the device and should be avoided.[69,99,100]

2.4.3. Charge Transport

Hopping Transport

In organics, charge carriers are typically restricted to individual molecules or short conjugated segments due to the absence of extended electronic bands. Their transport occurs via thermally activated hopping from one localised site to another. The Miller–Abrahams model describes this hopping between two sites i and j by a hopping rate ν_{ij} via

$$\nu_{ij} = \nu_o \cdot e^{-\gamma \cdot r_{ij}} \cdot e^{-\frac{\Delta E_{ij}}{k_B T}} \tag{2-51}$$

with the attempt frequency ν_o of the charge carrier, the inverse localisation radius γ and the energetic difference ΔE_{ij}. The Miller–Abrahams model is widely used for its simplicity but does not explicitly consider spatial and energetic disorder.[47]

The Marcus theory (cf. section 2.4.1 above) offers a more refined approach as it explicitly accounts for molecular reorganisation energy and electronic coupling. NFAs like Y6 exhibit exceptionally low reorganisation energies which reduce the thermal barrier for hopping. Also, their rigid and planar molecular structure and their strong π–π stacking lead to strong electronic coupling. In combination, these factors promote efficient charge carrier mobility for hopping in modern high-performance NFAs.[101,102]

Since charge transport in disordered domains is not homogeneous, kinetic Monte Carlo simulations based on the Miller-Abrahams model or Marcus theory can be used for tracking charge carrier paths across realistic morphologies while accounting for energetic disorder, shape and width of the DOS, domain structure and interruptions in continuous transport pathways. In addition, time-dependent simulations like non-adiabatic molecular dynamics or transient localisation theory describe the evolution of charge carriers on ultrafast timescales. Time-dependent simulations consider the transition from coherent to incoherent transport and the role of vibrational interactions. In combination, these simulations link molecular-scale processes with macroscopic transport behaviour.[89,103-105]

Band-like and Coherent Transport

Band-like transport arises when charge carriers remain delocalised and move coherently through the material. This regime is typically observed in highly ordered organic crystalline films or along well-aligned polymer backbones, where structural disorder is minimal. A characteristic feature of band-like transport is that mobility decreases with increasing temperature, due to enhanced phonon scattering because of the stronger lattice vibration at higher thermal energies. Although BHJ are generally disordered, for well-structured systems like PM6:Y6 it was shown that coherent transport can appear over short distances of about 1–10 nm. This short-range delocalisation can enable ultrafast initial transport before carrier motion becomes dominated by incoherent hopping. As a result, current material design strategies increasingly focus on promoting local structural order that supports transient delocalisation while maintaining morphological conditions that favour efficient long-range hopping.[89,106,107]

Nanostructure and Field Effects on Charge Transport

While the efficiency of formation and dissociation of CT states depends primarily on local energetics and molecular interactions, long-range charge mobility depends strongly on the connectivity and continuity of phase-pure transport pathways. Morphological features such as vertical phase separation, domain connectivity and crystallinity determine whether FC can reach their respective electrodes before recombination occurs. Solvent modification, donor dilution and thermal annealing have shown that mobility can be significantly increased by reducing interfacial mixing and improving directional pathways.[97,108,109]

The transport of FC is also influenced by electric fields. In BHJ materials, field-assisted hopping often follows the Poole–Frenkel mechanism, where mobility increases with the square root of the applied field. This effect arises because the electric field lowers the Coulombic potential barrier between localised states and supports thermally activated charge hopping, especially for regions with high energetic disorder or spatial limitations. Current transport models also consider quantum tunnelling, which allows

charge carriers to overcome energy barriers without thermal activation, thereby maintaining mobility even at very high electric fields where classical hopping becomes insufficient. In addition, local electric fields that arise at non-planar or compositionally graded donor–acceptor interfaces can influence both the direction and efficiency of charge drift. These nanoscale variations in local energy levels are increasingly considered as critical factors in enabling efficient charge extraction in high-performance organic photovoltaic devices.[89,97,110]

2.4.4. Charge Recombination

Geminate Recombination

Geminate recombination refers to the annihilation of an electron–hole pair that originates from the same photon. This process occurs either when the initial exciton is not able to dissociate or when the e–h pair of a CT state recombines before full separation. It is a first-order loss process often occurring on ultrafast timescales. For PM6:Y6 it was shown that CT states live long enough to dissociate spontaneously under short-circuit conditions, leading to minimal GR. However, under open-circuit conditions or at low temperatures, geminate recombination becomes more likely due to the reduced driving force for CS.[88,91]

A mechanism proposed in the literature to explain limited charge generation in PM6:Y6 is thermally activated reverse electron transfer, where from a bound CT state the electron on the acceptor site recombines with the hole on the donor site by hopping back across the interface, effectively restoring an exciton. This process has been suggested by Jasiūnas, et al. [111] based on temperature-dependent transient absorption spectroscopy and photoluminescence measurements, which show reduced delayed dynamics at low temperatures. This was interpreted as evidence for a thermal barrier that hinders CS and promotes interfacial recombination. However, the spectral regions used to extract these dynamics may also contain contributions from electroabsorption signals, which are associated with the presence of FC. This raises the possibility that the temperature dependence observed could at least partly reflect changes in the efficiency of CS rather than direct evidence of reverse electron transfer. Although this interpretation remains speculative without explicit spectral deconvolution, similar thermally activated recombination behaviours have been observed in other NFA systems, supporting the broader plausibility of reverse interfacial electron transfer as a potential loss pathway in PM6:Y6.[112]

Bimolecular Recombination

In the classical Langevin model, bimolecular recombination is described as diffusion-limited process where separated charges recombine as soon as they encounter each

other. Its rate is proportional to the sum of carrier mobilities and inversely proportional to the dielectric constant. However, PM6:Y6 blends exhibit recombination rates that are significantly lower than those predicted by the Langevin model. This deviation arises from the spatial separation of FC carriers in donor and acceptor domains and charge delocalisation, particularly of electrons in crystalline Y6 regions, where electrons delocalise over multiple molecules, making it less likely to get encountered by a hole. This results in a suppressed bimolecular recombination that is known as non-Langevin recombination.[88,113]

Trap-Assisted Recombination

Trap-assisted recombination occurs when one charge carrier becomes temporarily captured by trap state, followed by recombination with an oppositely charged free carrier. These trap states can arise from structural disorder, impurities or chemical degradation. They are often located at D–A interfaces and their origin and depth depends on processing condition and the degradation pathway. In fresh PM6:Y6 devices, trap densities are typically low. However, it was shown that ageing processes correlate with enhanced sub-gap states and increased non-radiative recombination. Traps are often located at D–A interfaces or in interlayers, their exact origin and energetic depth varies depending on processing conditions and degradation pathways.[88,114]

Triplet-Mediated Recombination

Triplet-mediated recombination can occur via geminate and non-geminate recombination pathways. In NFA systems like PM6:Y6, it is considered a significant pathway for non-geminate recombination. Since the encountering charge carriers do not originate from the same photon, they can exhibit parallel spin, which statistically leads to the formation of triplet states with a likelihood of up to 75 %. In the geminate case, ISC (cf. section 2.3) within the CT state can populate a triplet CT state before relaxation or separation. Triplets are typically non-radiative and long-lived and thus represent a significant voltage loss mechanism and potentially initiating degradation.

Triplet formation typically proceeds via a triplet CT state, a short-lived intermediate where electron and hole remain spatially separated but exhibit parallel spins. Depending on interfacial coupling and energetic landscape, this triplet CT state can either relax into a localised triplet exciton or dissociate back into FC, depending on delocalisation and energy. Strategies to reduce losses from triplet formation include increasing the triplet energy of the acceptor, modifying donor–acceptor energetics or enhancing interfacial coupling to favour re-dissociation. Recent studies show that tuning these parameters improves both open-circuit voltage and stability in PM6:Y6 and other NFA blends.[63,64,115]

Charge–Charge Annihilation

Charge–charge annihilation (CCA) refers to a nonlinear recombination mechanism that becomes prominent at high carrier densities in spectroscopic experiments. In contrast to classical bimolecular recombination, in CCA two independently generated charge carriers of the same sign (both electrons or holes) collide randomly and recombine. The probability of CCA scales quadratically with the population of separated charges. While CCA is negligible under linear conditions, it gets relevant in nonlinear excitation regimes. As a second-order process, the CCA rate is described via equation (2-30).[11,94]

Auger-like Recombination

Auger-like recombination is a trimolecular non-radiative process in which two oppositely charged carriers recombine and transfer their energy to promote a third charge carrier to a higher excited state. The third carrier can be either an electron (negative trion) or a hole (positive trion), depending on which carrier absorbs the recombination energy. While this mechanism is significant in systems with extreme carrier accumulation, such as OLEDs or perovskite devices under electroluminescent operation, it is generally negligible in OPVs, including PM6:Y6, due to their lower steady-state carrier densities and limited injection-driven accumulation.[116,117]

2.5. Photovoltaics and Photodiodes

Photovoltaics (PV) are based on semiconducting materials that can convert light into an electric current. PVs based on inorganic materials such as silicon, gallium arsenide and cadmium telluride feature delocalised electronic states due to highly ordered lattices allowing efficient charge transport. A photon with at least the energy of E_g creates an electron–hole pair by promoting an electron from the valence band into the conduction band. This electron–hole pair is afterwards separated due to the built-in field caused by the p-n (positive-negative) junction of the device, whereby electrons are driven to the n-side and holes to the p-side. The combination of high charge carrier mobility and long diffusion length (for silicon up to 200 µm[118]) leads to power conversion efficiencies (PCE) over 26 % for silicon single-junction and over 29 % for GaAs single-junction PVs, already approaching the Shockley–Queisser limit. The Shockley–Queisser (SQ) limit is the theoretical efficiency cap for an ideal single-junction solar cell under standard AM1.5G illumination. It is derived by equating radiative generation and radiative recombination in a thermodynamic framework where sub-band-gap photons are not absorbed, excess energy above the band gap thermalise to the band edge and Kirchhoff's law, that all recombination is radiative, with the cell emitting light with the same spectral response as it absorbs. Under these assumptions the maximum efficiency is about 33 % at an optimal band gap near 1.34 eV[119] A high PCE combined with a long lifetime of more than 25 years turned inorganic solar cells into the market-dominating technology. However, conventional inorganic PVs exhibit a long list of disadvantages e.g. still reasonably high production costs, high manufacturing energy consumption and thus a long energy payback time, limited low-light performance and rare, toxic and unflexible components, which motivates research into alternative technologies.[120-133]

In 1967 Alan J. Heeger, Alan G. MacDiarmid and Hideki Shirakawa demonstrated that polyacetylene exhibits a dramatic increase in electrical conductivity when doped with halogens.[134] This marks the beginning of organic semiconductors and will later be known as the discovery of the 'fourth generation of polymer materials', which was honoured with the Nobel Prize for Heeger, MacDiarmid and Shirakawa in 2000.[135] In the 1980s this was followed by the inventions of organic light emitting diodes (OLEDs),

as the first commercially successful application of organic semiconductors and organic photovoltaics (OPVs), which also celebrated its first real-world applications.[1,4,136-139]

A general distinction is made between single-component (homojunction) and multi-component (heterojunction) OPVs. Homojunction OPVs are based on a single material that integrates both acceptor and donor functionalities within the same molecule and can be categorised into D–A type copolymers and D–A type molecules, where charge separation occurs intramolecular. Unlike inorganic p–n junctions where the high dielectric constant and extended bands lead to weakly bound Wannier–Mott excitons or even free carriers at room temperature, organic semiconductors have low dielectric constants and localised electronic states.[59] Photoexcitation therefore creates tightly bound Frenkel excitons with binding energies on the order of 0.3–1 eV, far above thermal energy at 300 K. Thermal dissociation is insufficient, so an energetic driving force and interfacial electronic coupling are required to convert neutral excitons into CT states and charges. In heterojunction OPVs, this role is provided by an intermixed D–A network on the scale of the exciton diffusion length, ensuring that most excitons reach an interface before recombining.[62] In single-component systems, donor and acceptor are located within one molecule or polymer, so separation proceeds via intramolecular CT and the local electrostatics/delocalisation of the solid.[140]

D–A copolymers like PBDB-T-2F (PM6, cf. Figure 2-9), used in this thesis, have alternating donor and acceptor units along their polymer backbone, which generate local dipole moments to assist charge separation. Although D–A copolymers are easy to process from solution, they often have limited charge carrier mobility and a lower exciton dissociation efficiency than heterojunction OPVs due to a weak driving force. In D–A molecules such as Y6 and DCV2-5T, both acceptor and donor units are located within a single molecule. D–A molecules often exhibit better charge transport than D–A copolymers due to higher crystallinity, are more reproducible due to less batch-to-batch variation than polymers and offer a better tunability of HOMO and LUMO levels. On the other hand, they form less uniform films than polymers, suffer from solubility problems, which often require fabrication via vacuum deposition and can exhibit strong molecular aggregation, leading to inefficient charge separation. Heterojunction

OPVs consists of separate donor and acceptor materials in which charge separation occurs generally intermolecularly. The most basic type of a multi-component OPV is a planar heterojunction solar cell, where donor and acceptor are applied as two separate films with one sharp interface. The well-defined D–A interface offers low charge recombination rates and a good long-term stability but also leads to a diffusion limited charge generation. Only near-interface excitons can contribute, resulting in low device performance. In bulk heterojunction (BHJ) OPVs, donor and acceptor material are blended into one common layer, resulting in a nanoscale phase-separated morphology with a maximised interfacial area. Therefore, BHJ blends exhibit an improved exciton dissociation and offer a high PCE.[75,141-143]

Organic photodiodes (OPDs) are related to OPVs and thus are based on the same operating principle. However, OPDs serve a different purpose and are intended for light detection, e.g. in sensors, imaging and optical communication. While OPVs are designed for optimise light absorption and maximise PCE, OPDs often have thinner active layers to minimise capacitance and ensure rapid charge extraction to focus on low-light sensitivity, response time and light detection across various wavelengths.[11,144]

2.5.1. Device Design

A single-junction organic photovoltaic (OPV) or organic solar cell (OSC) usually consists of an active layer (AL) sandwiched by interlayers and an electrode on each side. When a quantum of the electromagnetic field, called a photon, gets absorbed in the AL, it promotes an electron from the HOMO to the LUMO, leaving a hole in its former position and thus creating a tightly bond electron–hole pair called exciton. Excitons can form charge–transfer (CT) states, which eventually separate and get extracted by electrodes. Choosing the material for the AL, factors like absorbing region, morphology, energy level alignment of D and A and phase separation play a crucial role for efficient devices. Also, the thickness of the active layer is important. While too thick layers can lead to recombination losses, too thin layers can result in insufficient light absorption. For blends with non-fullerene acceptors (NFA), a AL thickness of around

100nm is favourable.[145,146] The electrodes of a device should be chosen in a way, that the cathode exhibits a low work function, the anode a high work function and both aligning with the energy levels of the respective interlayers and the active material. In OPVs and OPDs indium tin oxide (ITO) is preferred as an anode material due to its suitable work function and its transparency. Semi-transparent thin layers of aluminium or silver are commonly used for cathodes to ensure sufficient light transmittance. While electrodes are responsible for collecting and extracting charges, IL enable transport from the AL to the respective electrodes. An electron transport layer (ETL) facilitates electron transport to the cathode and reduces recombination by blocking holes. ETL have a high electron mobility and should provide an energy level that aligns with the LUMO of the electron acceptor (A) to minimise energy losses. A hole transport layer (HTL) facilitates hole transport from the AL to the anode by providing a high hole mobility, an energy level aligning with the HOMO of the electron donor (D) and the ability of blocking electrons. The thickness of IL should be chosen in a way, that its thin enough for efficient charge extraction without implementing a significant series resistance.[147-151]

The presence of multiple thin layers can lead to optical microcavities, where the incident light undergoes multiple reflections at interfaces with different refractive indices. This leads to interference effects that can influence the efficiency and the optical characterisation of the device. A carefully optimised cavity resonance can lead to constructive interferences at wavelengths where the AL shows strong absorption. This can enhance exciton and thus charge generation and can lead to better device performance. If the cavity resonance is not optimised, the optical field can become non-uniform, leading to regions of over- and under-absorption, which can result in inefficient exciton dissociation, local charge accumulation and enhanced recombination losses. In OPDs cavity effects can additionally increase the RC time constant τ_{RC} or lead to uneven carrier extraction, affecting the device performance. In ultrafast spectroscopy like transient absorption spectroscopy (cf. section 3.5), interferences at the cavity can influence the spatial and spectral distribution of the optical field. Both probe beam (white-light continuum) and pump beam (excitation)

can therefore exhibit local intensity variations. This inhomogeneity can lead to distorted signals and dynamics.[152,153]

When manufacturing organic devices, it is often required that the active layer is exposed to a vacuum, e.g. when evaporating the electrode. However, a prolonged exposure of the AL to vacuum can lead to morphological changes like over-evaporation of residual solvents, excessive phase separation or other changes in the microstructure of the D–A blend. A disruption of the nanoscale phase separation can affect exciton dissociation and charge transport, which leads to degradation of the AL and compromises the performance of the device. Using solution-processed interlayers or vacuum-free electrode deposition minimises the vacuum exposure time and prevents degradation.[154-157]

Organic layers in optoelectronic devices are inherently sensitive to environmental influences such as moisture, oxygen and ultraviolet (UV) light. To avoid these factors, fabrication under inert conditions and an effective and robust encapsulation is required to protect them from degradation, preserve their performance and extend their operational lifetime. Common encapsulation techniques are cover-glass encapsulation by attaching a glass slide with edge sealing, thin-film encapsulation by vapor-deposition of parylene and hybrid multilayer encapsulation by combining thin-film and cover-glass encapsulation techniques.[158-160]

2.5.2. Performance Metrics of Devices

External and Internal Quantum Efficiency

Quantum efficiencies (QEs) are important parameters for both OPV and OPD. The external quantum efficiency (EQE) or Incident Photon-to-Current Efficiency (IPCE) describes the ratio between the number of charges that are generated and extracted n_{el} to the number of incident photons $n_{i,ph}$ when irradiated at a certain wavelength λ. It reflects how efficient OPVs convert photons into separated charges and how efficient OPDs responds to light. The EQE can be expressed with

$$EQE(\lambda) = \frac{n_{el}}{n_{i,ph}} = \frac{J_{ph} \cdot hc}{q \cdot \lambda \cdot P_{in}} \quad (2\text{-}52)$$

where the photocurrent density J_{ph} is multiplied with the Planck constant h and the speed of light c and divided by the elementary charge q, the excitation wavelength λ and the incident light intensity P_{in}. For EQE all incident photons and therefore all optical effects and losses are considered. To account for wavelength-dependent absorption strength, EQE is divided by the absorptance of the AL at a certain wavelength $A_\alpha(\lambda)$.

$$IQE = \frac{EQE}{A_\alpha(\lambda)} \quad (2\text{-}53)$$

As a result, the internal quantum efficiency (IQE) is obtained, which characterises the active layer by its ability to convert absorbed photons into extracted charges. Therefore, IQE can be described as the product of every needed step during the photoconversion.

$$IQE = \eta_{diff,Ex} \cdot \eta_{diss,Ex} \cdot \eta_{sep} \cdot \eta_{coll} \quad (2\text{-}54)$$

IQE consists of the exciton diffusion efficiency $\eta_{diff,Ex}$ to the interface before recombining, the exciton dissociation efficiency $\eta_{diss,Ex}$ at the interface into CT states, the charge separation efficiency η_{sep} for separation of CT states and the charge collection efficiency η_{coll} for transportation to and extraction of charges at the respective electrodes. In order to improve the performance of a device it is crucial to optimise all efficiency factors as they all play an important role in the overall IQE.[75]

Dark Current Density

In the absence of light, active layers of both OPV and OPD are not conductive. If AL in a device is embedded between two electrodes, the device acts as a diode in the absence of light and applying a reverse bias should result in capacitor behaviour. Neither OPV nor OPV should exhibit dark current. The dark current density J_{dark} is the

background current density in the absence of illumination and represents the dark current I_{dark} per unit area of the active layer. I_{dark} can be expressed as

$$I_{dark} = I_0\left(e^{q \cdot V / k_B \cdot T} - 1\right) \tag{2-55}$$

originating from the Shockley equation

$$I = I_0\left(e^{q \cdot V / k_B \cdot T} - 1\right) - I_{ph} \tag{2-56}$$

with the total current I, the dark saturation current I_o, the photocurrent I_{ph}, the applied voltage V the Boltzmann constant k_B at a temperature T. In the absence of light, $I_{ph} = 0$ resulting in $I = I_{dark}$.[161]

Dark current can occur due to thermally generated charge carriers, recombination of charge carriers, structural stability issues (e.g. pinholes), as well as trap states caused by defects and impurities in the AL and intra-gap states. A low J_{dark} is crucial for both OPV and OPD devices. In OPVs it lowers the diode saturation current which increases the open-circuit voltage V_{OC} and typically the fill factor FF, leading to higher PCE. For OPDs, a low J_{dark} lowers dark noise which improves detectivity and signal-to-noise ratio (SNR).[11,28,162,163]

Capacitance

The geometric capacitance C_g indicates the ability of OPVs and OPDs to store electrical charges by applying an external reverse bias. It is primarily dependent on geometry and permittivity of the active layer. Since both OPVs and OPDs are typically designed like a parallel-plate capacitor, C_g is obtained via

$$C_g = \frac{\varepsilon_0 \cdot \varepsilon_r \cdot A_x}{d} \tag{2-57}$$

with the pixel area A_x, the thickness of the active layer d, the vacuum permittivity ε_0, the dielectric constant of the active layer ε_r, typically in the range of $\varepsilon_r = 2 - 4$ and $C_g \propto \varepsilon_r$.[59,164,165] While a higher dielectric constant can lower the coulomb binding energy of excitons and facilitate separation, a too high capacitance can lead to charge

accumulation at the interface and thus to slower charge extraction and increased recombination. Correspondingly, a lower capacitance leads to faster extraction but can compete with an also lower ε_r.[144,166,167]

For OPDs, this speed of response is known as the RC time constant τ_{RC} and is expressed as

$$\tau_{RC} = R_L \cdot C_g \tag{2-58}$$

with the geometric capacitance C_g of the photodiode and the load resistance R_L. τ_{RC} is defined as the time it takes to charge the capacitor to around 63.2 % of the applied voltage or discharge to around 36.8 % of its initial voltage. For both OPV and OPD, an optimised capacitance is crucial for balancing charge generation and extraction processes. OPDs in particular benefit from a low C_g, as it accelerates response time, improves high-frequency performance and lowers the noise ratio.[144,168]

Power Conversion Efficiency

The power conversion efficiency (PCE) is next to EQE and IQE one of the most important parameters for evaluating OPVs. PCE is the ratio of the electrical power output P_{out} to the optical power input P_{in} and can be expressed with

$$PCE = \frac{P_{out}}{P_{in}} = \frac{J_{SC} \cdot V_{OC} \cdot FF}{P_{in}} \tag{2-59}$$

as the product of the short-circuit current density J_{SC}, the open-circuit voltage V_{OC} and the fill factor FF under the illumination of P_{in} with the intensity of one sun. For illumination the standardised global horizontal irradiance spectrum AM1.5G (cf. section 2.2.1, Figure 2-1) is used as representation of the yearly average irradiance on the terrestrial surface in temperature latitudes, with large population centres. One sun is defined as an irradiance intensity of 1000 W/m^2 in the wavelength range from 290 nm to 3000 nm.[141,169,170]

The short-circuit current density J_{SC} is the current density in the OPV device when the voltage across the solar cell is zero. Via the Shockley equation the short-circuit current I_{SC} can be described with

$$I_{SC} = -I_{ph} \tag{2-60}$$

as the applied voltage $V = 0\,V$.[171] In an ideal solar cell, the short-circuit current is equivalent to the photogenerated current and therefore the highest achievable current. A stronger photocurrent generation leads to a higher J_{SC}. The open-circuit voltage V_{OC} can be determined via the Shockley equation (2-56) with $I = 0$.

$$V_{OC} = \frac{k \cdot T}{q} \cdot \ln\left(\frac{I_{ph}}{I_o} + 1\right) \tag{2-61}$$

V_{OC} is the maximum available voltage that the solar cell generates during illumination when the current through the device is zero.[171,172]

The fill factor FF describes the 'squareness' of the OPV via

$$FF = \frac{V_{max} \cdot I_{max}}{V_{OC} \cdot I_{SC}} = \frac{P_{max}}{V_{OC} \cdot I_{SC}} = \frac{\text{area A}}{area\ B} \tag{2-62}$$

where FF is the ratio of the maximum power of the OPV P_{max} to the open-circuit voltage V_{OC} and short-circuit current I_{SC}. The FF measures the quality of the solar cell, i.e. how effectively charges are extracted. It is strongly affected by the two parasitic resistances shunt resistance R_{sh} and series resistance R_{se} . R_{se} represents the resistance for charge carrier transport and extraction and is mainly caused by poor electrode contacts, low charge carrier mobility in the AL and resistive losses in the IL. A higher R_{se} leads to reduced J_{SC}, shifts the maximum voltage V_{max} and lowers FF. R_{sh} represents leakage pathways originating from defects, impurities, pinholes, poorly defined interfaces and trap-assisted recombination. A lower R_{sh} leads to increased leakage current at low voltages and lowers FF. Therefore, a lower R_{se} and a higher R_{sh} is preferred as a higher FF means less resistive losses and a better charge extraction.[169,173]

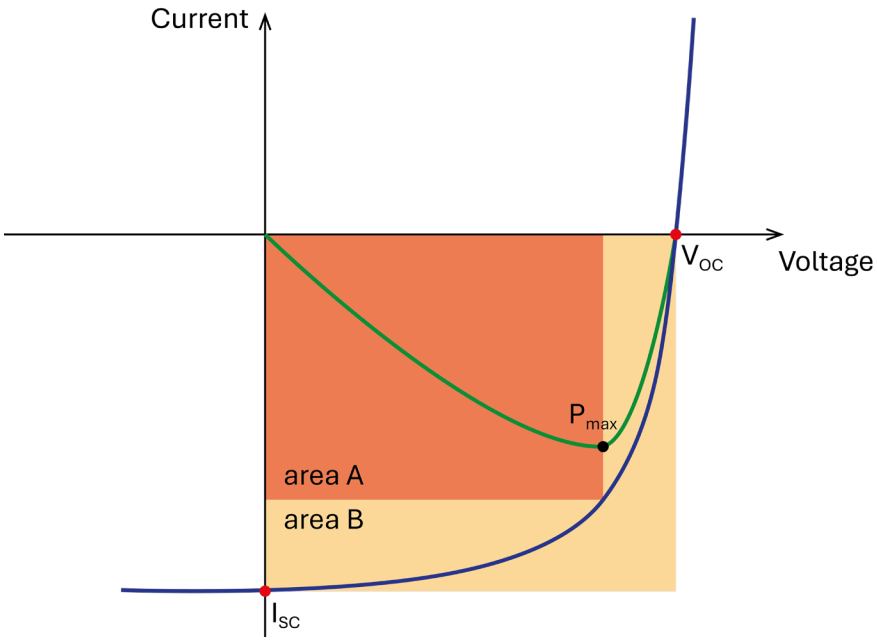

Figure 2-8: Schematic illustration of an I-V curve (blue) and the corresponding power output as a P-V curve (green) with the open-circuit voltage V_{OC}, the short-circuit current ISC, the maximum power output Pmax and the areas A and B, whose ratio corresponds to the fill factor FF.[28]

Responsivity

The responsivity R is an indicator for evaluating OPDs and is closely related to the EQE of the device.

$$R = \frac{I_{ph}}{P_{in}} = \frac{e}{h \cdot c} \cdot \lambda \cdot EQE \tag{2-63}$$

R is defined as the quotient of the measured photocurrent I_{ph} and the optical power input P_{in} and displays the obtained I_{ph} per illumination unit. A higher R represents a higher light sensitivity.[174]

Noise Equivalent Power and Specific Detectivity

For OPDs it is important to be sensitive to low incident light intensities. The detectivity D^* as the inverse of the noise equivalent power (NEP) displays how well the OPD detects weak signals and distinguish them from the detector noise. NEP is the minimum optical power required to produce a signal-to-noise ratio (SNR) of 1.

$$NEP = \frac{1}{D} = \frac{i_n}{R} \tag{2-64}$$

The specific detectivity D^* is obtained by normalising $D°$ by the detector area A_x and the bandwidth Δf and can be expressed with

$$D^* = D° \cdot \sqrt{A_x \cdot \Delta f} = \frac{R \cdot \sqrt{A_x \cdot \Delta f}}{i_n} \tag{2-65}$$

D^* measures the ability of an OPD to detect weak signals while minimising noise. Therefore, a higher D^* means better performance of the OPD.[161]

Linear Dynamic Range

The linear dynamic range (LDR) describes the linear detection range of the OPD. In this region the response of the OPD is proportional to the incident light intensity with NEP as the lower limit. A higher LDR corresponds to a higher ability of detecting strong and weak signals.[175]

2.6. NFA-Blended Systems

Early organic photovoltaics relied on fullerene acceptors. Ultrafast photoinduced electron transfer from conjugated polymers to C_{60} established that interfacial charge separation could outcompete geminate recombination in molecular semiconductors.[176] The bulk heterojunction (BHJ) architecture then emerged to create a bicontinuous donor–acceptor (D–A) network that improved exciton harvesting and charge transport, which set the template for two component devices for more than two decades.[177] Fullerenes, however, offered spectral and energetic limitations. Fullerenes primarily absorb in the UV region with a weak absorption extending into the visible (VIS) up to approximately 500 nm, where solar irradiance is only minor and where it would overlap with the absorption region of donor polymers. Because polymers typically absorb between 350 nm and 620 nm, a fullerene:polymer blend would not be able to utilise the solar spectrum beyond that, leaving a large fraction of it unused. Also, fullerenes are limited in their chemical and energetic tunability, which over time has made them the limiting factor for further improvements in OPV performance. This motivated research to move towards non-fullerene acceptor (NFA) materials that could absorb strongly and allow controlled energetics at the interface. Perylene-diimide and fused-ring systems such as the ITIC-family turned out to be reasonable alternatives to fullerenes, with stronger and more tuneable absorption and more precise control of interfacial energetics.[178] As the design developed further, it became apparent that NFAs suppress non-radiative energy losses compared to fullerene mixtures, placing the focus on materials that combine strong absorption with low energy losses.[179]

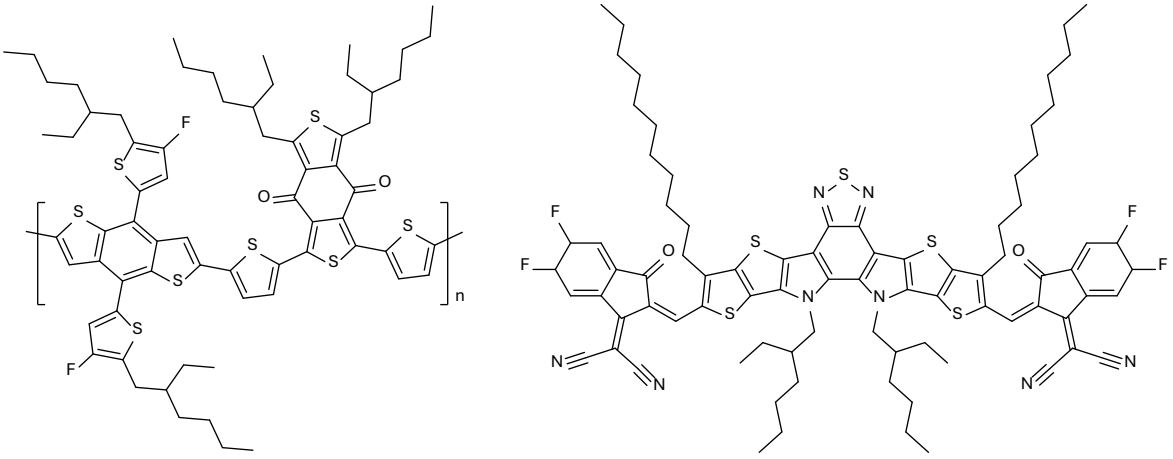

Figure 2-9: Molecular structures of the donor polymer PM6 and the non-fullerene acceptor Y6.

Modern non-fullerene acceptor blends led to a re-evaluation of the former view that large energy differences between donor and acceptor are essential for efficient generation of free charges. Instead, they shifted the focus towards how free charges form at low energetic offsets. By designing NFA materials with a low bandgap, in a polymer:NFA blend such as PM6:Y6 (cf. Figure 2-9), the absorption range of the blend could be extended over the entire Vis spectrum up to 1100 nm in the NIR, which improves the overlap with the solar spectrum and thus the light-harvesting efficiency.[180-184] Accordingly, PM6:Y6 is used in this thesis to probe wavelength and field effects on high-performance D–A blends.

2.6.1. Aggregation of Y6

According to Kasha, molecules can aggregate into two main types of aggregates, based on the alignment of their transition dipole moments. In H-type aggregates, transition dipole moments are arranged ‘side-by-side’ (parallel aligned dipoles). Here, the Coulomb coupling is destructive, which leads to a band of singlet states (excitons) in which the highest energy state utilises the entire oscillator strength. H-type aggregates typically exhibit a hypsochromic shift and a reduced 0–0 band intensity (relative to 0–1), thereby weakening the lowest-energy radiative transition.[29,185].

In J-type aggregates, transition dipole moments are arranged 'head-to-tail' (collinear aligned dipoles). Due to constructive excitonic coupling, this causes a bathochromic shift and a dipole-allowed lowest excitonic transition with high oscillator strength which often enhances photoluminescence. These aggregation behaviours are fundamentally governed by various intermolecular interactions. Permanent molecular dipoles cause dipole-dipole interactions that influence the energetic disorder and thereby the width of the DOS, depending on their orientation and uniformity within the thin film. While randomly orientated dipoles lead to electrostatic heterogeneity, which broadens the DOS and affects charge transport, aligned dipole orientations under controlled deposition conditions can improve electrostatic homogeneity, which effectively reduces energetic disorder and narrows the DOS. Intermolecular forces including dispersion, quadrupolar and dipole–dipole interactions can promote denser molecular packing and higher crystallinity, which can reduce energetic disorder and thus narrow the DOS.[29,185-187]

Y6 predominantly form J-type aggregates in both solution and films. Spectroscopic studies by Kroh, et al. [188] revealed the presence of two distinct J-type aggregates (I and II) for two transitions each, which were identified using a modified Franck-Condon model. Dipole-dipole interactions lead to splitting of the excited states, resulting in two allowed transitions between S_0 and S_n, splitting in a lower-energy transition T1, which is dominant in J-aggregates and a higher-energy transition T2, which is dominant in H-aggregates. Utilising Kasha's exciton model, the energy levels of the Y6 excitons states are symmetrically split by the exciton coupling strength β around the monomer transition energy E_M and the dispersion shift ΔD.

$$E_{T1/T2} = E_M + \Delta D \pm \beta \tag{2-66}$$

The magnitude of the exciton splitting ΔE_{Ex} results from the difference between the energy of the higher-energy transition E_{T2} and the energy of the lower-energy transition E_{T1}.

$$\Delta E_{Ex} = E_{T2} - E_{T1} = (E_M + \Delta D + \beta) - (E_M + \Delta D - \beta) = 2|\beta| \tag{2-67}$$

Accordingly, the splitting magnitude between T1 and T2 is defined by the exciton coupling strength β and arises from the Coulombic interactions between the transition dipoles. In molecular aggregates, the degree of π–π stacking and the relative orientation of neighbouring chromophores determine the extent of the orbital overlap. A stronger orbital overlap leads to a stronger β and thus to a larger T1-T2 energy splitting. [188,189]

Aggregate I is the dominant aggregation in Y6 and arises from strong π–π interactions, especially from dimers with core/core and terminal/terminal interactions (C/C–T/T) and dimers with core/terminal interactions (C/T–C/T). Although the C/T–C/T interactions involve colinearly aligned dipoles and are thus characteristic of J-aggregates, the dominant C/C–T/T interactions (parallel aligned dipoles) would, according to the classical Kasha model, be more indicative of H-aggregates. At first glance, this appears contradictory and suggests that the aggregation behaviour of Y6 cannot be fully explained by the classical Kasha model alone. This behaviour has been explained within the framework developed by Spano [189], in which strong vibronic coupling between electronic transitions and molecular vibrations reshapes the excitonic energy landscape. It redistributes oscillator strength among vibronic sublevels and allows the lowest excited state to become optically active. In addition, interactions arising from orbital overlap and intermolecular charge–transfer character (cf. section 2.4.1), further stabilising these low-energy excitonic states and enhancing their oscillator strength. These combined effects lead to J-type spectral characteristics despite the parallel dipole alignment. Therefore, both intermolecular interactions lead to a high delocalisation and a redshifted absorption, while the strong exciton coupling β with 205 meV leads to a large T1-T2 splitting. The T1 transition occurs at 1.52 eV (816 nm) and dominates the absorption spectra, while the T2 transition appears at 1.93 eV (642 nm) with a low intensity, which is typical for J-type aggregates. Aggregate II was first observed in cooled Y6 solutions below 195 K and is less prominent at RT. Aggregate II arises from terminal/terminal (T/T) interactions, is more ordered and emerges more slowly than aggregate I. Due to the weaker π–π interactions, the exciton coupling β with 105 meV is weaker than for aggregate I, which leads to a narrower T1-T2 splitting. Annealing or cooling below 195 K allows molecules to reorganise into

aggregate II. The T1 transition appears at 1.62 eV (765 nm) and the T2 transition at 1.83 eV (678 nm). Besides aggregate I and II, there is a significant fraction of Y6 molecules that remains unaggregated. Due to steric hindrance by branched side chains, kinetic limitations and thermodynamic heterogeneity, Y6 exhibits an amorphous phase leading to an absorption feature at 1.73 eV (717 nm). The entirety of all aggregation states results in the Y6 spectrum with a sharp peak around aggregate I, T1 and a broader distribution at shorter wavelengths. While aggregate I and II exhibit narrow DOS by themselves, the variety of energetically different domains, the variability in local microstructure and the presence of a disordered amorphous fraction cause Y6 to exhibit a broad absorption spectrum.[29,188-190]

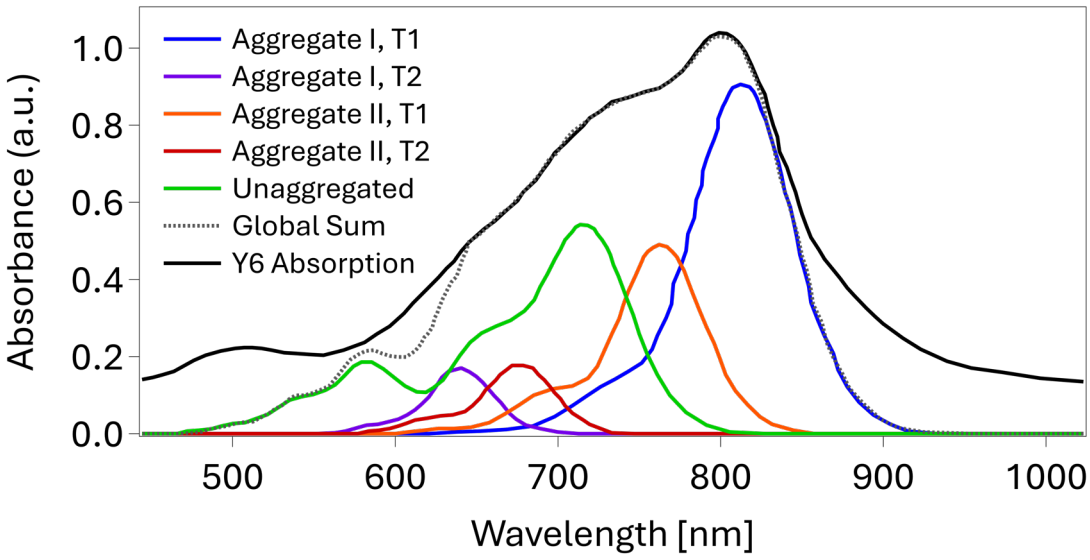

Figure 2-10: Steady-state absorption spectra by Kroh, et al. [188] of the two transitions of both Y6 J-type aggregates I, T1 (blue), I, T2 (purple), II, T1 (orange), II, T2 (red), the unaggregated Y6 phase (green) and the sum of all aggregation states (grey, dashed), compared to the spectrum of a Y6 film (black).

2.6.2. Charge Generation and Field Response in PM6:Y6

Barrierless or near-barrierless photocurrent generation was reported for PM6:Y6 with photoconversion efficiencies (PCEs) exceeding 19 %[191]. For well-optimized PM6:Y6, nearly uniform free charge generation with weak field sensitivity has been reported, which is now generally considered a characteristic feature of this mixture class.[70] It was further shown, that charge separation in PM6:Y6 can proceed endothermically

after rapid cooling due to an electronic landscape in which suitable configurations enable separation without relying on hot CT states or high-energy excitation.[90] Also, long exciton diffusion lengths in modern NFAs support a picture in which singlet excitons can migrate into lower-energy Y6 aggregates before interfacial charge transfer occurs.[43]

Several mechanisms have been proposed, yet their relative importance under device-relevant conditions remains unresolved. Delocalised or hybridised CT states with local excitons are reported to lower the effective barrier for separation, but how far this depends on the controls outcomes across nanoscales is unclear.[44,78,80,192-194] Y6 excitons can relax or migrate toward lower-energy aggregate sites, but the time available before thermalisation and the extent of competition with localisation are not yet clear.[195] Donor excitation form interfacial charges on sub-picosecond timescales, but population persistence appears to depend on whether those charges reach more delocalised acceptor regions.[196] At device level the reported bias response ranges from weak to measurable, depending on morphology and energetic offsets.[70,197] A clear boundary for when bias-driven charge collection is present or negligible is still missing. This requires time-resolved measurements that follow the earliest dynamics and connect them to the charges that persist in films and devices across relevant excitation energies. What is missing is a wavelength- and field-resolved investigation that links the earliest preparation of states to the charges that survive on later timescales in films and devices.[44]

2.7. Single-Component Systems

The majority of high-performing OPVs and OPDs are based on D–A heterojunctions, which allow efficient generation and separation of charges. However, these multi-component systems often introduce challenges and limitations such as morphological stability, reproducibility and manufacturing scalability. They often suffer from increased dark current and operational variability, limiting performance metrics such as sensitivity, detectivity and dynamic range, which are important for OPDs. The complexity of multi-component systems arises from phase separation and

energetic inhomogeneity at D–A interfaces and has long hindered the commercial applicability of organic optoelectronic devices.[144]

Single-component materials offer an alternative strategy by enabling charge generation within a chemically uniform system, by avoiding interfacial D–A charge transfer between different domains and thus the need for an optimisation of nanoscale phase separation. Studies on neat small molecules based on chloroboron subphthalocyanine (SubPc) and subnaphthalocyanine (SubNc) show that free-carrier yield is governed by the molecular driving force and can be modulated by external or internal electric fields. Depending on the system, photogeneration can occur with little field assistance or show a measurable field response.[91,198] At homojunction boundaries of α -sexithiophene (α-6T), orientation-dependent electrostatics can shift local energy levels and support hybridisation of charge-transfer and excitonic states, thereby facilitating charge separation.[199] Furthermore, neat photoactive layers based on partially chlorinated subphthalocyanines (Cl-SubPc) with large local multipole moments were used in high-performance photodetectors in which photocurrent arises primarily from direct generation within the neat layer.[200] Also, for neat Y6 films charge formation under 1 sun conditions was reported with 60–90 % of the excitons converting to charge carriers, while limitations are attributed to traps and bimolecular recombination.[91]

2.7.1. Motivation and Relevance of DCV2-5T

Oligothiophene donors including the DCVnT series have been investigated as donor components in fullerene BHJ blends, revealing relations between conjugation length, planarity, packing and device metrics.[201,202] Originally designed as OPV materials, these oligothiophenes offer strong intramolecular charge-transfer character and tuneable electronic properties. In a broader context, DCV5T-Me devices achieved single-junction efficiencies around 8 %[203] and over 10 %[204] in serially stacked triple-junction. Neat DCV-end-capped oligothiophenes form ordered thin films and support hole transport, which allows investigation of how excitation energy and electric fields influence charge formation and extraction without blend interfaces. In photodiodes,

single-component materials are targeted to reduce interfacial complexity while maintaining low dark current, high specific detectivity and fast response.[144,200]

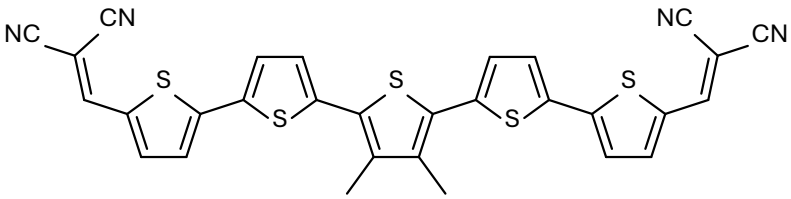

DCV2-5T

Figure 2-11: Molecular structure of the acceptor–donor–acceptor small molecule DCV2-5T.

Although neat small-molecule films can generate mobile carriers without a D–A interface, several aspects of the underlying mechanism remain unresolved. The general boundary between weak-field generation and field-assisted generation has been shown on a few systems, indicating a dependency on the thermodynamic driving force, while general framework across excitation energies and device architectures is missing.[198] Also, whether charge survival requires transient access to delocalised or hybridised configurations before thermalisation remains debated. While it can facilitate separation, general conditions remain not fully resolved.[199] Furthermore, it is debated whether the operation of single-component systems is generation-limited or extraction-limited. In specific cases, it is suggested that the external response limits even strong intrinsic charge generation.[91] Finally, electrodes influence the built-in field and transport layers the extraction barriers. However, ultrafast measurements are typically performed on films, while the picosecond to nanosecond influence of interlayers and electrodes is only rarely measured directly.[205]

Chapter 3

Experimental Methods

3.1. Sample Preparation

3.1.1. DCV2-5T

Sample preparation of DCV2-5T was performed in the lab of Prof. Karl Leo at IAPP Dresden in Germany. For the small molecule DCV2-5T (2,2'-[3'',4''-dimethyl-2,2':5',2'':5'',2''':5''',2'''':quinquethien-5,5''''-diylbis(methane-1-yl-1-ylidine)]di-malononitrile) from *Synthon Chemicals GmbH & Co. KG* encapsulated samples were prepared either with and without transport layers and with and without electrodes. The full-stack was fabricated in a geometry with ITO (indium tin oxide) as anode (90 nm), BPAPF:NDP9 ((9,9-bis[4-(N,N-bis-biphenyl-4-ylamino)phenyl]-9H-fluorene) : (*Novaled p-dopant #9)*; 30 nm) and BPAPF as HTL (5 nm), DCV2-5T as AL (40 nm), BPhen (Bathophenanthroline) as ETL (8 nm) and Ag as cathode (100 nm and 10 nm for semi-transparent devices for TA and EDA) with a 2 nm Ca cathode interlayer. The reference devices are using a DCV2-5T:C_{60} (2:1) bulk heterojunction blend with otherwise identical architecture. Devices labelled as '0 nm doped ETL' contain only an 8 nm undoped BPhen ETL, while '50 nm doped ETL' contain an additional 50 nm layer of caesium-doped BPhen doped with a molar ratio of 1:1.

Substrates are first cleaned in an ultrasonic bath in several steps using N-methyl-2-pyrrolidone, deionized water and ethanol, with a subsequent oxygen plasma treatment. Samples without electrodes are fabricated on glass substrates. All samples were fabricated using thermal evaporation in a vacuum chamber below 10^{-7} mbar. The deposition process was performed in a customised, single-chamber, semi-industrial deposition tool from *Lesker* for all layers of the respective sample configuration without air exposure in between. On top of pre-structured ITO substrates from *Thin Film Devices Inc.* with a sheet resistance of 32 Ω/□, layer materials are sublimated from melting pots, while the deposition rates are monitored by a quartz crystal microbalance and a deposition rate below 0.2 Å/s for DCV2-5T.

3.1.2. PM6:Y6 & PS:Y6

Sample preparation of PM6:Y6 and PS:Y6 thin films and devices was performed together with Manasi Pranav and Dr. Atul Shukla in the lab of Prof. Dieter Neher at University of Potsdam in Germany. The polymer PM6 (Poly[(2,6-(4,8-bis(5-(2-ethylhexyl-3-fluoro)thiophen-2-yl)-benzo[1, 2-b:4,5-b']dithio-phene))-alt-(5,5-(1',3'-di-2-thienyl-5',7'-bis(2-ethylhexyl) benzo[1',2'-c:4',5'-c']dithio-phene-4,8-dione)]) and the NFA Y6 (2,2'-((2Z,2'Z)-((12,13-bis(2-ethyl-hexyl)-3,9-diundecyl-12,13-dihydro-[1,2,5]thiadiazolo[3,4-e]thieno[2",3'':4',5']thieno[2',3':4,5]pyrrolo[3,2-g]thieno[2',3':4,5]thieno[3,2-b]indole-2,10-diyl)bis(methanylyl-idene))bis(5,6-difluoro-3-oxo-2,3-di-hydro-1H-indene-2,1-diylidene))di-malononitrile) were both obtained from *1-Material Inc.* and chloroform was obtained from *Carl Roth*. The devices were fabricated in a conventional geometry with ITO as anode, PEDOT:PSS (Poly(3,4-ethylenedioxythiophene) polystyrene sulfonate; *Clevios PVP.AL 4083*) as HTL, PM6:Y6 as AL, PDINN (2,9-Bis[3-[[3-(dimethylamino)propyl] amino]propyl]-anthra[2,1,9-def:6,5,10-d'e'f']diisoquinoline-1,3,8,10(2H,9H)-tetrone)) as ETL and Ag as cathode.

The pre-patterned ITO glass substrates from *Lumtec* were cleaned in an ultrasonic bath with acetone, *Hellmanex III*, deionized water and isopropanol for 10 min each with subsequent microwave oxygen plasma treatment for 4 min at 200 W. Afterwards, an aqueous solution of PEDOT:PSS (*Heraeus Clevios™ PVP.AL 4083*) was filtered with a 0.2 µm PTFE syringe filter, applied via spin coating at 5000 rpm for 30 sec and thermally annealed at 150 °C for 15 min. For both films and devices, a solution with a total concentration of 14 mg/mL with a 1:1.2 weight ratio of PM6 and Y6 were dissolved in chloroform ($CHCl_3$) from *Carl Roth*, stirred for 3 h at 40 °C in inert air. PM6:Y6 was spin coated at 3000 rpm for an active layer thickness of 116 nm, which was measured with a *Dektak XT* profilometer from *Bruker*. The PS:Y6 films were prepared with similar conditions and concentrations with polystyrene (PS) from *Sigma Aldrich*. Then, a 1 mg/mL solution of PDINN in methanol from *Sigma Aldrich* was spin coated at 1500 rpm. At the end, an Ag electrode was evaporated on top under 10^{-6}–10^{-7} mbar with a thickness of 5 nm for the semi-transparent electrode and a thickness of 100 nm for all other measurements not directly related to ultrafast spectroscopy. Pixel size

(active area) was 4 mm^2 for TA and EDA, 1 mm^2 for TDCF and 6 mm^2 for EQE and JV measurements.

From the same PM6 and Y6 batches, thick films of PM6:Y6 were prepared from a chloroform-based solution made under the same conditions as before for the thin-film substrates. A 1 mm thick double-side polished sapphire slide from *Crystran* (n_0 = 1.76) was used, cleaned in an ultrasonic bath with toluene, acetone and isopropanol, before the PM6:Y6 solution was drop casted on top with a layer thickness of 1 µm.

3.2. Film Characterisation

Absorbance

Absorbance was measured on films on glass substrates in transmission mode with a *Shimadzu SolidSpec-3700* from Jakob Wolansky in the lab of Prof. Karl Leo at IAPP Dresden in Germany for DCV2-5T and with a *Varian Cary 5000* spectrophotometer together with Manasi Pranav and Dr. Atul Shukla in the lab of Prof. Dieter Neher at University of Potsdam in Germany for PM6:Y6 and PS:Y6.

Photoluminescence

Photoluminescence for DCV2-5T was measured from Jakob Wolanski and Dr. Anton Kirch in the lab of Prof. Sebastian Reineke at IAPP Dresden in Germany with a collimated mounted *M505L3* 505 nm LED from *Thorlabs*, equipped with a *FBH510-10* bandpass filter from *Thorlabs*.

Atomic Force Microscopy

Atomic force microscopy (AFM) measurements for DCV2-5T were performed with a *Nanosurf AG Flex-Axiom* in tapping mode with *TAP-190Al-G* AFM tips from *BudgetSensors*. AFM measurements were performed by Jakob Wolansky with assistance of Dr. Shaoling Bai and Dr. Katherina Haase in the lab of Prof. Stefan Mannsfeld at *TU Dresden*, Germany.

Grazing Incidence Wide-Angle X-ray Scattering Spectroscopy

Grazing Incidence Wide-Angle X-ray Scattering (GIWAXS) for DCV2-5T are performed and analysed by Felix Talnack at the *SIRIUS beamline* at *Soleil* in France. The X-ray beam has a size of 500 µm horizontally and 40 µm vertically, an energy of 12 keV and an incident angle of 0.08 °. All measurements were done with a 40 nm DCV2-5T film on top of a 5 nm BPAPF layer on silicon substrates and recorded with a *Pilatus 1M* detector.

3.3. Device Characterisation

Solar Simulator

JV measurements of DCV2-5T were performed by Jakob Wolansky in the lab of Prof. Karl Leo at IAPP Dresden in Germany under ambient conditions and at RT using a custom-built setup. The solar simulator *16S-003-300-AM1.5* from *Solar Light Co.* with a 300 W xenon lamp *UXL-300D-0* from *Ushio* was used together with a *CAS 140CT* spectrometer from *Instrument Systems*, while the intensity is determined with a calibrated silicon photodiode *S1337* from *Hamamatsu Photonics* and can be adjusted with a neutral density filter from *Thorlabs*. The samples are illuminated with an AM1.5G solar spectrum at 100 mW/cm^2. The voltage-dependent current under illumination is measured with a *SMU 2400* from *Keithley Instruments*, while in the dark, the highly sensitive source-measurement unit *SMU 2635A* from *Keithley Instruments* is used.

JV measurements of PM6:Y6 were performed together with Manasi Pranav and Dr. Atul Shukla in the lab of Prof. Dieter Neher at University of Potsdam in Germany using a *Keithley 2400* SourceMeter in two-contact configuration. A filtered *Oriel Sol2A Class AA* xenon lamp was used for generating the AM1.5G solar spectrum at 100 mW/cm^2, while the intensity was monitored simultaneously with a Si photodiode. The solar simulator is calibrated with a *KG5* filtered silicon solar cell, certified by Fraunhofer ISE.

External Quantum Efficiency

EQE of DCV2-5T was performed by Jakob Wolansky in the lab of Prof. Karl Leo at IAPP Dresden in Germany on a custom-made setup with a 150 W xenon lamp *UXL-150SO* from *Ushio*, which was chopped at 21 Hz, directed into a *Cornerstone 260 1/4m* monochromator from *Newport* and delivered to the sample by an optical fiber, which is masked by a rectangular aperture of 2.997 mm^2. Under short-circuit conditions, the photocurrent is pre-amplified by a *SR570* from *Stanford Research* and converted to voltage before being analysed by a *SR 7265* lock-in amplifier from *Signal Recovery SR* and compared to the light intensity obtained from the calibrated silicon reference photodiode.

EQE of PM6:Y6 was measured together with Manasi Pranav and Dr. Atul Shukla in the lab of Prof. Dieter Neher at University of Potsdam in Germany using a broad white light from a *Phillips* 300 W halogen lamp chopped at 80 Hz with a *Thorlabs MC2000*, passed through a *Cornerstone* monochromator and coupled into an optical quartz fibre and calibrated with an *818-UV Newport* photodiode. The response of the OSC under various biases applied by a *Keithley 2400* SourceMeter is measured via an *SR 830* lock-in amplifier.

Electroluminescence Spectroscopy

Electroluminescence spectroscopy (EL) was performed by Dr. Huotian Zhang and Dr. Johannes Benduhn in the lab of Prof. Feng Gao at Linköping University, Sweden. A constant current is applied to the DCV2-5T sample with a *SMU2400* source-measurement unit from *Keithley Instruments*. The EL emission is coupled into a *Shamrock sr-303i* spectrometer from *Oxford Instruments* via an objective, optical coupling lenses and an optical fiber. A *Andor Newton EMCCD* Silicon detector array is used for Vis and an *Andor IDus InGaAs 1.7* InGaAs detector array is used for NIR, both from O*xford Instruments*. The optical system is calibrated with a *AvaLight-HAL-S-Mini* halogen light source from *Avantes*.

Dynamic Range Measurements

LDR was performed by Jakob Wolansky in the lab of Prof. Karl Leo at IAPP Dresden in Germany for DCV2-5T samples. All samples are illuminated with a 660 nm LED *M660L4* from *Thorlabs*, driven by a *Mightex Systems BLS-1000-2* LED driver and modulated at 21 Hz. Light intensity was varied over a wide range with a series of neutral density filters from *Thorlabs*. During the measurement, samples are placed in an electrically shielded box, decreasing external electrical noise sources and ambient stray light. The generated photocurrent is pre-amplified via a *DLPCA-200* low-noise preamplifier from *FEMTO Messtechnik GmbH* and directed into a *SR865A* lock-in amplifier from *Stanford Research Systems*. Calibration of the light intensity was performed with a *SM05PD3A silicon diode* from *Thorlabs*.

For measuring the photoresponse speed, the same setup was used. In addition, the LED frequency is modulated between 11 Hz and 4 MHz by the lock-in amplifier. Instead of the *DLPCA-200*, the *DHPCA-100* pre-amplifier *FEMTO Messtechnik GmbH* from was used.

Noise Spectral Density Measurements

The measurements of the DCV2-5T samples were performed in an electrically shielded box by Jakob Wolansky in the lab of Prof. Karl Leo at IAPP Dresden in Germany. The measured noise current in the absent of an applied bias is amplified by a *LCA 30–1T* very low-noise current to voltage preamplifier from *FEMTO Messtechnik GmbH*, by a *DLPCA-200* low-noise preamplifier from *FEMTO Messtechnik GmbH* and recorded with a *Tektronix DPO7354C* high-speed, low-noise oscilloscope with a 200 Samplings per second. The noise spectral densities are calculated from Welch's method and smoothed by a Savitzky-Golay filter.

Absorption Simulation

The open-source Python program Simojio[206] was used by Jakob Wolansky to simulate the device absorption of DCV2-5T. It is based on the transfer matrix model and was implemented by Byrnes [207] and described by Burkhard, et al. [208] to calculate layer absorption.

3.4. Time-Delayed Collection Field

In a time-delayed collection field (TDCF) experiment (cf. Figure 3-1), the device is kept under a defined pre-bias V_{pre} and gets photoexcited by a short laser pulse at a defined wavelength and fluence. Charge carriers that already extract under V_{pre} are measured separately as Q_{pre}. After a controlled timedelay, a strong extraction field V_{coll} is applied and the collected charges Q_{coll} are measured. By varying the excitation fluence in TDCF, it is possible to examine how the recombination mechanism responds to changes in carrier density and whether these recombinations are of a monomolecular or bimolecular nature.

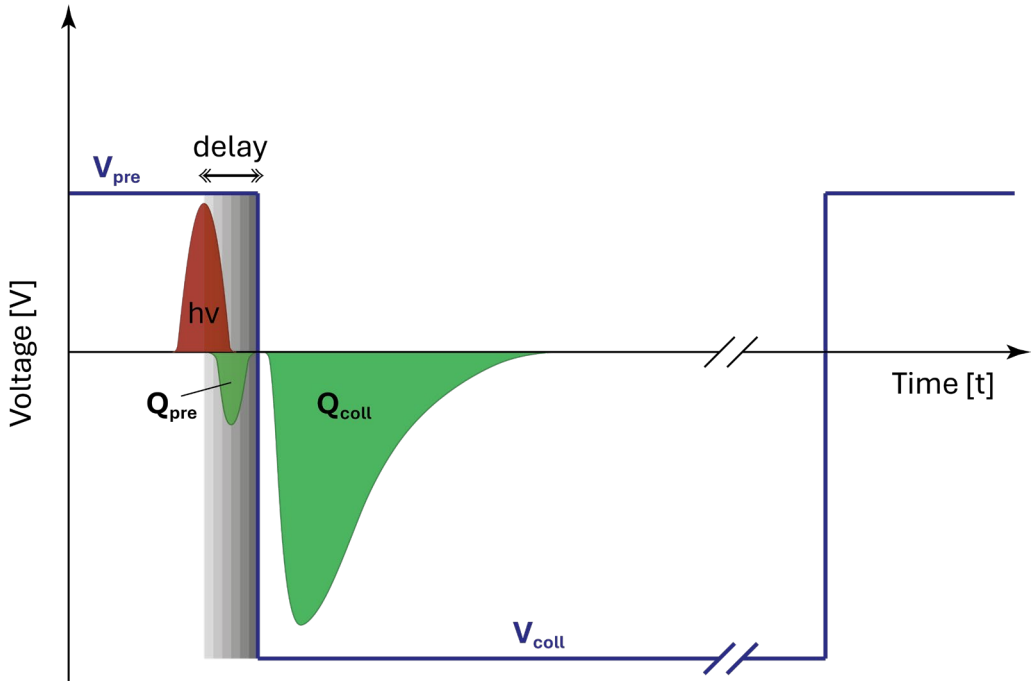

Figure 3-1: Schematic illustration of the Time-Delayed Collection Field (TDCF) experiment.

Several important relations are used to analyse the TDCF data. The total extracted charge Q_{tot} represents the sum of the extracted charge under pre-bias Q_{pre} and the collected charge under collection bias Q_{coll}.

$$Q_{tot} = Q_{pre} + Q_{coll} \tag{3-1}$$

The collected charge Q_{coll} is converted into an absolute carrier density n_{coll} via

$$n_{coll} = \frac{Q_{coll}}{q \cdot A_x \cdot d} \tag{3-2}$$

with the elementary charge q, the device area A_x and the thickness of the active layer d. The recombination rate R is calculated by

$$R = \frac{\Delta Q_{tot}}{\Delta t} = k_\delta \cdot n^\delta \tag{3-3}$$

with the time derivative of Q_{tot} over a small time interval Δt, the exponent δ of the empirical recombination order and the corresponding rate coefficient k_δ, where δ indicates the dominant recombination mechanism with $\delta = 1$ for monomolecular (trap-assisted or geminate), $\delta = 2$ for bimolecular and higher or lower values for mixed or complex processes. The instantaneous recombination order is extracted at each timedelay by plotting $\log R$ against $\log n_{coll}$ across all fluences and fitting the slope, following the standard equitemporal analysis. The global or aggregate recombination order is determined by combining data over a selected window of timedelays where the TDCF signal is robust and not dominated by artefacts.[99,209,210]

3.5. Transient Absorption Spectroscopy

Transient Absorption (TA) spectroscopy (cf. Figure 3-2) is a method to photoexcite and track the ultrafast evolution of excited states of a material with a femtosecond pulsed laser system. TA experiments were carried out on a home-build setup using a regeneratively amplified Ti:sapphire laser *Astrella* from *Coherent* (800 nm, 35 fs pulses, 1 kHz frequency, 6 mJ pulse energy). The fundamental beam is split with a beam splitter (BS) into the pump pulse which excites the sample and the probe pulse

which monitors the absorption changes of the material after photoexcitation. DCV2-5T was photoexcited at 650 nm and 400 nm. The 650 nm pump beam was frequency-converted with an *OPerA Solo System* commercial optical parametric amplifier (OPA) from *Coherent* by second harmonic generation (SHG) of the fundamental, while the 400 nm pump was performed with a *NLC01* beta barium borate (BBO) crystal from *Thorlabs* by SHG of the fundamental. Generating a white-light continuum for the probe pulse was achieved by pumping a 5 mm sapphire crystal from *Thorlabs* with the fundamental 800 nm beam, leading to nonlinear optical effects, mainly self-phase modulation (SPM) and four-wave mixing (FWM). The intensity of the white-light continuum is relatively small, compared to that of the fundamental, requiring it to be filtered out. Here, a 750 nm short pass filter was used for the visible continuum and an 850 nm long pass filter for the NIR continuum, leading to a gap in the spectra between 750–850 nm. With a physical delay stage, the beam length of the probe was varied to record the TA spectra at various timesteps after excitation. The visible and NIR spectra were recorded separately with two spectrographs each, one for the sample and one for the reference beam. The spectrographs consist of a prism combined with a camera. For the visible part, back-thinned silicon charge-coupled devices (CCDs) from *Hamamatsu* and for the NIR part, InGaAs arrays from *Hamamatsu* were used. The wavelength calibration was performed with five 10 nm bandpass filter each from *Thorlabs*.

For TA experiments of DCV2-5T, the fluence of the pump beam was set to $1.8 \cdot 10^{18}$ 'Ph'·cm^{-3} for measurements in the linear excitation regime and to $1.4 \cdot 10^{20}$ 'Ph'·cm^{-3} in the nonlinear excitation regime. The datasets were rescaled onto the same excitation density respectively before analysing and displaying. All DCV2-5T devices were measured under V_{OC} conditions for every performed TA experiment.

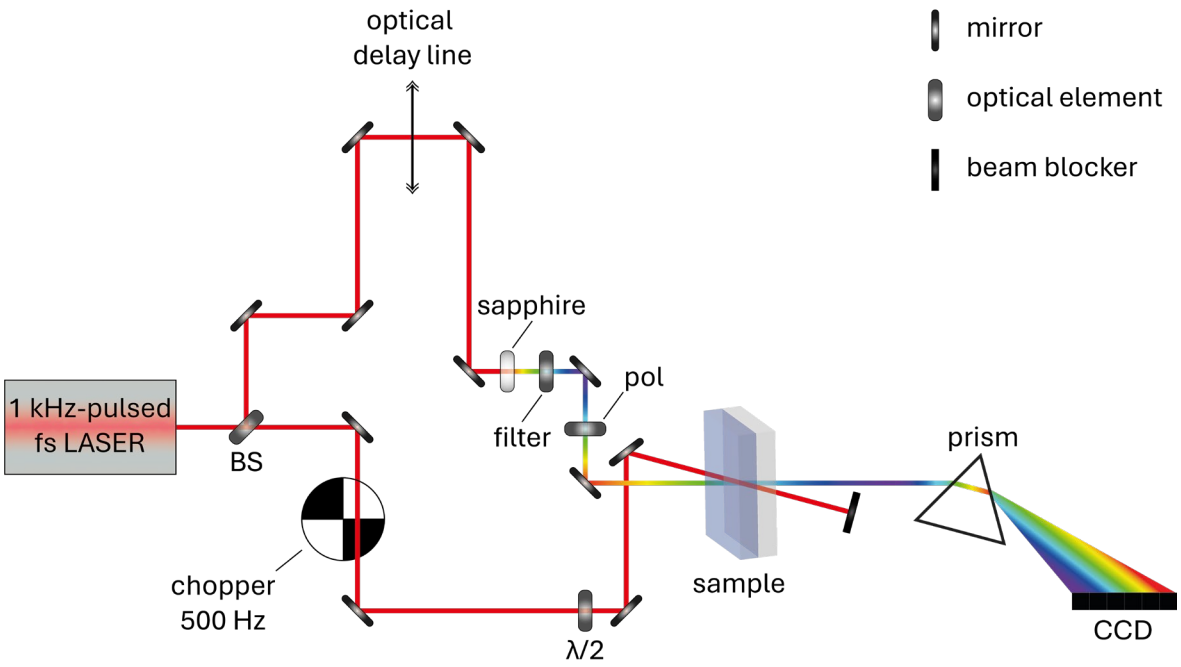

Figure 3-2: Schematic illustration of the home-built Transient Absorption (TA) setup.

TA measurements of PM6:Y6 devices in the visible and NIR were carried out on the same setup as described above for DCV2-5T. While for 800 nm the fundamental was used for the pump, 400 nm and 610 nm were generated with a BBO and OPA, respectively. During the measuring series of the PM6:Y6 device, the same short pass filter was used for the measurements in the visible, while the long pass filter was replaced with a notch filter to attenuate the fundamental beam to an intensity comparable to that of the white-light continuum. This led to a minimised gap between the visible and near-infrared region, resulting in a spectral overlap of both sides. This was done in order to be able to observe the GSB region of Y6 on this setup. However, the steep attenuation profile of the notch filter creates abrupt changes and possible instabilities, while residual fundamental fluctuations are not properly referenced out. As a result, the spectral region around the notch is vulnerable to baseline distortions and artificial absorption features, requiring careful data interpretation here.[211]

The visible TA spectra of the PM6:Y6, PS:Y6 and PM6 films were performed similarly, while the TA measurements in the NIR were performed on another TA setup with a different approach for the generation of the white-light continuum. An OPA was pumped with 800 nm to create a signal and idler around 1330 nm and 2000 nm

respectively via difference-frequency generation (DFG). Here, the 2000 nm idler was used in an yttrium aluminium garnet (YAG) crystal to generate a white-light continuum spanning from 600–1650 nm. This method also minimises the 750–850 nm gap and additionally allows a spectral extension further into the NIR. Nevertheless, relying on an OPA and generating a white-light continuum much closer to the nonlinear threshold when using a 2000 nm idler, even small shot-to-shot fluctuations in the OPA pulse cause significant changes in the continuum, leading to an overall increased spectral noise. However, to reduce and compensate for spectral fluctuations, in all performed TA measurements on both setups, the 'B-Matrix' method published by Feng, et al. [212] was used as a referencing scheme.

For TA experiments of PM6:Y6, PM6 and PS:Y6, the fluence of the pump beam was set to $8.8 \cdot 10^{16}$ 'Ph'$\cdot cm^{-3}$ in the linear excitation regime. The PM6:Y6 device was also measured in the nonlinear excitation regime with a pump beam fluence at $3.2 \cdot 10^{18}$ 'Ph'$\cdot cm^{-3}$. To enable comparison, they datasets were rescaled onto the same excitation density respectively before analysing and displaying. All PM6:Y6 devices were measured under V_{OC} conditions for every performed TA experiment.

The TA measurements of DCV2-5T were performed together with Jakob Wolansky, the ones of PM6:Y6, PS:Y6 and PM6 together with Dr. Kaila Yallum. All TA experiments were performed under inert atmosphere and in transmission mode, also for devices which were fabricated with semi-transparent electrodes (cf. section 3.1.1 & 3.1.2). The beam area of the pump was chosen two to three times larger than the beam size of the probe to ensure homogeneity. Beam sizes and overlap was checked and measured with a *BC106N-UV* CCD camera beam profiler from *Thorlabs*, while the overlap was optimised onto the signal maximum. All ultrafast measurements were performed in the magic-angle configuration, ensuring probing population dynamics exclusively by avoiding orientational or anisotropic effects. Here, the pump is set to the magic angle of 54.7 ° with appropriate zero-order half-wave plate (λ/2-plate) and linear polarisers from *Thorlabs*. The pump beam uses either the fundamental with single, well-defined linear polarisation or gets converted to another single wavelength via an OPA or BBO, creating a different phase-matching excitation wavelength. The probe however undergoes a continuum generation that scrambles polarisation to a certain extent.[32]

Therefore, the probe beam was cleaned with a polariser (pol) to ensure well-defined polarisation of the white-light continuum before the pump beam was set to the magic angle with a λ/2-plate. For the reference, the probe pulse is split before reaching the sample, where the second white-light beam bypasses the sample and thus provides a reverence pulse. In TA, the changes in absorption due to excitation of the material gets recorded. The pump pulse gets chopped to half of the probe pulse frequency, where the transient absorption signal is the differential between pumped and unpumped shot.

When the beam pulse travels across the measuring setup on the optical table, it interacts with various optical elements. For the white-light continuum, passing through different media results in the group velocity dispersion (GVD) effect which is defined as the second derivative of the spectral phase with respect to angular frequency. GVD describes the wavelength-dependent delay of pulse components and is responsible for temporal pulse broadening and the occurrence of a chirp. Therefore, chirp correction is required before any further data analysis in order to correct for the different arrival times of the various wavelengths of the probe pulse, which was performed with a homemade *IgorPro* script.

The transient absorption spectra show the changes in absorption due to the variation in occupied energetic states following photoexcitation. The presence of excited states leads to a positive photoinduced absorption (PIA) feature and their absence in the ground state results in an absorption loss called ground state bleach (GSB). Excited-state absorption (ESA) contributes to the PIA and refers to the absorption of the probe pulse by species that were promoted to an excited state by the pump pulse. In the weak-probe limit, the ESA signal amplitude is proportional to the population of the initially present state and the probe intensity.[213,214]

The resulting TA spectra is a time-resolved superposition of changes in absorption of all species present after excitation. To resolve their respective contributions to the absorption regarding their spectral shape and evolution, global and target analysis including Multivariate Curve Resolution (MCR) was performed for spectral deconvolution, as it was first reported by de Juan, et al. [215] and adapted for Python by Camp [216].

3.6. Electromodulated Differential Absorption Spectroscopy

Electromodulated Differential Absorption (EDA) is an ultrafast spectroscopic method based on transient absorption (TA) spectroscopy that provides detailed insights into charge separation, transport and recombination processes in optoelectronic devices such as OPVs and OPDs. EDA is measured on the same TA setup described in section 3.5 with a few modifications, shown in Figure 3-3. Most importantly, EDA requires the application of an external bias. Therefore, it is limited to devices and cannot be performed on films. The devices used for EDA were the same devices with semi-transparent electrodes which were used for TA experiments, described in the previous section 3.5, since EDA was also performed in transmission mode. While in TA the sample is pumped at a frequency of 1 kHz and probed at 500 Hz to obtain the differential absorption signal, pumping and probing in EDA takes place at the same frequency of 1 kHz. Here, the differential absorption signal is obtained by optically recording the electroabsorption (EA) which occurs by applying an external reverse bias with a frequency of 500 Hz.

EDA measurements were performed in the visible on the same setup which was used for TA und described in the previous section. The bias was applied with an *AFG3101C* function generator and the current response measured with a *MDO3034* oscilloscope, both from *Tektronix*. In EDA, the probe uniformly illuminates the full pixel area, while the pump beam still exceeds the size of the probe area. This ensures that EDA is measured accurately for the whole device, avoiding local inhomogeneities or spatial artefacts, since the extracted current also counts for the entire pixel area and represents the integrated response of the system. EDA measurements were performed in the linear regime. This was ensured by fluence dependence measurements of the extracted photocurrent at the highest applied bias that was used in a measuring series. EDA was measured on devices with a semi-transparent Ag back electrode, while devices were illuminated from the ITO side. Especially under high bias, EDA is a stressful measurement for optical devices. To ensure that the measured signal

reduction was caused by charge extraction and not by an irreversible degradation of the device, before and after each EDA measurement photocurrent and electroabsorption measurements were performed to check for identical behaviour before, during and after the measurement.

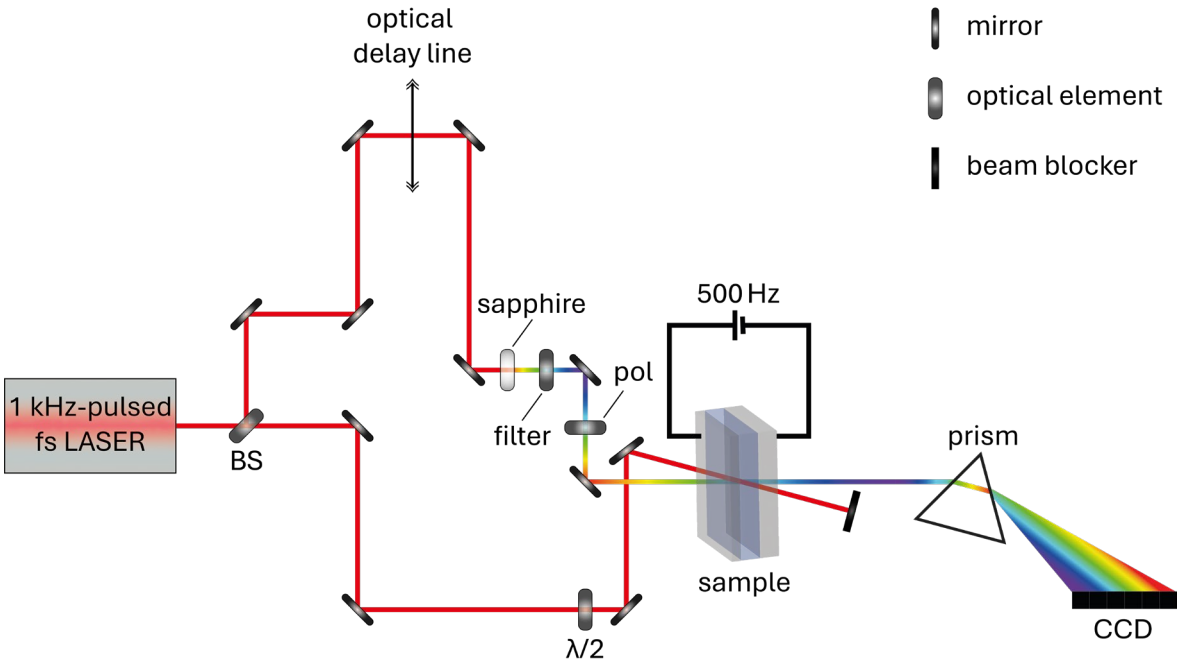

Figure 3-3: Schematic illustration of the home-built Electromodulated Differential Absorption (EDA) setup.

While EA is in principle a steady-state measurement, in EDA it is used in a time-resolved context, where EA is recorded over the whole process of charge generation. EA is based on the Stark effect that describes the modulation of optical transitions in the presence of an electric field which perturbs the electronic structure and energy levels of the AL and leads to a shift of the absorption spectra. Both linear and quadratic Stark effect are involved with the relative contribution of linear and quadratic Stark effect depending on the electronic properties of the material.[165,217,218]

The Stark effect can be described with the generalised approach

$$E(F) - E(0) \propto \Delta\mu \cdot F + \frac{1}{2}\Delta\alpha \cdot F^2 \qquad (3\text{-}4)$$

where $E(F) - E(0)$ is the energy shift, $\Delta\mu \cdot F$ contributes to the linear Stark effect and $1/2\,\Delta\alpha \cdot F^2$ to the quadratic Stark effect with $\Delta\mu$ as change in permanent dipole moment of the material, $\Delta\alpha$ as change in polarisability and F as applied electric field.[219,220]

Unlike in equation(2-13) where dynamic polarisability $\alpha(\omega)$ is discussed, for the quadratic Stark effect the difference between static polarisability $\alpha(0)$ of the ground state g and the excited state e is used.

$$\Delta\alpha = \alpha_e(0) - \alpha_g(0) = \alpha_e - \alpha_g \qquad (3\text{-}5)$$

The reason for this is that the external field has a frequency of 500 Hz, corresponding to a period of 2 ms, which is very long compared to the ultrafast timescales in EDA. Consequently, the field can be considered constant during the measurement cycle, every time a shot is taken.

In a transition with a large change in permanent dipole moment $\Delta\mu$, the energy shift changes linearly with the applied field. If the transition exhibits a significant change in polarisability $\Delta\alpha$, the external field-induced dipole interacts with the external field itself which leads to a quadratic energy shift. Active layers often exhibit an interplay of both linear and quadratic Stark effect. The resulting EA signal is therefore most pronounced at the beginning of the EDA measurement because neither excitons nor bound CT states feature an influence on the EA of the applied electric field. As soon as charges begin to separate, they develop their own local internal electric field between the separated charge carriers, which is oppositely directed to the applied one. This leads to a reduction of the total electric field and thus to a reduction of the EDA signal over time.[217,219,221]

To quantify the EDA signal reduction on an absolute scale, a calibration curve is needed. Therefore, the EA signal is measured in the absence of a pump beam at a range of various biases to plot the integral of the EA signal against the respective applied bias, resulting in a field dependence curve for calibration. This calibration matrix is then applied on the integrated EDA signal at every time step in order to obtain a time-

resolved voltagedrop $\Delta V(t)$ that quantifies the respective time-resolved signal reduction.

Comparing voltagedrop dynamics requires a normalisation.[165] In the absence of excitation, the AL, which is enclosed by two parallel electrodes, behaves like an insulator, which basically makes the device a plate capacitor. When an external reverse bias is applied, it charges this capacitor, leading to a displacement current I_{acc} peak due to the accumulated charges q_{acc} at the electrodes.

$$q_{acc} = \int I_{acc}(t)dt \tag{3-6}$$

By integrating I_{acc} the obtained accumulated charges q_{acc} are used in an approximation to determine the capacitance C of the device.[165]

$$C \approx \frac{q_{acc}}{V_{app}} \tag{3-7}$$

During charge generation, the photoexcited device eventually exhibits separation and extraction of charges. At the point of full charge extraction, the device got discharged by the total amount of extracted charges q_{ext}.

$$q_{ext} = \int I_{photo}(t)dt \tag{3-8}$$

This state can be described as the total voltagedrop $|V_{tot}|$. $|V_{tot}|$ is estimated by dividing the integrated photocurrent q_{ext} by the capacitance of the device C.[222]

Accordingly, the normalised voltagedrop $\Delta V(t)/|V_{tot}|$ is determined with

$$\frac{\Delta V(t)}{|V_{tot}|} = \frac{\Delta V(t) \cdot C}{q_{ext}} \approx \frac{\Delta V(t) \cdot \int I_{acc}(t)dt}{\int I_{photo}(t)dt \cdot V_{app}} \tag{3-9}$$

to correct for device-specific properties and experimental variations. $\Delta V(t)/|V_{tot}|$ ranges between 0 and −1, where 0 means that no charge has been extracted so far and −1, that all charges have been extracted. While EDA spectroscopy is measured on ultrafast timescales within the first two nanoseconds but the supporting electrical measurements for normalisation are performed on significant longer timescales,

reaching a normalised voltagedrop of −1 remains a theoretical scenario for the visual voltagedrop evolution, as long as the charge extraction process exceeds the EDA time window. EDA spectroscopy enables the investigation of an optoelectronic device with respect to excitation wavelength and field dependence for variations in charge separation and transport processes.

3.7. Optical-Pump Terahertz-Probe Spectroscopy

Optical-pump terahertz-probe (OPTP) spectroscopy (cf. Figure 3-4) was used to investigate carrier dynamics of a PM6:Y6 thick film with 1 µm. OPTP experiments were performed together with Dr. Julien Réhault. The Ti:sapphire laser *Astrella* from *Coherent* (800 nm, 35 fs pulses, 1 kHz frequency, 6 mJ pulse energy) was used to generate the fundamental 800 nm beam for both pump and probe. The THz probe pulse was generated by optical rectification in a 1 mm thick (110)-oriented zinc telluride (ZnTe) crystal and focused onto the sample using off-axis parabolic mirrors. The transmitted THz pulse was subsequently detected by electro-optic sampling (EOS) in a second (110)-oriented ZnTe crystal, using an 800 nm gate pulse. The change in polarisation of the gate pulse, induced by the transient THz electric field, was analysed with a Wollaston prism and a pair of balanced photodiodes (PDs). The temporal delay between the optical pump and the THz probe was controlled by a mechanical delay stage in the THz beam path, allowing mapping of the pump-induced changes in the THz field as a function of pump-probe delay time. The transmitted THz field was recorded for both pumped and unpumped with the pump pulse chopped to half the frequency (500 Hz)

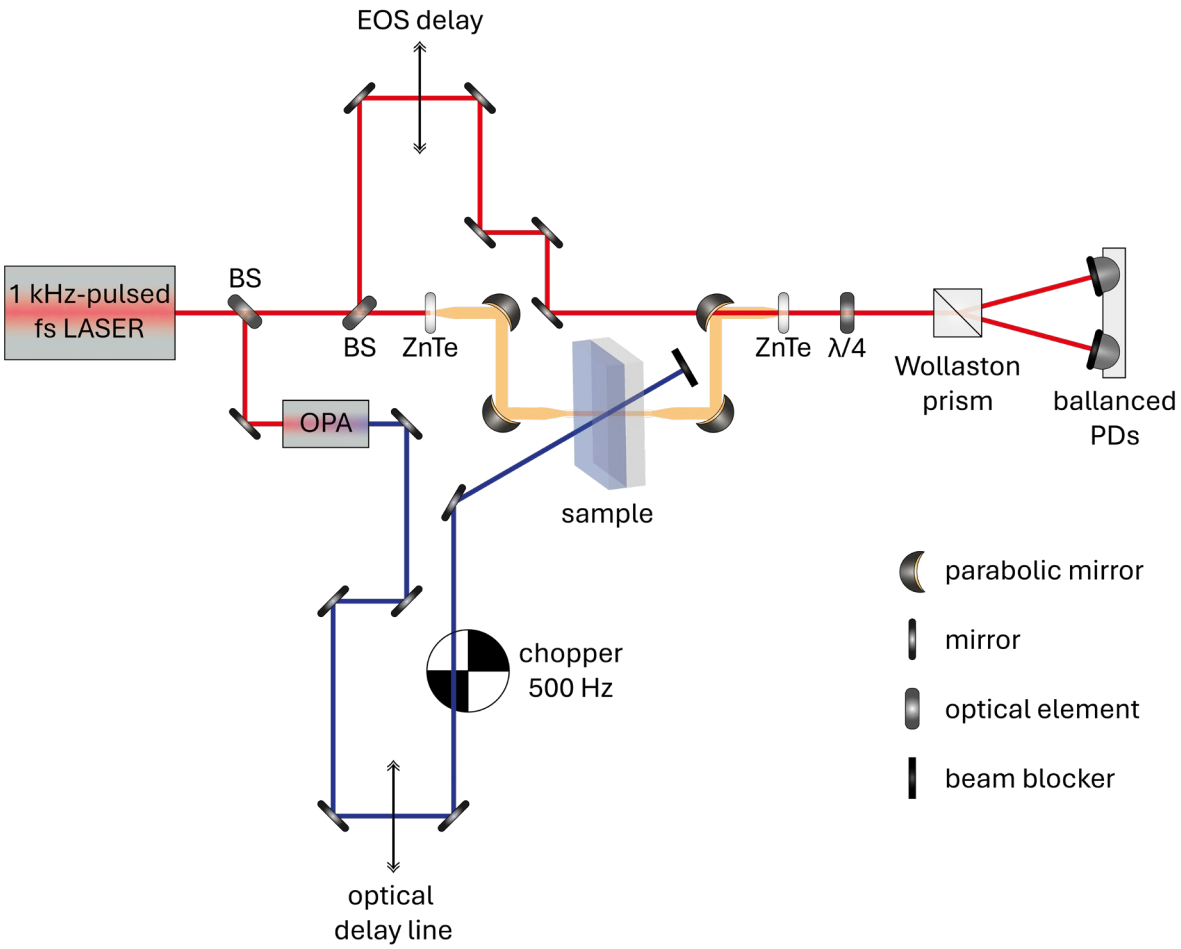

Figure 3-4: Schematic illustration of the home-built Optical-Pump Terahertz-Probe (OPTP) setup.

For OPTP measurements of the frequency-resolved photoconductivity, the experimental setup was identical to that described above for THz dynamics, while the pump–probe delay was fixed at a chosen timedelay. The resulting time-domain signals were Fourier-transformed to obtain the frequency-domain electric fields to calculate the complex photoconductivity spectrum according to the thin-film approximation[223]

$$\sigma(\omega) = \frac{n_0 + n_{air}}{Z_0 d} \cdot \frac{E_{pump}(\omega) - E_0(\omega)}{E_0(\omega)} \qquad (3\text{-}10)$$

with the complex photoconductivity σ at an angular frequency ω, the refractive index of the sapphire slide n_0, the refractive index of air n_{air}, the impedance of free space Z_0, the effective photoexcited region d and the Fourier-transformed electric field of the transmitted THz pulse after optical excitation E_{pump} and without excitation E_0.[224]

The data were analysed using the Drude-Smith model, which extends the classical Drude approach by accounting for carrier localisation and backscattering effects typically observed in organic semiconductors. The measured conductivity spectrum $\sigma(\omega)$ is fitted according to

$$\sigma(\omega) = \frac{N \cdot q^2 \cdot \tau}{m^*} \cdot \frac{1}{1 - i \cdot \omega \cdot \tau} \cdot \left[1 + c_1 \cdot \frac{1}{1 - i \cdot \omega \cdot \tau}\right] \tag{3-11}$$

with the density of photoexcited charge carriers N, the carrier scattering time τ, the effective mass of the charge carrier m^* and the Drude-Smith parameter c_1, which quantifies the degree of carrier backscattering and localisation. When $c_1 = 0$, the model reduces to the classical Drude case, while carrier localisation or backscattering increases with a more negative c_1.[224,225]

Chapter 4

Ultrafast Charge Formation in DCV2-5T

This chapter is based on the article 'Sensitive Self-Driven Single-Component Organic Photodetector Based on Vapor-Deposited Small Molecules', Adv Mater 36, e2402834, doi:10.1002/adma.202402834 (2024) published by J. Wolansky, C. Hoffmann, M. Panhans, L. C. Winkler, F. Talnack, S. Hutsch, H. Zhang, A. Kirch, K. M. Yallum, H. Friedrich, J. Kublitski, F. Gao, D. Spoltore, S. C. B. Mannsfeld, F. Ortmann, N. Banerji, K. Leo, J. Benduhn under CC BY-NC 4.0 licence.[226] *The device fabrication, steady-state characterisation and simulations were carried out by Jakob Wolansky of the group of Prof. Dr. Karl Leo at the Institute of Applied Physics at Dresden University of Technology and others. The main topic of this chapter is the contribution in ultrafast spectroscopy which was carried out together with Jakob Wolansky and is shown and discussed in section 4.2.2.*

4.1. Introduction

In the context of section 2.7, the vacuum processed A–D–A structured small-molecule DCV2-5T is a promising candidate for investigating charge generation mechanisms in single component materials due to its uniform films with controlled thickness and low roughness. DCV2-5T combines high optical absorbance in the visible range with a molecular structure optimised to promote intramolecular charge transfer (CTx), strong π–π stacking and efficient electronic coupling between neighbouring molecules.

Here, the first aim is device optimisation to quantify the influences of film morphology, layer thickness, processing parameters and architecture on the device response and performance, in particular for OPD applications. Afterwards, the second aim and also the central focus of this chapter is to investigate the ultrafast photophysical processes that leads to efficient charge formation in neat DCV2-5T. Time-resolved TA measurements are performed on a series of sample configurations, including films, transport-layer stacks and fully-stack devices, to evaluate the influence of device architecture in addition to the intrinsic material properties of DCV2-5T on the excited-state population and their dynamics on an ultrafast timescale.

4.2. Results

4.2.1. Steady-State Properties

The organic small molecule DCV2-5T (Figure 4-1 a) exhibits an A–D–A structure that enables π–π stacking between molecules, allowing efficient delocalisation and transport. Here, DCV2-5T was investigated in a neat device stack (SC-OPD) and in a fullerene-blended DCV2-5T:C_{60} device stack (BHJ-OPD) with a 2:1 ratio, using ITO and opaque Ag electrodes, BPAPF + BPAPF:NDP9 layers as HTL and a BPhen layer as ETL (cf. Figure 4-1 b–d). The interlayers, as well as an active layer thickness of 40 nm, were selected based on device optimisation studies (cf. Figure S 4-2). BHJ-OPD results are kept as a reference, while the focus is on neat DCV2-5T which will be investigated on ultrafast timescales afterwards DCV2-5T exhibits a broad absorption band between 400–700 nm, peaking at around 580 nm and a PL spectrum peaking at around 790 nm, resulting in a stokes shift of about 210 nm. Such a pronounced stokes shift typically arises from energetic disorder, strong vibrational coupling and local reorganisation of the excited state. Steady-state PL measured on films with and without transport layers shows no significant quenching (cf. Figure S 4-3), indicating that charge generation is predominantly located within the DCV2-5T bulk rather than occurring at TL interfaces.

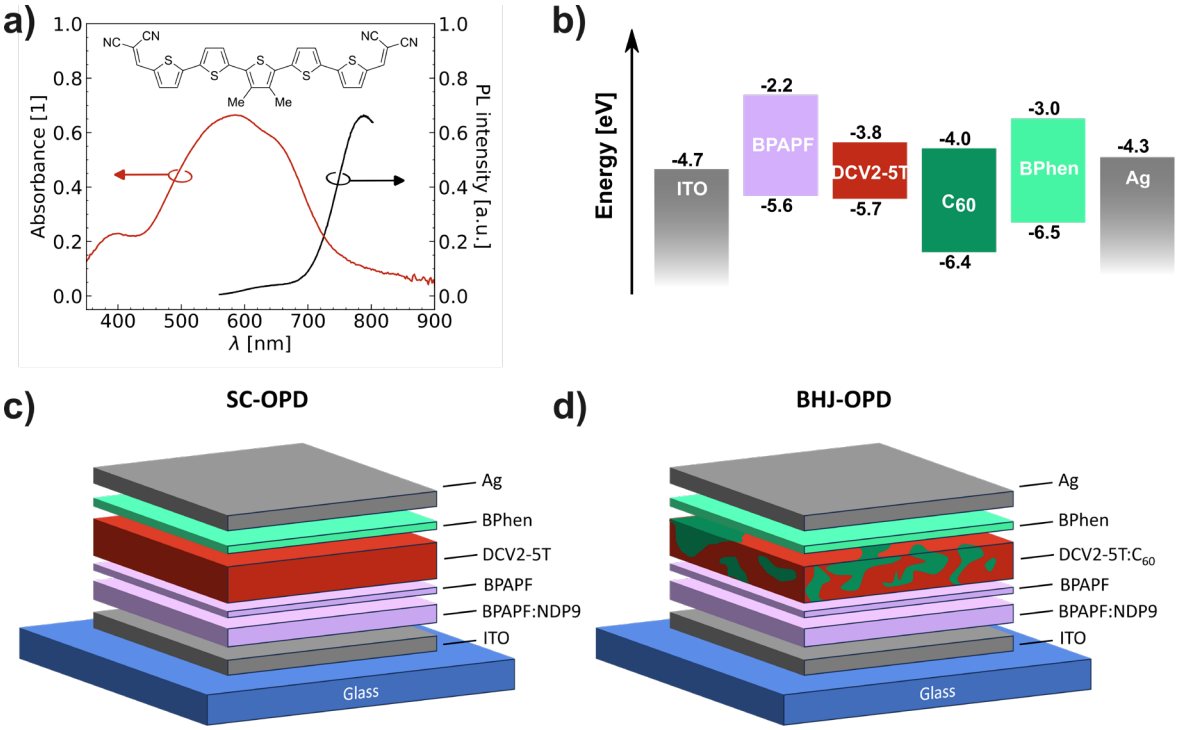

Figure 4-1: a) Chemical structure of DCV2-5T and its absorbance (red) and photoluminescence (black) measured of an encapsulated 40 nm neat film; b) energy levels of DCV2-5T (red), electrodes (grey), the HTL BPAPF (purple), the ETL BPhen (green) and the an additional C_{60} fullerene acceptor (dark green); c) schematic illustration of the structure of the neat DCV2-5T full-stack device (SC-OPD) and the fullerene-blended DCV2-5T:C_{60} full-stack device (BHJ-OPD).[226]

From the intersection of the absorption and electroluminescence (EL) spectra of DCV2-5T, an optical gap of 1.74 eV for a device with a BPhen and without a doped BPhen ETL and 1.71 eV for a device with BPhen and a Cs-doped BPhen ETL were determined (cf. Figure S 4-1). Cs-doping of BPhen increases electron conductivity and lowers the cathode injection barrier. The morphology of DCV2-5T films is highly dependent on the temperature of the substrate during deposition. GIWAXS measurements (cf. Figure S 4-4) reveal distinct diffraction peaks at room temperature, though they are broader and weaker than for heated depositions, which indicates semicrystalline order with shorter coherence lengths and increased lattice disorder. When increasing the substrate temperature to 343 K and 363 K during deposition, sharper and more intense out-of-plane and in-plane diffraction peaks were observed, demonstrating higher crystallinity and long-range order. The morphological change was further quantified by AFM (cf. Figure S 4-5). Root mean square (RMS) roughness

increases from 1 nm at RT to 24 nm at 343 K and 37 nm at 363 K, leading to larger grain sizes and an increased surface roughness. While a higher crystallinity may favour charge carrier mobility, the increased roughness of the film is associated with a higher density of shunt pathways, reducing shunt resistance and increasing the dark current of the device (cf. Figure S 4-2 & Figure S 4-6). Consequently, the samples used for transient absorption experiments in the following section 4.2.2 were fabricated using room-temperature deposition to minimise roughness and shunt pathways, which led to the lowest dark current and best overall OPD performance.

JV measurements exhibit diode-like behaviour and photovoltaic response in both neat and blended device (cf. Figure 4-2). With a 8 nm undoped BPhen ETL, at −0.1 V, a dark current density of $2.4 \cdot 10^{-9}$ A/cm^2 was achieved, while devices with an additional 50 nm BPhen:Cs (1:1) doped ETL reduce the dark current even to $3.4 \cdot 10^{-11}$ A/cm^2 (cf. Figure **S 4-7**), which is among the lowest reported[227,228] and even below that of a typical silicon diode[229]. At zero bias, the primary noise source was determined as thermal noise. A linear dynamic range (LDR) of 150 dB with the additional doped ETL and a LDR of 190 dB without the doped ETL layer were achieved (cf. Figure S 4-7e), which matches or even exceeds that of commercially available silicon photodiodes and were limited by the sensitivity of the measurement setup (0.5 fA/Hz$^{1/2}$) for all measured devices.[226] Although Cs-doping of BPhen increased electron conductivity and lowered the cathode injection barrier, the cut-off frequency got reduced to about 200 kHz relative to about 330 kHz without doping. With the doped ETL, the LDR was also lowered from about 190 dB to about 150 dB and a photocurrent saturation appeared at higher light intensities, due to transport limits in the thicker ETL. As a consequence, for the time-resolved ultrafast measurements, only the 8 nm undoped BPhen layer was used.

While the reference BHJ-OPD reached an EQE maximum at 68 %, the SC-OPD exhibits a broad EQE, peaking at 20 %, which is remarkably high for a vacuum-processed, single-component small molecule OPD (cf. Figure 4-2). Previous publications based on single-component small molecules such as SubNc and SubPc achieved at the absorption maxima EQEs up to 35–40 % but with a significant higher dark current[198,230]. Recently, Rana, et al. [200] achieved for a neat Cl_6-SubPc device a zero-bias EQE of 7 % with a two orders of magnitude lower D*, than what was achieved with DCV2-5T (cf. Figure **S 4-7**). In comparison, the 20 % EQE for DCV2-5T represents a significant efficiency boost, placing DCV2-5T in a competitive position in its class.

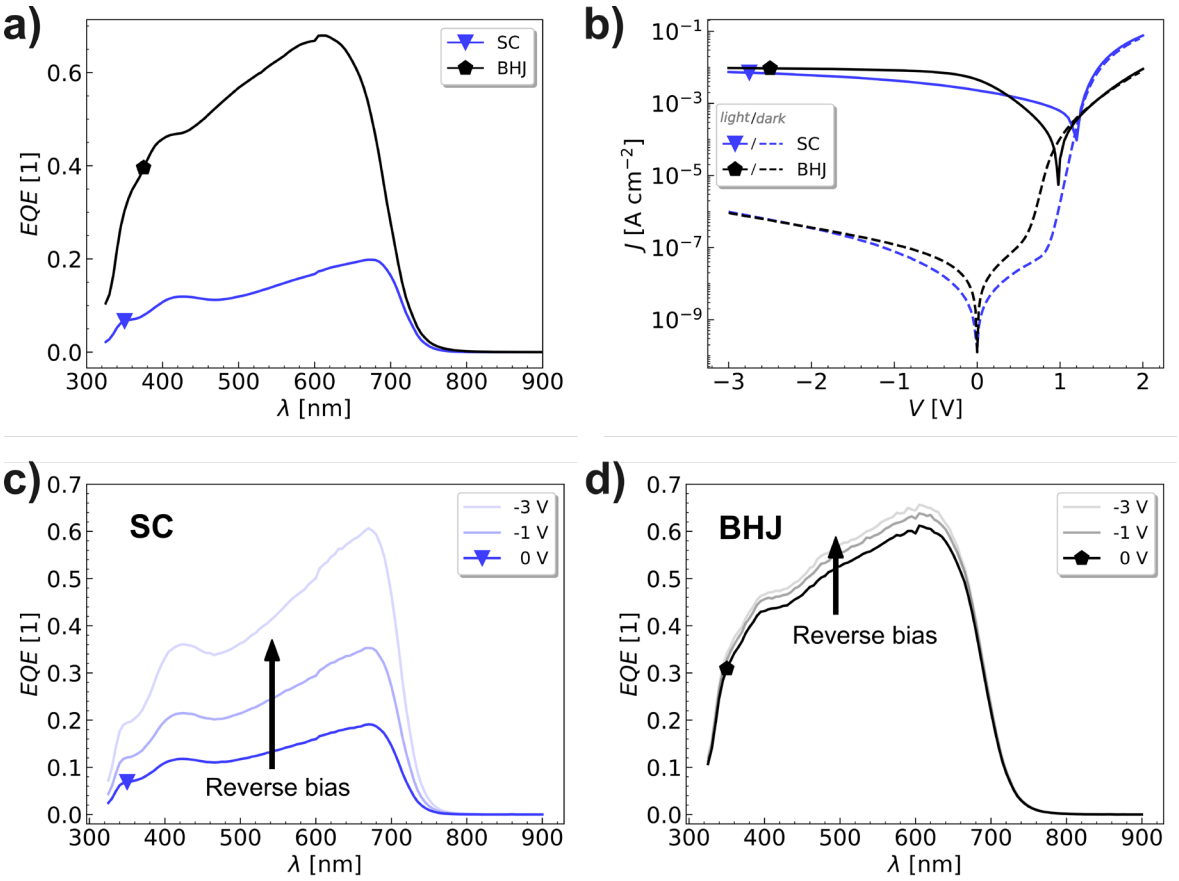

Figure 4-2: a) EQE at zero bias and 21 Hz and b) JV curves under 1 sun (full) and in the dark (dashed) of a neat DCV2-5T (blue) and a DCV2-5T:C_{60} (black) device and the bias-dependent EQE spectra at 21 Hz for the c) neat DCV2-5T and d) DCV2-5T:C_{60} device.[226]

The estimated internal quantum efficiency (IQE) was calculated from the ratio of EQE to simulated absorption in the active layer. The simulated absorption reveals that comparable amounts of photons are absorbed from the AL in both devices, SC-OPD and BHJ-OPD (cf. Figure 4-3). It is therefore suggested that differences in the EQE between SC-OPD and BHJ-OPD are primarily arising from less efficient charge generation and extraction processes in the SC-OPD. Under –3 V reverse bias, the EQE of neat DCV2-5T increases to 60 %, indicating field sensitivity in the steady state (cf. Figure 4-2 above). Obtained performance parameters are displayed in Table 4-1.

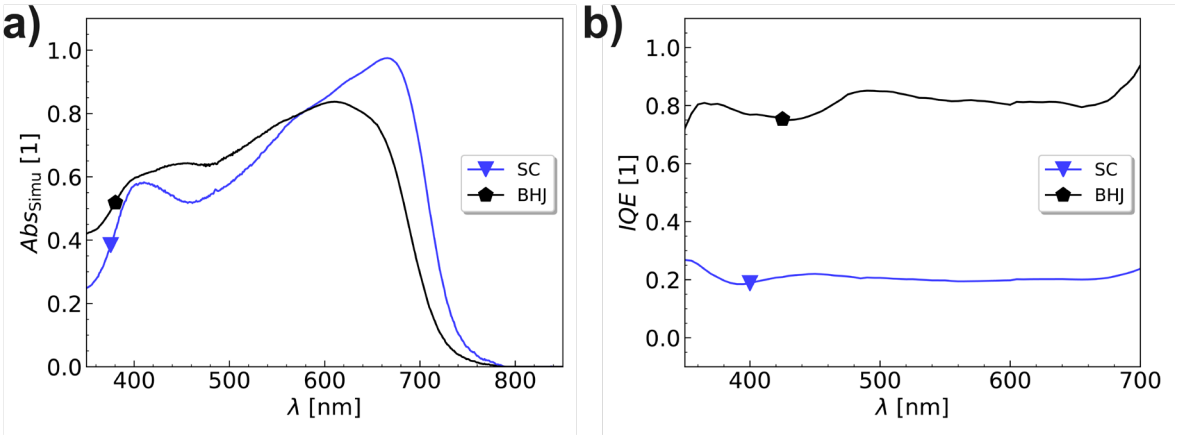

Figure 4-3: a) Simulated absorption of the AL within a full-stack device and b) estimated IQE spectra calculated from the measured EQE at zero bias and by using a) for the a neat DCV2-5T device (blue) and a DCV2-5T blend (black).[226]

Table 4-1: Obtained performance parameters of DCV2-5T and DCV2-5T:C_{60} devices, each with 8 nm undoped BPhen layer

	DCV2-5T	DCV2-5T:C_{60}
V_{OC} [V]	1.20	0.98
J_D [A/cm^2]	$2.4 \cdot 10^{-9}$	$9.6 \cdot 10^{-9}$
EQE (%)	20	68
D* [Jones]	$7 \cdot 10^{11}$	$2 \cdot 10^{12}$
E_g^{opt} [eV]	1.72	1.73
E_{CT} [eV]	–	1.53
V_{rad} [V]	1.38	1.27
$\Delta V_{OC,nr}$ [V]	0.18	0.29

4.2.2. Transient Absorption

Sample Configuration of DCV2-5T used for Ultrafast Spectroscopy

The excited-state dynamics of DCV2-5T were investigated via transient absorption (TA) spectroscopy and varying the interfaces at the active layer. This was done using four different sample geometries (cf. Figure 4-4): a neat film of DCV2-5T on glass (FN), a DCV2-5T film with transport layers (FS), DCV2-5T in a device without electrodes (DN) and a DCV2-5T full-stack device (DS). Here, the devices were measured under open-circuit conditions. The investigation of those four configurations allows to distinguish whether the observed behaviour of the excited state is intrinsic to the material or introduced by additional layers or electrodes. BPhen is used as an ETL and BPAPF and BPAPF:NDP9 are used as HTL. In contrast to section 4.2.1 above, the opaque Ag electrode was replaced by a semi-transparent Ag electrode, allowing transient absorption in transmission mode.

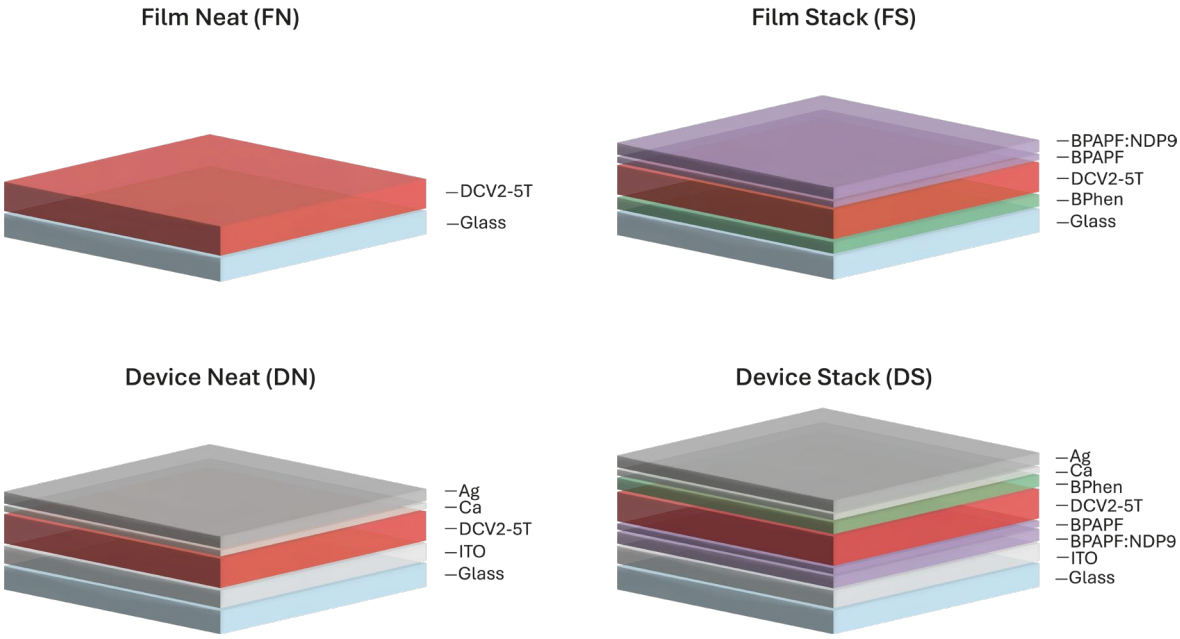

Figure 4-4: The four sample geometries of DCV2-5T in a film (FN), in a film with additional transport layers (FS), in a device with electrodes (DN) and in a full-stack device with transport layers and electrodes (DS), used for time-resolved measurements during Chapter 4 & 5.

During TA spectroscopy of neat DCV2-5T (cf. Figure 4-5), all four sample geometries were excited at 650 nm beyond the absorption maximum (cf. Figure 4-1a). At early times, both films and devices exhibit a GSB signal in the visible, spanning across the

absorption region of DCV2-5T, indicating the depopulation of the ground state due to photoexcitation. Simultaneously, a broad PIA signal is observed in the NIR, peaking around 1000 nm. Since it is initially dominant across all samples, this peak is attributed to the ESA of the DCV2-5T singlet exciton. Already within the first picosecond, devices exhibit a major difference to the films.

For FN, the ESA at 1000 nm dominates at early times and decreases while simultaneously a shoulder arises at around 870 nm, which is attributed to the presence of charge carriers. For FS, the presence of additional transport layers leads to a more pronounced 870 nm shoulder at late times, in comparison to FN. For both device configurations DN and DS, the 870 nm band emerges even more rapidly and with higher intensity. Already at early times, the exciton absorption peak at 1000 nm is less dominant, pointing towards an acceleration of charge formation in the presence of electrodes.

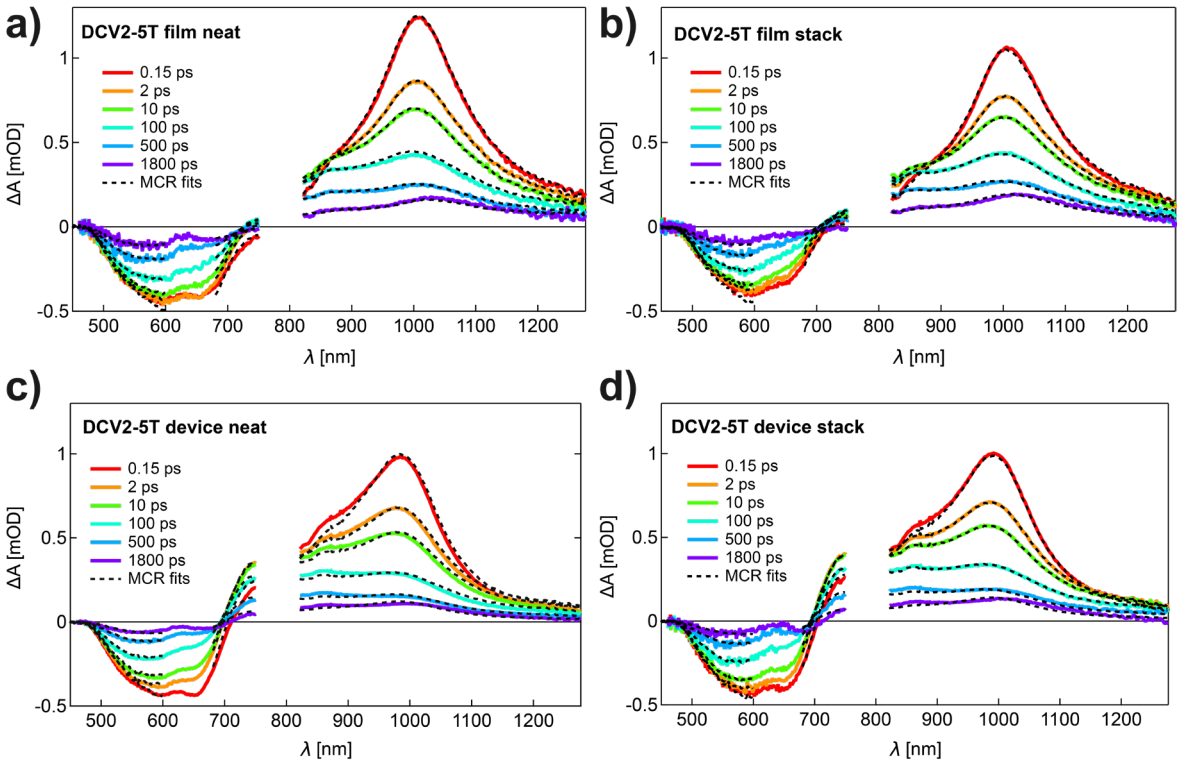

Figure 4-5: Time-resolved TA spectra of the DCV2-5T films a) FN, b) FS and the DCV2-5T devices c) DN and d) DS at various timedelays after excitation at 650 nm.

At late time delays, all sample configurations exhibit a significant positive absorption signal in the NIR, indicating the presence of long-lived excited states. Besides the broad signal at 870 nm, which is attributed to DCV2-5T charges, another signal is observable, especially in the FN and FS. Both films exhibit a peak similar but redshifted to the ESA of the exciton near 1020 nm. Since its appearance is at lower energies than the exciton and seems to appear only at late times, it suggests the presence of triplet states.

Spectral Deconvolution

Prior to extraction of the spectral guesses, all TA spectra were divided by the density of absorbed photons, so that the spectral shapes used for MCR are normalised to ΔA per absorbed photon. Based on the TA spectra in Figure 4-5 above and the suggested appearance of the species present in DCV2-5T, spectral guesses of the components were selected manually for the exciton from FN at early times, for the charge from DS at late times and for the triplet from FN at late times. These spectral guesses were used as starting points for a MCR which refined them and returned the spectral shapes displayed in Figure 4-6 and the corresponding population dynamics shown in Figure **4-7**. Due to the excitation at 650 nm, the bleach signal in the visible was affected by pump scatter, which limited the information for assigning the GSB shape to the spectral components, especially to the triplet. Therefore, the spectral region near the pump wavelength was masked to reduce its influence during MCR.

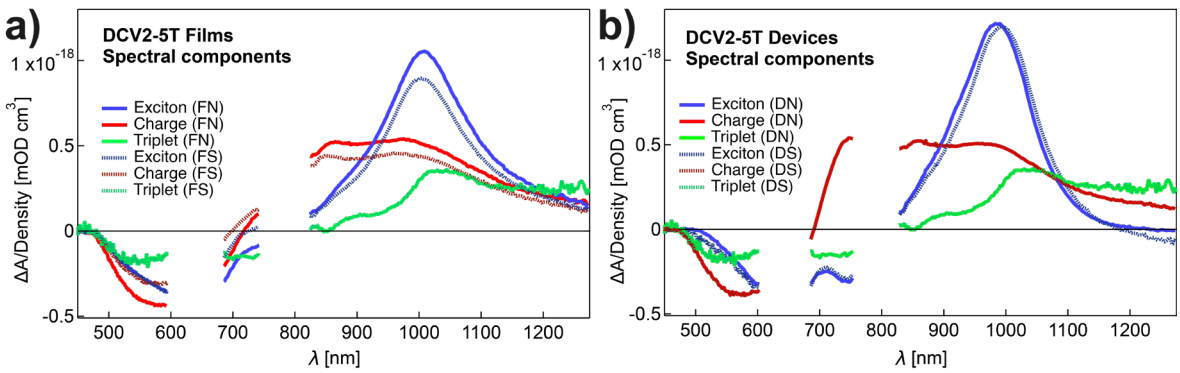

Figure 4-6: Spectral shapes of excited state species present in DCV2-5T, obtained via MCR of the TA spectra of FN, FS, DN and DS after 650 nm excitation for a) films and b) devices.

Transient absorption spectra of all four configurations were further investigated by MCR analysis and decomposition. The resulting MCR dynamics are displayed in Figure **4-7**, while Table S 4-1 shows the time constants obtained via multiexponential fits of the MCR dynamics via

$$y(t) = \sum_i A_i \cdot e^{(-t/\tau_i)} + y_0 \qquad (4\text{-}1)$$

with the amplitudes A_i of an exponential decay/rise i, the associated time constants τ_i and the offset y_0 of very long-lived species.

In all samples, the exciton population decays rapidly with time constants τ_1 & τ_2 of 0.4 ps & 18.0 ps for devices and 0.8 ps & 41.6 ps for films, indicating a rapid conversion from excitons into charges, which is even faster for devices. Exciton dynamics and constants are identical for FN and FS, suggesting no significant influence on the behaviour of excitons when only transport layers are present. This is reinforced by the exciton dynamics within in the devices. Although DN and DS exhibit a faster exciton decay than FN and FS, with both τ_1 and τ_2 smaller for devices, the differences due to the presence of TL are negligible, suggesting the presence of electrodes is responsible for the observed acceleration in the decay of exciton dynamics.

The charge population exhibits the same time constants for the initial rise with 0.8 ps for films and 0.4 ps for devices. Across all measured DCV2-5T samples, a charge population is already present at the earliest measured delays after excitation. While both FN and FS exhibit a similar rise of the charge component, their dynamics differ after the first 10 ps. Charge dynamics of FN starts to plateau before reaching 20 ps, while for FS they still exhibit a decent rise before both start to decrease beyond 100 ps. This suggests that TLs are responsible for a longer-lived charge species, which is supported by the longer decay time constants of the charge dynamics with 1019 ps for FN and 1202 ps for FS. The charge population in the devices rises essentially within the experimental temporal resolution, indicating stronger and more rapid charge formation in the presence of electrodes, and their decay time constants are 1188 ps for DN and 1400 ps for DS. In addition, the charge population of DS is slightly higher than the charge population of DN across the entire measured time window, similar to the slower

charge dynamics decrease for FS. Since the TA spectra were normalised to the density of absorbed photons beforehand, the initial charge population was about 60 % for the devices and about 20 % for the films of the total excitation density, indicating a significant improvement of early-time charge formation when electrodes are present. At longer timedelays, the charge population becomes comparable across all samples, indicating that the presence of electrodes improves the charge formation efficiency at early times but does not increase the long-time yield under open-circuit conditions. Also, the presence of TLs only slightly suppresses recombination at longer timedelays. Furthermore, TLs have a negligible effect on the formation of charges, indicating that the formation occurs predominantly within the DCV2-5T bulk rather than at TL interfaces.

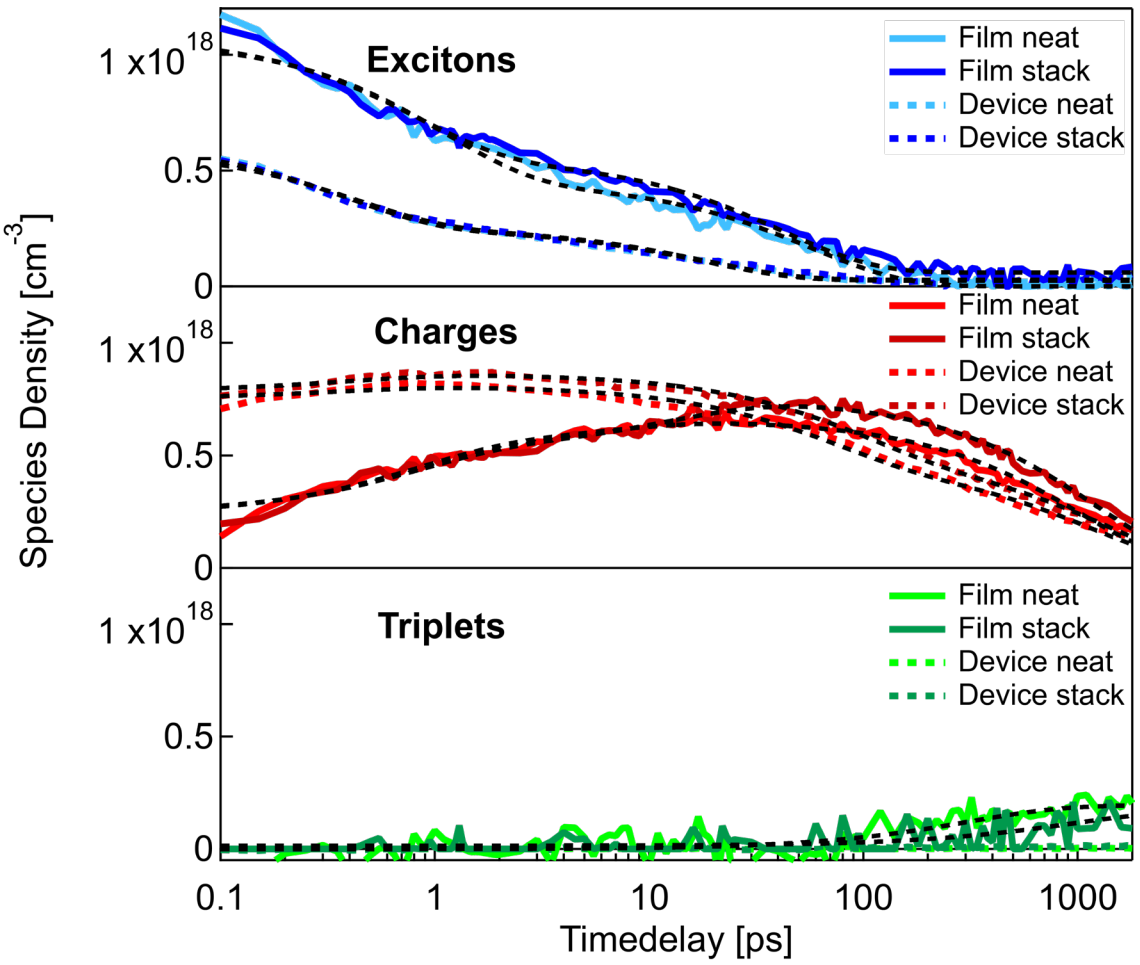

Figure 4-7: Evolution of excited state species in the TA spectra of all four configurations FN, FS, DN and DS, obtained via MCR analysis with respective multiexponential fits (black dashed lines).

MCR analysis suggests a weak triplet contribution for DCV2-5T films after 100 ps. Remaining pump scatter reduced the information content in that spectral region and thus most likely led to significant uncertainties in the MCR assignment. Within these limits, the films show a delayed rise of a longer-lived triplet population. However, no triplet population could be resolved for the devices. Triplet formation can occur either by direct ISC or via CT-mediated pathways. Due to weak spin-orbit coupling and the strong ultrafast formation of charges, direct ISC is unlikely to dominate. Consequently, CT-mediated triplet formation is expected.[231] If devices separate charges faster and more efficiently than films, this reduces the CT population and lifetime, leading to a weaker and later triplet signal in devices than in films. Considering the already weak triplet signal in films and the MCR uncertainties, this could explain why no triplet dynamics were detectable for the devices, as their contribution remained below the resulting assignment limitations. In any case, this will be further investigated, refined and explained in chapter 5 in connection with varied excitation energy in transient absorption and electromodulated absorption spectroscopy.

4.3. Conclusion

The steady-state results in this chapter show a significant influence of film morphology and device architecture on shunt resistance, dark current and the overall device performance. Minimising surface roughness can reduce leakage current, while a higher crystallinity can enhance charge transport but often increases dark current due to the formation of shunt pathways. The best-performing DCV2-5T device achieved an exceptionally low dark current and a LDR comparable to commercial silicon photodiodes. An EQE of about 20 % achieved for DCV2-5T devices at zero bias with an opaque Ag electrode is among the highest reported for vacuum-processed, single-component small-molecule devices. The IQE based on simulated absorption reveals incomplete charge extraction as the main limitation in neat DCV2-5T devices.

TA measurements performed on films and devices demonstrate that charge generation occurs on sub-picosecond timescales for all sample configurations. MCR analysis shows that the kinetics of exciton and charge populations are not substantially affected by the presence of transport layers alone but are strongly influenced by the presence of electrodes, highlighting the importance of internal electric fields for efficient charge generation. While the initial charge formation in DCV2-5T greatly benefits from the presence of electrodes, this does not translate into a higher longer-lived population under open-circuit conditions. Triplet formation is observed as a minor and delayed process in film samples, while no robust triplet signal was resolved in the devices.

Together, DCV2-5T exhibits efficient and ultrafast charge generation within the bulk without the need for a conventional D–A interface. The device performance is ultimately determined by the interplay between the material-related charge generation and the subsequent extraction process, governed by the energetic alignment between the active layer and the contacts. However, the role of triplet states could not be fully resolved and will be systematically addressed in the following chapter 5, using alternative excitation conditions and spectroscopic methods.

4.4. Appendix

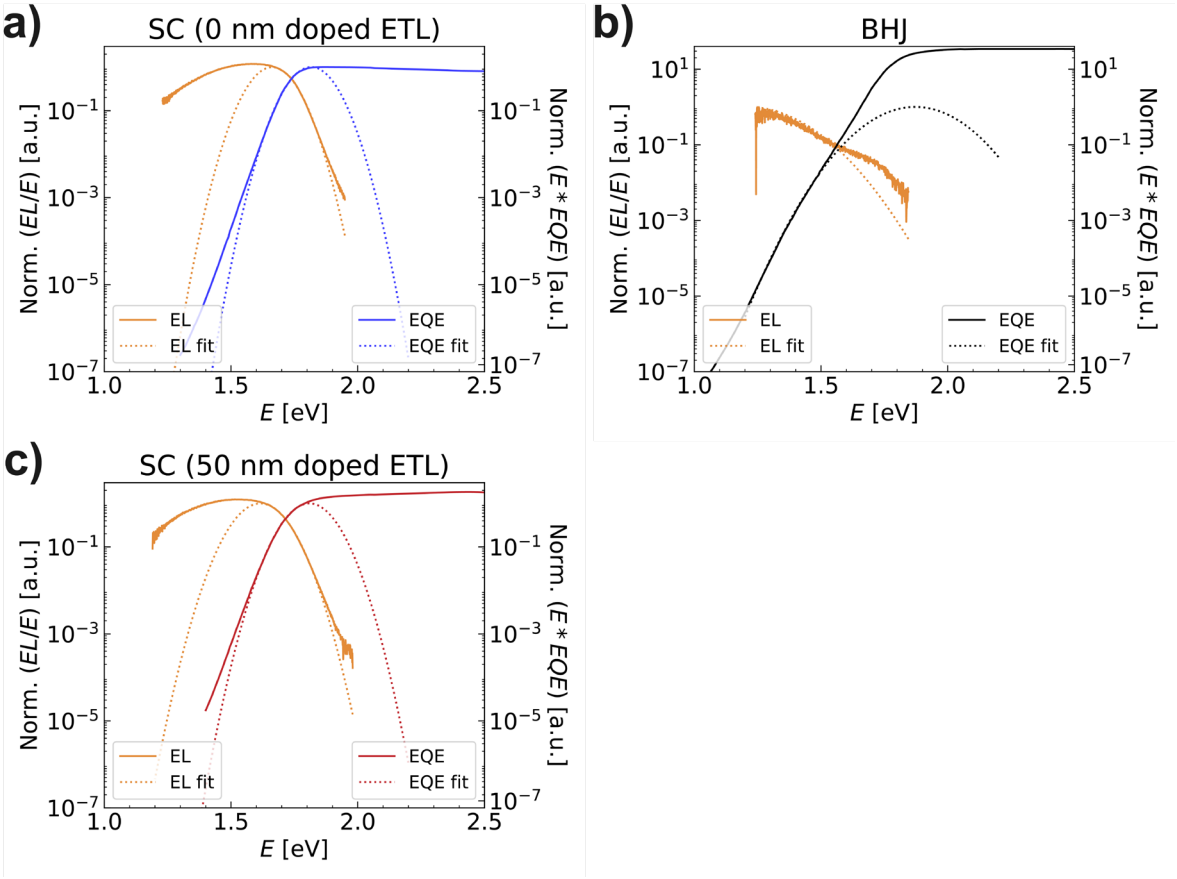

Figure S 4-1: Reduced and normalized EL and us-EQE for the DCV2-5T device a) without a doped BPhen ETL and c) with a 50 nm 1:1 ratio caesium-doped BPhen ETL and b) for the DCV2-5T:C_{60} blend. During the EL measurement a constant current of a) 100 µA, b) 500 µA and c) 500 µA is applied and no sub-gap emission peak is observed for DCV2-5T and a strong CT-state emission for DCV2-5T:C_{60}. The Gaussian fitted absorption and emission curves exhibit optical gaps of a) 1.74 eV, b) 1.55 eV and c) 1.71 eV.[226]

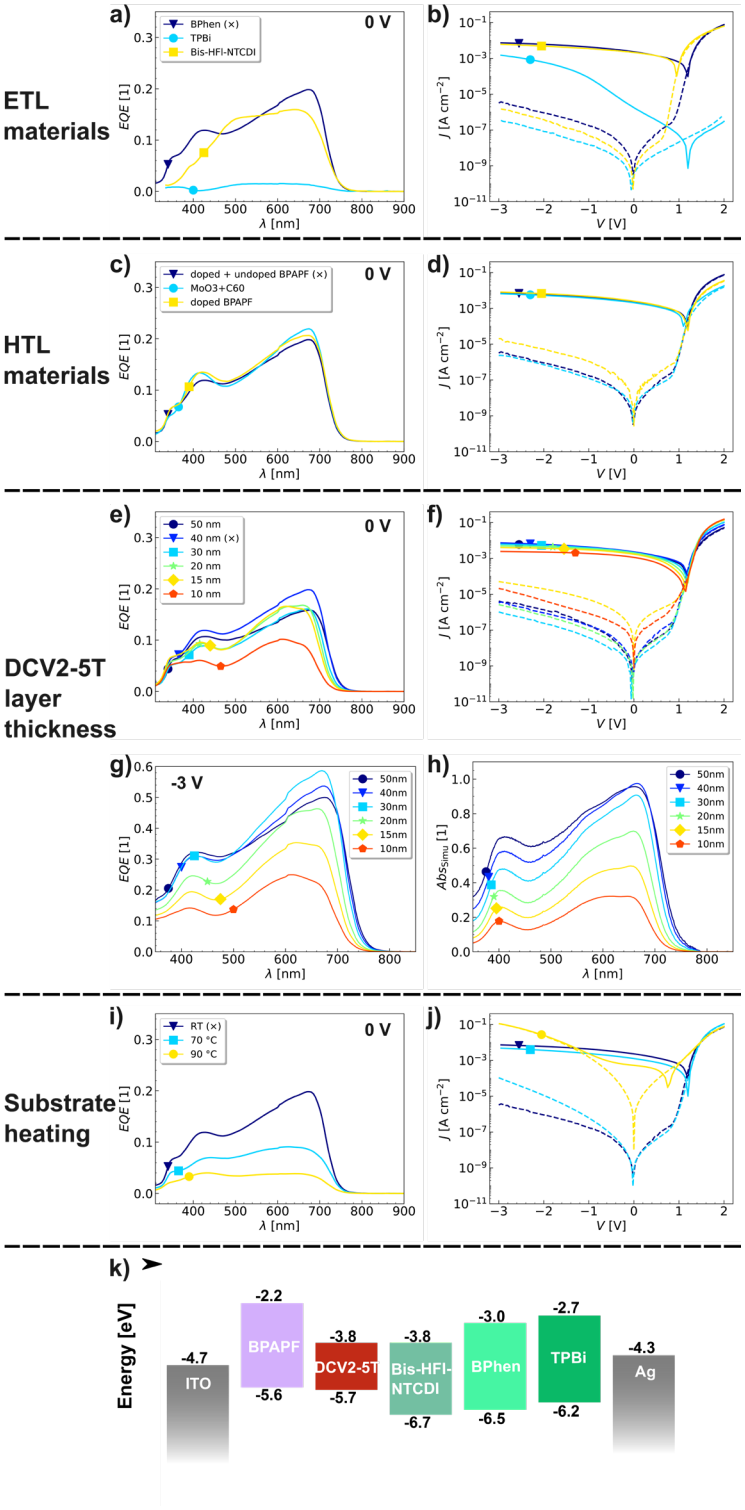

Figure S 4-2: Variation of the stack of the DCV2-5T device with EQE spectra measured at 21 Hz and 0 V and JV curves measured under 1 sun illumination in the dark for: a) & b) various ETL materials, where TPBi leads to an energy barrier and Bis-HFi-NTCDI reduces V_{OC}, c) & d) various HTL materials without noticeable effects on the OPD performance, e) & f) various AL thicknesses, where the chosen 40 nm represents the sweet spot between high absorption and efficient charge extraction and i) & j) substrate heating which mainly decreases shunt resistance due to higher surface roughness; g) the EQE at −3V and h) the simulated absorption for various active layer thicknesses; k) the energy levels of the ETL materials.[232,233] Curves of the used DCV2-5T stack are labelled with (x).[226]

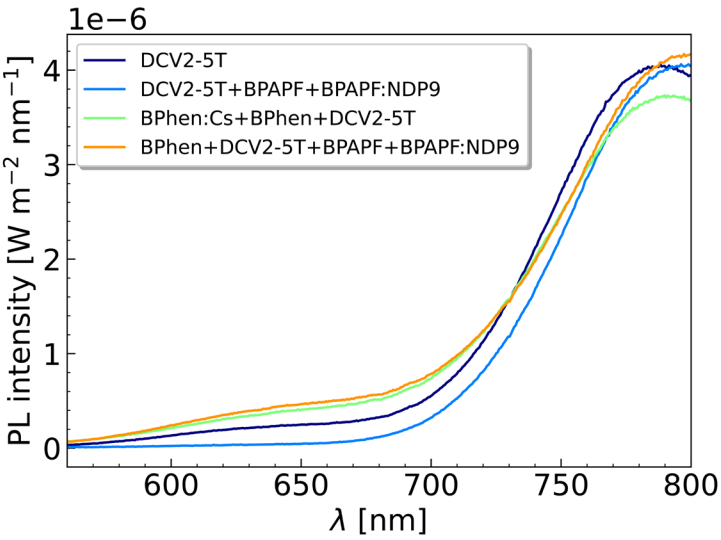

Figure S 4-3: Steady-state photoluminescence (PL) spectra for DCV2-5T films with different interlayers. The similar amplitudes and minor peak shifts indicate that the addition of transport layers including BPAPF:NDP9, BPAPF, BPhen and BPhen:Cs does not induce significant exciton quenching.[226]

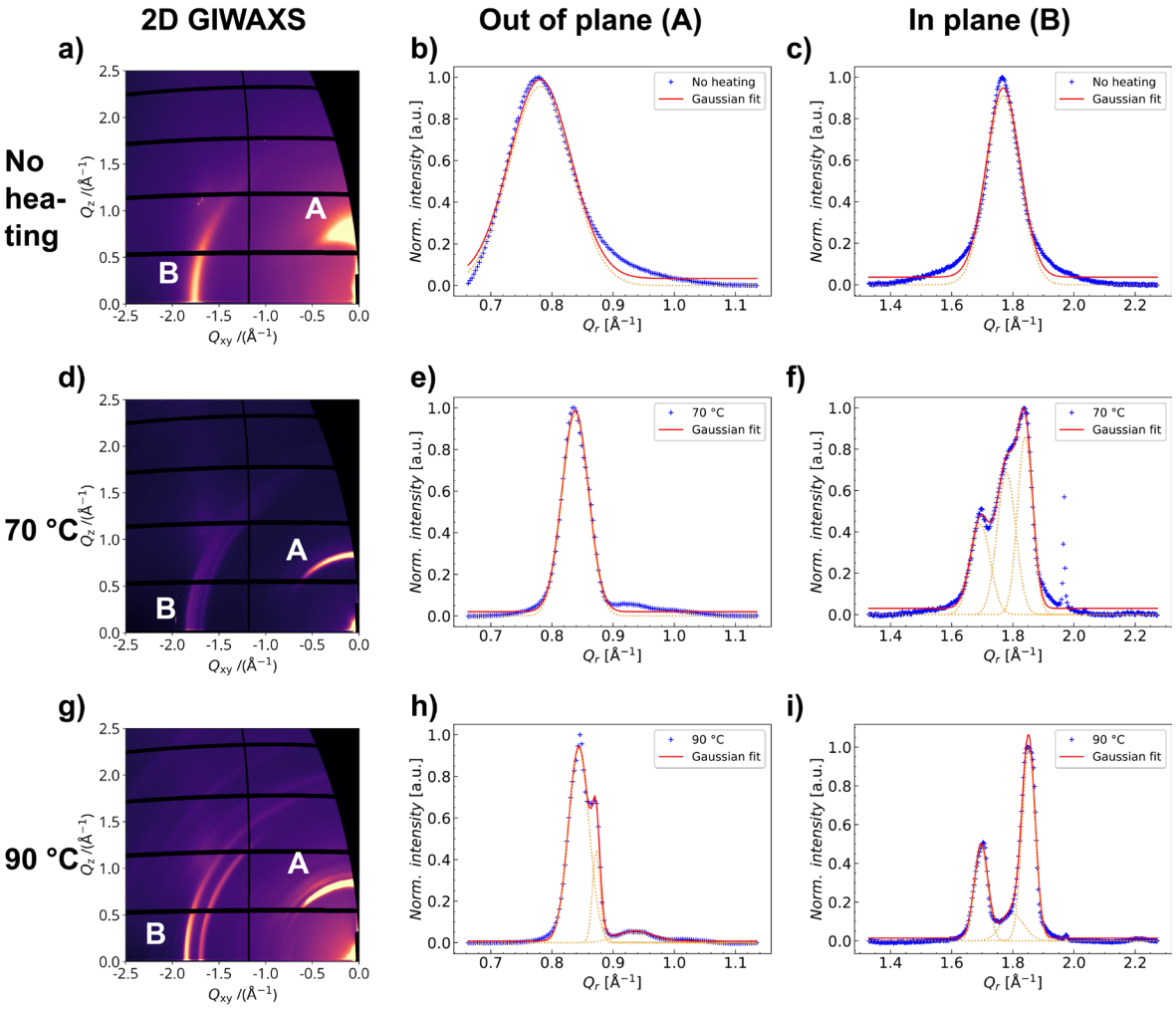

Figure S 4-4: 2D GIWAXS plots for 40 nm DCV2-5T films on 5 nm BPAPF a) without substrate heating, d) at 343 K and g) at 363 K and the respective out-of-plane cuts of peak A b), e), h) and the respective in-plane cuts of peak B c), f), i), confirming lower disorder in the neat DCV2-5T films with increased temperatures.[226]

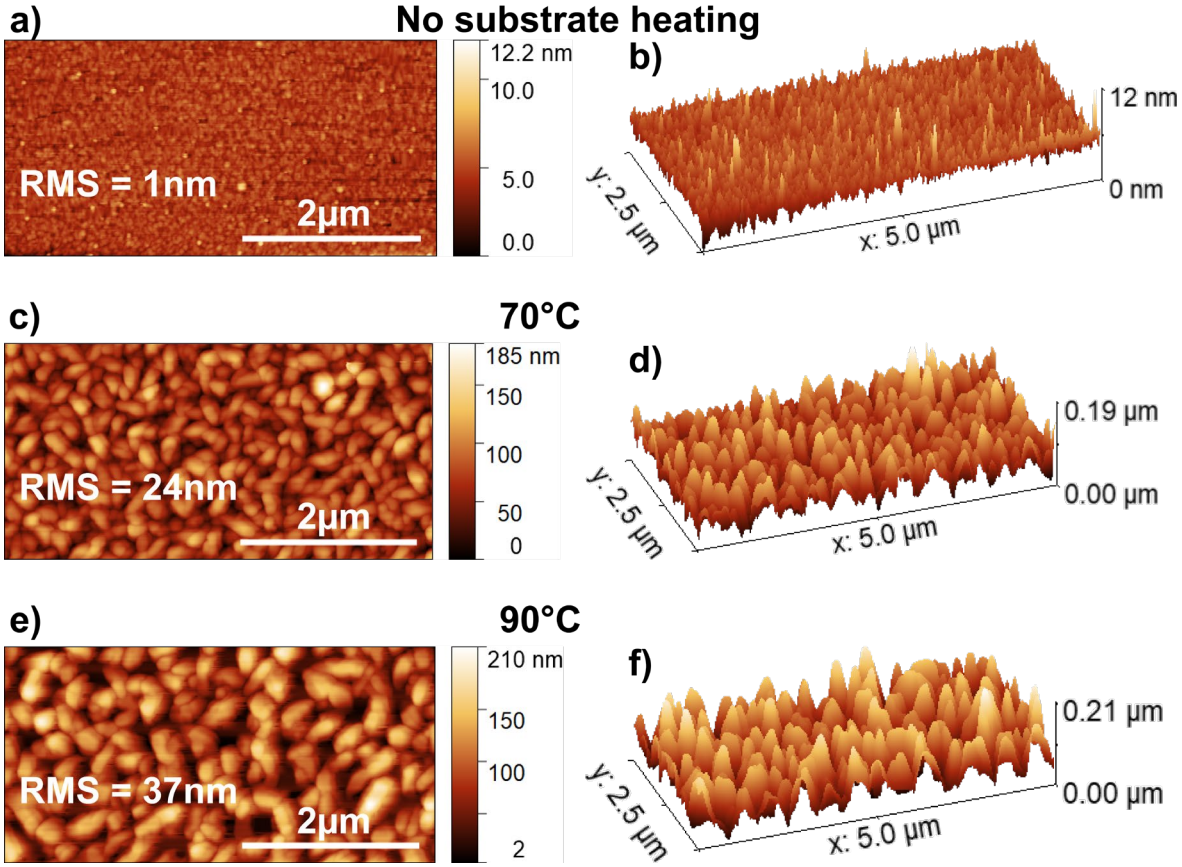

Figure S 4-5: AFM images for 40 nm DCV2-5T films on 5 nm BPAPF a) & b) without substrate heating, c) & d) at 343 K and e) & f) at 363 K, indicating the formation of bigger grains and an increased surface roughness by heating the substrate (RMS = 1 nm at RT, RMS = 24 nm at 343 K, RMS = 37 nm at 363 K).[226]

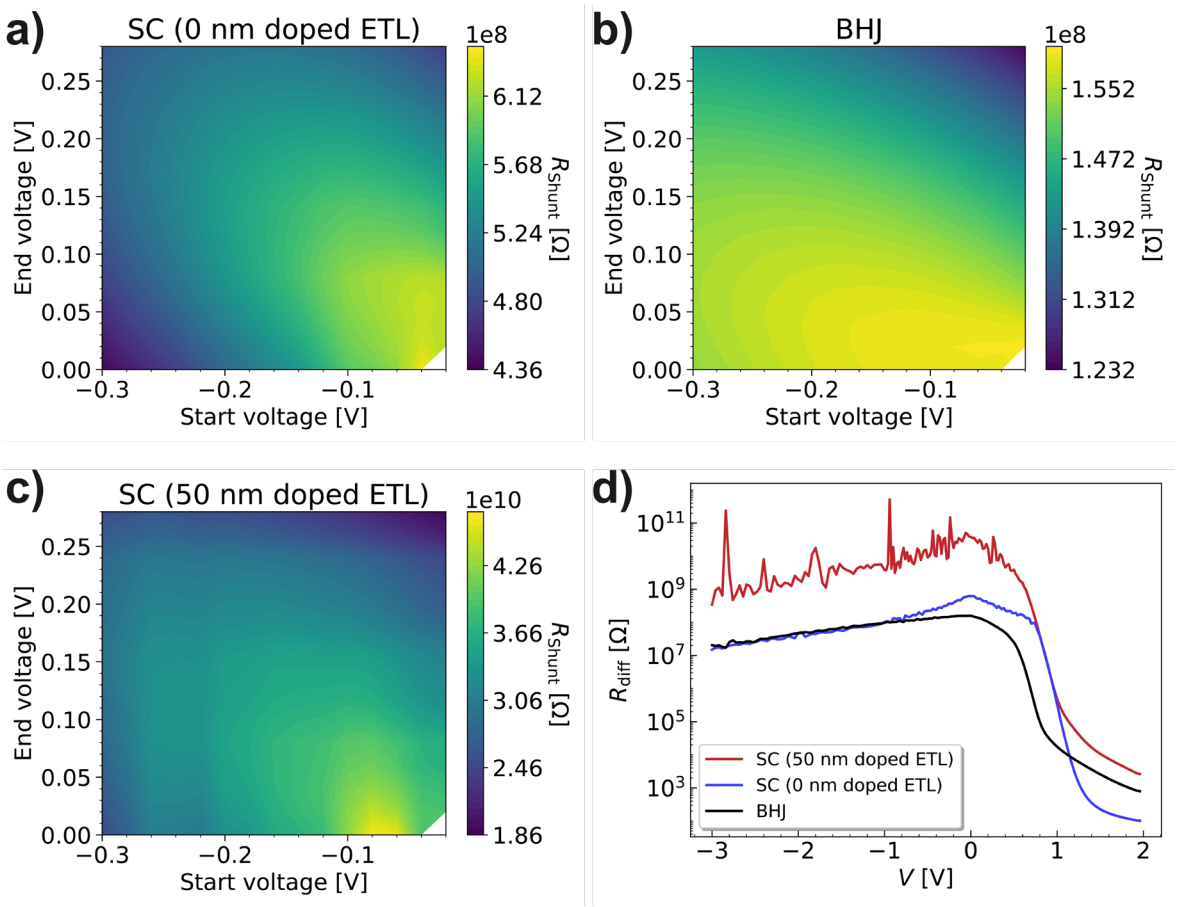

Figure S 4-6: R_{Shunt} calculated from linear fits of JV curve in dependence of start and end voltages within the fitting region for a DCV2-5T device a) without a doped ETL, c) with a 50 nm Cs-doped BPhen ETL, b) for a DCV2-5T:C_{60} BHJ device and d) the calculated differential resistance from JV curves of all three devices.[226]

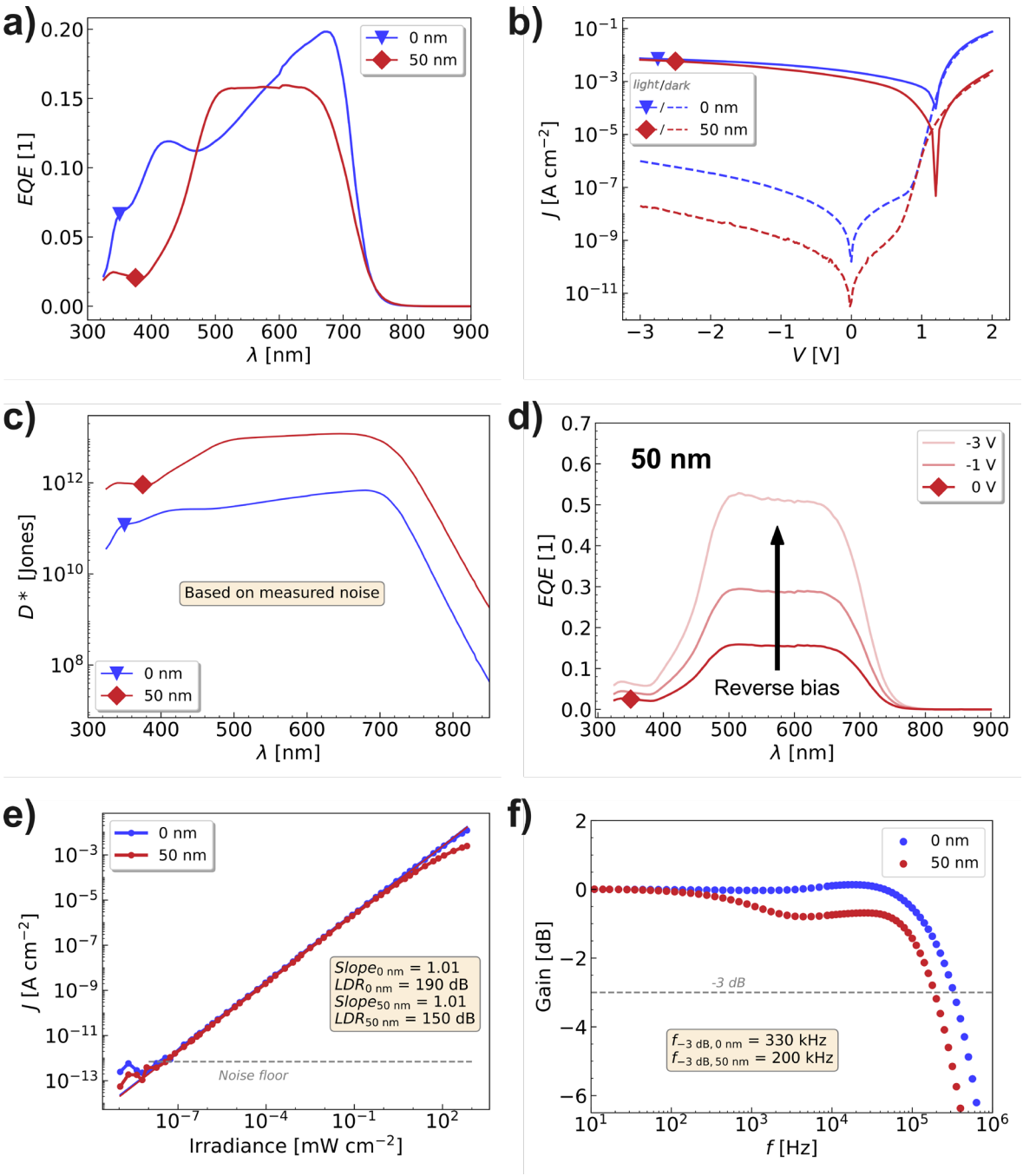

Figure S 4-7: a) EQE at zero bias, b) JV curves under 1 sun illumination (full) and in the dark (dashed), c) specific detectivity D* spectra at zero bias, d) bias dependent EQE, e) linear dynamic range (LDR) under illumination at 660 nm with 21 Hz without applied bias and f) photocurrent response at different light switching frequencies (λ = 660 nm and 33 mW/cm²) for a neat DCV2-5T device without (blue) and with a 50 nm Cs-doped BPhen ETL (red).[226]

Table S 4-1: Time constants of the evolution of excited state species in DCV2-5T obtained via multiexponential fits of MCR dynamics with the relative amplitudes of the decay (positive) and rise (negative) components with regard to the density of absorbed photons in brackets and a relative offset for very long-lived species.

	Species	τ_1 [ps]	τ_2 [ps]	τ_3 [ps]	Offset
FN650	Ex	0.8 (41 %)	41.6 (33 %)	–	4.5 %
	Ch	0.8 (−23 %)	6.3 (−10 %)	1019 (50 %)	0.3 %
	Tr	314 (−15 %)	–	–	15 %
FS650	Ex	0.8 (48 %)	41.6 (44 %)	–	5.4 %
	Ch	0.8 (−25 %)	13.5 (−21 %)	1202 (57 %)	0.4 %
	Tr	937 (−12 %)	–	–	13 %
DN650	Ex	0.4 (29 %)	18.0 (17 %)	–	1.9 %
	Ch	0.4 (−4.5 %)	68.1 (27 %)	1188 (35 %)	0.3 %
DS650	Ex	0.4 (26 %)	18.0 (17 %)	–	2.2 %
	Ch	0.4 (−6.1 %)	92.2 (28 %)	1400 (38 %)	−0.1 %

Chapter 5

Excitation Energy and Electric-Field Effects on Charge Formation and Separation in DCV2-5T

This chapter further expands and refines the time-resolved investigation of single-component DCV2-5T systems, focussing on the influence of excitation energy and external bias in this neat system. The device fabrication and steady-state measurements were performed by Jakob Wolansky of the group of Prof. Dr. Karl Leo at the Institute of Applied Physics at Dresden University of Technology. Ultrafast spectroscopy measurements were performed together with Jakob Wolansky.

5.1. Introduction

The previous chapter demonstrated that neat DCV2-5T exhibits efficient and rapid charge generation on ultrafast timescales, confirming its potential as a single-component material for optoelectronic devices such as OPDs and OPVs. This chapter builds up on these results and investigates how excitation wavelength, excitation density and field effects influence charge formation, separation and extraction in the neat DCV2-5T material.

Based on section 2.7, it is investigated whether the device performance of DCV2-5T is rather limited by the charge formation or extraction, if and to what extent the excitation wavelength influences charge population and evolution and how excitation density alters the behaviour of excited species in DCV2-5T. Furthermore, the role of device periphery on charge formation, separation and extraction is investigated and if field effects vary depending on excitation energy.

Ultrafast charge formation in neat DCV2-5T is efficient, while the dominant limitation is the stabilisation and extraction of those charges at the contacts. Excitation near the main absorption band prepares populations with greater survival and weaker field dependence than higher-energy excitations. Nonlinear excitation mainly increases singlet–singlet annihilation and non-geminate recombination, lowering the fraction of charges available for extraction.

DCV2-5T is therefore investigated in various sample configurations using transient absorption (TA) and electromodulated differential absorption (EDA) spectroscopy, to refine and extend the results of the previous chapter and clarify the mechanisms underlying charge generation, separation and extraction processes in DCV2-5T.

5.2. Results

5.2.1. Steady State

The steady-state characterisations of the DCV2-5T film and device were already performed during the previous chapter. However, it was beneficial to perform additional measurements tailored to the films and devices used in this chapter (cf. Figure 4-4), considering the transport layers and semi-transparent electrodes used. Unless otherwise specified, the respective layer thicknesses are identical for all samples, as described together with the preparation methods in section 3.1.1.

The steady-state absorbance spectra (cf. Figure 5-1) of the neat film (FN) and the stack film (FS) shows a broad absorption band across the visible region with a peak around 580 nm. FS exhibits a reduced absorbance between 450–850 nm, likely due to optical losses from reflection or interferences of the transport layers. Below 400 nm, the increased absorbance observed for FS originates from parasitic absorption of the TLs and independent of DCV2-5T, as confirmed by the steady-state spectra of FN. Here, the transmitted intensity falls below the dynamic range of the spectrometer, causing apparent absorbance saturation.

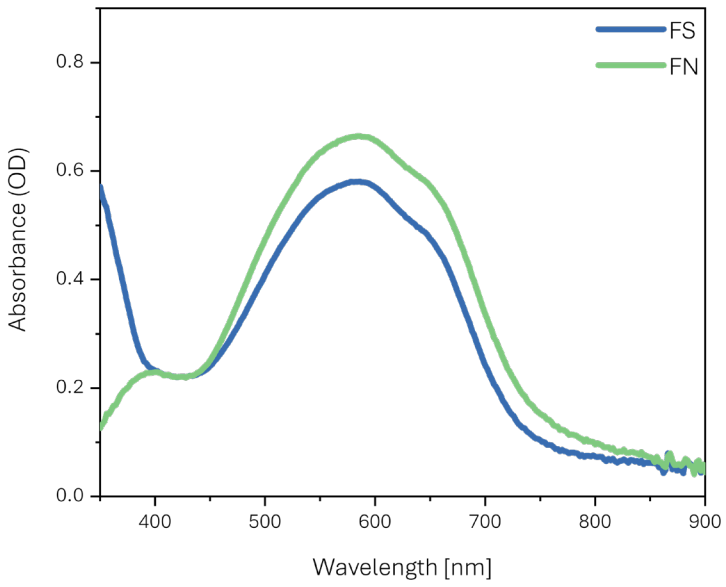

Figure 5-1: Absorbance of DCV2-5T films with (FS, blue) and without transport layers (FN, green).

When comparing the EQE of the DCV2-5T device with an opaque/untransparent Ag electrode (cf. Figure 4-2 a), the EQE of the device stack (DS), which is identical in layer sequence but uses a semi-transparent Ag electrode to allow transmission-mode measurements, is significantly reduced (cf. Figure 5-2(a)). Many OPV and OPD devices are typically illuminated from the ITO side with an opposite opaque electrode to utilise back reflections, which improves EQE results. However, since all ultrafast spectroscopic measurements were performed in transmission mode, the opaque Ag electrode had to be replaced with a semi-transparent one, which is why no back-reflection-driven EQE enhancement occurs here.

In Figure 5-2(a), DS exhibits a significant EQE between 400–700 nm with an increasing efficiency for higher wavelengths, resulting in an EQE of around 12 % at 650 nm and 8 % at 400 nm. Also, a strongly reduced EQE for DCV2-5T is observed in DN in the absence of TL, while the relative wavelength-dependence gets slightly reduced (cf. section 5.2.3, Table 5-1). The significant higher EQE of DS relative to DN indicates a higher incident photon to extracted charge ratio in the quasi-steady state. This already suggests an important role of transport layers within the DCV2-5T device, as they may enhance charge extraction or lower energetic extraction barriers.

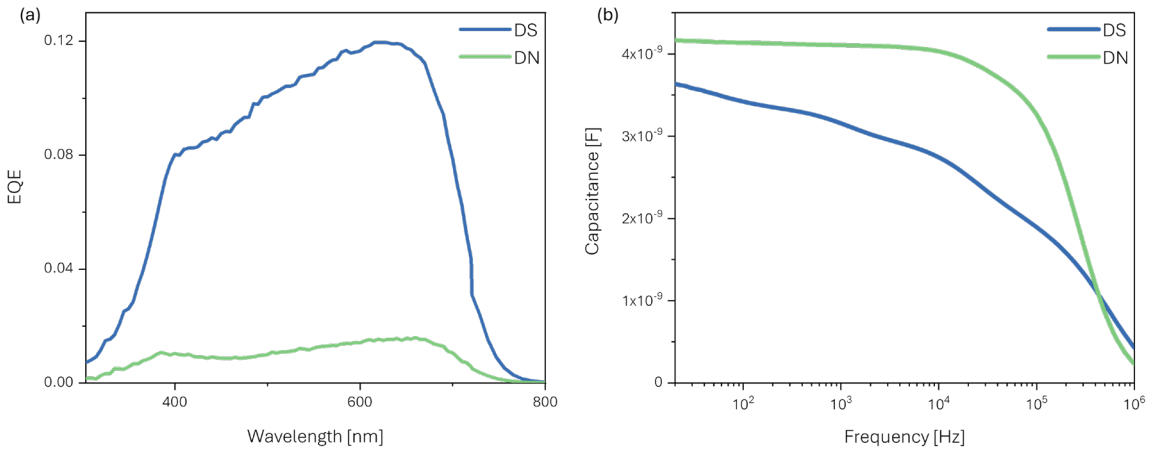

Figure 5-2: (a) EQE at zero bias and 21 Hz and (b) capacitance of the device neat (DN, green) and the device stack (DS, blue) with a semi-transparent Ag electrode.

By applying a small AC voltage to the devices and measuring the resulting AC current, the complex impedance Z(ω) was obtained and converted into the frequency-dependent capacitance, displayed in Figure 5-2(b). Basically, DS exhibits a lower capacitance than DN across the entire frequency range which is a direct consequence of the device architecture. In DN, the capacitance is determined by the thickness of the active layer and its dielectric constant, maximising the storable charges and measured capacitance at a given bias. TL however act as dielectrics in series with the AL and increase the effective thickness of the device. Since the total capacitance is limited to the smallest one for capacitors in series, a device like DS always exhibits a lower capacitance than a device like DN, as long as the capacitance of the AL is not the limiting factor.

The DCV2-5T device without TL exhibits a mostly frequency-independent capacitance response between 10^1–10^4 Hz before a significant decrease is observable at even higher frequencies, indicating unblocked diode-behaviour. Here, the AL is in direct contact with the electrodes, enabling rapid charge accumulation. As a result, slow processes that could hinder the device's field response are negligible, allowing for an almost unimpeded field-dependent behaviour. DS on the other hand reveals a frequency-dependent response of charge accumulation. The capacitance decreases with increasing frequency and indicates the presence of slower processes due to the additional interfaces introduced by the TL. At those interfaces, charges can accumulate or become temporarily trapped, leading to a delayed response to the applied electric field that becomes more pronounced with increasing frequency, as the charge accumulation at the electrodes cannot keep up with the faster alternating field. This suggests that the initial field-driven charge extraction can be slowed down by the presence of TLs, even though these layers support charge extraction, as shown in Figure 5-2(a) under steady-state conditions.

5.2.2. Transient Absorption

5.2.2.1. Transient Absorption Spectra of DCV2-5T

DCV2-5T Films

The TA spectra of the film without transport layers excited at 650 nm (FN650) and excited at 400 nm (FN400) are both displayed in Figure 5-3. The TA spectra of all films and devices, excited at 400 nm and 610 nm, were measured in the linear excitation regime and normalised to represent the same density of absorbed photons with $1.8{\cdot}10^{18}$ 'Ph'·cm^{-3} (cf. section 3.5), which enables direct comparison of all measured spectra and dynamics. When comparing both excitation wavelengths, a significant difference can be observed primarily at early times. The shoulder around 870 nm, which is associated with DCV2-5T charges, is more pronounced at early times, indicating faster initial charge formation with 400 nm excitation. These initial differences quickly diminish within the first 50 ps. Besides the charge absorption feature, both late time spectra exhibit a significant second peak close to 1040 nm. Across the TA spectra, this absorption peak seems to arise from a redshift of the exciton ESA signal. Since it is only appearing at late times, it is associated with the presence of triplet states.

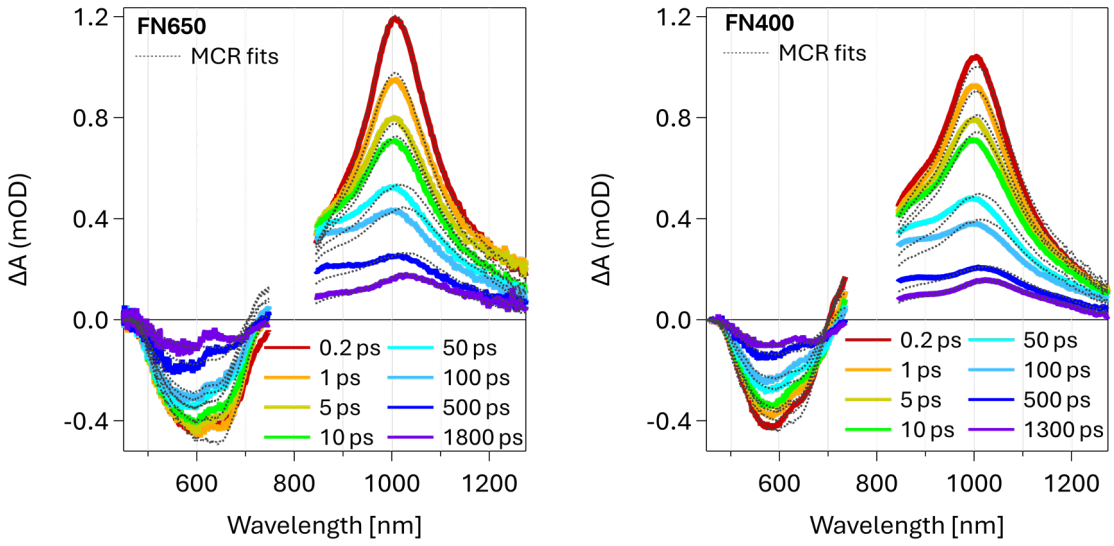

Figure 5-3: DCV2-5T TA spectra of the film neat (FN) excited at 650 nm (l.) and 400 nm (r.) for a series of pump-probe delays.

A similar trend is observed for the film with transport layers when excited at 650 nm (FS650) and at 400 nm (FS400) as shown in Figure 5-4. Also here, FS400 exhibit a stronger initial charge signal when comparing to FS650, while both FS exhibit a significant triplet signal at late times.

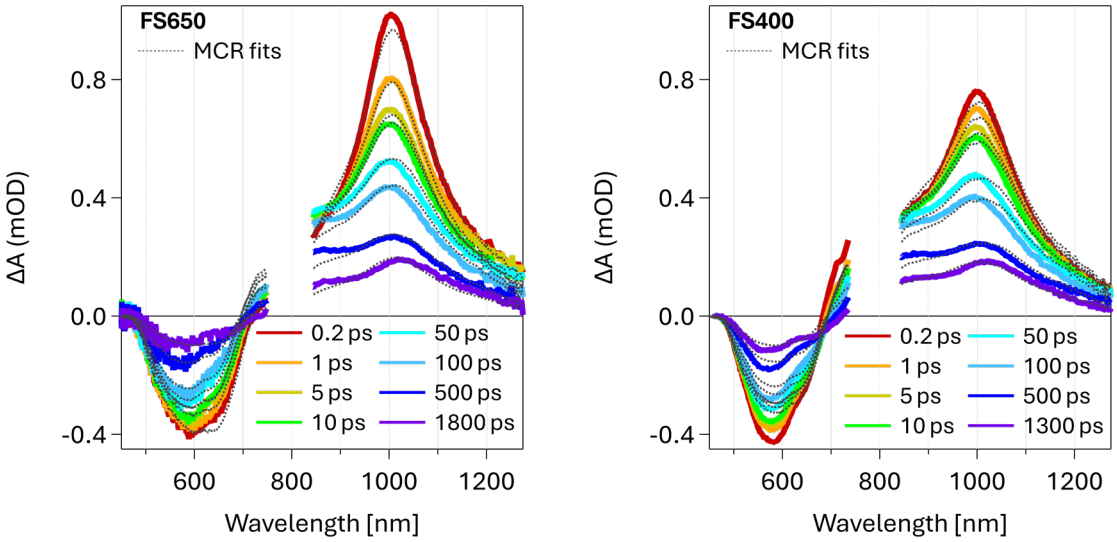

Figure 5-4: DCV2-5T TA spectra of the film stack (FS) excited at 650 nm (l.) and 400 nm (r.) for a series of pump-probe delays.

DCV2-5T Devices

Figure 5-5 shows the TA spectra of the DCV2-5T device without TL excited at 650 nm (DN650) and excited at 400 nm (DN400). At early times, both DN650 and DN400 exhibit a significantly higher shoulder around 870 nm than the films, indicating a rapid and more efficient charge generation on sub-200 fs timescales than observed in the absence of electrodes. Similar to the films, this ultrafast charge formation is more pronounced under higher incident photon energy. Over time, both DN650 and DN400 TA spectra start to converge, exhibiting a comparable shape after 50 ps. At late times, both DN predominantly show a persisting charge fraction with a small peak beyond 1000 nm, redshifted to the exciton ESA, indicating the presence of triplet states. This feature is less pronounced than for the films in absence of electrodes, suggesting a reduced triplet fraction at late times.

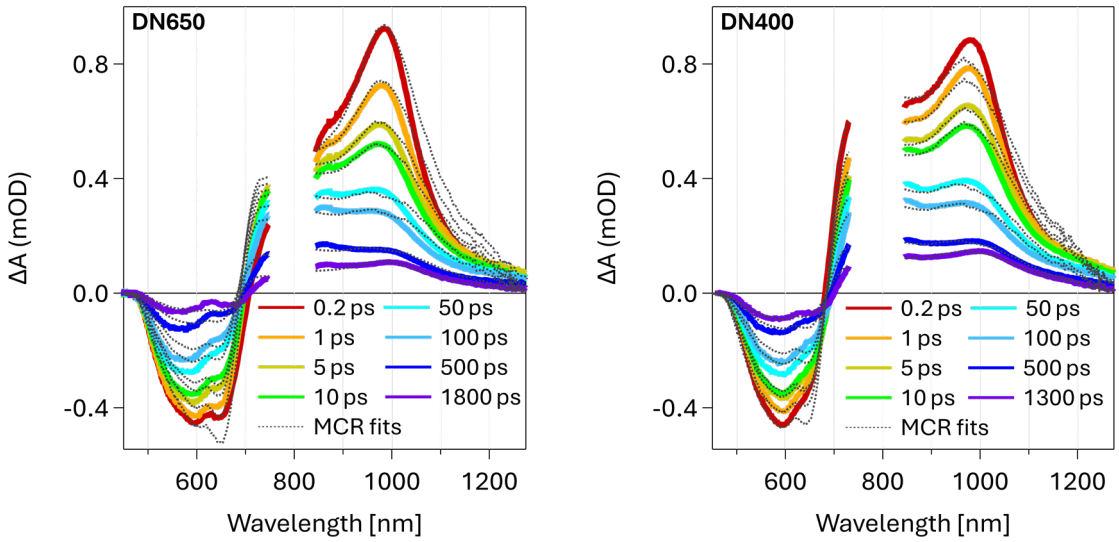

Figure 5-5: DCV2-5T TA spectra of the device neat (DN) excited at 650 nm (l.) and 400 nm (r.) for a series of pump-probe delays.

By adding TL to the device, DS show similar TA spectra to DN at both photon energies respectively (cf. Figure 5-6). During 400 nm excitation (DS400), also DS400 indicates a higher initial charge population than DS excited at 650 nm (DS650), following the trend of DN. For DS, both TA spectra seem to converge after 50 ps, without significant differences at later times.

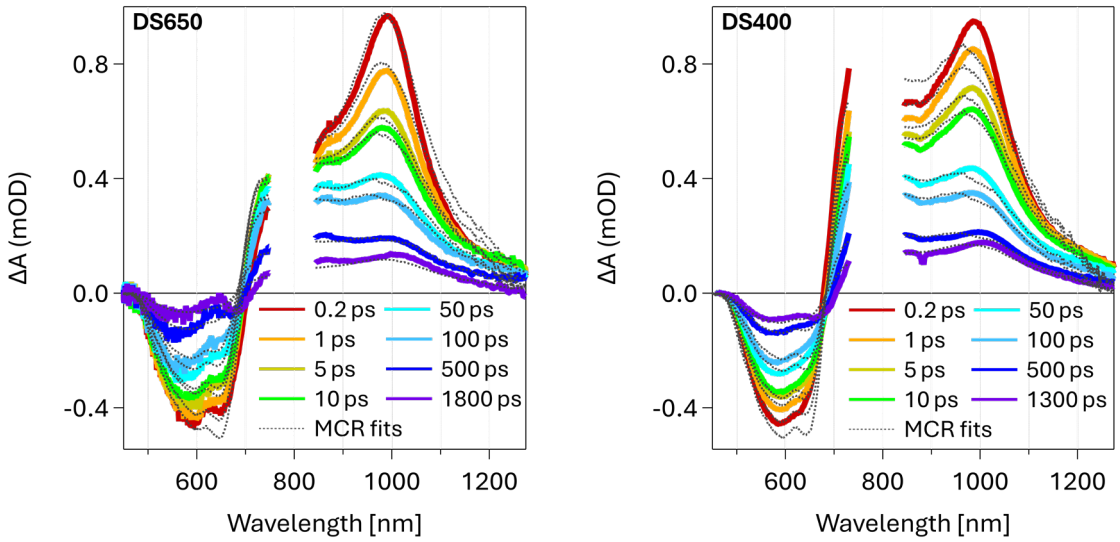

Figure 5-6: DCV2-5T TA spectra of the device stack (DS) excited at 650 nm (l.) and 400 nm (r.) for a series of pump-probe delays.

When comparing the spectral appearance of the DCV2-5T devices, measured under V_{OC}, with that of the films, the region around 720–750 nm exhibits a feature with mixed origin that cannot be assigned solely to one of the excited state species. This observation is attributed to electroabsorption (EA), arising from internal fields between photogenerated e–h pairs. In films, these internal fields are distributed over many orientations and the associated EA evolves in parallel with the charge population. This EA contribution is spectrally superimposed with and kinetically correlated to the charge signal. Within the fit tolerance, its contribution is most likely already captured within the charge spectrum.[234,235] In contrast, the presence of electrodes provides a preferred axis that biases these photoinduced fields and increases the net EA amplitude. This results in a directional internal field that induces a Stark shift and modulates the TA spectra, making a consideration as an additional spectral feature necessary. In contrast to other systems like PM6:Y6 (cf. chapter 6), DCV2-5T as a classical push-pull chromophore exhibits intramolecular CT character (a significant polarity between its donor and acceptor groups). During excitation, the formation of CTx states therefore leads to a significant change in the dipole moment and an EA contribution is expected to appear immediately with charge formation.

5.2.2.2. Multivariate Curve Resolution Analysis

Spectral Shapes of Excited States

The spectral shapes for excitons, charges and triplets, used for MCR, were extracted from the TA spectra as initial guesses and refined by a global MCR across multiple datasets to minimise spectral overlap between the species. The exciton shape was taken from the early-time film spectrum at 650 nm, the charge component from late times of the devices at 400 nm and the triplet from late times of the film at 400 nm under nonlinear excitation conditions, as presented later on in section 5.2.2.3. Also, the NIR parts of all components used for the devices are blueshifted by around 20 nm. In principle, such shifts could arise from changes in the dielectric environment or cavity effects when electrodes and interlayers are present, but this would affect the entire spectra und not just the NIR region.[208] Therefore, it is more likely that this systematic shift arises from a slightly shifted calibration of the white light. The spectral shapes of the components present in DCV2-5T samples are displayed in Figure 5-7.

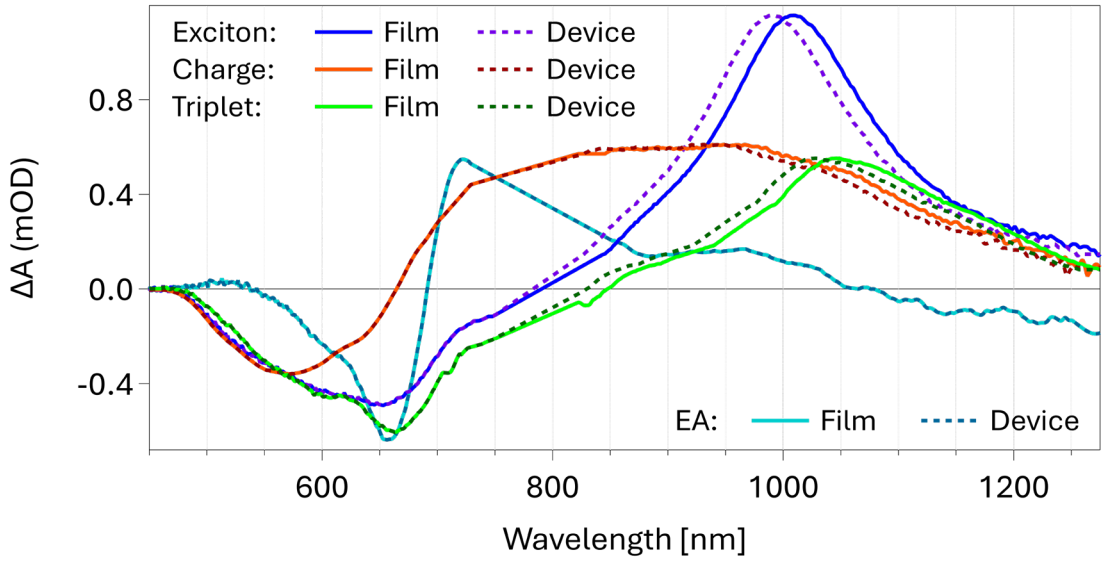

Figure 5-7: Spectral shapes of species present in the TA spectra: singlet DCV2-5T exciton (blue), DCV2-5T charge (orange), DCV2-5T triplet (green) and the directional electroabsorption signal (turquoise) for DCV2-5T films and devices.

To obtain an appropriate spectral shape of the electroabsorption in DCV2-5T, two independent approaches were used. Since DCV2-5T was also investigated using EDA spectroscopy (cf. section 5.2.3), the EA signal prior to excitation was extracted. Applying an external bias results in the spectral shape of the induced Stark shift, which is inverted to the spectral shape expected from an internal electric field. However, EDA is only measured in the visible region. In order to obtain an EA signal spanning the entire wavelength range, the late time spectra of a DCV2-5T device and film were subtracted, considering also the present triplet population and compared to the EDA-based EA signal (cf. Figure 5-8). Because DCV2-5T shows negligible steady-state absorbance in the NIR, the negative EA contribution near 1200 nm is expected to be minimal and most likely arise as an artefact from the device–film late-time subtraction method used. This approach[219,236,237] is further explained for PM6:Y6 in section 6.2.4.2 under 'Spectral Deconvolution'.

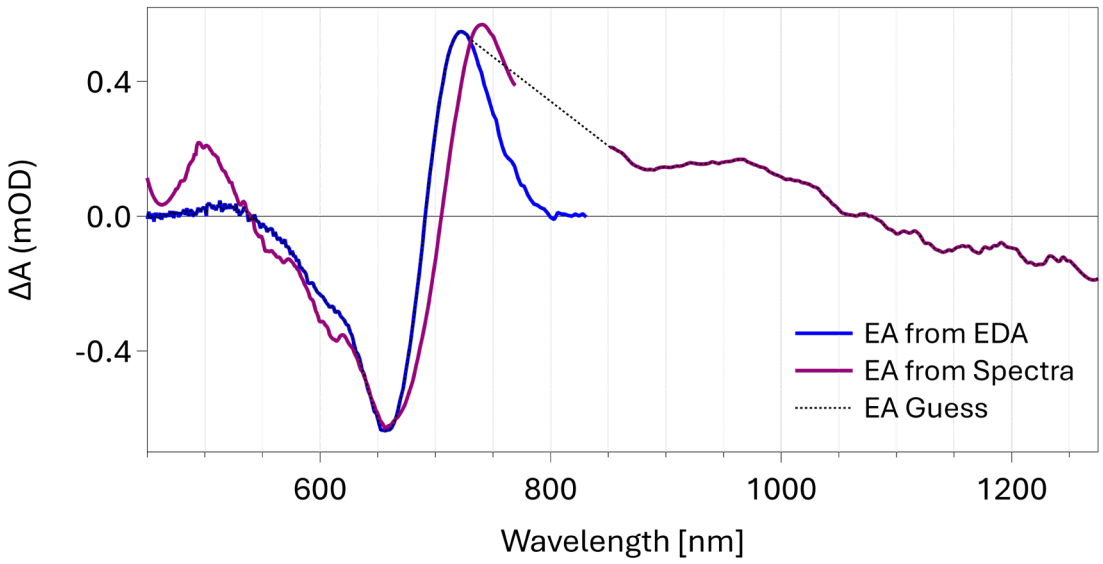

Figure 5-8: Derivation of the spectral shape of electroabsorption (dotted) from the differential late-time spectra of DCV2-5T film and device (fuchsia) and the electroabsorption of the DCV2-5T device in EDA prior to excitation (blue).

DCV2-5T Films

The DCV2-5T films during 400 nm excitation were further analysed by spectral deconvolution using MCR (cf. Figure 5-9). Also, the MCR analysis of the films during 650 nm excitation from the previous chapter was refined. All films are analysed and displayed with the same density of absorbed photons within the linear excitation regime (cf. section 3.5). The 400 nm data allowed an extraction of spectral shapes without distortions caused by pump scatter. Here, component amplitudes can differ from Chapter 4 because here a single global set of species spectra was used across all films for both excitation wavelengths, with also including an explicit EA component, whereas Chapter 4 used separate spectral shapes for FN, FS, DN and DS. Including the cleaner 400 nm dataset reduces pump-scatter artefacts and mixing between components, which can change the relative amplitudes between the same species in different samples and produce small shifts in the extracted time constants. Here, similar spectral shapes for the same components were used across the samples to improve identifiability and reduce mixing between components in kinetic fits.[238]

The rise of the exciton species occurs beyond the TA resolution for all films, followed by an ultrafast population decrease within a few picoseconds and a subsequent slower decay. The exciton population decays with time constants τ_1 & τ_2 of 2.0 ps & 46.8 ps for FN400 and 4.2 ps & 50.8 ps for FS400, while the time constants for 650 nm excitation with τ_1 & τ_2 of 1.6 ps & 40.0 ps for FN650 and 1.3 ps & 60.5 ps for FS650 slightly increased, compared to the results of chapter 4. For both FN and FS, excitation at 650 nm leads to a higher initial exciton population and a lower initial charge population when comparing to 400 nm. Furthermore, a comparable exciton behaviour is observed between FN and FS, where FN exhibits a higher initial population than FS, for both excitation wavelengths. During mid times, the population of excitons for all films converges, exhibiting similar late-time behaviour.

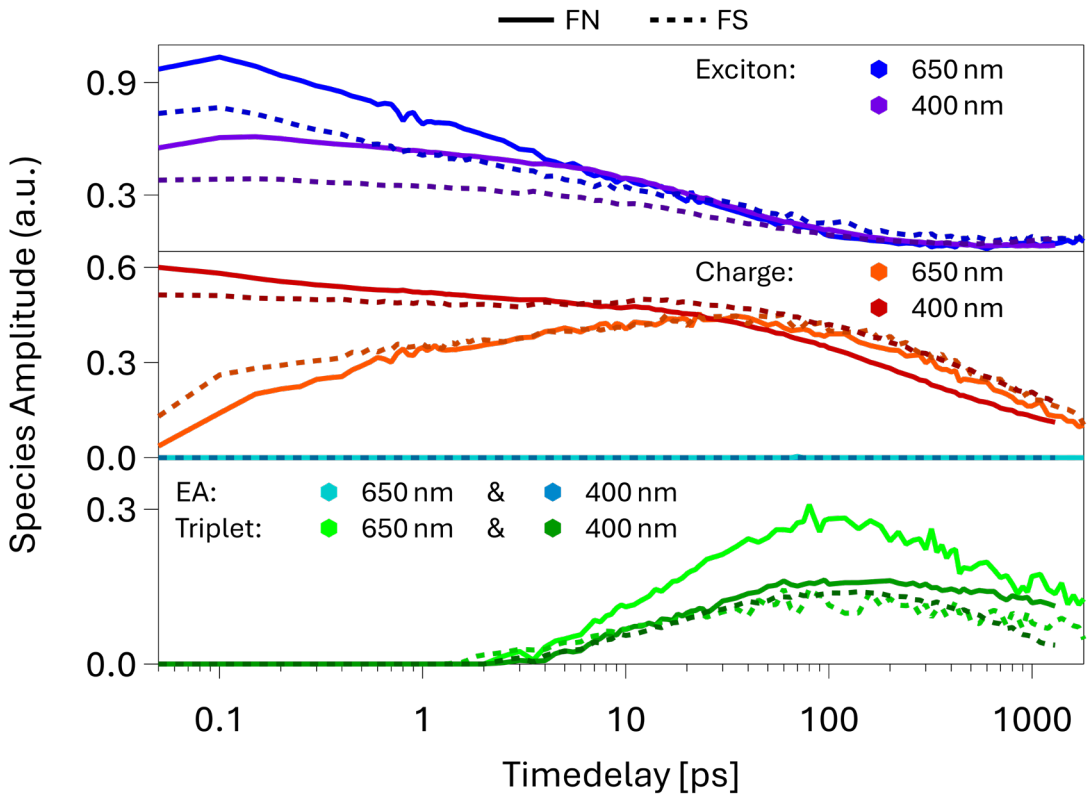

Figure 5-9: Time-resolved relative contribution to the measured ΔA of each species: DCV2-5T singlet exciton (top), DCV2-5T charge (middle) and DCV2-5T triplet states (bottom), present in the DCV2-5T films FN & FS and obtained via MCR analysis.

The differences in evolution of the charge population correlate closely with those of the excitons. During 650 nm excitation, charge formation arises for both FN and FS from near zero with a subsequent fast growth. When excited at 400 nm, both films exhibit a significantly faster and more efficient charge formation. This follows an excess-energy mechanism. In DCV2-5T, absorption at 400 nm gives access to energetically higher-lying singlet states. These states exhibit a higher delocalisation and have stronger electronic coupling to intramolecular CT states, increasing the transfer-probability before cooling and thermalisation.[50,239] At longer timedelays, charge populations formed during 650 nm and 400 nm excitation start to converge, revealing the loss of the 400 nm-advantage. The late-time charge population for 650 nm points towards a slightly suppresses recombination when TLs are present. A similar trend is observed for 400 nm, where FS400 and FS650 exhibit similar late-time charge populations, while the longer-lived charge population of FN400 is significantly reduced, compared to

FN650. This indicates that the charge population formed via excess-energy pathways is more vulnerable to loss pathways when not stabilised by TLs.

The MCR analysis of the films were also performed by including the EA component. As explained earlier in this section, a separable EA response is not expected in the films. Accordingly, fits with an unconstrained EA component returned no distinct EA contribution at any delay for none of the FN and FS spectra. This supports the EA spectral shape used and indicates no contributions from other excited state species.

Triplet states arise delayed relative to the charge formation. The dominant formation for triplet states is attributed to CT-mediated formation pathways, as suggested in chapter 4. This means that ISC occurs predominantly from a CT state, while direct ISC from S_1 is less likely. Kinetics suggest a significant population rise across all films with time constants of 12–14 ps. FN generally shows a higher triplet population than FS. This is attributed to the charge-stabilising character of the TL, which shortens the 'residence time' of a CT state in a relatively tightly bound configuration for ISC, resulting in reduced triplet formation.[64] FS exhibit a similar amplitude in triplet dynamics under both excitation conditions, while for FN650 the amplitude is significantly higher than for FN400. This likely results from an overestimation of the triplet amplitude during mid times. A similar triplet behaviour would be expected for FN400 and FN650, as it is the case for FS400 & 650.

The MCR analysis of FN and FS under 650 nm and 400 nm excitation reveals a clear dependence on the incident photon energy. For both FN400 and FS400, higher photon energy result in a more rapid exciton decay along with an earlier and stronger initial charge formation, than under 650 nm excitation. The influence of the higher photon energy reduces at later times, leading to a comparable charge population between 650 nm and 400 nm excitation for FS. The influence of TLs during 650 nm excitation remains less pronounced, reinforcing the observations of chapter 4, while 400 nm charges seem to be more vulnerable to recombination when TLs are not present. A significant difference was observed for the triplet state population. A comparable rise was observed across all measurements, while the observed triplet population was less for FS than for FN, which may result in a more stabilised charge population in the presence of TL, leading to reduces triplet formation.

DCV2-5T Devices

The DCV2-5T devices during 400 nm excitation were further analysed by spectral deconvolution using MCR (cf. Figure 5-10). Also, the MCR analysis of the devices during 650 nm excitation from the previous chapter was refined. All devices are analysed and displayed with the same density of absorbed photons (identical to that of the films with $1.8{\cdot}10^{18}$ 'Ph'·cm^{-3}) within the linear excitation regime (cf. section 3.5).

During 650 nm excitation, the MCR dynamics of both DN650 and DS650 (cf. Figure 5-10) exhibit a higher initial exciton population than for 400 nm excitation. This indicates a more rapid charge formation for both devices during 400 nm excitation. After 10 ps, exciton dynamics of 400 nm and 650 nm converge, before depleting within the first 100 ps for all devices. Overall, the exciton population in devices persists for a significantly shorter time period than in films due to the presence of electrodes, indicating a substantially higher efficiency of exciton conversion. MCR dynamics of all films and devices excited at 400 nm are shown in Figure S 5-1.

The observations of exciton dynamics of the devices are reinforced by the lower initial charge population, when comparing DN650 and DS650 to DN400 and DS400. At 650 nm, both DN and DS exhibit a significantly reduced rapid charge formation on sub-200 fs timescales. Kinetics exhibit time constants between 0.1–0.2 ps during 650 nm excitation of the devices, while it is faster than the resolution of the TA setup for 400 nm. DS exhibits slightly elevated charge population than DN for both excitation wavelengths. Not only higher-energy photons accelerate and increase the formation of charge carriers in DCV2-5T, also the presence of electrodes significantly improves this process by lowering the activation barrier for the formation of CT states, as observable by the direct comparison between device and film dynamics in Figure S 5-1.

For both excitation wavelengths, DN and DS exhibit comparable dynamic-traces for the fitted EA component. Differences in contributions of EA between 400 nm and 650 nm excitation remain negligible. Nevertheless, the higher initial charge population of DN400 and DS400 is not recognisable in the EA dynamics. In DCV2-5T the EA amplitude reflects not only the number of photoinduced charges but also the effective internal field per charge, which depends on the average electron–hole separation and

orientation. Consequently, a larger early charge amplitude does not imply a proportionally larger EA signal. It is assumed that at late times FC should significantly contribute to the charge population and therefore dominate the late times EA signal.

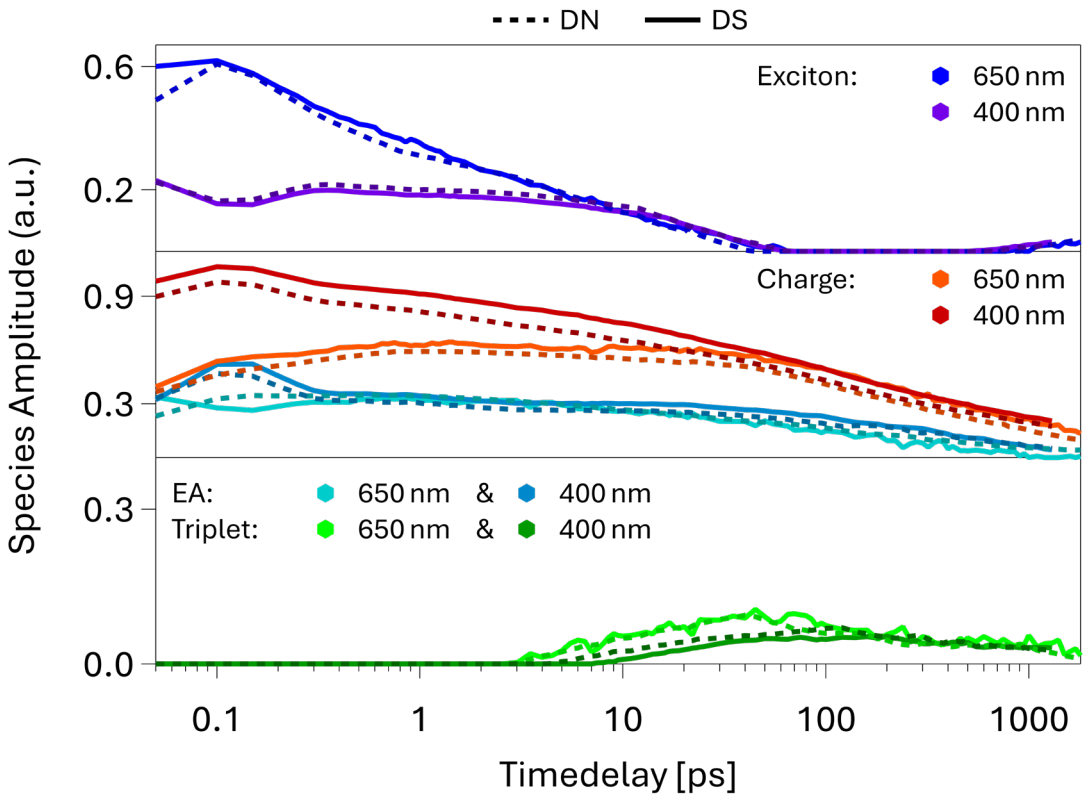

Figure 5-10: Time-resolved relative contribution to the measured ΔA of each species: DCV2-5T singlet exciton (top), DCV2-5T charge (middle), electroabsorption (middle) and DCV2-5T triplet states (bottom), present in the DCV2-5T devices DN & DS and obtained via MCR analysis.

Devices also exhibit a delayed appearance of triplet states after excitation. In chapter 4, a reliable triplet component could not be extracted, causing it to be present only minimally in films and even absent in devices. It becomes clear why this happened when examining the spectral shapes displayed in Figure 5-7 above, in particular the shape of the triplet component. In the visible range up to 600 nm, the spectral shapes of the components barely differ, while the visible region over 600 nm lost a significant part of its informational content due to pump scatter. This masked the characteristic triplet feature peaking at around 660 nm and explains why reliable extractions of triplet dynamics was previously not successful.

Triplet formation in DN and DS appear at comparable timescales during 400 nm excitation, similar to FN and FS with time constants between 12–23 ps (cf. Table S 5-2). The formation of triplet states occurs dominantly via CT-mediated ISC and is a relatively slow process, occurring when most of the excitons are already converted into charge carriers. Devices exhibit a constantly lower triplet state contribution in the TA spectra than films, because electrodes stabilise charges and shorten the 'residence time' of tightly bound CT configurations that feed ISC, lowering the triplet yield. While there was still a significant difference in the population of triplet states between FN and FS, similar dynamics were observed for DN and DS, indicating electrodes and their built-in potential as the main reason for preventing triplet formation. The triplet population also appears slightly delayed for both DN and DS at 400 nm compared to 650 nm. At later times, triplet populations converge, exhibiting similar traces. Triplet formation proceeds from tightly bound CT states which are expected to be temporarily reduced, resulting in a slower early triplet formation. When comparing to the evolution of the charge species, both observations correlate with the efficiency of initial charge generation and stabilisation. When more charges are stabilised rapidly, it reduces the pool of tightly bound CT states available, lowers the probability of ISC and suppresses the triplet-state formation. As a result, triplet formation appears to be reduced in devices and under 400 nm excitation. Across all TA measurements of DCV2-5T in the linear excitation regime, MCR analysis suggest a decrease of the triplet component within the first two nanoseconds which will be discussed in the following section 5.2.2.3 along with the triplet behaviour in the nonlinear excitation regime.

5.2.2.3. Nonlinear Excitation Conditions

DCV2-5T films and devices were further investigated with regard to the behaviour of excited species under nonlinear excitation conditions at an absorbed photon density of $1.4 \cdot 10^{20}$ 'Ph'·cm^{-3} (cf. section 3.5).

The visible region of FN650nl (cf. Figure 5-11) exhibits a very strong spectral distortion around 650 nm due to the pump scatter that dominates this region, removing the informational content here. This is also the case for the following nonlinear (nl) TA spectra of FS650nl, DN650nl and DS650nl. Both FN650nl and FN400nl exhibit a pronounced charge feature at early times. Due to the high excitation density, nonlinear effects such as exciton-exciton annihilation (EEA) become more pronounced. This significantly reduces the exciton population at early times, so the relative charge contribution appears larger at early delays. However, the charge-associated shoulder around 870 nm diminishes relatively fast, indicating a nearly complete charge population loss at late times. In contrast, the signal around 1000 nm shows a clear redshift at later times. Overall, both FN650nl and FN400nl exhibit a late-time appearance that strongly suggests a more or less exclusive contribution of the triplet component. Therefore, the late times of FN400nl were used for the spectral shape of the triplet state. Similar trends were observed with no major differences for FS650 and FS400 in Figure S 5-2.

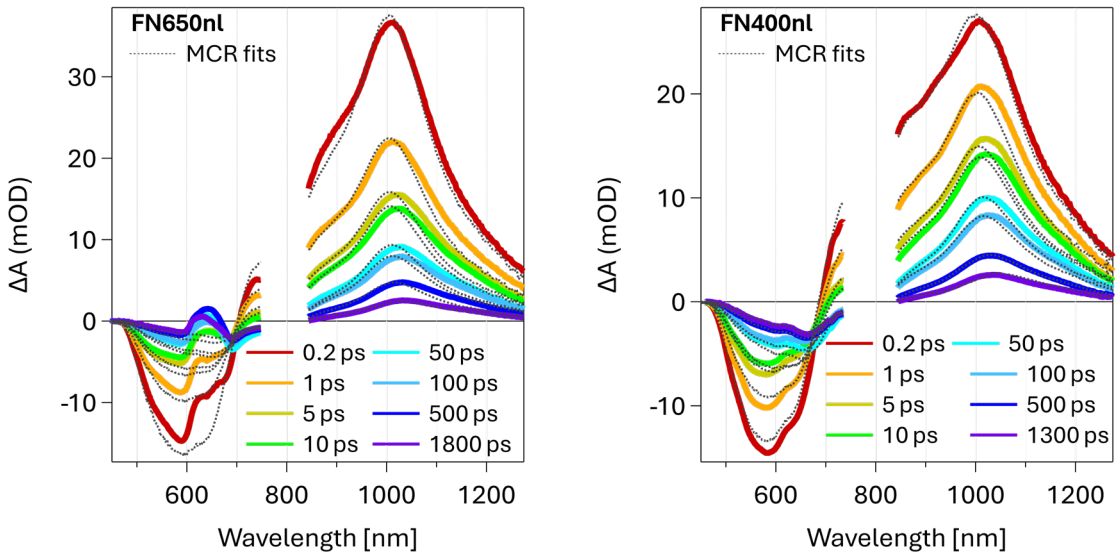

Figure 5-11: DCV2-5T TA spectra of the film neat (FN) excited at 650 nm (l.) and 400 nm (r.) at nonlinear (nl) excitation density ($1.4 \cdot 10^{20}$ 'Ph'·cm^{-3}) for a series of pump-probe delays.

Under nonlinear conditions, both devices DS (cf. Figure 5-12) and DN (cf. Figure S 5-3) exhibit a faster rapid charge formation than the respective films at the same excitation density. Additionally, all devices exhibit a very strong EA-associated signal at early times, which decreases relatively fast across the measured time window, underlining strong charge recombination. While for FN and FS the charge population nearly disappears, devices still exhibit a recognisable contribution at later times. This long-lived charge population persists to a slightly higher extent during 400 nm excitation than 650 nm at same timedelay.

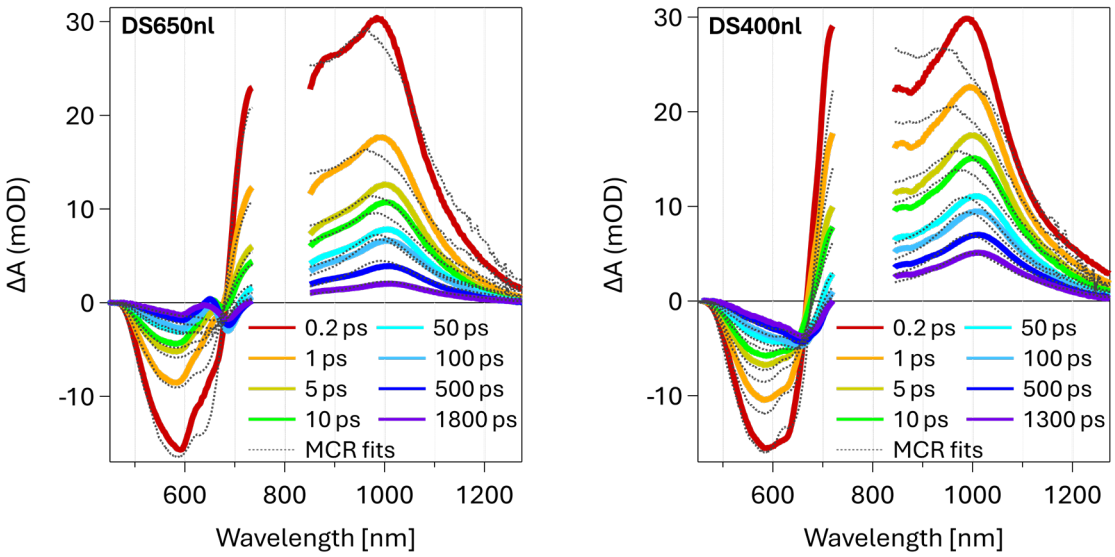

Figure 5-12: DCV2-5T TA spectra of the device stack (DS) excited at 650 nm (l.) and 400 nm (r.) at nonlinear (nl) excitation density ($1.4 \cdot 10^{20}$ 'Ph'·cm^{-3}) for a series of pump-probe delays.

Overall, all nonlinear TA spectra exhibit an initially higher charge population in relation to the exciton population when compared to the TA spectra during linear excitation. This is associated with EEA which significantly reduces the exciton population under nonlinear excitation densities. For all samples, also a significant acceleration of charge population depletion is observed. This is primarily attributed to bimolecular recombination because as a second-order recombination it scales with n^2 and is thus much faster under nonlinear conditions.

Spectral Deconvolution

MCR analysis was done on nonlinear TA datasets of all DCV2-5T films (cf. Figure S 5-4) and devices (cf. Figure S 5-5) for both excitation wavelengths. For a direct comparison between linear and nonlinear excitation regime, TA spectra were divided by their respective density of absorbed photons and displayed in Figure 5-13 (for FN) and Figure 5-14 (for DS). It is directly observable that the differences seen in the linear between 650 nm and 400 nm excitation strongly minimise under nonlinear conditions. Right from the beginning, exciton populations are significantly reduced in the nl data, when comparing to the linear. This indicates a significantly faster exciton population decrease that occurs even before the time resolution of the TA setup. However, no simultaneous stronger formation of another species was observed, suggesting rapid EEA due to nonlinear exciton densities.

At early times, the charge amplitude for FN650nl is comparable to that of FN650 in the linear. While the charge population of FN650 exhibits a significant rise within tens of picoseconds, the charge population of FN650nl starts immediately to decrease, resulting in a complete loss of charges within hundreds of picoseconds. Both observations are linked to nonlinear effects. While strong EEA supresses a further formation of charges, the already present ones most likely undergo bimolecular recombination, leading to a fast charge population reduction. Furthermore, the early-time advantages of excess-energy excitation at 400 nm seen in the linear appears completely absent in the nonlinear regime, while the evolution of the charge species appears nearly similar between 400 nm and 650 nm for films and devices, respectively. This is attributed to rapid EEA. Higher-excited excitons are often more delocalised than 'conventional' S_1 excitons[240], which significantly increases their probability of recombination before CT states can be formed.

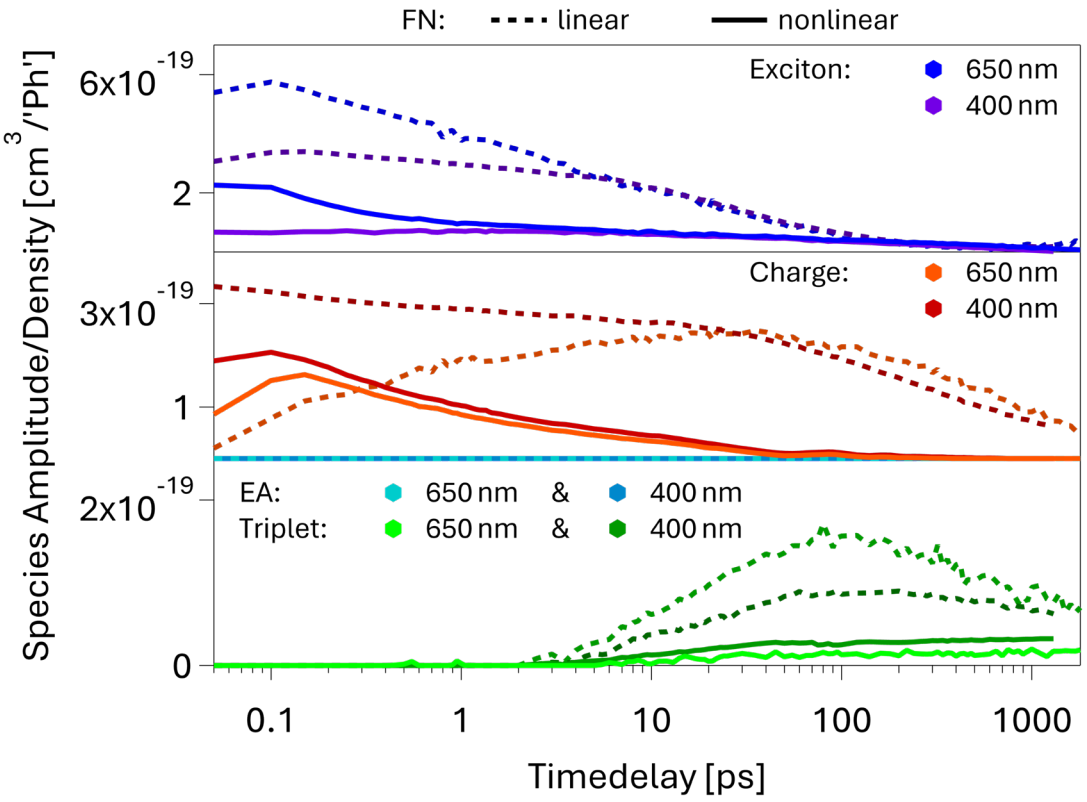

Figure 5-13: Time-resolved relative contribution to the measured ΔA divided by the excitation density of each species in the linear ($1.8 \cdot 10^{18}$ 'Ph'·cm^{-3}) and in the nonlinear ($1.4 \cdot 10^{20}$ 'Ph'·cm^{-3}) excitation regime: DCV2-5T singlet exciton (top), DCV2-5T charge (middle), electroabsorption (middle) and DCV2-5T triplet exciton (bottom), present in FN at nonlinear (full lines) and linear (dashed lines) excitation densities, obtained via MCR analysis.

The triplet population occurs in the films with similar timedelays in the nonlinear as in the linear regime, while a much weaker triplet formation is observed in the nl, when setting in relation to the respective excitation density (cf. Figure 5-13). This is attributed to the lower population of CT states for ISC due to the significantly reduced exciton population under nonlinear conditions. When triplet formation occurs, the present charge population is already strongly reduced, which lowers the probability of triplet formation. This, in relation to the linear data, reduced triplet formation is also observed for devices in Figure 5-14. However, dynamics show a later appearance of the triplet population in devices under nonlinear conditions, which most likely arises from an incorrect assignment by MCR. It is not expected that a higher excitation density leads to a delayed triplet formation. Instead, the shallow rise and the low amplitude of the triplet component most likely led to an initial underestimation of the triplet

component. this would agree with the unusual behaviour of the exciton dynamics in the nonlinear data, in particular for the devices. What appears to be late exciton formation occurs at timescales where triplet formation becomes relevant. Therefore, it would be more plausible to attribute this misattributed exciton feature to the triplet population.

Furthermore, the direct comparison of the triplet dynamics of all samples between linear and nonlinear excitation regime reveals a deviant behaviour at later times, which would underline that CT-mediated pathways are dominant for triplet formation in DCV2-5T. While all nonlinearly excited samples reveal a triplet component that persists constantly after formation, all linearly excited samples exhibit a more or less pronounced decrease of the triplet population at later times. In principle, a strong reduction seems rather unlikely within this time window and could be considered as an artefact, but a slight reduction to a certain extent could be explained with occurring triplet–charge quenching (TCQ). At low excitation densities, a strong population of charges persists until very late times after excitation. The simultaneous presence of triplet states and delocalised charges could in principle lead to a small probability of encountering and quenching each other. This would result in a gentle population reduction of both charges and triplets at the same time, as observed in all linear MCR dynamics in Figure 5-9 and Figure 5-10. When the excitation density is increased to nonlinear regimes, as shown in Figure S 5-4 and Figure S 5-5, nonlinear effects occurring on early- and mid-timescales lead to a significant reduction of the charge population. As soon as the charge population is considered to be almost completely extinct, the triplet populations across all samples remains at a constant amplitude. At this point, only the triplet component contributes to the TA spectra, excluding any interactions with other excited species. Also, triplet states are generally more localised and exhibit very short diffusion lengths of a few nanometres because triplet diffusion occurs via dexter transfer which requires strong wavefunction overlap.[62,241] Consequently, an encounter between two triplet states for triplet–triplet annihilation (TTA) is highly unlikely, leaving only ground state relaxation as the dominant pathway. The spin flip which is required for spin-forbidden relaxation from T_1 to S_0 occur with a very low probability. This leads to a long lifetime of triplet states, typically within the

micro- to milliseconds range for OPD and OPV materials, which explains the persisting population in the nonlinear regime when triplet states are isolated.

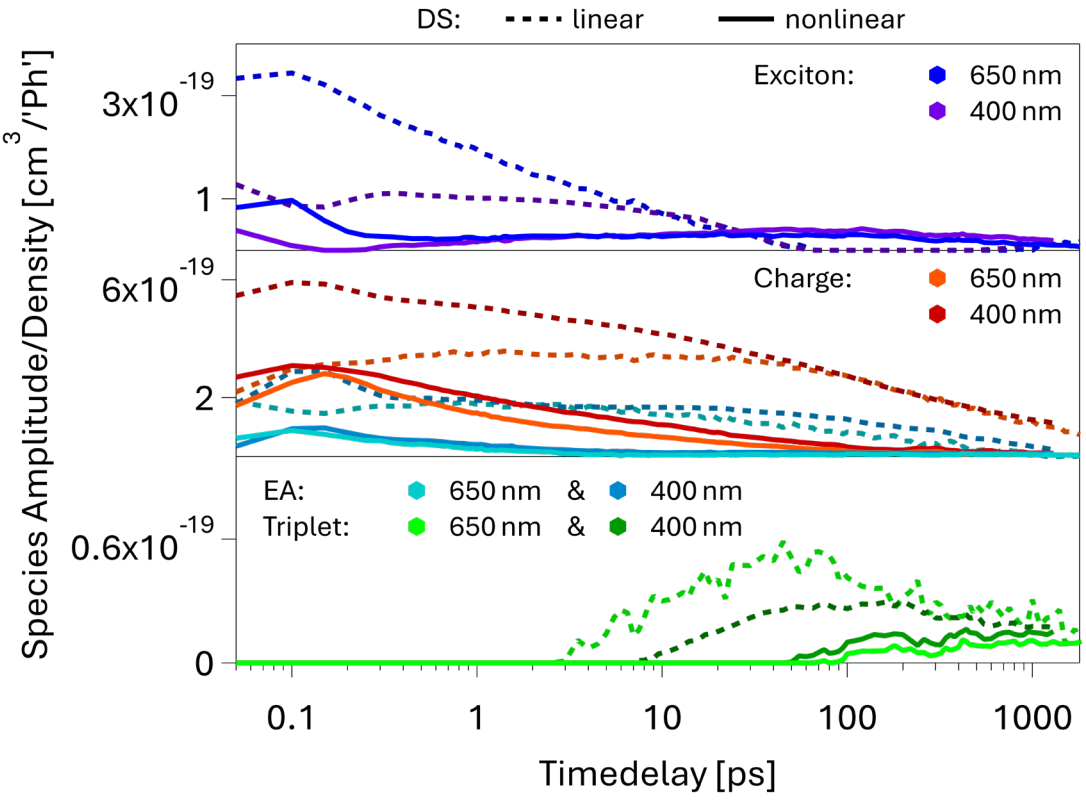

Figure 5-14: Time-resolved relative contribution to the measured ΔA divided by the excitation density of each species in the linear ($1.8 \cdot 10^{18}$ 'Ph'·cm^{-3}) and in the nonlinear ($1.4 \cdot 10^{20}$ 'Ph'·cm^{-3}) excitation regime: DCV2-5T singlet exciton (top), DCV2-5T charge (middle), electroabsorption (middle) and DCV2-5T triplet exciton (bottom), present in DS at nonlinear (full lines) and linear (dashed lines) excitation densities, obtained via MCR analysis.

5.2.3. Electromodulated Differential Absorption

The DCV2-5T devices DN and DS were further investigated via electromodulated differential absorption (EDA) spectroscopy at both excitation wavelengths 400 nm and 650 nm. As described previously, the reduction of the EDA signal, caused by an internal electric field that counteracts the applied external reverse bias, is transformed into a time-resolved voltagedrop. Figure 5-15 displays the voltagedrop curves of DN and DS under −2 V reverse bias after excitation at 400 nm and 650 nm with similar excitation densities.

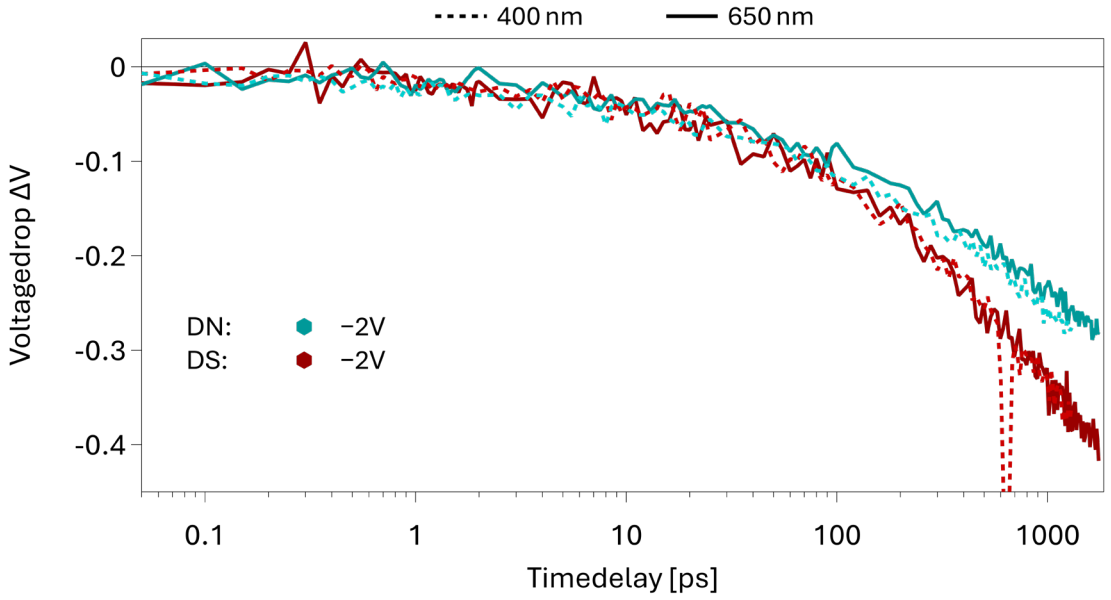

Figure 5-15: Voltagedrop curves of the DCV2-5T device neat (DN, turquoise) and device stack (DS, red) excited with a 400 nm (dotted lines) & 650 nm (full lines) pump beam under an applied external reverse bias of −2 V.

Normalisation was performed as explained during section 3.6, using total extracted charges and device capacitance shown in Table S 5-5. When normalising the voltagedrop as shown in Figure 5-16, the voltagedrop appears to be faster in the absence of TL. Nevertheless, the normalised voltagedrop curves exhibit similar behaviour as they run in parallel across the measured time window. When normalising DN again in a way, that both DN and DS exhibit the same voltagedrop at 20 ps (cf. Figure S 5-6), both exhibit identical voltagedrop curves under 650 nm excitation. EDA tracks charge separation, drift and extraction. In DS, charges must additionally to the AL also

cross the transport layers and additional interfaces before they reach the electrodes. This extra transit slows the increase in the reduction of the internal field within the measurement window, even though these layers allow a larger total amount of charges to be extracted. Because the normalisation uses the total extracted charges, DS can show a slightly smaller normalised voltagedrop while still yielding a larger absolute number of extracted charges.[236] Together, this indicates that the presence of additional layers in DS significantly enhances the overall number of extracted charges but at the same time also introduces minor delays in extraction.

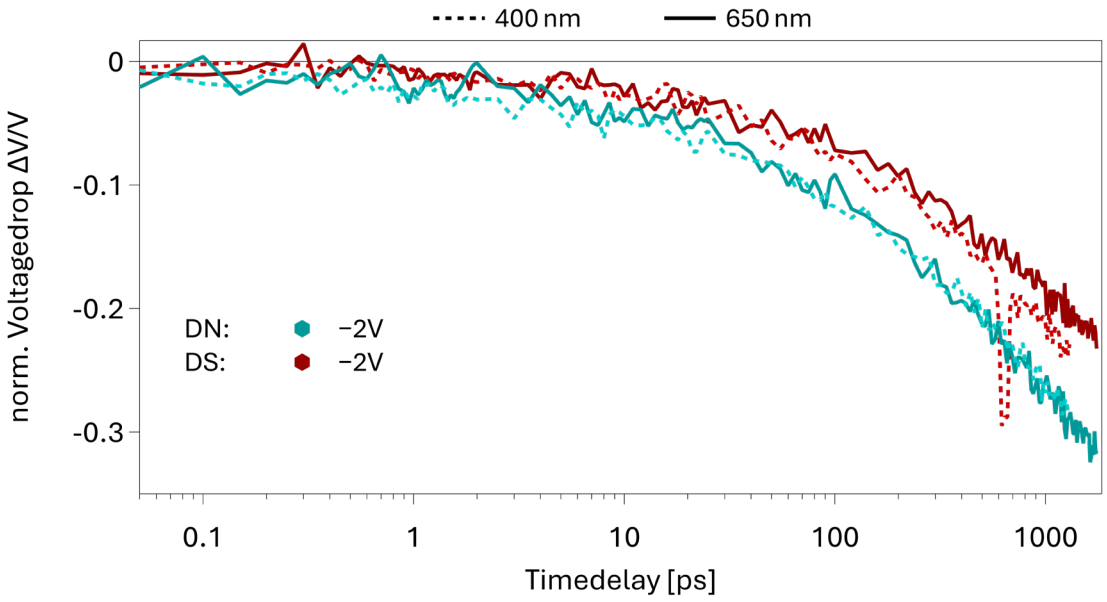

Figure 5-16: Normalised voltagedrop curves of the DCV2-5T device neat (DN, turquoise) and device stack (DS, red) excited with a 400 nm (dotted lines) & 650 nm (full lines) pump beam under an applied external reverse bias of −2 V.

DS was further investigated with EDA spectroscopy when excited at 400 nm and 650 nm under higher reverse biases, as shown in Figure 5-17. DS exhibits an early time voltagedrop feature that is nearly bias-independent and identical under all measurement conditions when providing a similar excitation density. At early timedelays, the pump creates a dense population of e–h pairs at very short separation. The Coulomb fields of these pairs dominate the local field experienced by the neutral transitions that produce the EA signal, so the initial decrease is set mainly by this photogenerated population and the local dielectric response, while it shows only a weak dependence on the applied bias.[165] This is particularly observable for a material

like DCV2-5T due to its significant charge-transfer character arising from its push-pull A–D–A structure.[242] The associated significant changes in dipole moment and polarisability of neutral excitations increase Stark sensitivity, so a given early field change produces a comparatively large EA amplitude. After the first tens of picoseconds, charges start to separate, drift and get extracted, which is tracked by the EDA signal and scales with the applied bias, even in cases/for materials where it is considered 'bias-independent'. This results from the fact that the same separated charge distribution screens a larger absolute field when the applied reverse bias is higher.[222,243]

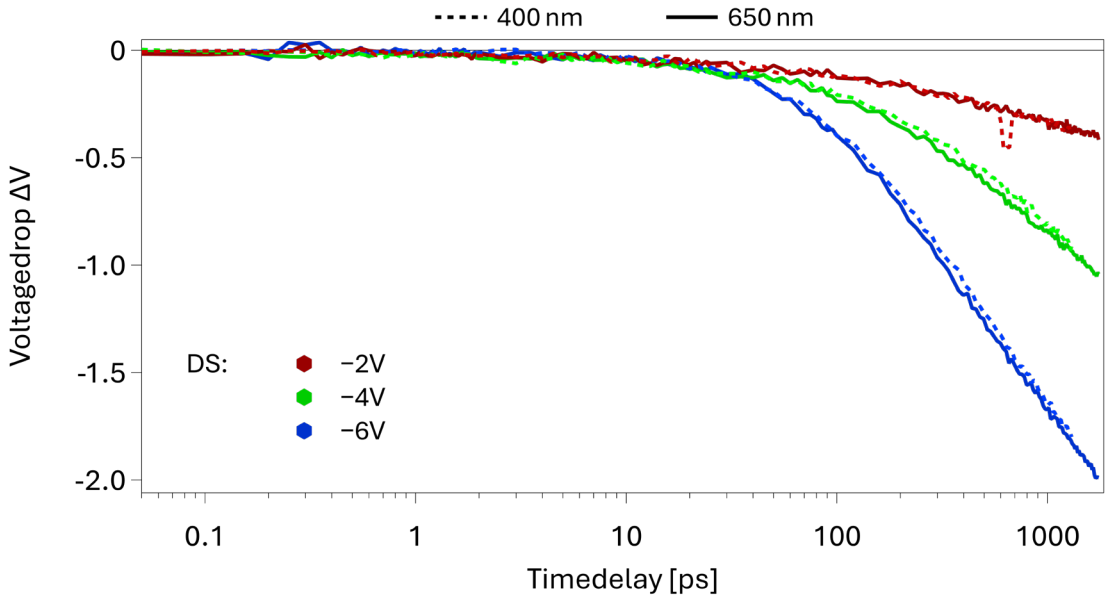

Figure 5-17: Voltagedrop curves of the DCV2-5T device stack (DS) excited with a 400 nm (dotted lines) & 650 nm (full lines) pump beam with applied external reverse bias of −2 V (red), −4 V (green) and −6 V (blue).

The normalised voltagedrop of DS650 and DS400 in Figure 5-18 reveals a clear bias dependence at later times. When increasing the applied bias for both excitation wavelengths, a saturation effect is observable, meaning reduced changes in the normalised voltagedrop and in EQE with further increases of the reverse bias. This indicates, that once internal energetic barriers such as the Coulomb binding energy are largely overcome by an electric field, the bias-driven improvement of charge extraction gets less pronounced, indicating a significant extraction bottleneck, which is less pronounced the stronger field-assisted effects are.

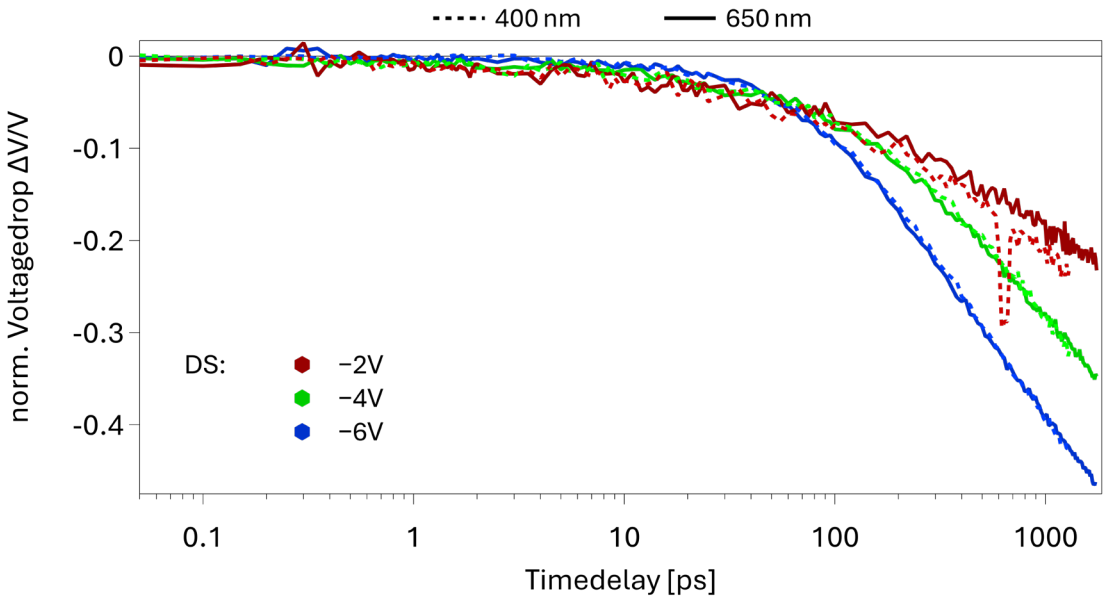

Figure 5-18: Normalised voltagedrop curves of the DCV2-5T device stack (DS) excited with a 400 nm (dotted lines) & 650 nm (full lines) pump beam with applied external reverse bias of −2 V (red), −4 V (green) and −6 V (blue).

In direct comparison, DS400 exhibits a faster normalised voltagedrop than DS650 at a lower reverse bias within the tracked time window, shown in Figure 5-18. These differences become less pronounced as the external field is increased. For DS at −2 V, this arises due to the initially faster charge formation via higher-energy photon excitation, as it is also observed in TA under open-circuit conditions. Apparently, this accelerates the initial charge separation and/or extraction within the shown time frame, while not accounting for later occurring extraction losses as discussed below. At higher biases, the faster normalised voltagedrop of 400 nm is less observable because it gets superimposed by field-assisted extraction.

To also compare the extracted charges during the EDA measurements, the IQE of DN and DS was estimated from the electrical measurements performed in association with EDA. The IQE is determined via

$$IQE(\lambda, V) = \frac{Q_{ext}(\lambda, V)}{q \cdot n_{ex} \cdot A_x \cdot d} \tag{5-1}$$

with the total extracted charges Q_{ext}, the elementary charge q, the excitation density n_{ex}, the illuminated area A_x and the thickness of the active layer d. The relation

between IQE and EQE is estimated with the absorptance A_α determined from the steady-state absorbance A of the active layer via

$$EQE(\lambda, V) = IQE(\lambda, V) \cdot (1 - 10^{-A}) = IQE(\lambda, V) \cdot A_\alpha(\lambda) \tag{5-2}$$

where a reflectance of zero is assumed. The calculated quantum efficiencies are displayed in Table 5-1 for DN and DS under all applied biases and in comparison to the steady-state EQE from the previous section. The relative efficiency gain $\Delta EG_{x-y}(\lambda)$ at a wavelength λ between two biases x and y is given by

$$\Delta EG_{x-y}(\lambda) = \frac{EQE_y(\lambda, V) - EQE_x(\lambda, V)}{EQE_x(\lambda, V)} \tag{5-3}$$

and reflects the increase in efficiency due to an external electric field. To further isolate the additional bias-dependent gain of 400 nm with respect to 650 nm, $\Delta EG_{x-y,ad}$ is determined via

$$\Delta EG_{x-y,ad} = \frac{\Delta EG_{x-y}(400\ nm) - \Delta EG_{x-y}(650\ nm)}{\Delta EG_{x-y}(650\ nm)} \tag{5-4}$$

EQE and IQE of DCV2-5T reveal a noticeable dependence on both excitation wavelength and applied bias, whereby they are consistently lower for 400 nm than for 650 nm excitation in both DN and DS configuration. While EQE depends also on the absorption efficiency, IQE only reflects the pathway between absorbing a photon and extracting charge carriers. As a consequence, while 400 nm demonstrated a more efficient initial charge formation during TA spectroscopy, a higher fraction of those is lost to recombination or trapping before being able to get extracted, when comparing to 650 nm. This agrees with the EDA curves appearing similar on ultrafast timescales. It is expected that the additional losses for 400 nm excitation occur predominantly on timescales beyond EDA resolution. They do not appear within the ultrafast time window seen by the EDA spectra and do not affect the resolved dynamics but are captured by the longer timeframe used to record the number of extracted charges. This behaviour is likely related to relaxation dynamics of excited states formed at different excitation energies. Excitation at 400 nm results in higher-lying excited states that are able to improve rapid charge formation and separation but also provide additional

pathways for ultrafast recombination and trapping. This could indicate that those charges are particularly sensitive to losses when not extracted quickly enough. This is further supported by the bias-dependence of the quantum efficiency, following the Onsager-Braun model where field-assisted charge separation competes with geminate recombination. At lower reverse bias, the efficiency is significantly reduced under 400 nm excitation. When the external field gets increased, a much larger relative extraction improvement for 400 nm is observed, showing that those charges can be 'rescued' with a sufficiently strong extraction field. In contrast, 650 nm charges are formed via lower-energy states which are more stable and less dependent on external electric fields, resulting in a lower relative improvement of the quantum efficiency. This relative efficiency gain ΔEA of 400 nm with respect to 650 nm (cf. Table 5-1) is over 22 % when increasing the external bias from −2 V to −4 V. When further increased from −4 V to −6 V, this efficiency gain ΔEA reduces to around 7 %, indicating a diminishing field effect as it further approaches a 'sufficiently strong' status. Although an external bias led to a reduced efficiency gap between excitation wavelengths, the IQE remains lower for 400 nm, even at the highest bias tested, indicating that the intrinsic limitation of 400 nm could not be overcome completely within this bias regime. In DN however, ΔEA is already significantly smaller between 0 V (steady state) and −2 V.

As stated earlier, transport layers in DS add interfaces that can slow initial extraction dynamics. Nevertheless, they are essential to reduce energetic barriers at the interface between AL and the contacts and thus are highly important for efficient charge extraction. This is indicated by the DN efficiency which is only 13 % of that of DS due to a dominant energetic barrier at the AL-contact interface when no TLs are present. As a result, increasing the electric field has a less strong influence, indicated by a lower ΔEG of 10 % already between the steady state and a reverse bias of −2 V.

Table 5-1: EQE and IQE of DCV2-5T in the steady state and extracted from EDA under bias for DN and DS with a semi-transparent Ag electrode and the relative efficiency gain ΔEG between two biases (from left to right) for 650 nm, for 400 nm and in vertical bars for the gain of 400 nm with respect to 650 nm.

		EQE (%)		IQE (%)	
		650 nm	400 nm	650 nm	400 nm
DS	Steady State	11.8	8.0	17.2	12.9
	−2 V	7.1	4.3	10.4	6.9
	−4 V	11.9	7.8	17.4	12.5
	−6 V	17.0	11.3	24.8	18.3
	ΔEG_{2-4} |diff.|	67.1 %	82.3 %	|22.5 %|	
	ΔEG_{4-6} |diff.|	42.7 %	45.7 %	|6.9 %|	
	ΔEG_{2-6} |diff.|	138.6 %	165.6 %	|19.5 %|	
DN	Steady State	1.6	1.0	2.3	1.7
	−2 V	5.2	3.7	7.7	6.0
	ΔEG_{0-2} |diff.|	234.3 %	258.0 %	|10.1 %|	

However, it should be mentioned that an anomaly occurred for DS between the steady-state EQE shown in section 5.2.1 and the EQE estimated from EDA. Those EQE values are not fitting to each other, whereas the did for DN. While all measurements were performed with the same devices under the same conditions and thus measurement artefacts can very likely be excluded, the origin of this anomaly remains unresolved. Nevertheless, the overall EQE improvement of DN by applying an external reverse bias as well as the EQE improvement-trends of DS obtained during EDA directly correlates with the observed bias-EQE trends displayed in chapter 4, Figure 4-2 for the SC-OPD DCV2-5T full-stack device with an opaque Ag electrode. Based on DN (cf. Table 5-1), introducing an external reverse bias of −2 V results in a two to three times higher EQE for DCV2-5T. A further increase of the bias would still improve the EQE but to a lower extend the more the bias is increased (cf. Table 5-1). This underlines the presence of a saturation effect and supports the conclusion that field-assisted charge separation and extraction is at the end limited to the intrinsic characteristics of the material and its interfaces.

5.3. Conclusion

Summary

This chapter examined ultrafast processes in vacuum-deposited DCV2-5T, using TA and EDA spectroscopy next to steady-state characterisation methods under varying excitation wavelengths, fluences, electric fields and device architectures. It reinforced the findings of chapter 4 and extended them by clarifying how these parameters modulate the evolution and behaviour of charge carriers in DCV2-5T. TA revealed that excess-energy excitation leads to a stronger and faster charge generation via higher-excited state pathways, while EDA and EQE confirmed that such charges are more vulnerable to recombination and that their extraction is more field-dependent. Charges generated via lower-energy excitation exhibited slower early-time dynamics but higher stability and were less electric field-sensitive. Nonlinear excitation fluence introduced EEA processes, which have a significantly stronger influence on more delocalised higher-excited excitons from excess-energy pathways, eliminating the early-time charge formation advantage of 400 nm excitation. Additionally, nonlinear excitation densities increased charge carrier recombination. This suppressed the triplet formation and led to a relatively lower but persisting triplet population, which was in contrast higher under linear conditions but showed a slight reduction at later times. The presence of electrodes facilitated early charge separation and charge extraction was found to be highly bias-driven. Transport layers stabilised charges and facilitated charge extraction, while a slight initial slowing of the charge extraction process in devices is suggested. Their influence on ultrafast charge formation in films remained minor.

Conclusion

The findings of this chapter demonstrate that the central limitation in neat materials like DCV2-5T is not the rate or yield of ultrafast charge formation, but the incomplete extraction of these charges before rapid recombination and relaxation occur. This is attributed to a stronger Coulomb binding in the absence of a D–A interface in neat materials, while transport-limited collection further increases losses.[167,244] Even at strong extraction biases, field-driven efficiency gains become progressively smaller, demonstrating that a significant fraction of photogenerated charges recombine or localise before reaching the contacts.

Consequently, device architecture plays an important role, as electrodes accelerate charge separation and extraction before competing processes can occur. Transport layers further reduce extraction barriers by ensuring energetic alignment. The observed highest relative efficiency gain at lower extraction biases suggests that neat DCV2-5T devices could benefit from electrodes with a greater workfunction difference, particularly at lower excitation wavelengths. Even in operational conditions in the absence of an external bias, such configuration would increase the internal electric field and help compensate for ultrafast losses, if transport layers are selected accordingly. However, additional layers can slow down initial charge extraction, leading to a trade-off between improved efficiency and response speed, which is especially important for OPDs. While device design and field engineering can partially compensate for the intrinsic limitations of DCV2-5T, they cannot fully suppress ultrafast loss channels characteristic of single-component systems. Therefore, future improvements will require strategies that delay or suppress these ultrafast losses and stabilise charge states to overcome the efficiency limitations of such materials.

5.4. Appendix

Table S 5-1: Time constants of the evolution of excited state species in DCV2-5T films FN & FS after excitation at 650 nm & 400 nm obtained via multiexponential fits of MCR dynamics.

	Species	τ_1 [ps]	τ_2 [ps]	τ_3 [ps]
FN650	Ex	1.6	40	–
	Ch	0.2	4.6	591.0
	Tr	11.8	40.5	434.2
FS650	Ex	1.3	60.5	–
	Ch	0.1	8.4	676.9
	Tr	14.0	980.2	1018.9
FN400	Ex	2.0	46.8	–
	Ch	0.6	42.8	371.3
	Tr	12.1	29.0	1188.1
FS400	Ex	4.2	50.8	–
	Ch	1.0	3.2	384.3
	Tr	14.8	97.6	786.6

Table S 5-2: Time constants of the evolution of excited state species in DCV2-5T devices DN & DS after excitation at 650 nm & 400 nm obtained via multiexponential fits of MCR dynamics.

	Species	τ_1 [ps]	τ_2 [ps]	τ_3 [ps]
DN650	Ex	0.3	11.2	–
	Ch	0.2	106.0	860.8
	EA	12.7	283.6	–
	Tr	12.1	–	146.1
DS650	Ex	0.6	13.2	–
	Ch	0.1	97.6	496.9
	EA	16.5	196.4	–
	Tr	12.6	–	175.3
DN400	Ex	23.8	–	–
	Ch	2.7	149.7	251.8
	EA	0.7	285.1	–
	Tr	18.6		384.1
DS400	Ex	24.6	–	–
	Ch	5.0	172.5	279.0
	EA	0.7	295.9	–
	Tr	23.2	–	268.7

Table S 5-3: Time constants of the evolution of excited state species in DCV2-5T films FN & FS after excitation at 650 nm & 400 nm at nonlinear excitation density obtained via multiexponential fits of MCR dynamics.

	Species	τ_1 [ps]	τ_2 [ps]	τ_3 [ps]
FN650nl	Ex	0.2	6.2	332.2
	Ch	0.7	16.8	–
	Tr	15.0	656.8	–
FS650nl	Ex	0.3	4.6	90.7
	Ch	1.5	37.2	–
	Tr	19.1	593.4	–
FN400nl	Ex	22.1	389.5	–
	Ch	0.5	16.1	–
	Tr	11.9	385.0	–
FS400nl	Ex	10.7	388.3	–
	Ch	0.8	31.9	–
	Tr	17.0	577.6	–

Table S 5-4: Time constants of the evolution of excited state species in DCV2-5T devices DN & DS after excitation at 650 nm & 400 nm at nonlinear excitation density obtained via multiexponential fits of MCR dynamics.

	Species	τ_1 [ps]	τ_2 [ps]	τ_3 [ps]
DN650nl	Ex	0.6	15.0	360.5
	Ch	0.8	26.2	–
	EA	0.2	1.1	–
	Tr	30.7	–	–
DS650nl	Ex	0.06	8.2	589.3
	Ch	0.7	23.4	–
	EA	0.1	1.2	–
	Tr	230.1	–	–
DN400nl	Ex	0.6	37.9	267.2
	Ch	0.8	28.7	–
	EA	0.2	1.9	–
	Tr	34.7	448.4	
DS400nl	Ex	0.7	18.5	509.6
	Ch	1.1	31.7	–
	EA	0.2	2.0	–
	Tr	76.8	811.3	–

Table S 5-5: Capacitance and total extracted charges of the neat DCV2-5T devices DN and DS under 400 nm and 650 nm excitation. Values are extracted from electrical measurements via an oscilloscope, performed in association with EDA.

	DS400	DS650	DN400	DN650
Capacitance [F]	$2.51 \cdot 10^{-9}$		$3.72 \cdot 10^{-9}$	
tot. Charges at −2 V [C]	$4.22 \cdot 10^{-9}$	$4.50 \cdot 10^{-9}$	$3.69 \cdot 10^{-9}$	$3.32 \cdot 10^{-9}$
tot. Charges at −4 V [C]	$7.70 \cdot 10^{-9}$	$7.52 \cdot 10^{-9}$		
tot. Charges at −6 V [C]	$1.12 \cdot 10^{-8}$	$1.07 \cdot 10^{-8}$		

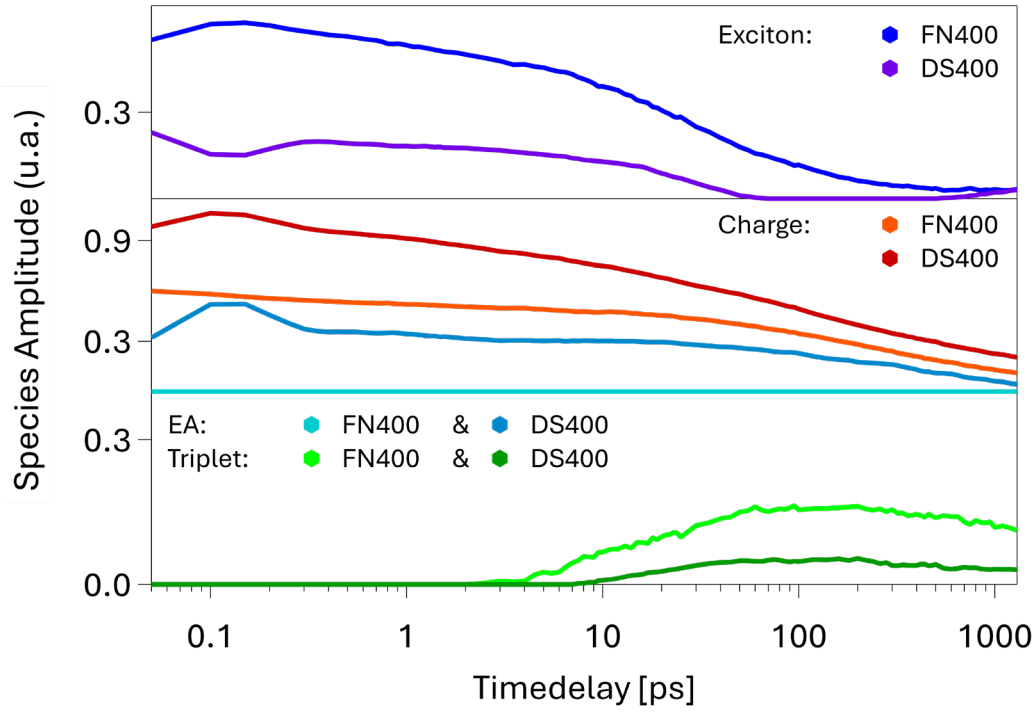

Figure S 5-1: Time-resolved relative contribution to the measured ΔA of each species: DCV2-5T singlet exciton (top), DCV2-5T charge (middle), electroabsorption (middle) and DCV2-5T triplet states (bottom), present in the DCV2-5T samples FN & DS excited at 400 nm and obtained via MCR analysis.

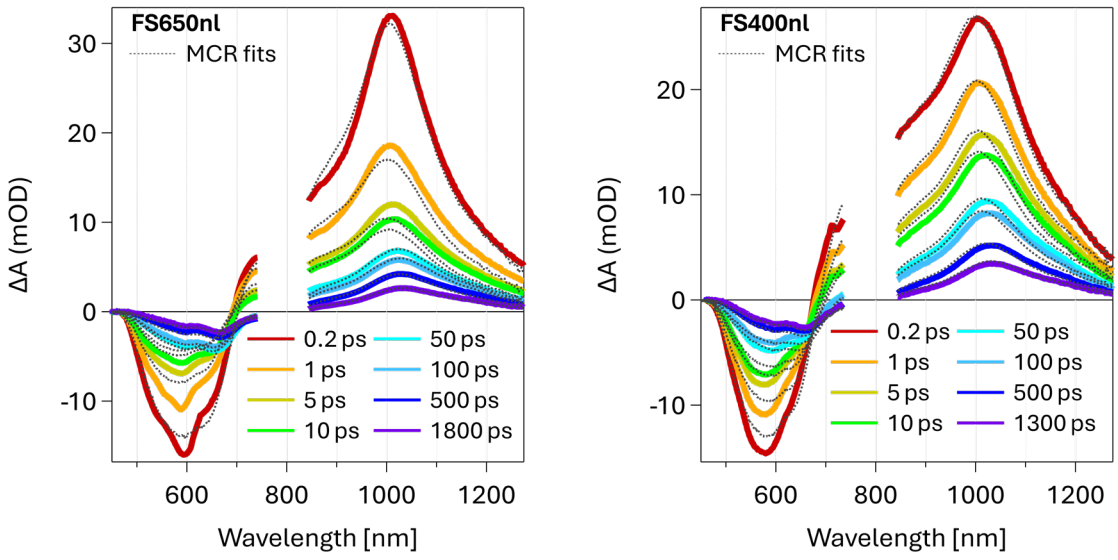

Figure S 5-2: DCV2-5T TA spectra of the film stack (FS) excited at 650 nm (l.) and 400 nm (r.) at nonlinear (nl) excitation density ($1.4 \cdot 10^{20}$ 'Ph'·cm^{-3}) for a series of pump-probe delays.

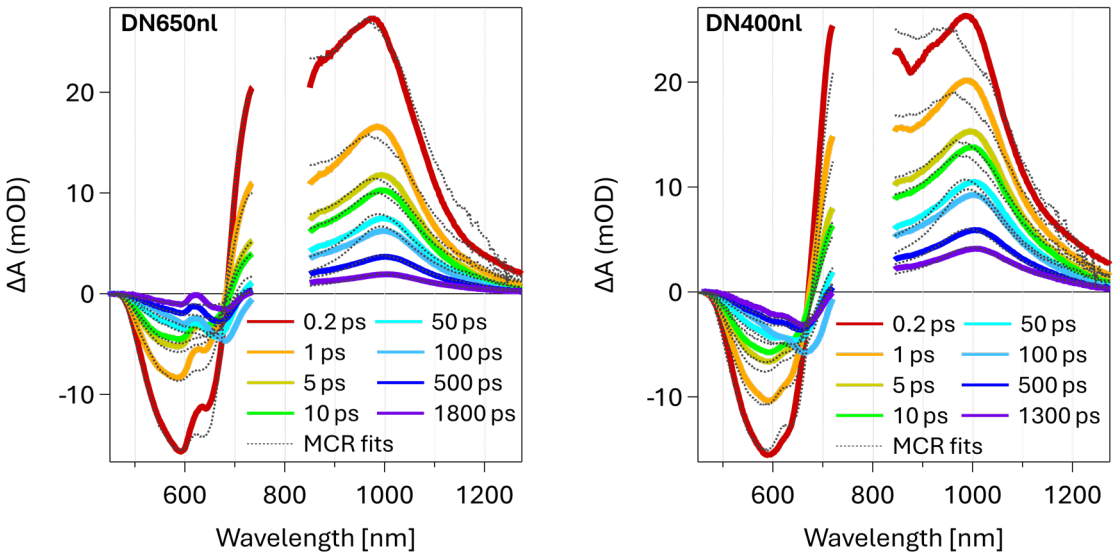

Figure S 5-3: DCV2-5T TA spectra of the device neat (DN) excited at 650 nm (l.) and 400 nm (r.) at nonlinear (nl) excitation density ($1.4{\cdot}10^{20}$ 'Ph'·cm^{-3}) for a series of pump-probe delays.

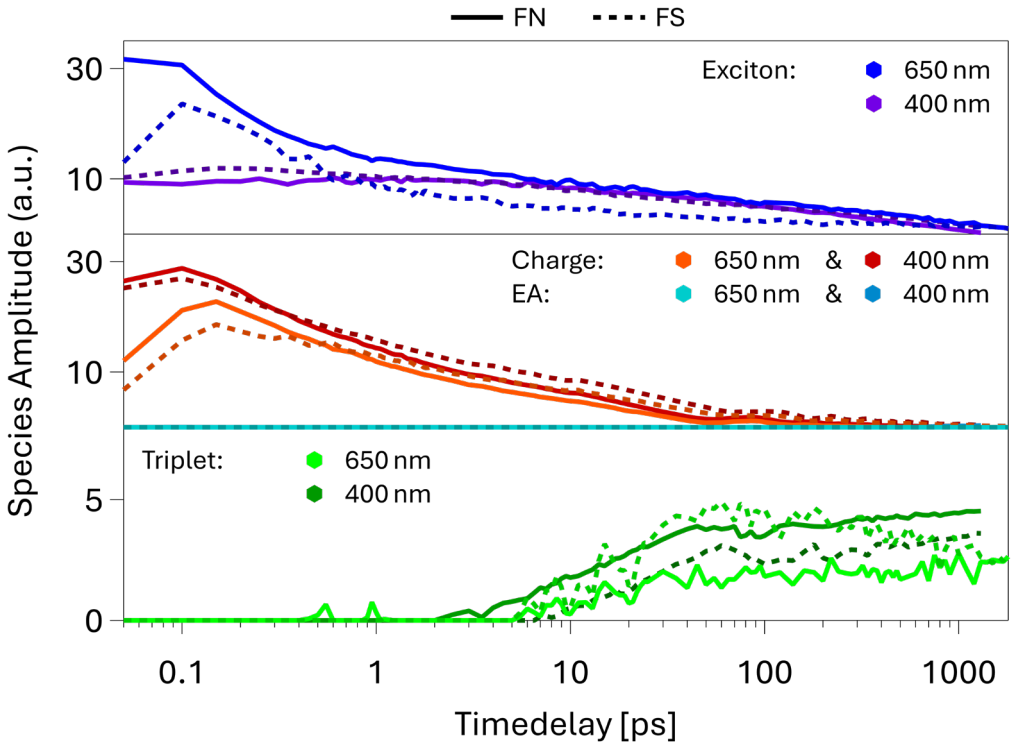

Figure S 5-4: Time-resolved relative contribution to the measured ΔA of each species: DCV2-5T singlet exciton (top), DCV2-5T charge (middle), electroabsorption (middle) and DCV2-5T triplet states (bottom), present in the DCV2-5T films FN & FS at nonlinear excitation ($1.4{\cdot}10^{20}$ 'Ph'·cm^{-3}) density and obtained via MCR analysis.

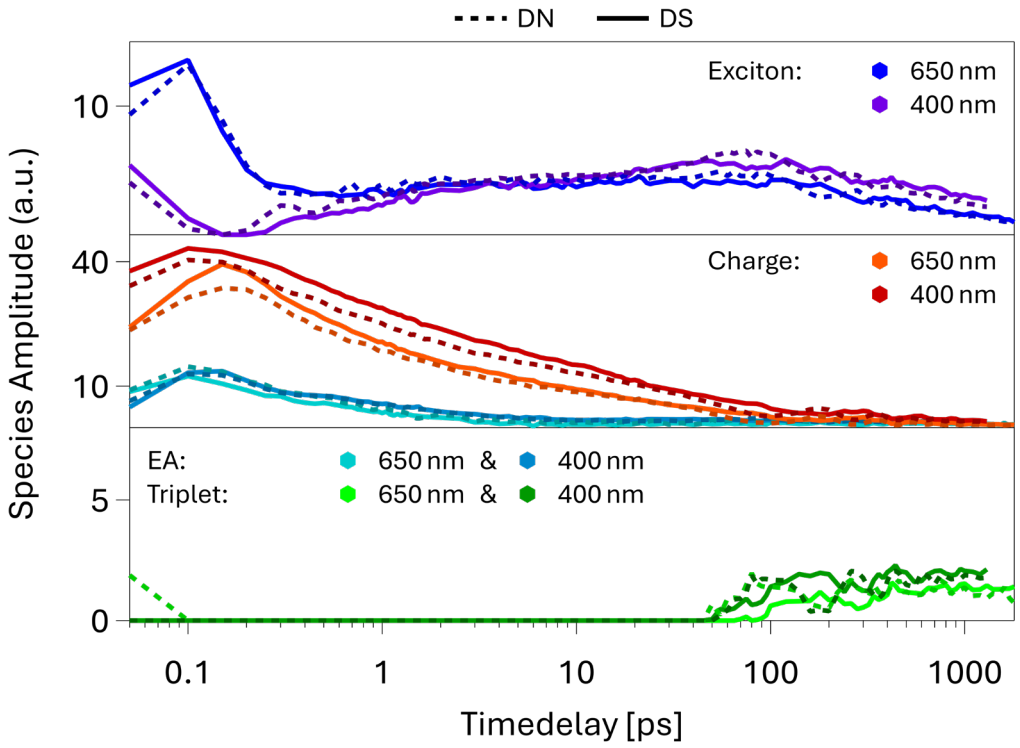

Figure S 5-5: Time-resolved relative contribution to the measured ΔA of each species: DCV2-5T singlet exciton (top), DCV2-5T charge (middle), electroabsorption (middle) and DCV2-5T triplet states (bottom), present in the DCV2-5T devices DN & DS at nonlinear excitation density ($1.4 \cdot 10^{20}$ 'Ph'·cm^{-3}) and obtained via MCR analysis.

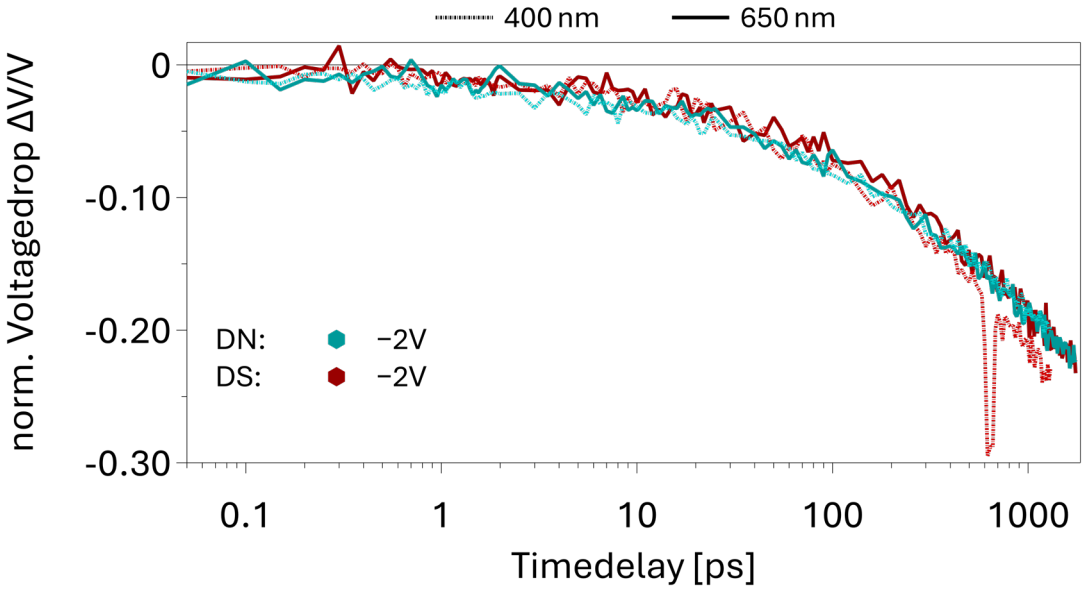

Figure S 5-6: Normalised voltagedrop curves of the DCV2-5T device neat (DN, turquoise) and device stack (DS, red) excited with a 400 nm (dotted lines) & 650 nm (full lines) pump beam under an applied external reverse bias of −2 V, followed by a second normalisation of DN onto the same offset at a timedelay of 20 ps.

Chapter 6

Excitation Energy and Electric-Field Effects on Charge Formation and Separation in PM6:Y6

This chapter discusses charge generation, separation, extraction and their influences in PM6:Y6 systems. The device fabrication, the steady-state and TDCF measurements and their data treatment were carried out together with Manasi Pranav and Dr. Atul Shukla of the group of Prof. Dr. Dieter Neher at University of Potsdam. TA measurements of the films were performed with Dr. Kaila Yallum, THz measurements and data treatment were carried out together with Dr. Julien Réhault and Dr. Demetra Tsokkou.

6.1. Introduction

Building on section 2.6, this chapter addresses how excitation wavelength and field effects influence the ultrafast evolution of photoexcited populations in PM6:Y6 and how in devices these dynamics determine subsequent charge carrier extraction.

It needs to be clarified how excitation wavelength influences donor- and acceptor-centred populations and to what extent does access to lower-energy Y6 aggregates and mixed local-exciton or charge-transfer character determine the survival of charge. Under which nanostructures and offsets is the influence of an electric field negligible and under which conditions do field effects assist separation or collection. A further question is whether wavelength-selective excitation leads to a lasting influence on the charge population and its separation and extraction.

The working hypothesis is that efficient generation at small energetic offset occurs when early excitation provides rapid access to aggregate environments with sufficient delocalisation and charge-transfer character, enabling endothermic separation after cooling with only a weak sensitivity to the internal electric field. When such access is limited by nanostructure or when singlet-decay competes with dissociation, field effects become measurable.

This chapter investigates these points by mapping wavelength and bias dependences in films and devices and by relating the earliest dynamics to the populations that remain on later timescales. To separate Y6-specific behaviour from blend effects, polystyrene-diluted Y6 (PS:Y6) films are first used to obtain the spectral shapes of Y6 excitons and neat Y6 charges (charges stabilised on Y6 without the donor material PM6 being involved). These references support the analysis of PM6:Y6 under three excitation energies. Several spectroscopic methods are used: TA for the evolution of excited states, EDA for field-assisted charge separation and extraction and OPTP for the mobility and localisation of THz-active carrier populations, while steady-state measurements and TDCF provide a supporting context.

6.2. Results

6.2.1. Steady State

The steady-state absorption spectra provide fundamental information about the optical response of the material. The optical absorption properties of PM6:Y6 were investigated in 116 nm thin films and compared with a PS:Y6 reference, where polystyrene (PS) serves as an optically inert matrix. The PM6:Y6 spectrum displays two characteristic absorption bands: a prominent donor-associated peak at 620 nm and a broader acceptor-associated one at 800 nm. The PS:Y6 spectrum exhibits only the absorption of Y6 since polystyrene (PS) has negligible absorption above 320 nm.

Quantitative analysis of the measured absorption spectra (Figure 6-1) reveals wavelength-specific absorption ratios within the PM6:Y6 blend. At 400 nm the absorption is dominated by PM6 at 610 nm both components absorb roughly to a similar extend and at 800 nm only Y6 absorbs. Accordingly, these wavelengths were used to investigate the influence of different excitation wavelengths on the excited states behaviour in PM6:Y6 on ultrafast timescales.

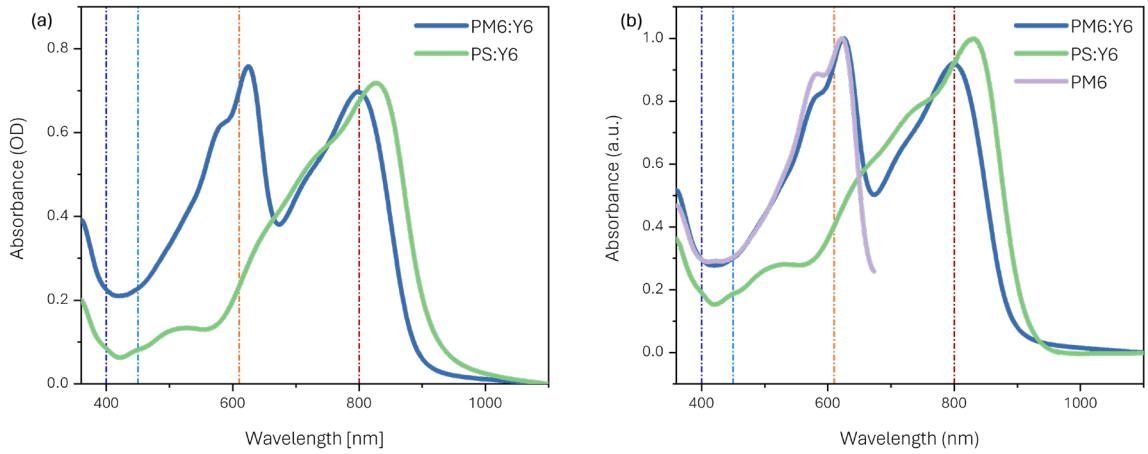

Figure 6-1: (a) Steady-state absorption spectra of PM6:Y6 (blue), PS:Y6 (green) and (b) normalised steady-state absorption spectra of PM6:Y6 (blue), PS:Y6 (green) with extracted PM6 part (purple) and the excitation wavelengths 400 nm (dark blue), 450 nm (blue; only TDCF), 610 nm (orange) and 800 nm (red).

The photovoltaic performance of the PM6:Y6 device under standard 1 sun illumination is summarised in Table 6-1. The JV characteristics of the PM6:Y6 device (cf. Figure 6-2) revealed an open-circuit voltage V_{OC} of 0.845 V, a short-circuit current density J_{SC} of 26.1 mA/cm^2, a fill factor FF of 66 % and a power conversion efficiency PCE of 14.7 %. These results are representative of single-junction high-performing PM6:Y6 solar cells, which typically exhibits PCEs of 15 % to 16.5 %[102,245-247] and recently even above 19 %[191]. The dark JV curve confirms strong rectification and minimal leakage current, indicating good diode behaviour and a low density of shunt pathways.

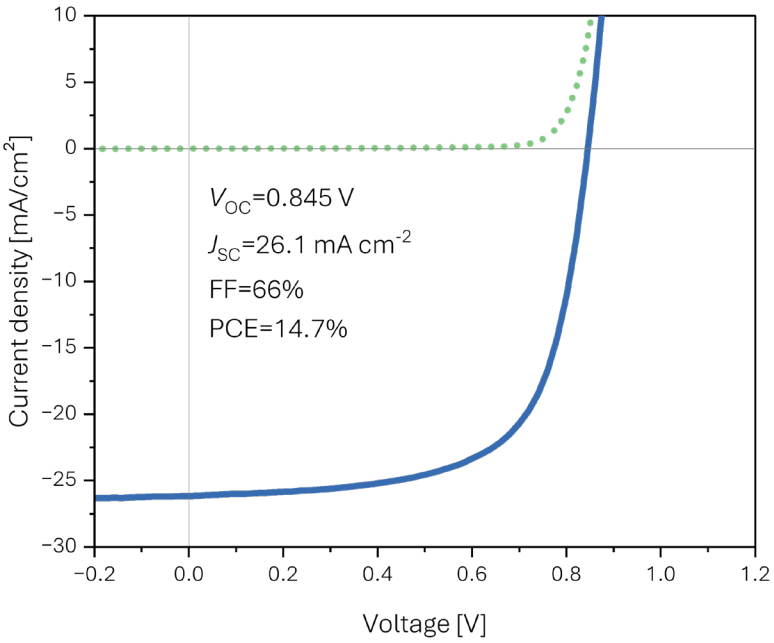

Figure 6-2: JV curve of the PM6:Y6 device under 1 sun (blue) and in the dark (green).

The EQE shown in Figure 6-3 was measured on a PM6:Y6 device with an opaque Ag electrode. PM6:Y6 exhibit efficient photon-to-charge conversion at 800 nm (77 %) and at 610 nm (81 %), while it was significant reduced at 400 nm (52 %) and at 450 nm (67 %). Here, the bias-dependent EQE curves show only negligible variation within the small bias window used in the steady state for both forward and reverse bias. Field-independence is characteristic of well-optimised blends in which photogenerated charges can be efficiently separated and extracted without the need for an external field due to favourable energetics and nanostructure. However, it does not provide information on the actual timescales of CS but rather reflects the cumulative result of all photophysical processes under device operation.[70,246]

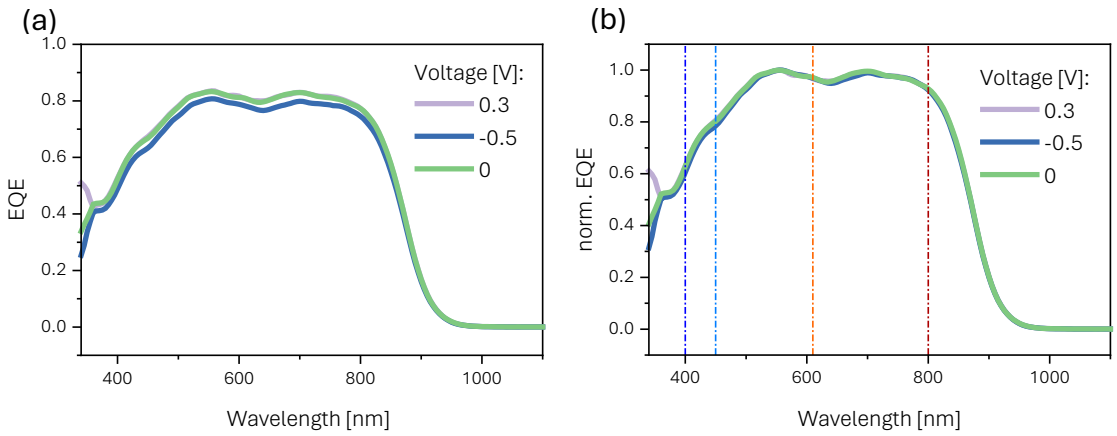

Figure 6-3: (a) External Quantum Efficiency and (b) normalised External Quantum Efficiency of the PM6:Y6 device with an opaque Ag electrode without an external bias (green), with reverse bias (blue), forward bias (purple) and the used excitation wavelength 400 nm (dark blue), 450 nm (blue; only TDCF), 610 nm (orange) and 800 nm (red).

6.2.2. Time-Delayed Collection Field

Time-delayed collection field (TDCF) probes the intermediate nanosecond to microsecond regime and bridges the gap between ultrafast spectroscopy and the steady state. This allows investigation of charge carrier extraction and recombination dynamics after the initial formation processes but before full equilibration in the steady state is reached.

Charge Collection Dynamics

The TDCF results in Figure 6-4 shows the collected charge Q_{coll}, the extracted charge under pre-bias Q_{pre} and the total extracted charge Q_{tot} as a function of time delay for several excitation fluences at 450 nm and 800 nm. At shorter timedelays, Q_{coll} increases nearly proportionally with fluence, reflecting efficient extraction before significant recombination occurs. As the excitation fluence increases, Q_{coll} no longer rises linearly and declines with increasing delay, approaching zero at long delays as the remaining carrier reservoir is depleted by recombination, reflecting an increased probability of bimolecular recombination at higher carrier densities before collection.

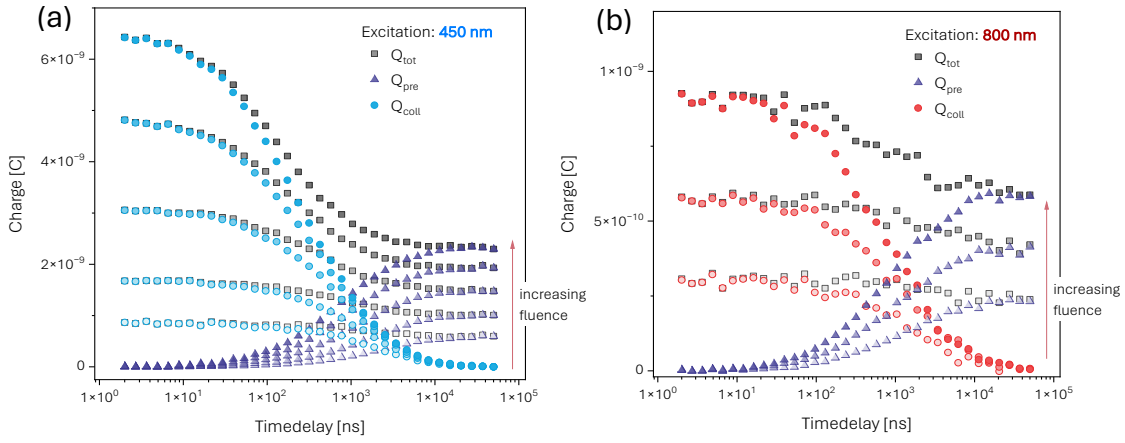

Figure 6-4: Time-resolved charge extraction from TDCF measurements of a PM6:Y6 device. Collected Charge Q_{coll}, extracted charge under pre-bias Q_{pre} and total extracted charge Q_{tot} during (a) 450 nm excitation and (b) 800 nm excitation.

Recombination Rate and Order

To further analyse the recombination dynamics, the recombination rate R is plotted against the collected charge carrier density n_{coll} on a double logarithmic scale. Across all wavelengths and fluences, the slope δ remains close to 2 in the intermediate time window, indicating that recombination is dominated by bimolecular kinetics. Deviations above δ = 2 at higher excitation densities does not refer to true higher-order recombination like Auger recombination (cf. section 2.4.4 above). In OPVs, it is instead attributed to carrier crowding, trap-assisted recombination, spatial inhomogeneity, experimental artefacts or limitations of the fitting procedure. The plots in Figure 6-5 are constructed using data from a selected range of intermediate timedelays. Early and late times are excluded to ensure physical relevance and reliability of the extracted recombination order in accordance with TDCF literature standards.[99,209,210]

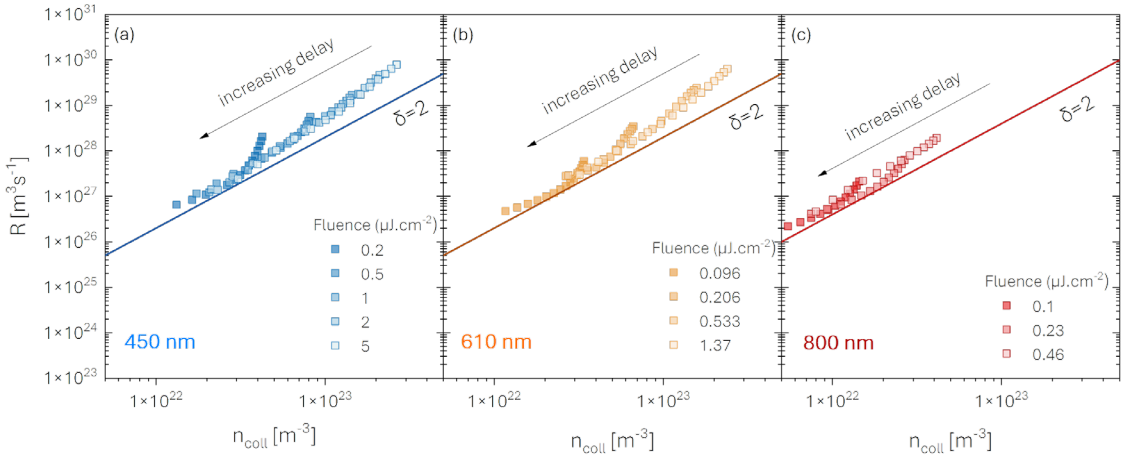

Figure 6-5: TDCF recombination rate R as a function of collected carrier density n_{coll} for a PM6:Y6 device, shown for (a) 450nm, (b) 610nm and (c) 800nm excitation with the slope δ, indicating the recombination order. Different shades of the data points represent the fluencies shown in the legend in [μJ/cm²].

Figure 6-6 shows the evolution of the instantaneous recombination order δ as a function of the timedelay for every excitation wavelength. For 450 nm and 800 nm excitation, equitemporal fit starts near of δ = 1 at 1 ns, increasing to a maximum in the sub-microsecond range before decreasing afterwards. For 610 nm excitation, δ begins near 2 and follows a similar trend. In TDCF, δ is typically evaluated after exceeding the maximum, when it first returns near δ = 2. This regime is recognised in the literature as

corresponding to the onset of true bimolecular recombination under quasi-steady-state conditions, where artefacts and noise are minimised.[209,210] However, OPVs und thus also PM6:Y6 typically do not show a broad plateau or steady-state region due to the combined effects of carrier extraction dynamics, measurement response and signal-to-noise limitations. Instead, they exhibit a distinct crossing at δ = 2 after the maximum which represents the point at which bimolecular recombination becomes the dominant process in the system.

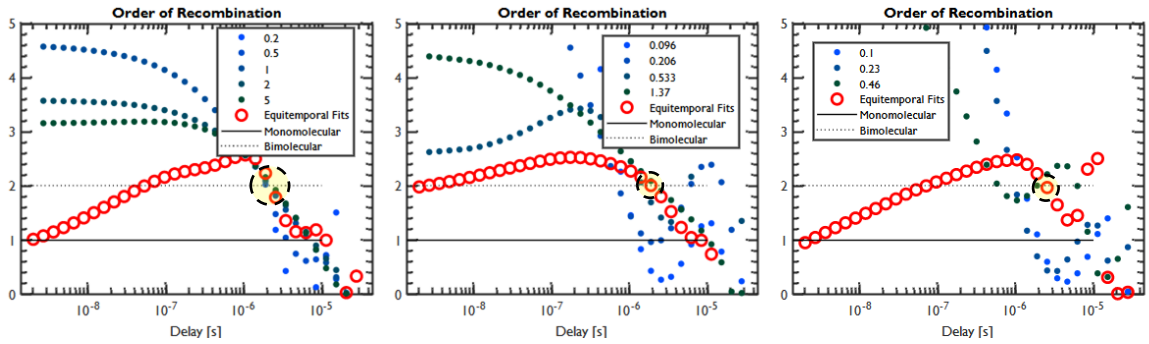

Figure 6-6: Evolution of the recombination order δ from equitemporal fits under (a) 450 nm, (b) 610 nm and (c) 800 nm. Colours from blue to green of the data points represent the fluencies shown in the legend in [μJ/cm^2].

It is important to note that the values of δ of the initial and late times should not be overinterpreted. At early times, the excitation at 610 nm may shows δ = 2, which could be interpreted as an efficient CS due to immediately dominant bimolecular recombination, suggesting a wavelength dependence while 400 nm and 800 nm only show δ = 1. Instead, this regime is strongly affected by instrument response and extraction artefacts. Similarly at long delays, δ can decrease even below 1 as the signal diminishes and noise increases. Therefore, only the value of δ at the specific crossing point after the maximum is considered to reliably represent the true recombination regime, which occurs for this PM6:Y6 device at approximately 2–3 μs for all three excitation wavelengths, indicating that bimolecular recombination is the dominant loss process.

Bimolecular Recombination Constant

The bimolecular recombination constant k_2 was determined for each excitation wavelength in the temporal window where δ = 2. Exciting the PM6:Y6 device at 800 nm leads to an increased k_2-value of $6.6 \cdot 10^{-18}$ m^3/s, indicating a more rapid bimolecular recombination. In contrast, the lower k_2-values observed for excitation at 450 nm ($3.4 \cdot 10^{-18}$ m^3/s) and 610 nm ($3.8 \cdot 10^{-18}$ m^3/s) indicating a more spatially distributed charge generation profile and possibly lower bimolecular encounter rates in these regimes. These values are consistent with those previously reported for PM6:Y6 and other well-optimised NFA blends.[99,209,210]

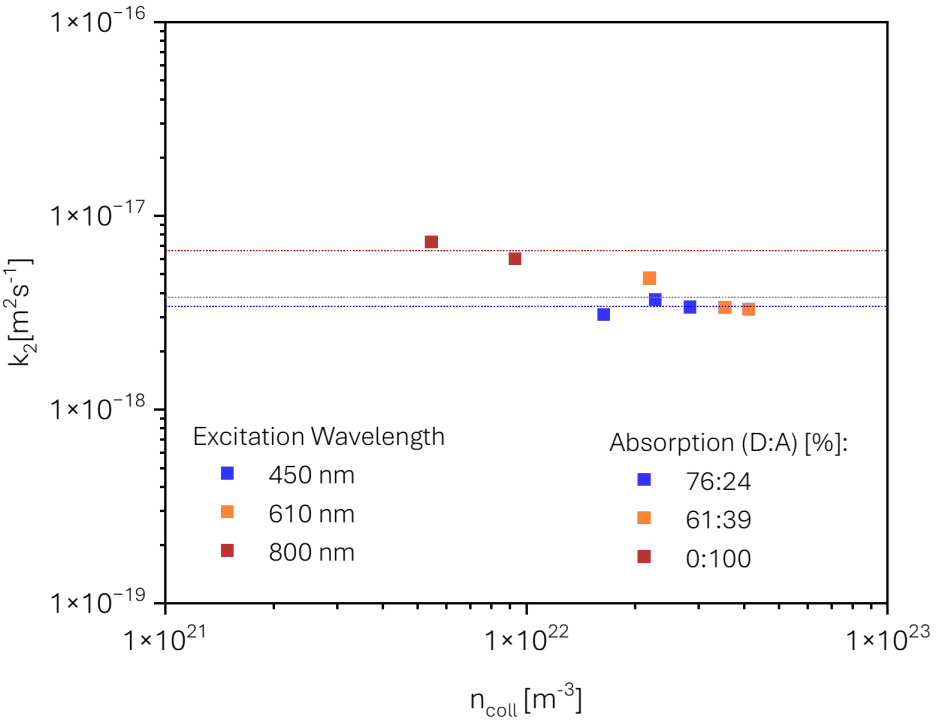

Figure 6-7: Bimolecular recombination coefficients k_2 as a function of collected carrier density ncoll for PM6:Y6 devices excited at 450 nm (blue), 610 nm (orange) and 800 nm (red).

The full set of parameters obtained in this section are listed in Table 6-1. Across all excitation wavelengths, charge carrier recombination is best described by a bimolecular mechanism, as indicated by the evolution of the recombination order δ and the extracted values of the bimolecular recombination constant k_2. The TDCF evaluation of excitation wavelength effects on recombination and extraction dynamics provides an important basis for interpreting the results of ultrafast time-resolved spectroscopic experiments discussed in the following sections.

Table 6-1: Parameter of PM6:Y6 film and device extracted from steady-state and TDCF measurements.

Parameter	400 nm	450 nm	610 nm	800 nm
V_{OC}	0.845 V			
J_{SC}	26.1 mA/cm^2			
FF	66 %			
PCE	14.7 %			
Abs (D:A)	76:24	76:24	61:39	0:100
EQE	52 %	67 %	81 %	77 %
k_2	–	$3.4 \cdot 10^{-18}$ m^3/s	$3.8 \cdot 10^{-18}$ m^3/s	$6.6 \cdot 10^{-18}$ m^3/s

6.2.3. Transient Absorption in Neat PM6 and PS:Y6 Films

Time-resolved transient absorption (TA) spectroscopy was used on neat PM6 and PS:Y6 films to determine the spectral shapes of present species. By mixing Y6 into an inert polystyrene (PS) matrix with a 1:1.2 ratio (cf. section 3.1.2), intermolecular aggregation and interaction effects should be reduced to some extent but are not fully eliminated. The aim is to approximately simulate and investigate the intrinsic optical and photophysical properties in a more molecularly dispersed state, as it was already applied in earlier studies to other NFAs such as ITIC.[248] Excitation at 400 nm, 610 nm and 800 nm allowing selective investigation of higher- and lower-excited states and providing spectral shapes of the components for subsequent decomposition of the measured PM6:Y6 blend data.

6.2.3.1. Neat PM6 Film

The TA spectra of neat PM6 (cf. Figure 6-8) exhibits a ground state bleach (GSB) with a strong peak at 635 nm and a second peak at 575 nm, corresponding to the absorption of PM6 in the steady state. Also, a broad positive photoinduced absorption (PIA) signal is observed across the near-infrared (NIR) region, plateauing between 850–1150 nm.[249] Within this absorption band, a weak signal is observed peaking near 850–950 nm and becoming more pronounced at later times. This could in principle points towards a small contribution of a $PM6^{+}$ cation, observed by Harris, et al. [250] via spectroelectrochemistry. Such a feature could be possible but remains only weakly developed. Triplet states however are less likely and would exhibit a spectral feature near 1650 nm.[63,251] The absence of quenching pathways results in a relatively long-lived exciton population, in contrast to when blended with an acceptor material. Early times of the spectra are used later as a spectral shape of the PM6 exciton species during MCR analysis of the PM6:Y6 samples.

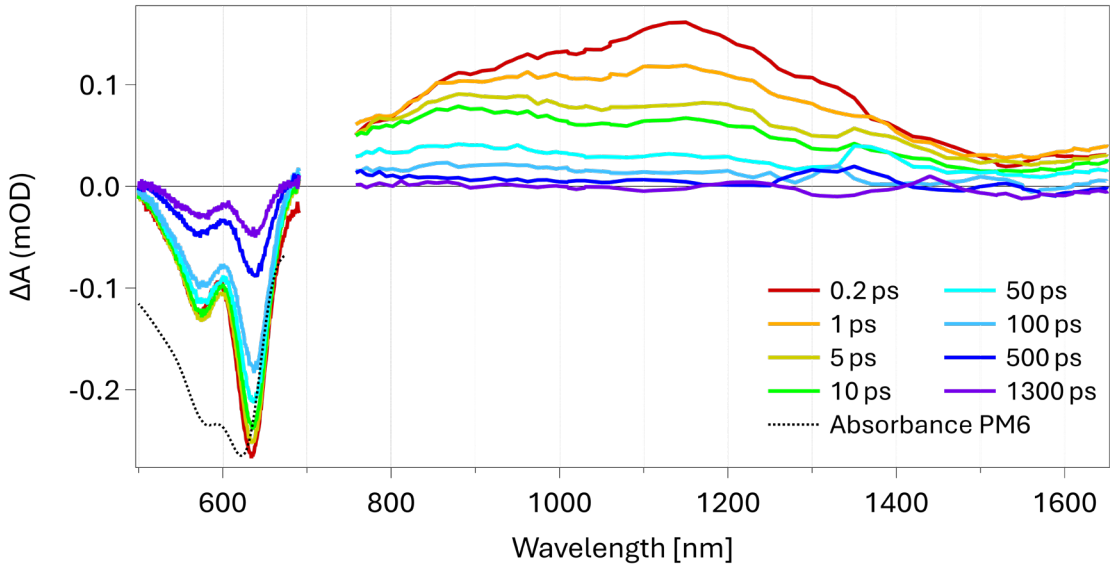

Figure 6-8: TA spectra of a neat PM6 thin film excited at 610 nm for a series of pump-probe delays.

6.2.3.2. Diluted Y6 Film

Transient Absorption Spectra of PS:Y6

The TA spectra resulting from the excitation of PS:Y6 at 800 nm is shown in Figure 6-9. At early times, the TA spectra exhibit a broad GSB between 620 nm and 890 nm, peaking at 850 nm, in the region of the steady-state absorption of Y6. At the same time, PS:Y6 exhibits a positive signal ESA signal of Y6, rising directly after the GSB and peaking at 920 nm with a shoulder up to 1000 nm. The early times also exhibit a second positive signal which slowly arises beyond 1200 nm and reaches its maximum in a broad peak between 1500 nm and 1600 nm. This feature is assigned to the absorption of neat Y6 charges ($Y6^+$ and $Y6^-$) which are formed on sub-picosecond timescales after photoexcitation. In neat Y6 and PS:Y6, the formation of positive and negative charges is limited to Y6. Therefore, the formation of $Y6^+$ and $Y6^-$ charge is balanced and consequently not separable in a TA spectra of PS:Y6.[64,91] At longer timedelays, both GSB and PIA amplitudes decrease continuously towards zero and the GSB peak shifts from 850 nm to 860 nm which is also distinctive for the presence of charges.[64,252]

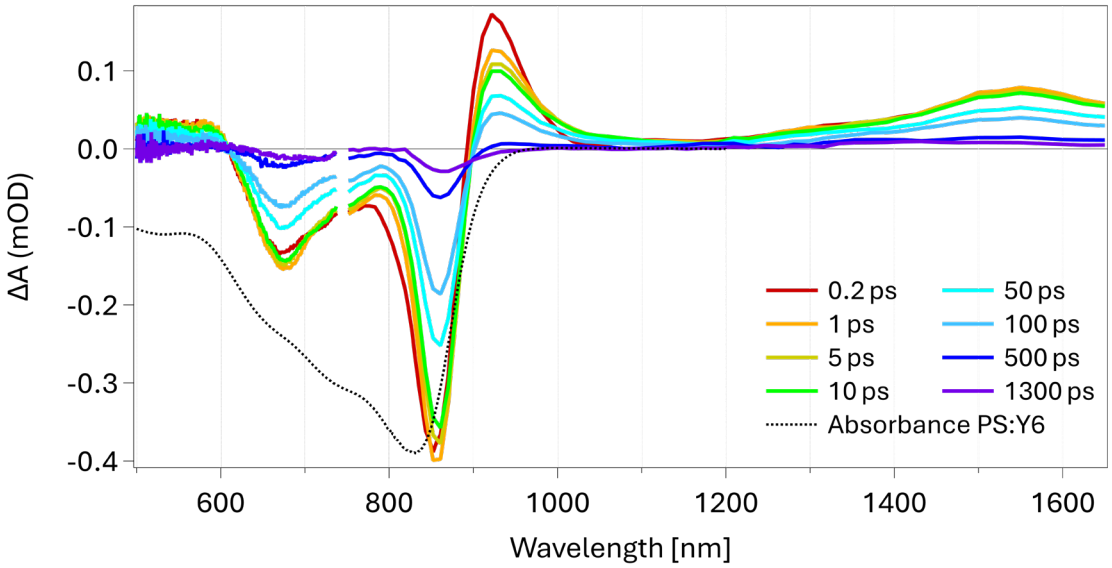

Figure 6-9: TA spectra of a PS:Y6 thin film excited at 800 nm for a series of pump-probe delays.

After excitation at 610 nm (cf. Figure S 6-1), the TA spectra display a slightly different pattern. A positive PIA at 920 nm with a shoulder towards 1000 nm is also observed for 610 nm excitation, as well as the broad absorption band between 1500 nm and 1600 nm for the neat Y6 charge. The peak of the GSB appears to be smaller and slightly blueshifted within the first picosecond. It peaks at 840 nm which is closer to the absorption maximum of the steady state, indicating a proportionally larger exciton population than with 800 nm excitation. Since the GSB of the Y6 exciton and the neat Y6 charge are shifted, an overlap leads to partial cancellation and an apparently lower GSB amplitude.[64,91]

Notably, the amplitude of the broad absorption band between 1500 nm and 1600 nm assigned to neat Y6 charge appears slightly larger after excitation at 610 nm compared to 800 nm, even though the density of absorbed photons was matched for all measurements on the PS:Y6 film and the 800 nm excitation spectra of PS:Y6 indicates a higher neat Y6 charge proportion at 0.2 ps. This is most likely attributable to experimental artefacts such as probe misalignment, slight deviations in detector sensitivity or errors in calibration and not to intrinsic wavelength dependencies in PS:Y6.

Upon excitation at 400 nm (cf. Figure S 6-2), the TA spectra of PS:Y6 exhibit certain differences in peak positions. After 0.2 ps, the PIA of the Y6 exciton is slightly blueshifted to 910 nm. Also, the GSB peaks at 835 nm, overlapping directly with the absorption spectra of PS:Y6 in the steady state and exhibits a slightly higher amplitude than with 610 nm excitation. When PS:Y6 is excited at 400 nm, within the first picosecond the majority of the excited species are excitons and thus a GSB peak closer to 835 nm and a PIA closer to 910 nm indicates a more dominant presence of Y6 excitons, while a GSB peak at 850 nm and a PIA at 920 nm points towards a higher proportion of neat Y6 charges. However, there is a significant difference observed in the spectral amplitude of the 400 nm spectra at higher probe wavelengths. The signal above 1000 nm is significantly weakened in the 400 nm TA spectra. This suppression is not physical but arises from experimental artefacts, probably due to reduced probe intensity and detection sensitivity in the NIR range during the 400 nm measurements of the PS:Y6 and PM6:Y6 films. In contrast to the other excitation wavelengths, this resulted in the loss of most of the information content, which is why, contrary to expectations, no significant PIA signal was observed above 1500 nm. Accordingly, the film data for 400 nm excitation in the NIR must be considered with care.

Spectral Deconvolution

The identification of the spectral shapes of exciton, charge and triplet in PS:Y6 was achieved by selecting specific time delays and excitation conditions that maximise the presence of each species while minimising spectral overlap. For the PS:Y6 film, this MCR-optimised spectral shapes of the Y6 exciton, neat Y6 charge and Y6 triplet are extracted and displayed in Figure 6-10, in accordance with recent ultrafast spectroscopic publications.[64,91,252] The shape of the initial Y6 exciton guess was chosen by taking the TA spectrum at 0.2 ps after 400 nm excitation, as this condition predominantly generates localised singlet excitons on unaggregated Y6 molecules[188], which is supported by the blueshifted GSB peak at 835 nm and the PIA signal peaking at 910 nm. The initial guess for the neat Y6 charge spectrum was taken from later times during the 800 nm excitation, where GSB and PIA are most red-shifted to 860 nm and 920 nm, respectively, with a shoulder extending to 1200nm and a second absorption

signal centred at 1550–1600 nm. In PS:Y6, as in all single-chromophore Y6 systems, the formation of positive $Y6^+$ and negative $Y6^-$ charges are inherently balanced, leading to an overlap of their spectral features, making separate identification impossible within the TA spectrum and would require spectroelectrochemistry. The initial guess for the Y6 triplet was derived from late times spectra during 400 nm excitation, where a small band at around 1450 nm emerges. This signal is absent under both 610 nm and 800 nm excitation. Since triplet excitons exhibit the same GSB as singlet excitons, their appearance in the spectra is in principle similar. Since this feature is not unique to triplets, in combination with the occurring artefacts under 400 nm excitation, it was not possible to extract a correct amplitude relation between GSB and ESA and thus only the ESA of the Y6 triplet is included, which is a common practice in literature but may lowered the informational content regarding the Y6 triplet contribution.[64]

However, the excited species were mostly only present mixed together within the spectra, which applies in particular for the charge species. For neat Y6 films, it was shown that under 800 nm excitation Y6 excitons can also persist at longer timescales.[253] Therefore, at least some fraction of Y6 excitons are expected to contribute to this initial Y6 charge guess too. Therefore, the selected guesses were fit into the PS:Y6 data sets via MCR analysis to refine and optimise the spectral shapes of the respective excited species. The obtained spectral shapes are further used for Multivariate Curve Resolution (MCR) analysis of PM6:Y6 blends in section 6.2.4.

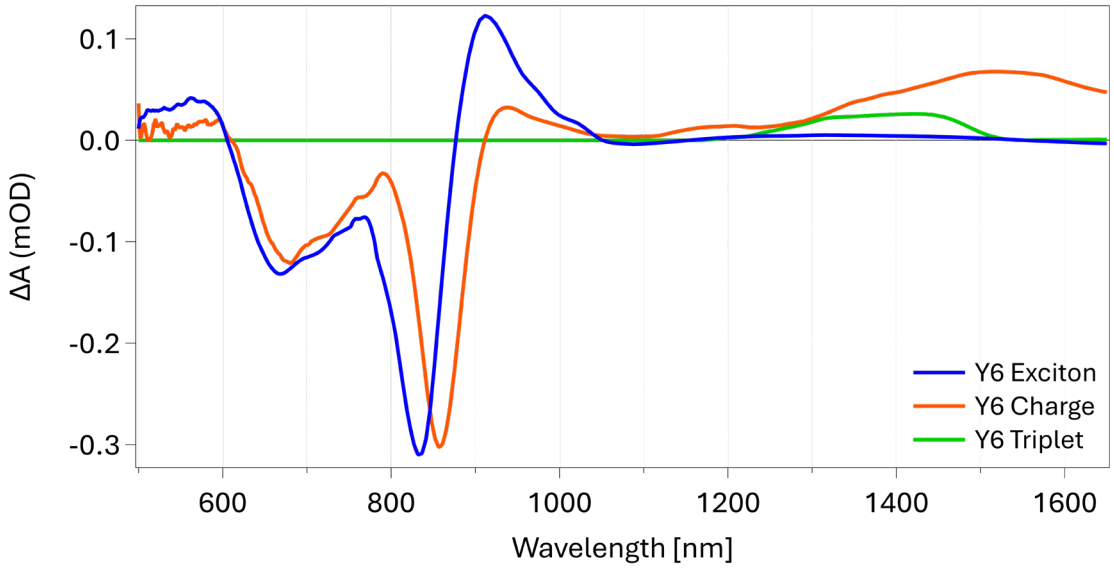

Figure 6-10: Spectral shapes of the excited state species: singlet Y6 exciton (blue), neat Y6 charge (orange) and the absorption signal of the triplet Y6 exciton (green), present in a PS:Y6 film and extracted during wavelength-dependent excitation.

The MCR analysis applied to the PS:Y6 TA data under three excitation wavelengths reveals the population dynamics shown in Figure 6-14. The upper panel displays the exciton dynamics, exhibiting a pronounced dependence on excitation energy. The 400 nm excitation generates the largest initial exciton population, followed by 610 nm, with 800 nm exhibiting the smallest population. At approximately 3 ps, exciton population for 400 nm and 610 nm converge and continue with an identical decay. In contrast, exciton population of 800 nm remains consistently lower.

In the middle panel of Figure 6-14, the displayed Y6 charge populations exhibit also an excitation wavelength dependence. Here, the 800 nm excitation leads to a dominant and nearly instantaneous charge population that decays over the probed time window. For both 800 nm and 610 nm excitation, charge populations arise on sub-picosecond timescales and decrease with time constants around 30 ps and 230 ps for both. The charge dynamic trace for 610 nm exhibits a similar shape to 800 nm excitation but with an overall smaller amplitude, due to the higher relative exciton population. In contrast, 400 nm excitation exhibits a negligible charge population at early times that increases gradually and plateaus after several tens of picoseconds, indicating a delayed charge formation.

A triplet signal appears only during 400 nm excitation with a delayed rise beyond 100 ps and a time constant of 496 ps. However, no triplet population was observable at lower photon energies at 610 nm and 800 nm excitation in PS:Y6 films.

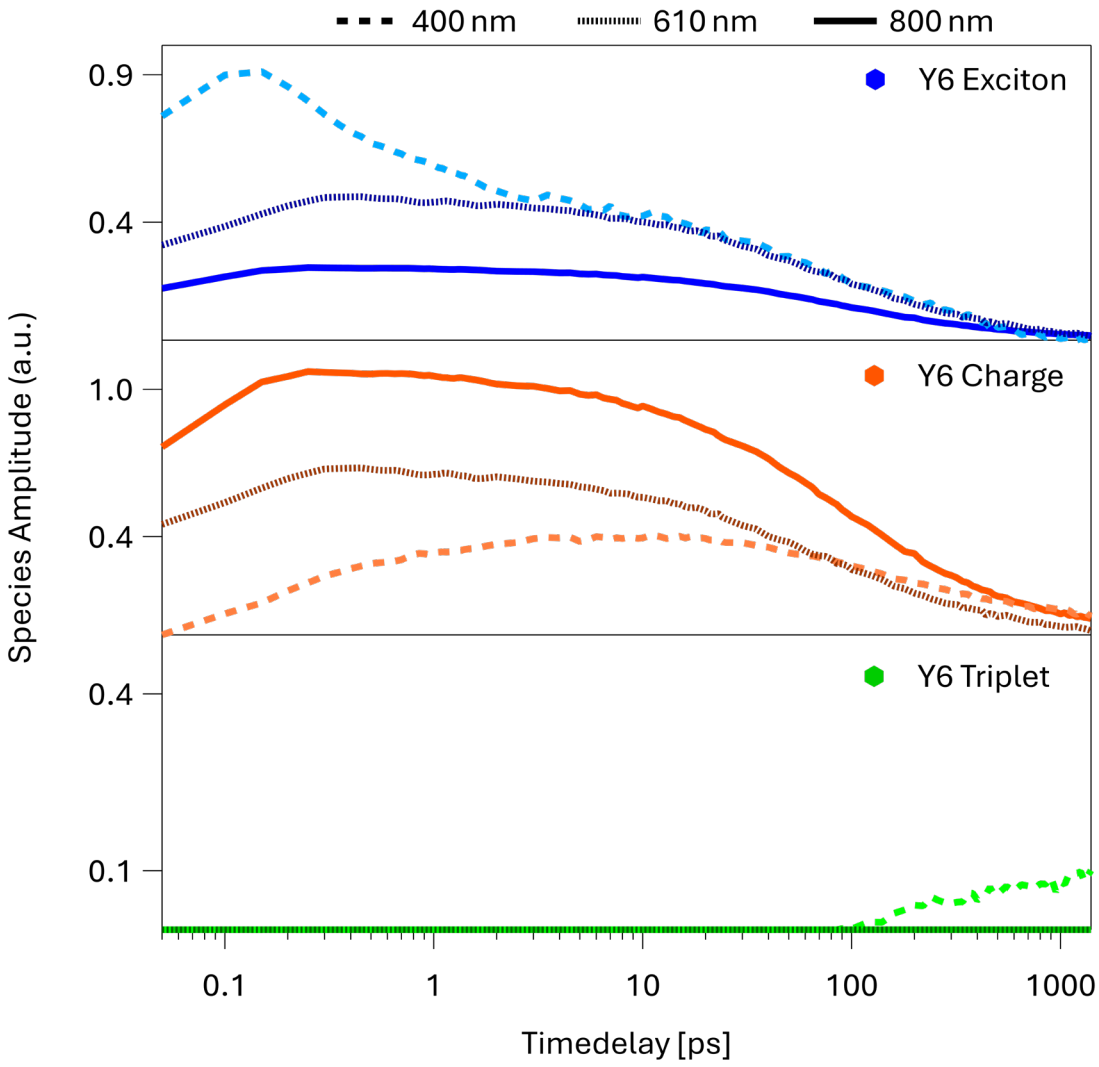

Figure 6-11: Time-resolved relative contribution to the measured ΔA of each species in PS:Y6 during wavelength-dependent excitation for singlet Y6 exciton (blue), neat Y6 charge (orange) and the absorption signal of the triplet Y6 exciton (green), obtained using MCR.

This behaviour is best explained by the wavelength-dependent excitation of different aggregated region of Y6. 800 nm excites the low-energy Y6 aggregate I, leading to a rapid formation of Y6 charges due to stronger π–π coupling. In contrast, 400 nm predominantly excites unaggregated Y6 domains with only weak coupling, where excitons are spatially localised.[188] This results in a stronger Coulomb binding, hinders and slows down Y6 charge formation. The PS matrix intensifies this effect by diluting

Y6, which further limits exciton diffusion towards aggregated sites. A triplet population emerges at 100 ps under 400 nm excitation. Very long-lived excitons are still present when triplets start to evolve. However, this is also the case for 800 nm and 610 nm, w which in contrast to 400 nm show no detectable triplet formation. This suggests that triplet formation occurs in PS:Y6 not dominantly via direct (intersystem crossing) ISC, but proceeds predominantly via CT-mediated back transfer, as shown for neat Y6 films by literature.[252] This points towards an aggregate-depended triplet state formation in PS-diluted Y6. Neat Y6 charges in more aggregated regions can be more delocalised, while neat Y6 charges in unaggregated regions tend to be more short-range bound. 800 nm excitation exhibits rapid Y6 charge formation in aggregated Y6 domains, 400 nm excites unaggregated Y6, while 610 nm addresses a mixture of aggregate I & II, together with unaggregated Y6 domains.[188] Consequently, a formation of triplet states in PS:Y6 by 800 nm excitation would be less expected, while charges in unaggregated Y6 regions during 400 nm excitation are more likely to form triplet states. For 610 nm, a mixed response und thus a smaller triplet contribution was expected. Since the triplet amplitude during 400 nm excitation was already weak, a possible triplet response most likely merged into another component during MCR analysis. This expected mixed behaviour for 610 nm is also reflected by the evolution of the exciton and charge populations. The excitation of the aggregated domains provided 610 nm with a charge population evolution closer to 800 nm. In contrast, the fraction of Y6 excited in unaggregated regions, reduced the amplitude of the Y6 charge signal across the entire time window, while late times exhibits a slightly reduced shape, similar to the charge signal for 400 nm at late times.

Overall, the observed differences are attributed to the degree of aggregation of the excited Y6 domain. Higher delocalised states lead to a faster and stronger formation of Y6 charges, while a direct influence of higher-lying excited states could not be observed in this diluted Y6 film. The extracted MCR constants are displayed in Table S 6-1, while the MCR-refined spectral shapes from Figure 6-10 are used in the following analysis of PM6:Y6 blends and devices.

6.2.4. Transient Absorption in PM6:Y6

6.2.4.1. PM6:Y6 Film

Transient Absorption Spectra of the PM6:Y6 Film

All measurements were performed in the linear excitation regime and normalised to represent the same density of absorbed photons with $8.8 \cdot 10^{16}$ 'Ph'·cm^{-3} (cf. section 3.5), which allows for a direct comparison of all measured spectra and dynamics.

The TA spectra obtained by the excitation of a PM6:Y6 film at 800 nm is displayed in Figure 6-12. As PM6 does not absorb at 800 nm, direct photoexcitation is restricted to Y6. Similar to PS:Y6, an ultrafast formation of CTx states on sub-picosecond timescales is also expected for PM6:Y6. However, at 0.2 ps, the GSB in the visible region already differs significantly from that of PS:Y6 and exhibits similarities with the shape of the steady-state absorption of the PM6:Y6 film. Since excitation at 800 nm is not expected to lead to a formation of PM6 excitons and ESA of the PM6 exciton is also absent in the NIR, this spectral variation indicates a formation of interfacial CT states within the first picosecond. Here, the photoexcited Y6 acceptor transfers a hole to the PM6 donor across an interface, which occurs simultaneously with the formation of CTx states within the Y6 domains. Between the GSB of PM6 peaking at 635 nm and the GSB of Y6 peaking at 835 nm, another ESA arises. Also, the PIA peak at 920 nm broadens and shifts towards 980 nm, indicating the increasing presence of interfacial PM6:Y6 charges, while the previously to neat Y6 charges attributed signal around 1550 nm diminishes significantly after 10 ps. The TA spectra for 800 nm exhibits rapid formation of interfacial PM6:Y6 charges, whose absorption signal at around 1000 nm rises quickly within the first 50 ps before decreases slightly afterwards, indicating minimal recombination.

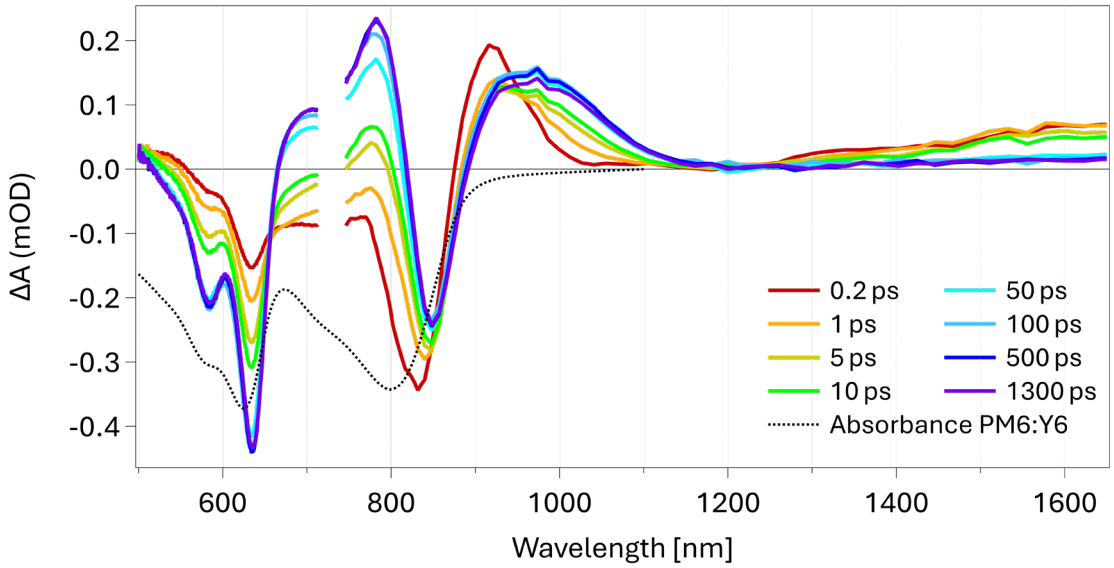

Figure 6-12: TA spectra of a PM6:Y6 thin film excited at 800 nm for a series of pump-probe delays.

During the excitation at 610 nm (cf. Figure 6-13), both donor and acceptor are excited in a comparable relation. This leads to the initial formation of a PM6-dominated shape of the GSB in the visible, indicating the immediate appearance of both PM6 and Y6 excitons. This is supported by the GSB at early times and the short-lived broad signal between 1000–1400 nm, which occurs within the first picosecond after excitation and is attributed to the PIA of PM6 excitons. Here, the NIR signal attributed to interfacial charges also rises rapidly within the first 10 ps, but in contrast to 800 nm excitation, reduces relatively fast after 50 ps. This could indicate a population loss but also the presence of an artefact since the visible region in the TA does not reflect this decay.

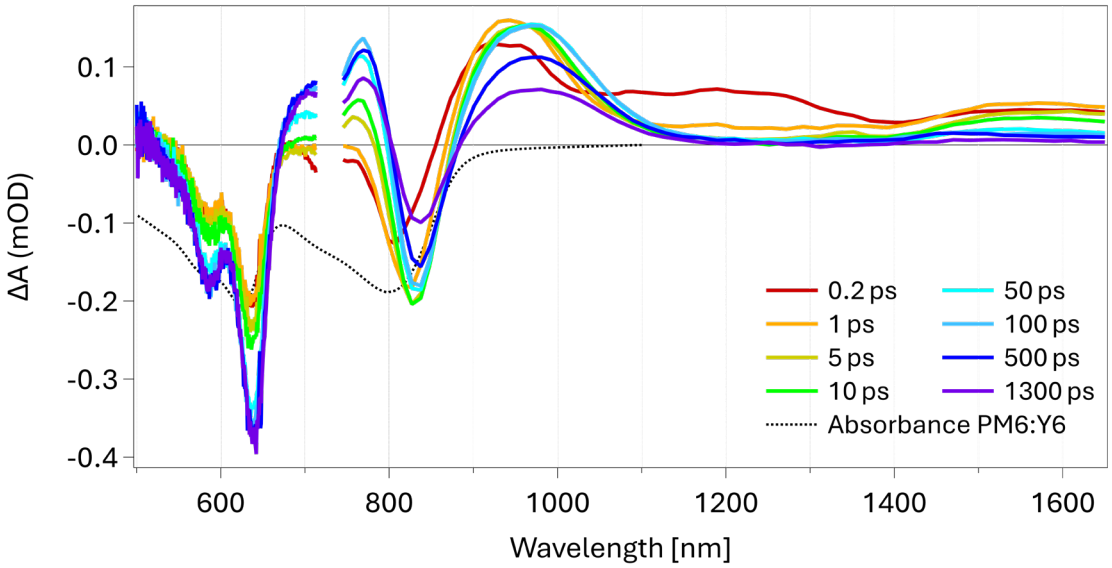

Figure 6-13: TA spectra of a PM6:Y6 thin film excited at 610 nm for a series of pump-probe delays.

Figure S 6-3 displays the excitation of the PM6:Y6 film at 400 nm, which dominantly excites the donor and the unaggregated Y6 fraction.[188] After an ultrafast formation of interfacial charges, the late-time spectra do not exhibit any notable decay. Similar to the PS:Y6 film at 400 nm excitation (cf. Figure S 6-2), also the TA spectra of the PM6:Y6 film did not provide the expected Y6 PIA between 1400 nm–1600 nm. This is also attributed to experimental artefacts which led to a loss in signal strength, preventing a direct amplitude comparison between the different excitation energies and requires a careful evaluation of the dynamics in the NIR, as discussed earlier during section 6.2.3.2.

Spectral Dynamics of the PM6:Y6 Film

When comparing the spectral dynamics of the GSB at 640 nm (Figure 6-14), both 400 nm and 610 nm excitation exhibit a higher initial signal amplitude than 800 nm. This region is dominated by the GSB of PM6, which is, in contrast to 800 nm, also excited during 400 nm and 610 nm excitation. At longer timescales, the spectral traces of all three excitation wavelengths converge. At 780 nm in the lower panel of Figure 6-14, all three excitation conditions start with similar magnitudes and exhibit a similar

slope before crossing zero at around 3 ps and convert into a positive signal. This is attributed to an absorption signal caused by the formation of interfacial charges which decrease and overlay the bleach signal of both Y6 excitons and neat Y6 charges. After transforming into a positive signal, 800 nm excitation exhibits the steepest slope before plateauing beyond 100 ps. The signal increase for 400 nm is slightly slower but finally exhibits a similar signal amplitude. In contrast, 610 nm diverges as an absorption signal from the others and even starts to show a signal reduction after 100 ps. As stated before, this could either indicate an artefact, an enhanced loss pathways or recombination of states initially populated in different morphologic regions.[64,70,86]

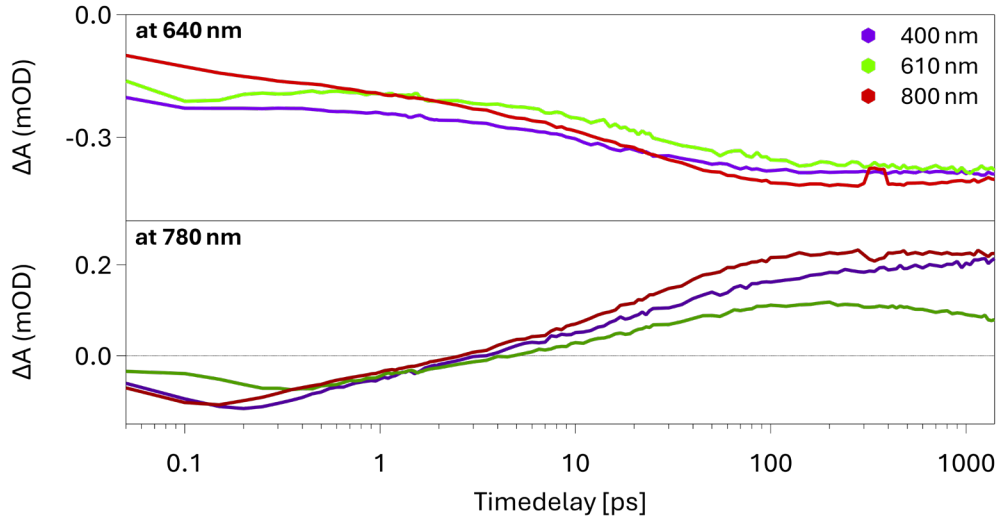

Figure 6-14: Spectral dynamics of a PM6:Y6 thin film excited at 800 nm (red), 610 nm (green) and 400 nm (purple) across the GSB signal.

In Figure 6-15, the spectral dynamics at 965 nm and 1050 nm are used to probe the excited states compared to the evolution of PM6:Y6 charges. The spectra at 1050 nm are assigned to represent mostly interfacial charges, besides the PM6 exciton absorption. The TA spectra at 965 nm represent the combination of photoexcited species in PM6:Y6. The rising signal amplitudes at 800 nm and 400 nm excitation suggest an efficient generation of persistent excited states. When comparing with the dynamics at 1050 nm, both exhibit a significant transformation into longer-lived interfacial charges, which becomes even more pronounced after normalisation and is

typical for blends with optimised morphology and efficient D–A interfaces.[64,70,86] Here, all curves were divided by their respective amplitude at a timedelay of 10 ps. On the other hand, the spectral dynamics at 610 nm excitation exhibit a lower proportion of PM6:Y6 charges formed, combined with an overall significant signal reduction after 100 ps.

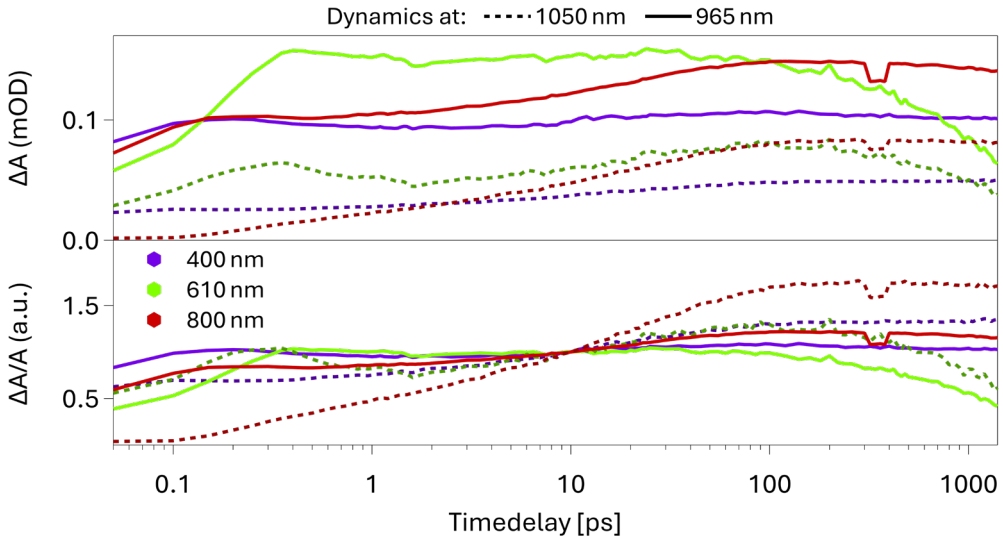

Figure 6-15: Spectral dynamics of a PM6:Y6 thin film excited at 800 nm (red), 610 nm (green) and 400 nm (purple), normalised at 10 ps for identification of the interfacial charge fraction.

Similar to PS:Y6, TA dynamics of PM6:Y6 at 1550 nm are attributed to charges, while the TA spectra at 1450 nm contain an additional absorption feature of Y6 triplets. When comparing the dynamics at 1550 nm of PM6:Y6 to them of PS:Y6 (cf. Figure 6-16), signal amplitudes are relatively stronger quenched in PM6:Y6, indicating a significant formation of PM6:Y6 charges arising from neat Y6 charges. This represents a loss channel for neat Y6 charges that is not existing in PS:Y6 due to the lack of a separate donor material.

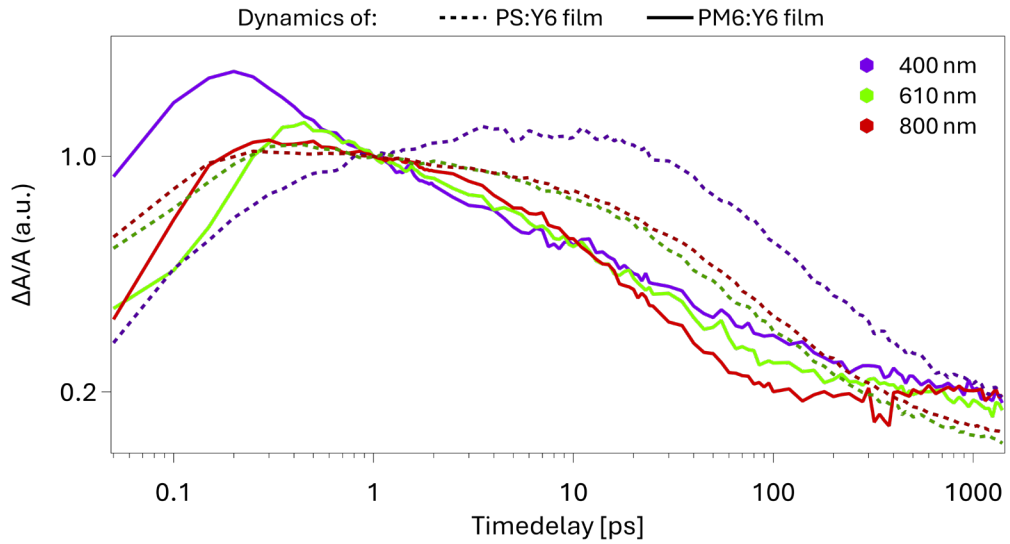

Figure 6-16: Spectral dynamics of PS:Y6 (dashed lines) and PM6:Y6 (full lines) thin films excited at 800 nm (red), 610 nm (green) and 400 nm (purple), normalised at 1 ps after excitation.

Normalising the spectral dynamics exhibits a deviation between 1450 nm and 1550 nm for all three excitation wavelengths which could originate from the formation of Y6 triplet states. The triplet-influenced absorption signal is more pronounced after 400 nm excitation compared to the other two excitation wavelengths, which is consistent with the observations for PS:Y6 and attributed to an enhanced triplet generation during excess-energy excitation.[64,70]

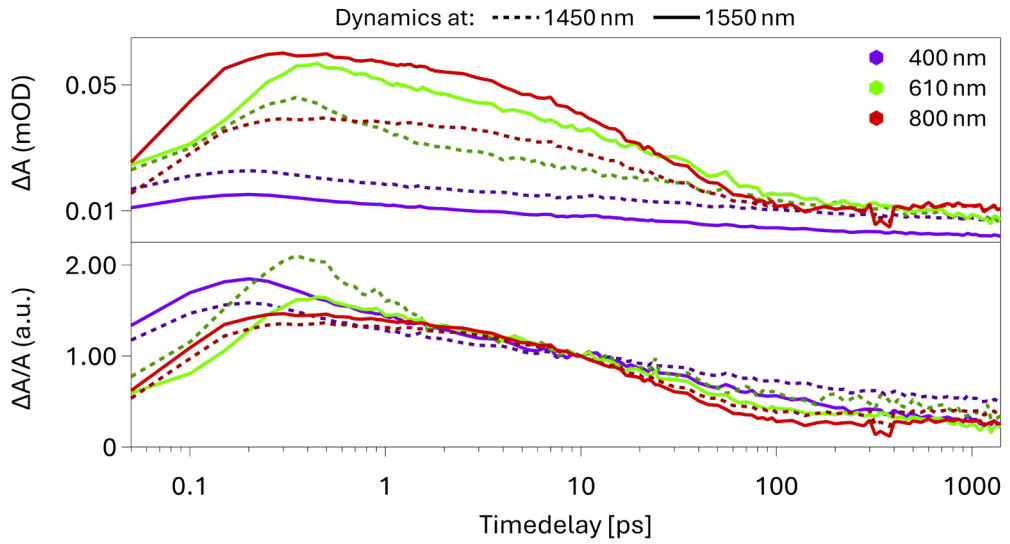

Figure 6-17: Spectral dynamics of a PM6:Y6 thin film excited at 800 nm (red), 610 nm (green) and 400 nm (purple), normalised for identification of the Y6 triplet fraction.

Spectral Deconvolution

The spectral deconvolution of the PM6:Y6 film shown in Figure 6-18 is based on the spectral components determined during the previous sections. The still required spectral shape for PM6:Y6 charges originates as an initial guess from the late-time TA spectra of PM6:Y6 after 800nm excitation, which is expected to exhibit primarily interfacial charges. The displayed spectral shape was received after the MCR refinement.

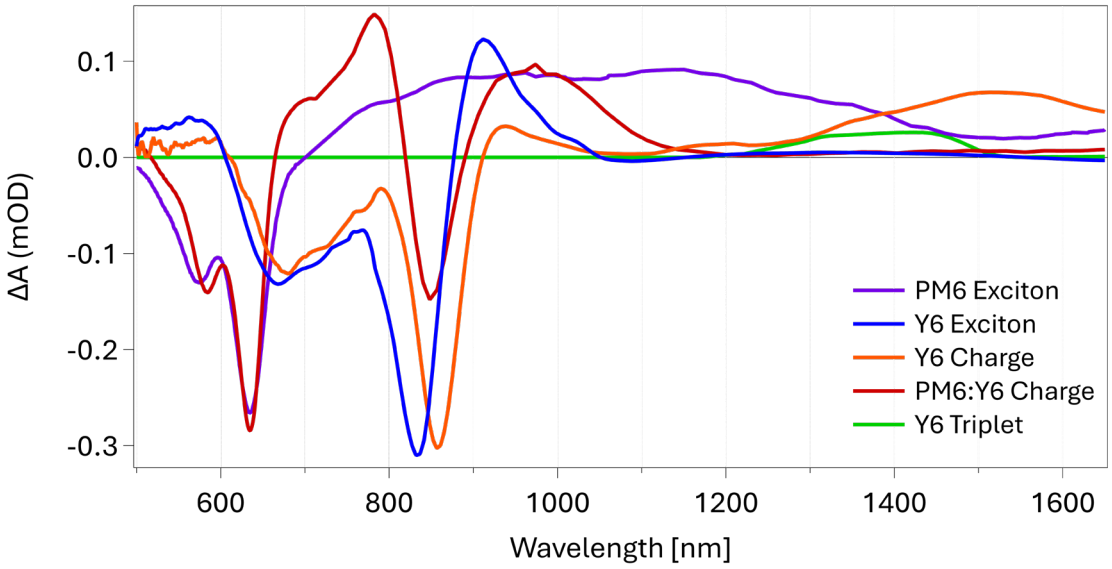

Figure 6-18: Spectral shapes of the excited state species: singlet PM6 exciton (purple), singlet Y6 exciton (blue), neat Y6 charge (orange), PM6:Y6 charge (red) and the absorption signal of the triplet Y6 exciton (green), present in a PM6:Y6 film and extracted during wavelength-dependent excitation.

Applying MCR to the TA data of the PM6:Y6 film provides a further perspective on the population dynamics during wavelength-depended photoexcitation and allows a direct comparison of the species population evolution (cf. Figure 6-19) with the previous interpretations.

During the 800 nm excitation, MCR supports previous interpretations that an exclusive photoexcitation of Y6 leads to rapid and efficient formation of both PM6:Y6 and neat Y6 charges with a simultaneous decay of Y6 exciton population with extracted time constants displayed in Table S 4-1. The decay of the Y6 exciton population is described by time constants of τ_2 =0.3 ps and τ_3 =14.9 ps, while the rise of the neat Y6 charge

occurs with τ_1 = 0.2 ps and its decay is characterised by τ_2 = 13.1 ps and τ_3 = 634.2 ps. The formation of PM6:Y6 charges arises with time constants of τ_1 = 1.1 ps and τ_2 = 24.9 ps. The significant presence of neat Y6 charges at early times, followed by their gradual reduction as they transform into interfacial charges by transferring their hole to PM6, leading to a persistent plateau of PM6:Y6 charges. This supports previous spectral analysis and is supported by other ultrafast spectroscopy studies.[64,70,188] The absence of a PM6 exciton signal under these conditions is expected, since PM6 is not absorbing in this wavelength region.

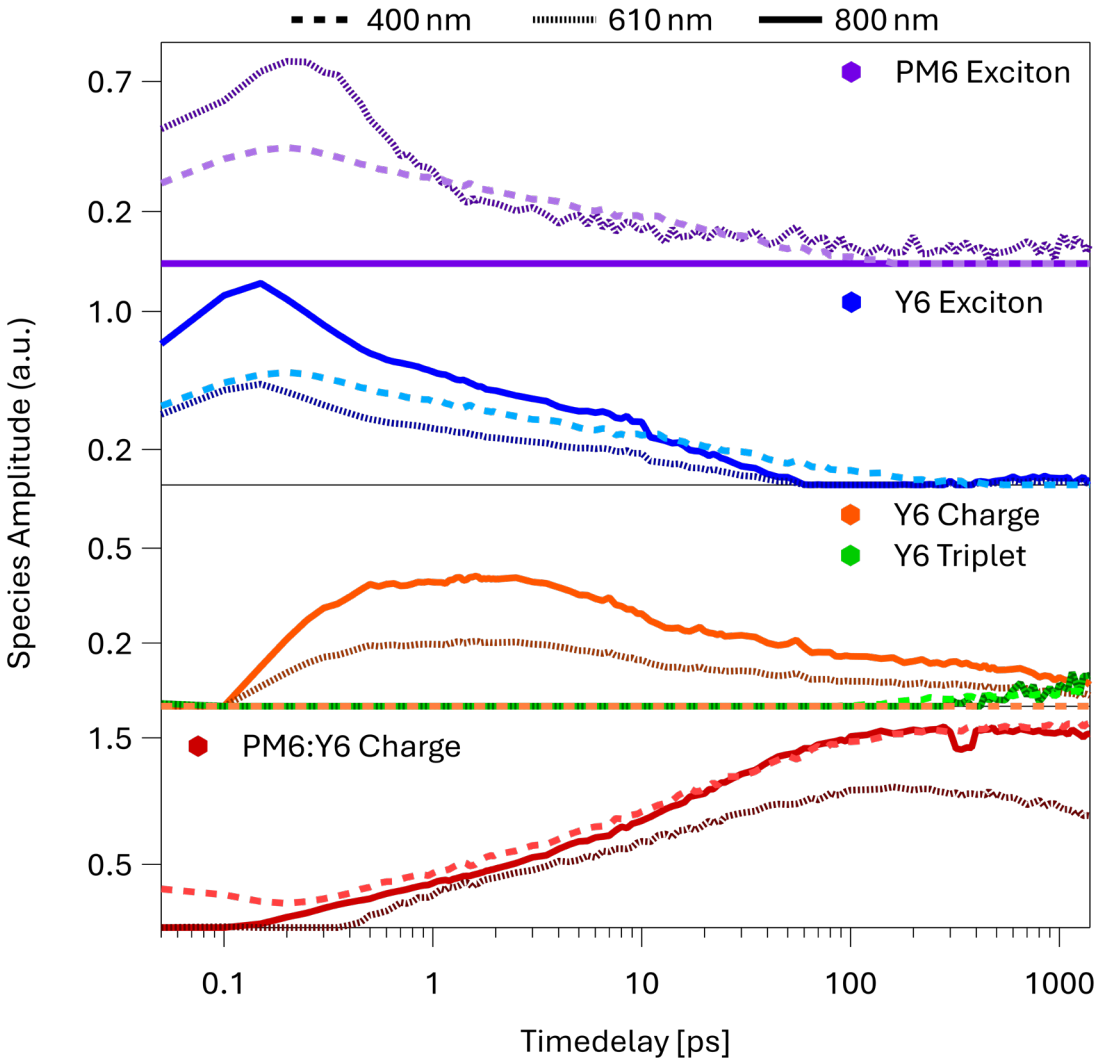

Figure 6-19: Time-resolved relative contribution to the measured ΔA of each species: singlet PM6 exciton (purple), singlet Y6 exciton (blue), neat Y6 charge (orange), PM6:Y6 charge (red) and the absorption signal of the triplet Y6 exciton (green), present in a PM6:Y6 film and obtained using MCR.

For 610 nm excitation, both the PM6 and Y6 exciton populations rise immediately after excitation, matching the expectation for simultaneous donor and acceptor excitation. The decay of PM6 and Y6 excitons is comparable to 400 nm and the rise of neat Y6 charges is rapid and follows the trend of 800 nm with a reduced signal amplitude. MCR dynamics suggest a slightly delayed rise of the interfacial PM6:Y6 charge population, compared to both other excitation wavelengths. The earlier observed decay in the PM6:Y6 charge population after 100 ps is also reflected by the MCR dynamics. While this could originate from an experimental artefact, it could also indicate increased recombination or loss channels under 610 nm excitation and will be discussed later together with TA and EDA results of PM6:6 devices and THz results of PM6:Y6 films in the following sections 6.2.4.2, 6.2.5 & 6.2.6.

During 400 nm excitation, the PM6:Y6 film revealed singlet exciton dynamics comparable to those of the other excitation wavelengths. Also, a triplet contribution was observed for all excitation wavelengths, which appeared rather weak and late with a higher uncertainty. With time constants of τ_1 = 2.5 ps and τ_2 = 40.7 ps, 400 nm exhibit rapid charge formation within the first picosecond. Overall, the PM6:Y6 charge dynamics do not show significant differences between 400 nm and 610 nm excitation. An important difference to the other excitation wavelength, however, is the clear absence of neat Y6 charges.

6.2.4.2. PM6:Y6 Device

Transient Absorption Spectra of the PM6:Y6 Device

All measurements were performed in the linear excitation regime and normalised to represent the same density of absorbed photons with $8.8{\cdot}10^{16}$ 'Ph'·cm^{-3} (cf. section 3.5), which allows for a direct comparison of all measured spectra and dynamics. During TA experiments, devices were measured under V_{OC} conditions.

The TA spectra of the PM6:Y6 device during 800 nm excitation is shown in Figure 6-20. At 0.2 ps, the spectra exhibit two GSB signals, a prominent peak at 835 nm from Y6 and a second smaller one at 635 nm from PM6. The GSB in the NIR also possesses an unusually sharp feature, which is particularly present at early times. This artefact is caused by an edge effect of the notch filter used for blocking the 800 nm fundamental used to generate the white light continuum in the TA measurements of the PM6:Y6 device. Both GSB signals exhibit a slight redshift at longer timedelays. The absorption signal of Y6 peaking at 920 nm quickly shifts and broadens towards 955 nm, indicating the fast formation of PM6:Y6 charges. This is additionally supported by the rise of the positive band between PM6 and Y6 related GSB signals. The limited spectral window in the NIR during the TA measurements of the device furthermore does not reveal any triplet state features. Since the characteristic absorption feature of Y6 triplet states is typically observed above 1400 nm, which is far beyond the measurable range, they are not discussed in the device-section.

The TA spectra after 800 nm excitation also exhibit an unexpected broad absorption signal above 1050 nm that persists across the entire measurement. An early-time signal at this position would indicate the presence of PM6 excitons but would rapidly disappear. In any case, such a PM6 exciton absorption signal would not occur during 800 nm excitation, since PM6 does not absorb here. In addition to a PM6 PIA signal, this unusual feature is also present under 610 nm (cf. Figure 6-21) and 400 nm excitation (cf. Figure 6-22), which is why device-specific phenomena must be considered. Unlike PM6:Y6 films, the PM6:Y6 devices contain additional layers such as an ITO and a semi-transparent silver electrode, a PEDOT:PSS layer (HTL) and a PDINN layer (ETL) (cf. section 3.1.2). Literature agrees that these layers individually

provide only negligible TA signals due to low absorption at relevant wavelengths and weak ultrafast responses, especially in the NIR region.[254-257] Nevertheless, their combined presence in a device can lead to microcavity effects, such as optical interference, reflection and scattering. Here, the probe beam interferes with itself after multiple partial reflections at all interfaces within the multilayer stack, leading to spectral modulation of the transmitted probe. This spectral modulation varies across the spectrum as microcavity effects are wavelength dependent. Although this effect is less visible at wavelengths of strong absorption, it is generally stronger in the NIR, because the total absorption in this region is less and the probe wavelength is comparable to the optical path length of the device stack from one electrode to the other.[256-258]

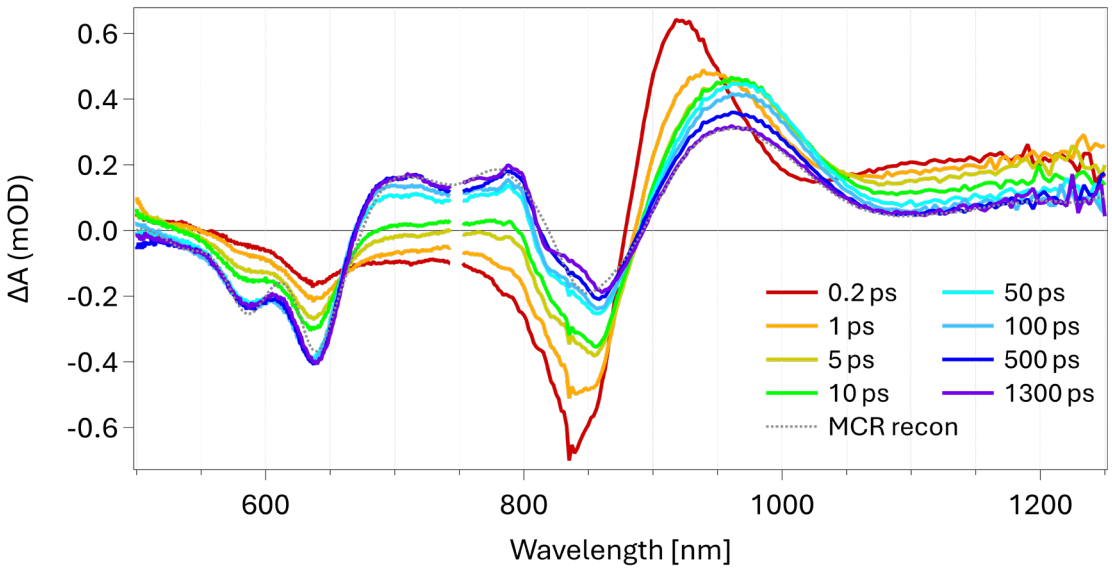

Figure 6-20: TA spectra of a PM6:Y6 device excited at 800 nm for a series of pump-probe delays. The late-time spectrum at 1300 ps after photoexcitation was reconstructed (dotted line) using the spectral components and their respective dynamics obtained by MCR analysis.

As explained later in this section under 'Spectral Deconvolution', the contribution of a charged-induced electroabsorption (EA) signal cannot be fully excluded and can in principle return a signal response in this region. In this context, the observed spectral features of the PM6:Y6 device in the NIR region could be explained by the combined influence of microcavity effects with an EA contribution. The EA response does not produce a uniform shift of the entire absorption spectrum but rather causes

wavelength-dependent changes whose shape and size is determined by the underlying absorption profile.[243,259] When combined with microcavity-induced spectral modulation, which is able to shift, broaden or compress spectral features, this leads to differences between device and film measurements. Spectral features such as the absorption signal of interfacial PM6:Y6 charges peaks at 980 nm in the PM6:Y6 film, while it appears blueshifted in the device at 955 nm. Furthermore, the PIA signal attributed to neat Y6 charges in films starts at around 1120 nm and reaches its maximum near 1550 nm. There is a possibility that in devices, this signal could start to appear at shorter wavelengths, i.e. between 1050 and 1100 nm. The combined influence of EA and microcavity effects thus could explain both, the persistent broad NIR absorption and the altered spectral positions observed in the device TA spectra.

The TA spectra of the PM6:Y6 device after 610 nm excitation are shown in Figure 6-21. At 0.2 ps, the visible GSB directly exhibits a shape characteristic for PM6 and similar to the PM6:Y6 film during 610 nm excitation. The absorption signal at 930 nm already appears broadened, with a shoulder extending towards higher wavelengths. This indicates the initial presence of PM6 excitons, as expected during excitation of both donor and acceptor. While the PIA of the PM6 exciton rapidly decreases, the absorption signal at 930 nm shifts towards higher wavelength, indicating an ultrafast formation of PM6:Y6 charges. When comparing with the TA spectra of the PM6:Y6 film excited at 610 nm (cf. section 6.2.4.1, Figure 6-13), the NIR region at later times exhibits a smaller but still present signal decrease than for the film. Between 50 ps and 1300 ps, the NIR peak around 1000 nm exhibits half of the amplitude-loss for the device that was observable for the film. Nevertheless, no simultaneous signal loss in the visible range was detected in neither of the two measurements. This observation together with the results presented later through this chapter point towards a real spectral indication of population decrease in the 610 nm-excited film, even though an unnatural contribution cannot fully be excluded.

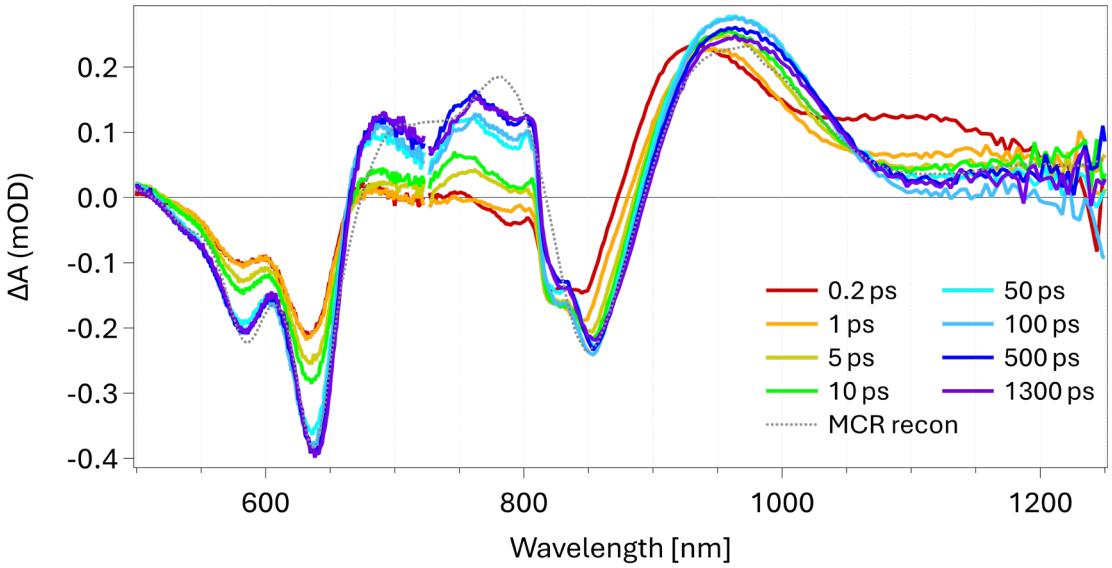

Figure 6-21: TA spectra of a PM6:Y6 device excited at 610 nm for a series of pump-probe delays. The late-time spectrum at 1300 ps after photoexcitation was reconstructed (dotted line) using the spectral components and their respective dynamics obtained by MCR analysis.

Similar to the TA spectra of the PM6:Y6 device at 800 nm excitation, also the spectra of 610 nm exhibit an edge effect of the notch filter. It appears at around 800 nm in the spectra, observable as a sharp feature in the adjacent peaks. In contrast to 400 nm and 800 nm excitation, the spectral region between the PM6 GSB and the Y6 GSB exhibits a shape that closely resembles that of the PM6:Y6 film during 610 nm excitation. The shoulder around 780 nm appears more pronounced under this excitation condition. Similar to the 800 nm excitation, the NIR region reveals a broad microcavity-induced absorption modulation in combination with a delayed EA feature, as explained later under ' Spectral Deconvolution'. This feature overlaps at early times with the PIA signal of PM6, since both donor and acceptor are excited at 610 nm.

The TA spectra during 400 nm excitation (cf. Figure 6-22) exhibit an initial PM6 characteristic GSB in the visible due to the formation of PM6 excitons. The overall shape closely matches the early-time signal during 400 nm excitation of the PM6:Y6 film. Also here, the spectral region near 800 nm could be affected by a notch filter artefact, even though this region appears less sharp and unnatural. After 400 nm, the spectral shift in the NIR and the growth of a positive absorption feature between both GSB signals over time exhibit a rapid formation of interfacial charges. The NIR region

starting of 1050 nm indicates the presence of PM6 exciton absorption at early times before rapidly decreasing.

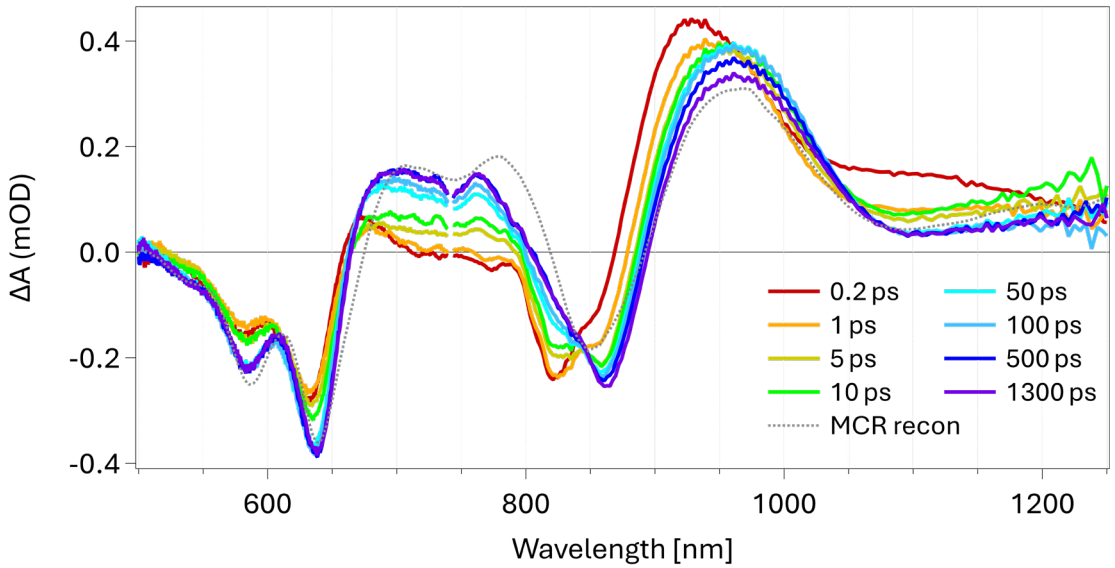

Figure 6-22: TA spectra of a PM6:Y6 device excited at 400 nm for a series of pump-probe delays. The late-time spectrum at 1300 ps after photoexcitation was reconstructed (dotted line) using the spectral components and their respective dynamics obtained by MCR analysis.

Spectral Deconvolution

The spectral components used for the deconvolution of the TA spectra of the PM6:Y6 device is shown in Figure 6-23 and based on the results of the previous sections. Due to the wavelength-range in the NIR during the TA measurements of the device, spectra are limited to 1250 nm, which prevents a consideration of triplet states. Instead, an additional feature for electroabsorption is introduced which was extracted by the differential of the late-time spectrum of the PM6:Y6 film and of the PM6:Y6 device under identical excitation and at open circuit conditions (cf. Figure 6-24).

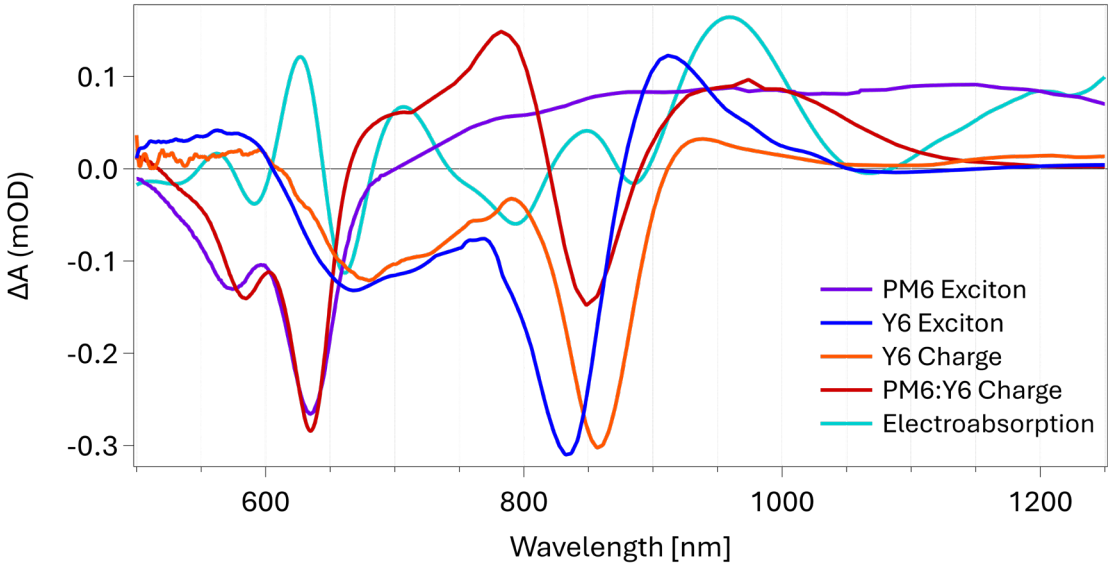

Figure 6-23: Spectral shapes of species present in the device TA spectra: singlet PM6 exciton (purple), singlet Y6 exciton (blue), neat Y6 charge (orange), PM6:Y6 charge (red) and the directional electroabsorption signal (turquoise).

In literature, also other methods are used for estimating EA contributions like an approach based on first and second derivative of the steady-state absorption spectrum or a direct field-modulation of the film.[219,260] In contrast, the method used here follows the same principle as for the DCV2-5T data (cf. sections 5.2.2.1 & 5.2.2.2): local internal fields from photogenerated charges are also present in films but are distributed over many orientations and the associated EA evolves in parallel with the charge population. This EA contribution is spectrally superimposed with and kinetically correlated to the charge signal. Within the fit tolerance, its contribution is

most likely already captured within the charge spectrum.[234,235] In contrast, the presence of electrodes provides a preferred axis that biases these photoinduced fields and increases the net EA amplitude. This results in a directional internal field that induces a Stark shift and modulates the TA spectra, making a consideration as an additional spectral feature necessary. This approach is supported by Sahoo, et al. [237] and Jasinskas, et al. [236], demonstrating that field-induced EA features in organic device architectures can be robustly probed and interpreted and that the device-specific EA is dominated by the directional field across the active layer. The EA spectral shape in the visible was additionally justified by the EA signal of the PM6:Y6 device extracted from EDA prior to excitation (cf. section 6.2.5). However, it is important to note the limitations of the approach used here. As shown by Liu, et al. [219], optical interference and microcavity effects in multilayer device stacks can introduce additional spectral features or distortions, particularly in the NIR region. These effects overlap with the EA signal, limiting the ability to extract a pure field-induced EA spectrum in the NIR region. Therefore, it is assumed that the estimation of the EA signal also compensates for the spectral modulation in the NIR. Since an EA response is likely to be weaker in the NIR than in the visible range, only a part of the NIR signal is expected to be EA-induced.

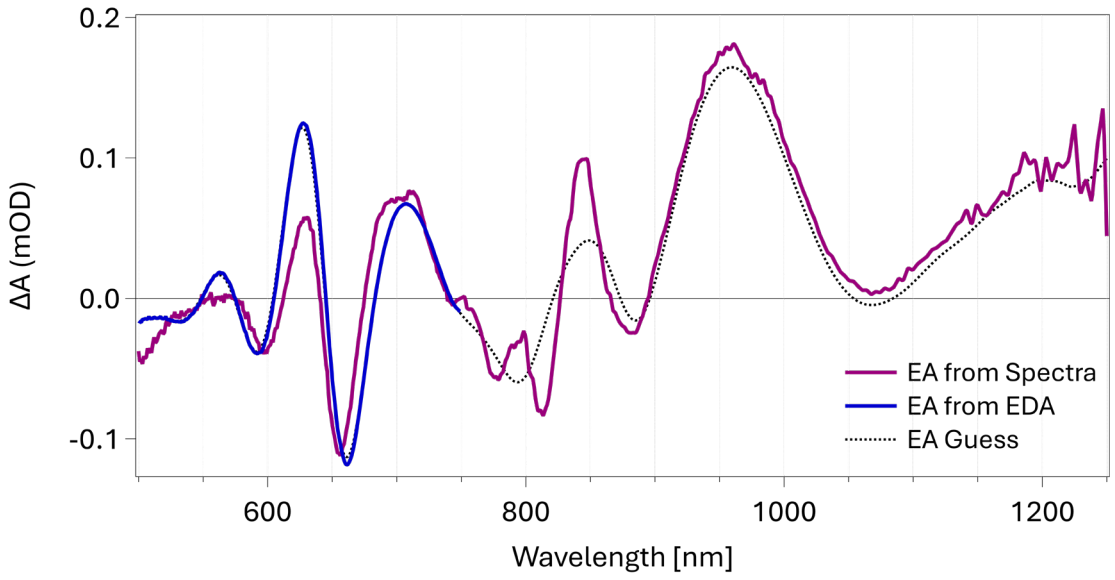

Figure 6-24: Derivation of the spectral shape of electroabsorption (dotted) from the differential late-time spectra of PM6:Y6 film and device (fuchsia) and the electroabsorption of the PM6:Y6 device in EDA prior to excitation (blue).

The MCR analysis for 800 nm excitation in Figure 6-25 is consistent with the previously made observations. A strong Y6 exciton population is observed, while no PM6 exciton signal is present during exclusive excitation of the acceptor material. The rapid decrease of the Y6 exciton population leads to the formation of both neat Y6 charges and interfacial PM6:Y6 charges. Within the first several picoseconds, the population of neat Y6 charges rapidly decreases and further accelerates the formation of interfacial charges PM6:Y6 charges by hole transfer from the Y6 donor group to PM6. After around 40 ps, the PM:Y6 charge population approaches a plateau, while the neat Y6 charge signal vanishes. This indicates the formation of neat Y6 charges as an intermediate state for PM6:Y6 charge formation, besides direct formation via Y6 excitons. The EA trace arises delayed within the first 10 ps, indicating separation of charge carriers.

400 nm excitation leads to the formation of both PM6 and Y6 excitons. The MCR analysis shows similar dynamics for both excitons, originating from a comparable excitation ratio of donor and acceptor. In contrast to the other excitation wavelengths, no neat Y6 charge formation is observed. The PM6:Y6 charges initially rise faster than under 800 nm excitation (τ_1 = 0.7 ps, τ_2 = 14.9 ps) but later follow a similar dynamical path. The EA signal appears more rapid when compared to 800 nm excitation, indicating a slightly faster initial charge separation when excited with excess energy. Time constants of the PM6:Y6 device obtained during MCR analysis are displayed in Table S 6-4.

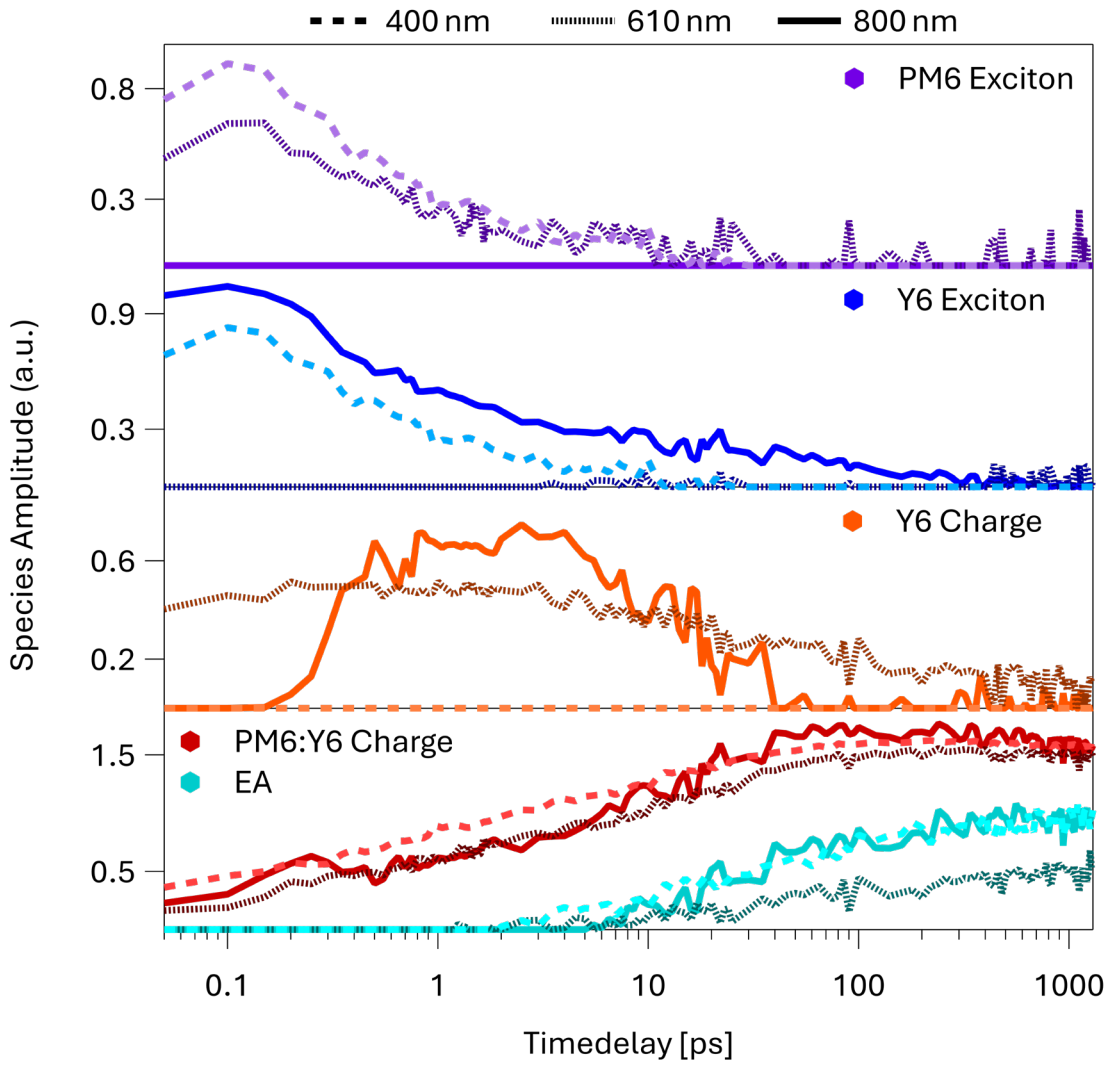

Figure 6-25: Time-resolved relative contribution to the measured ΔA of each species: singlet PM6 exciton (purple), singlet Y6 exciton (blue), neat Y6 charge (orange), PM6:Y6 charge (red) and the directional electroabsorption signal (turquoise), present in a PM6:Y6 device and obtained using MCR.

Under 610 nm excitation, MCR analysis suggest the initial presence of PM6 excitons but no signal of Y6 excitons was observed. Since both donor and acceptor get excited at 610 nm, the presence of Y6 excitons is also expected, hence this is considered an artefact of the deconvolution. It most likely arises from an overlap or partial misattribution with neat Y6 charges during MCR analysis. The neat Y6 charge signal in the PM6:Y6 device is initially present, which was neither the case during 800 nm excitation of the device nor could it be observed in the PM6:Y6 film spectra. Furthermore, the formation of neat Y6 chares scales with the degree of intermolecular coupling and is thus favoured in aggregated Y6. Since 610 nm excites also a significant

amount of unaggregated Y6[188], which is negligible during 800 nm excitation, neat Y6 charge formation is expected to be lower for 610 nm, as it was previously observed for PM6:Y6 and PS:Y6 films too. However, the neat Y6 charge population during 610 nm excitation appears comparably strong to 800 nm during mid times, suggesting an overestimation of the neat Y6 charge contribution, while simultaneously underestimating the Y6 exciton population. Neat Y6 charges in 610 nm are expected to occur comparable in chape but reduced in amplitude, in comparison to 800 nm excitation. The interfacial PM6:Y6 charge formation appears to be similar to that at 800 nm within the first picoseconds. Afterwards, 610 nm excitation exhibits a slightly lower amplitude. Notably, the EA dynamics at 610 nm appear significantly slower and exhibit a reduced slope compared to both other excitation wavelengths, potentially reflecting less efficient CS.

Transient absorption data of PM6:Y6 samples exhibit a lot of similarities between films and devices at the respective incident photon energy. 400 nm excitation revealed a comparable population ratio of both PM6 and Y6 excitons. A stronger rapid formation of PM6:Y6 charges was observed in the absence of a neat Y6 charge population for both film and device. Mainly unaggregated Y6 is excited at 400 nm. Due to the more disordered local packing and the reduced π–π stacking in unaggregated domains, the formation of neat charges is less likely here.[91] During 800 nm excitation, rapid formation of interfacial charges was less than for 400 nm, while the excitation of aggregated Y6 led to a fast formation of neat Y6 charges in both film and device. The declining population of neat Y6 charges during mid times led to a strong population increase in PM6:Y6 charges. The maximum neat Y6 charge population thereby correlated with the steepness of the population increase of PM6:Y6 charges during mid times. While it was most pronounced during 800 nm excitation, it appeared reduced during 610 nm and was absent during 400 nm excitation.

However, several differences between PM6:Y6 film and device were observed. The device consistently achieved a stronger formation of both interfacial PM6:Y6 charges (cf. Figure 6-26) and neat Y6 charges (cf. Figure S 6-4) at the respective excitation wavelength, while a neat Y6 charge signal remained absent for 400 nm excitation. Furthermore, the formation of PM6:Y6 charges got slightly accelerated, besides the

dynamics in Figure 6-26 and Figure S 6-4 also indicated by the smaller time constants of the devices (cf. Table S 6-3) in comparison to those of the films (cf. Table S 6-2). The most significant difference was observed for 610 nm excitation. Exciting PM6:Y6 at 610 nm should represent a mixture of 400 nm and 800 nm, as it excites the donor PM6 and both aggregated and unaggregated Y6 domains. While this 'mixed behaviour' was observable for excitons and neat Y6 charges in both PM6:Y6 and PS:Y6 samples, 610 nm revealed a significant divergence in PM6:Y6 charge evolution. Not only was the formation of interfacial charges reduced when compared to the other excitation wavelengths, within 200 ps a significant decrease of PM6:Y6 charge population was observable. The presence of electrodes in the device introduces a built-in potential that helps stabilising PM6:Y6 charge carriers and leads to a more persistent PM6:Y6 charge signal during 610 nm excitation.[70] As a result, the PM6:Y6 device exhibits a similar interfacial charge population during 610 nm excitation, as it was the case for 400 nm and 800 nm. However, the significantly lower evolution of the EA signal suggests a less strong charge separation, indicating a localisation issue for 610 nm excitation.

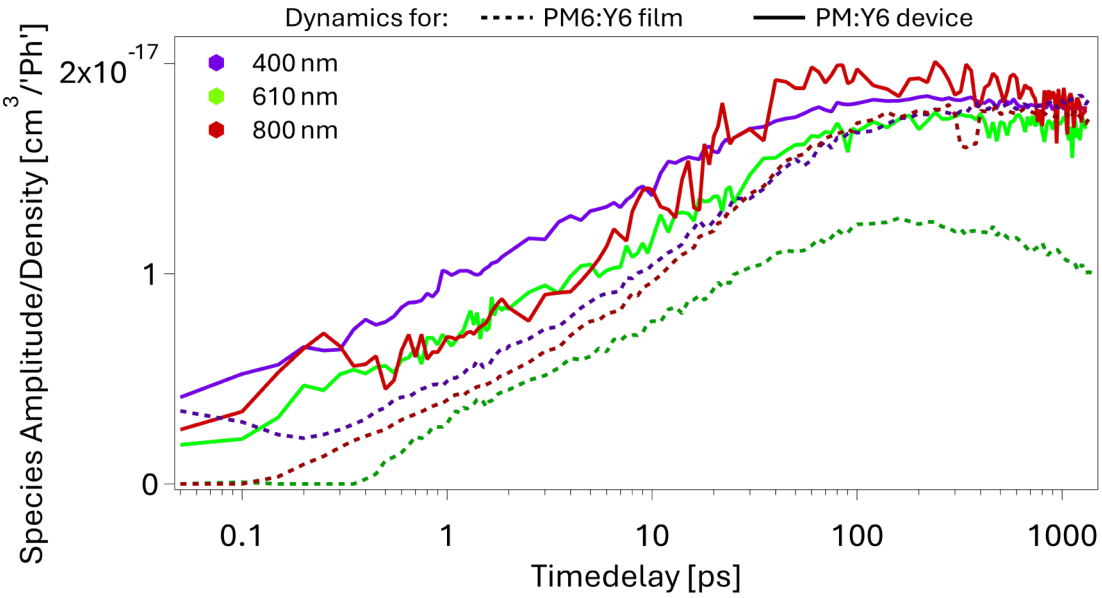

Figure 6-26: Time-resolved relative contribution to the measured ΔA divided by the excitation density of the PM6:Y6 charge species in the linear ($8.8 \cdot 10^{16}$ 'Ph'·cm^{-3}) excitation regime for 400 nm (purple), 610 nm (green) and 800 nm (red) excitation present in the PM6:Y6 film (dashed lines) and device (full lines) and obtained using MCR.

The PM6:Y6 charge population during 800 nm excitation gets stabilised due to delocalisation in aggregated domains.[36] This is only partly the case for 610 nm, but not at all for 400 nm excitation. Consequently, the behaviour of 610 nm seems plausible, whereas the behaviour of 400 nm raises questions. While 800 nm excites the low energy Y6 aggregate I, 610 nm excites a mixture of aggregate I and II together with unaggregated Y6, where the initially present excitations are more localised on average.[44,188] While intra-aggregate relaxation is expected, inter-aggregate transfer into aggregate I depends on morphological connectivity and is assumed to occur within the first 100 ps[195], which favours rapid cooling and localisation within the micro-domain which was initially excited. Nevertheless, 400 nm does not exhibit such behaviour, but is rather similar to 800 nm. This strongly suggests an influence of excess-energy during 400 nm excitation. These higher-lying excited states are transiently more delocalised, which increases their effective migration distance, allowing downhill funnelling into the energetically lower Y6 aggregate I prior to full localisation when connected pathways are present, even though efficient charge generation does not require excess energy.[192,195,240] Once excitons reached aggregate I, they follow the same pathway as 800 nm excitation, explaining similar behaviour under both excitation wavelengths. This funnelling most likely occurs towards nearby D–A interfaces[44], while the excitation at 800 nm leads to an exciton formation across the entire Y6 aggregate I. Nevertheless, this pathway is not restricted to the excess-energy excitation at 400 nm and can also occur after 610 nm excitation, providing that the initial excitations have access to connected pathways leading to lower-energy Y6 aggregate I. The crucial factor is a nanoscale connectivity to these more favourable sites. Because higher-lying excitations are transiently more delocalised, the probability and rate of reaching such sites before thermalisation are greater at 40 nm than at 610 nm excitation.

Nonlinearity

To evaluate the effects of high fluence excitation in PM6:Y6 devices, TA measurements were performed under nonlinear excitation conditions at an absorbed photon density of $3.2 \cdot 10^{18}$ 'Ph'·cm^{-3} (cf. section 3.5) for 800 nm (cf. Figure S 6-5), 610 nm (cf. Figure S 6-6) and 400 nm excitation (cf. Figure S 6-7). The dynamics of the excited states species (cf. Figure 6-27) were obtained by MCR analysis, using the spectral shapes from the previous section. Relative to the excitation density (cf. Figure S 6-8), no general acceleration of the exciton population decay was observable.

A major difference is observed for the rise and decay of both neat Y6 and interfacial PM6:Y6 charge dynamics with time constants displayed in Table S 6-4. In the nonlinear regime, all charge populations evolved on similar timescales as observed for the linear regime. For neat Y6 charges, also the population decrease occurred on relatively similar timescales. This indicates that the effect of nonlinearity was for neat Y6 charges only observable in an overall reduced population amplitude, relative to the density of absorbed photons. After the similar onset of the PM6:Y6 charge formation observed in the nonlinear regime for all excitation wavelengths, all interfacial charge populations start to plateau and decrease relatively fast within the first tens of picoseconds. This effect appears first during 400 nm excitation, while the population of PM6:Y6 charges decreases delayed for 610 nm and 800 nm excitation. Nevertheless, PM6:Y6 charge populations approach similar amplitudes at late times for all three excitation wavelengths. This is comparable to the converging dynamics under linear conditions, while, relative to the excitation density, the overall charge loss is significantly greater at nonlinear excitation conditions. This is attributed to non-geminate recombination which is increased at high carrier density.

The EA signal is most prominent during 800 nm excitation since separation-capable geometries are directly accessible. Within the first 100 ps, the 800 nm EA signal plateaus before slightly decreasing at late times. This is attributed to the higher density of separated charges, leading to non-geminate recombination. When reaching a specific density of separated charges, non-geminate recombination equalises further charge separation and thus 'maintaining' a roughly comparable number of separated charge carriers, leading to a nearly constant EA signal height. In contrast, both 400 nm

and 610 nm excitation exhibit a different EA shape. The rise of the EA component during 610 nm excitation appears more linear and resembles the same behaviour as under linear excitation conditions. At 400 nm, which showed similar behaviour like 800 nm in the linear, now exhibits EA dynamics more comparable to 610 nm. A t high fluence, the rapid funnelling channel from unaggregated Y6 into aggregated domains near D–A interfaces becomes transiently saturated by the high density of excited states.[261] Consequently, slower, diffusion-limited routes within unaggregated Y6 domains dominate, resulting in an EA response for 400 nm that resemble that at 610 nm.

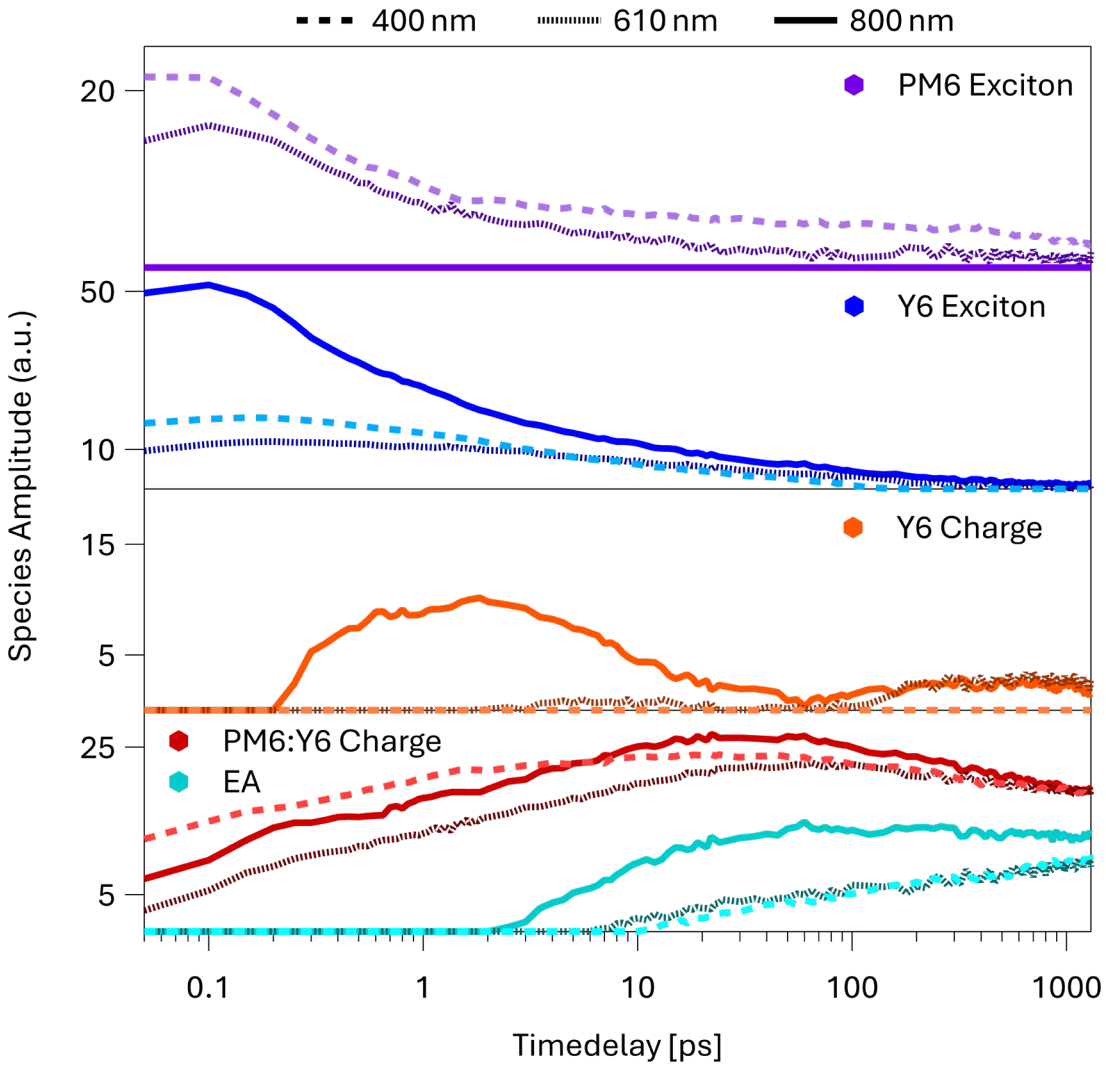

Figure 6-27: Time-resolved relative contribution to the measured ΔA of each species: singlet PM6 exciton (purple), singlet Y6 exciton (blue), neat Y6 charge (orange), PM6:Y6 charge (red) and the directional electroabsorption.

6.2.5. Electromodulated Differential Absorption

The results achieved via EDA spectroscopy are analysed and transformed into a time-resolved voltagedrop, which was normalised to the capacitance of the PM6:Y6 device, the applied external bias and the number of extracted charges during the measurement. Figure 6-28 displays the normalised voltagedrop under 400 nm, 610 nm and 800 nm excitation and at a reverse bias of −2 V. The voltagedrop starts after approximately 4 ps. Between 11–360 ps, the 800 nm excitation exhibits a slightly slower voltagedrop when compared to the other two excitation wavelengths. Since only 800 nm is limited to Y6 excitation, this delay during mid times is attributed to the Y6 pathway for charge generation. It most likely arises due to the diffusion of Y6 excitons within neat Y6 domains to the D–A interface.[64] At later times, the dynamics for 800 nm converge with those of 400 nm and 610 nm excitation, suggesting that after initial kinetical differences like exciton diffusion, following processes take place with similar efficiency.

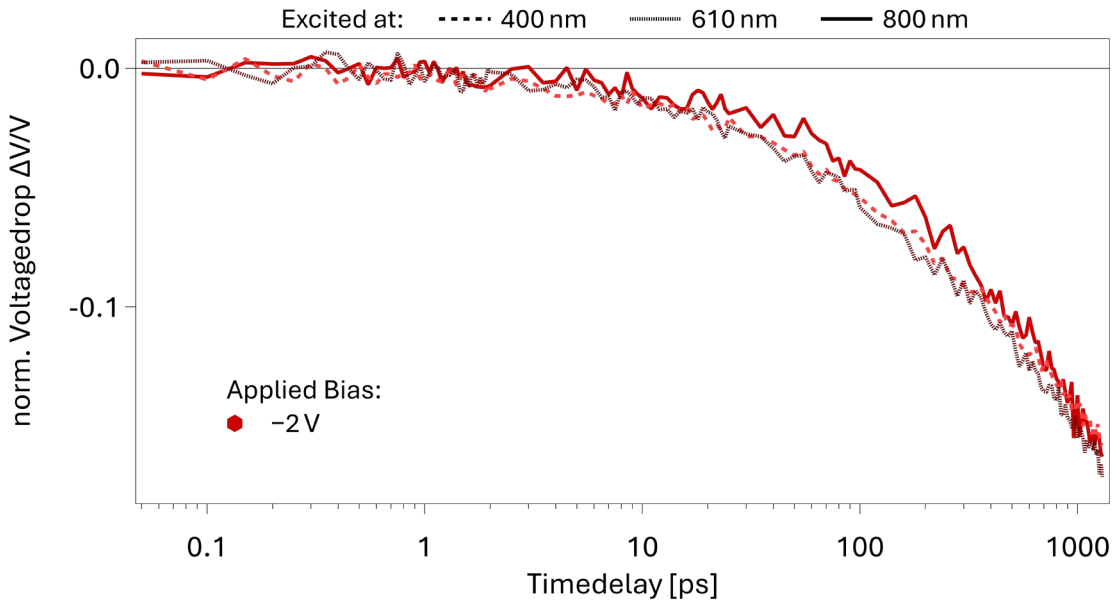

Figure 6-28: Normalised voltagedrop curves of a PM6:Y6 device obtained via EDA spectroscopy at −2 V reverse bias under 400 nm (dotted), 610 nm (dashed) and 800 nm (full) excitation.

When applying higher reverse biases (cf. Figure 6-29), several differences are of the PM6:Y6 device are observable. Although the voltagedrop was normalised with the capacitance and the number of extracted charges (cf. Table S 6-6), it still exhibits

noticeable field dependence. Gillett, et al. [64] demonstrated that increased fields can accelerate charge separation by lowering the effective barrier for the separation of CT states. This aligns with the observation made during EDA spectroscopy, that a stronger electric field lowers the Coulomb binding energy of CT states and increases the probability of their separation into FC. The differences in voltagedrop are most prominent between −2 V and −4 V. When further increasing the applied bias, their relative influence becomes less pronounced, while between −6 V and −8 V, the lowest bias-induced voltagedrop change was observed. This indicates a saturation of the field-induced acceleration of charge extraction. Also, the onset time of the voltagedrop shifts to earlier delays as the bias increases. At −2 V, the voltagedrop starts at around 3–4 ps, while it is already clearly observable within the first picosecond at −8 V. This indicates that stronger electric fields not only support CS but also increases their drift velocity towards the electrodes and thus accelerates carrier extraction. This is quantitatively reflected in the bias-dependent time constants obtained from biexponential fits to the voltagedrop curves. For all three excitation wavelengths, time constants shift towards earlier times with an increasing reverse bias, which indicates a more rapid carrier extraction at higher fields. All EDA time constants are displayed in Table S 6-5.

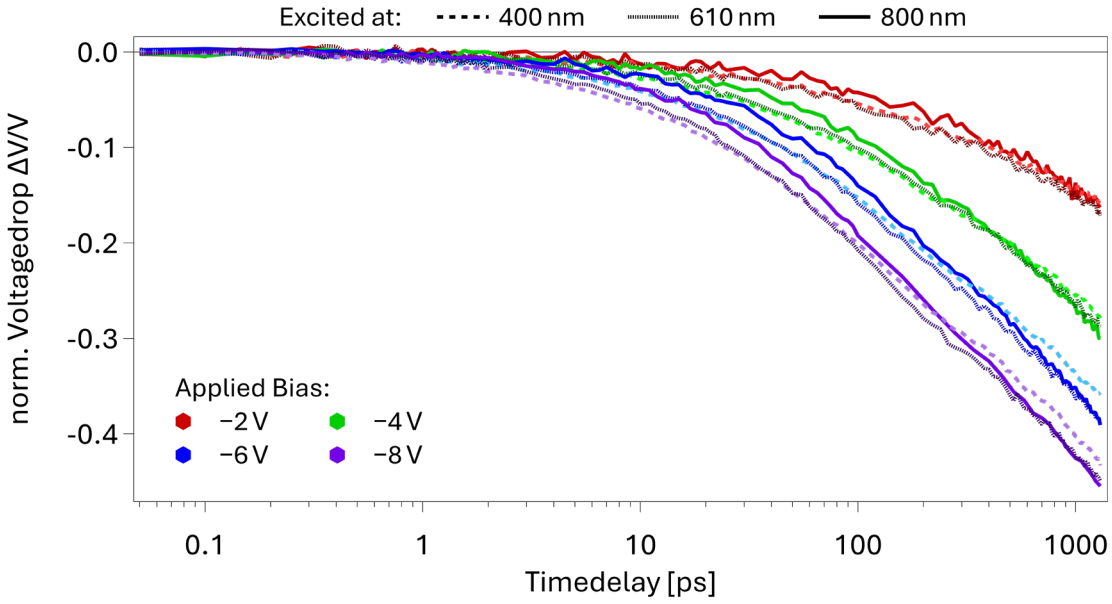

Figure 6-29: Normalised voltagedrop curves of a PM6:Y6 device obtained via EDA spectroscopy at −2 V (red), −4 V (green), −6 V (blue) and −8 V (purple) reverse bias under 400 nm (dotted), 610 nm (dashed) and 800 nm (full) excitation.

For all excitation wavelengths, the respective onset time is similar, arising from excitons formed at or close to a D–A interface. Afterwards, only 800 nm exhibits this temporally slower voltagedrop, while 400 nm and 610 nm are similarly fast. When the applied bias is increased, the deviation observed for 800 nm excitation during mid times changes. With an increasing bias, it becomes more pronounced and shifts towards earlier times, while its duration shortens. This is associated with a diffusion bottleneck since exciton migration cannot be accelerated by an electric field. While Y6 domains are excited at all three excitation wavelengths, 400 nm and 610 nm also simultaneously excite the PM6 donor. This pathway for charge generation offers an additional source for charge carrier formation. This channel provides an additional source of carriers whose early-time separation is more field sensitive than diffusion limited. When a higher bias is applied, the voltagedrop onset shifts towards earlier times which indicates a stronger field dependence.

The voltagedrop curves exhibit also wavelength-dependent behaviour at later times. Due to the normalisation all voltagedrop curves approach the same final value of $\Delta V/V = -1$ after a sufficiently long time, which is well beyond the time window observable by EDA. At higher biases, the 800 nm trace remains faster and increasingly deviates from that of 400 nm and 610 nm excitation within the ultrafast time window. 400 nm and 610 nm, however, appear slower at later times, the further the reverse bias is increased, while it is most prominent during 400 nm and less during 610 nm excitation. This can be explained by the presence of a minority population of the excitons which are generated in donor-rich or more disordered regions. While the majority population is quickly separated, extracted and dominates the early- and mid-times window, these minority must first diffuse to a D–A interface, located in regions with limited connectivity to percolation pathways. This results in a slower extraction of this charge population fraction, even when strong electric fields are present.[50,64,219]

This is further supported by the EQEs, estimated from the electrical measurements performed in association with EDA spectroscopy and displayed in Table 6-2, using equations (5-1) to (5-4). When increasing the external bias from −2 V to −8 V, the EQE increases from 83.2 % to 91.7 % for 800 nm, from 68.2 % to 77.6 % for 610 nm and from 35.1 % to 40.2 % for 400 nm, corresponding to relative gains of 10.2 %, 13.7 % and

14.4 %. This relative efficiency gains are considered modest with the majority occurring from −2 V to −4 V. Nevertheless, the efficiency gain for 610 nm and 400 nm is 35 % and 42 % higher, respectively, when considered in relation to the efficiency gain for 800 nm excitation. This supports a stronger field dependence for the PM6-excitation channels due to generation pathways from less favourable regions. Although all charges ultimately form at D–A interfaces, the excitation wavelength sets where excitons are initially created and how far they must migrate to reach an interface. At 800 nm, excitons are generated in Y6 aggregates that show longer exciton diffusion and increased delocalisation, which favours rapid interface encounter.[44] At 400 nm, excitons are generated mainly in PM6, which has a shorter exciton diffusion length[41], so a larger fraction must travel through donor-rich regions before reaching an interface, increasing the contribution of field-assisted late-time separation and extraction. This effect is stronger for 400 nm and weaker for 610 nm, due to the respective donor-excitation contributions and the shorter exciton diffusion length for PM6 compared to Y6.

Table 6-2: EQE of the PM6:Y6 device extracted from EDA under various biases with a semi-transparent Ag electrode and the relative efficiency gain ΔEG between two biases for 800 nm, 610 nm and 400 nm.

	EQE_{800nm} (%)	EQE_{610nm} (%)	EQE_{400nm} (%)
−2 V	83.2	68.2	35.1
−4 V	87.0	73.3	37.7
−6 V	89.1	75.8	38.9
−8 V	91.7	77.6	40.2
ΔEG_{2-4}	4.5	7.4	7.4
ΔEG_{4-6}	2.5	3.5	3.1
ΔEG_{6-8}	2.9	2.3	3.3
ΔEG_{2-8}	10.2	13.7	14.4

6.2.6. Optical-Pump Terahertz-Probe Spectroscopy

During optical pump terahertz probe (OPTP) spectroscopy, a PM6:Y6 thick film (1 µm) was investigated, excited at 400 nm, 610 nm and 800 nm. The change in transmittance ΔT/T (cf. Figure 6-30) was normalised, while a recovery of ΔT/T from −1 towards 0 is interpreted as a time-resolved decay of the pump-induced THz response, caused by the THz-active carrier population. At 800 nm excitation, THz dynamics change only slightly from −1 to around −0.8 within the measured time window, indicating a stable THz-active population with only minor losses. This weak decay agrees with the persisting charge population observed in TA for 800 nm excitation of the PM6:Y6 film. At 400 nm, ΔT/T is noisier but follows a comparable trend, showing a modest decrease and approaching −0.6 at late times. The THz dynamics for 610 nm excitation are also consistent with the observations made during TA spectroscopy. 610 nm THz dynamics decrease fast towards −0.4 within the first picoseconds, then stabilises and approaches −0.2 at late times, suggesting a strong reduction of the THz-active response due to population loss and/or mobility reduction within the measured time window. This observation matches the results for PM6:Y6 films obtained during TA spectroscopy, showing a significant loss in charge populations.

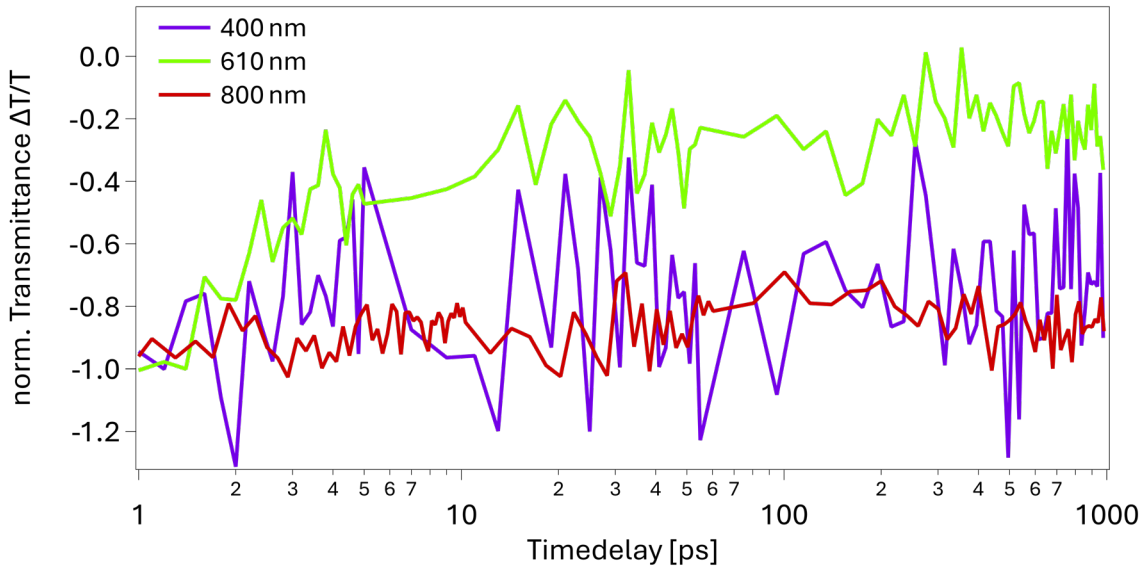

Figure 6-30: Normalised THz dynamics of a PM6:Y6 thick film under 400 nm (purple), 610 nm (green) and 800 nm (red) excitation.

THz conductivity spectra of the same film at representative early and late timedelays was determined using a Drude-Smith model (cf. section 3.7 and Figure S 6-14) to further analyse the degree of carrier localisation and mobility. Here, the real part (Re) gives the in-phase photoconductivity, while the imaginary part (Im) captures the out-of-phase response and indicates partial localisation or backscattering.

For 800 nm excitation (cf. Figure 6-31), the real part of the conductivity remains stable over time and the imaginary part consistently negative, with both showing similar behaviour at early and late time delays. After normalisation, the frequency dependence and magnitude of the imaginary conductivity are characteristic of partially localised but mobile carriers and exhibit no significant changes. This behaviour confirms that the population generated at 800 nm excitation is long-lived and does not undergo significant localisation.

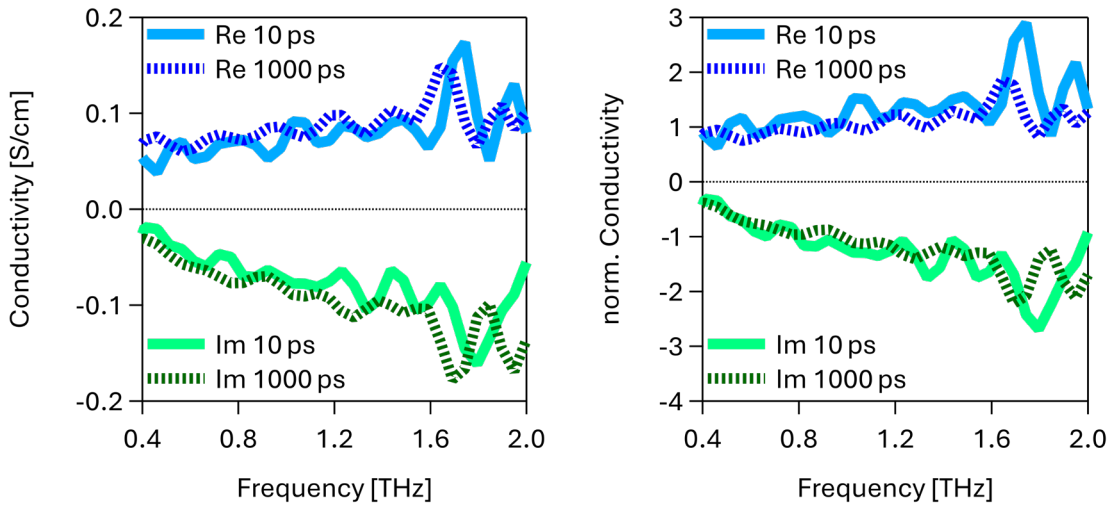

Figure 6-31: Non-normalised (left) and normalised (right) THz conductivity of a PM6:Y6 thick film under 800 nm excitation with the real part (blue) and imaginary part (green) at 10 ps (full) and 1000 ps (dashed) after excitation.

In contrast, 400 nm excitation (cf. Figure 6-32) exhibits a reduction of the real part at late times. After normalisation, the early- and late-time spectra for both Re and Im overlap without a detectable change in shape. This indicates a lower THz-active carrier density at late times, without a detectable change in localisation.

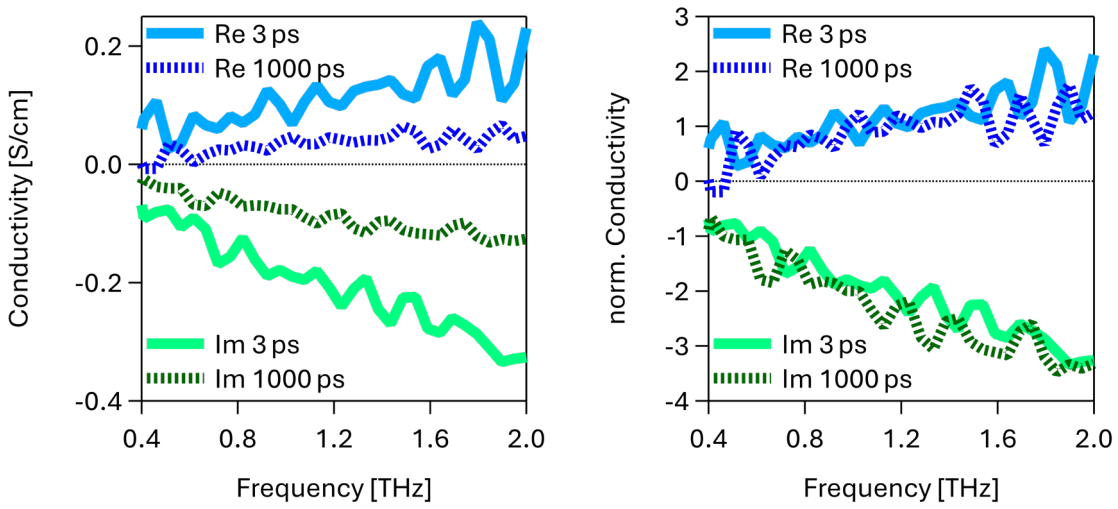

Figure 6-32: Non-normalised (left) and normalised (right) THz conductivity of a PM6:Y6 thick film under 400 nm excitation with the real part (blue) and imaginary part (green) at 3 ps (full) and 1000 ps (dashed) after excitation.

For 610 nm excitation (cf. Figure S 6-13), reliable THz conductivity could only be obtained at early times. It it was not possible to separate a signal from the background noise for the late-time measurement. Consequently, statements about a change in location cannot be reliably made.

When comparing all three excitation wavelengths (cf. Figure 6-33), the normalised Im is similar for 800 nm and 610 nm. However, it is more negative for 400 nm, indicating a stronger backscattering/partial localisation for 400 nm at early times.

This is notable despite the higher excess photon energy at 400 nm and indicates that a larger fraction of carriers is formed in donor-rich or less ordered regions. This agrees with the EDA results, revealing a stronger field dependence at 400 nm and thus a greater contribution from less favourable generation channels.

Both 400 nm and 610 nm excite PM6 and less-delocalised Y6 domains, but 610 nm nevertheless exhibits a rapid ΔT/T decay. At 3 ps, THz dynamics indicate a strong

reduction of the THz-active population for 610 nm, so the surviving early-time response represents carriers from more favourable environments similar to those accessed at 800 nm. In contrast, 400 nm exhibits a mixed contribution of carriers originating from more and less favourable channels. Here, the excess energy accelerates also the slower, less-favourable channels from more localised regions, leading to a mixed contribution of more and less mobile carriers. As a result, this lowers the overall conductivity already at 3 ps. This is further supported by the normalised Im at 1000 ps. Although the THz-active carrier population decreased, the similar normalised Im indicates that the mobility of the remaining carriers persists. Consequently, some fraction of these less mobile carriers would have been expected for 610 nm too. Unfortunately, no reliable late-time conductivity response was extractable for 610 nm at 1000 ps, so no reliable statement can be made here. From a hypothetical point of view, this could nevertheless confirm the small population at late times. The signal-to-noise ratio in OPTP scales linearly with the signal amplitude and only as the square root of averaging. Maintaining a comparable signal-to-noise ratio would in principle require an averaging, which scales approximately with the inverse square of the pump-induced THz amplitude. Hence, the THz field response most likely merged with the background.

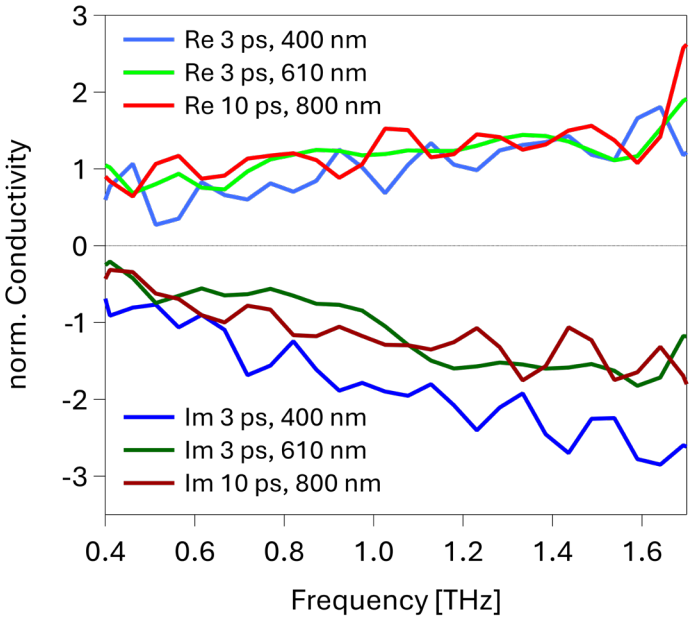

Figure 6-33: Normalised THz conductivity for PM6:Y6 thick film excited at 400 nm, 610 nm & 800 nm.

6.3. Conclusion

Summary

Prior to the blend analysis, PS:Y6 films were measured to isolate Y6-only behaviour and to provide Y6 exciton and neat-Y6 charge signatures for the deconvolution of the PM6:Y6 data. In PS:Y6 the response is determined by aggregation. Excitation at 800 nm addresses aggregated Y6 domains, leading to a rapid formation of neat Y6 charges. Excitation at 400 nm addresses unaggregated Y6 domains with spatially localised excitons, which slows the formation of neat Y6 charges and enables a triplet formation in diluted Y6. Excitation at 610 nm addresses both aggregated and unaggregated Y6 domains, leading to a mixed behaviour in neat Y6 charge formation, between 400 nm and 800 nm excitation.

In PM6:Y6 films, 800 nm excited aggregated Y6 domains, which led to a rapid formation of both interfacial PM6:Y6 and neat Y6 charge carriers, resulting in a strong population of longer-lived interfacial PM6:Y6 charges. At 400 nm, exciton formation takes place in both PM6 and unaggregated Y6 domains. The excess energy of incident photons led to a formation of transiently more delocalised higher-lying excited singlet states, which can increase exciton funnelling from localised unaggregated Y6 regions into delocalised aggregated Y6 region, when they are in reach. This led to PM6:Y6 charge dynamics more comparable to those for 800 nm excitation within the probed time window. At 610 nm, excitons are formed in PM6, but also in aggregated and unaggregated Y6 domains. The absence of higher-excited states decreased the probability of inter-aggregate transfer and left a larger fraction of excitons in less favourable micro-domains. Consequently, a fraction of charge carriers remained in regions of higher localisation, resulting in recombination within ultrafast timescales.

THz dynamics revealed a persistent response of longer-lived carrier population for 800 nm excitation. For 400 nm, the THz response decayed modestly, while the remaining THz-active population did not exhibit a change in mobility. With 610 nm, however, a strong early-time decrease of THz-active population was observed. THz conductivity at early delay reveals a more negative imaginary part for 400 nm than for 800 nm and 610 nm, indicating stronger backscattering or partial localisation for

400 nm. Comparing early and late times for 400 nm and 800 nm, the normalised spectral shapes remain similar, which indicates no additional localisation over time, whereas the absolute response decreases at late times for 400 nm is consistent with a reduced THz-active population. Together with EDA, the THz data indicate that 400 nm represents a broader mix of micro-domains, including more localised channels, whereas 800 nm is dominated by delocalised Y6 regions. At 610 nm excitation, the early-time mobility signature resembles 800 nm, but the carrier population decays rapidly.

In devices, the presence of TL and electrodes not only accelerated early-time formation of PM6:Y6 charges across all three excitation wavelengths, the electrodes-induced electric field also significantly increased the persistence of interfacial PM6:Y6 charges during 610 nm excitation. While all three excitation wavelengths indicated comparable PM6:Y6 populations at late times, the extracted EA response for 400 nm was similar to that for 610 nm and significantly lower than for 800 nm excitation. This was attributed to a saturation of these pathways, making less favourable ones in localised regions more dominant and resulting in a charge carrier behaviour more similar to 610 nm, while the larger proportion of excited PM6 maintained the initially stronger PM6:Y6 charge formation for 400 nm.

Nonlinear excitation densities did not influence the exciton dynamics of the device for the respective excitation wavelength, when compared to the linear regime. The initially present charge population remained similar to the linear, relative to the excitation density, but was followed by significant bimolecular recombination. This indicates strong charge separation. TDCF measurements confirmed this for all three excitation wavelengths. On microsecond timescales, the apparent bimolecular loss was faster after 800 nm excitation, pointing towards a more efficient separation for 800 nm excitation.

For the PM6-excitation pathway, EDA spectroscopy supported an initial rapid formation of PM6:Y6 charges, which most likely originated from interfacial regions but also a significant fraction of delayed separating carriers from PM6 excitation. Due to the excellent performance of PM6:Y6 blends, even under strong reverse bias, the overall bias-driven charge extraction remained modest. However, a higher bias-driven

efficiency increase was revealed for the PM6-excitation pathway for both 400 nm and 610 nm, supporting the assumption that the separation of these charges is intrinsically hindered by the material.

Conclusion

It was demonstrated that ultrafast performance in PM6:Y6 is determined by early access to delocalised Y6 aggregates and by which micro-domains the mobile carrier population is supplied. When excited states reach delocalised domains before localisation, subsequent charge separation and stabilisation benefits. When excitation is limited to more localised or poorly connected regions, rapid losses dominate. When excess-energy leads to the formation of higher-excited states, it can mitigate this limitation by supporting migration into aggregated, more delocalised domains prior to thermalisation and compensate initially unfavourable starting conditions, as long as more favourable regions are within reach of the exciton. This is, however, not limited to excess-energy excitation, even though higher-lying excited states increase the probability of such process due to a higher delocalisation. It is therefore expected that higher-lying excited states exhibit an extended range for inter-aggregate transfer prior to CT state formation. Additionally, excitation through the donor pathway gives a kinetic head start for interfacial charge formation at early times, especially in devices where the built-in field promotes separation. Field-assisted charge extraction occurs even in a high-performing PM6:Y6 device. Here, the electric field improves the extraction of charges originating from less favourable regions to a higher extent, relative to charges from more favourable ones. However, the overall degree of extraction still depends on early access to delocalised environments and the subsequent charge formation and separation. Increasing the electric field can further improve the yield from less favourable sites, but this effect is limited and cannot compensate for intrinsic limitations.

6.4. Appendix

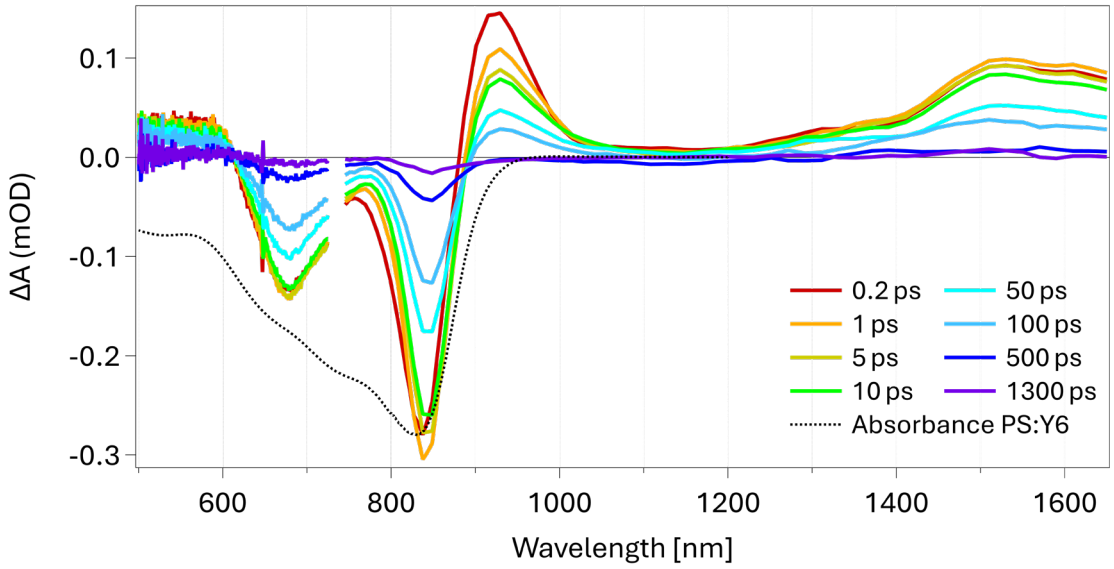

Figure S 6-1: TA spectra of a PS:Y6 thin film excited at 610 nm under linear excitation conditions ($8.8 \cdot 10^{16}$ 'Ph'·cm^{-3})for a series of pump-probe delays.

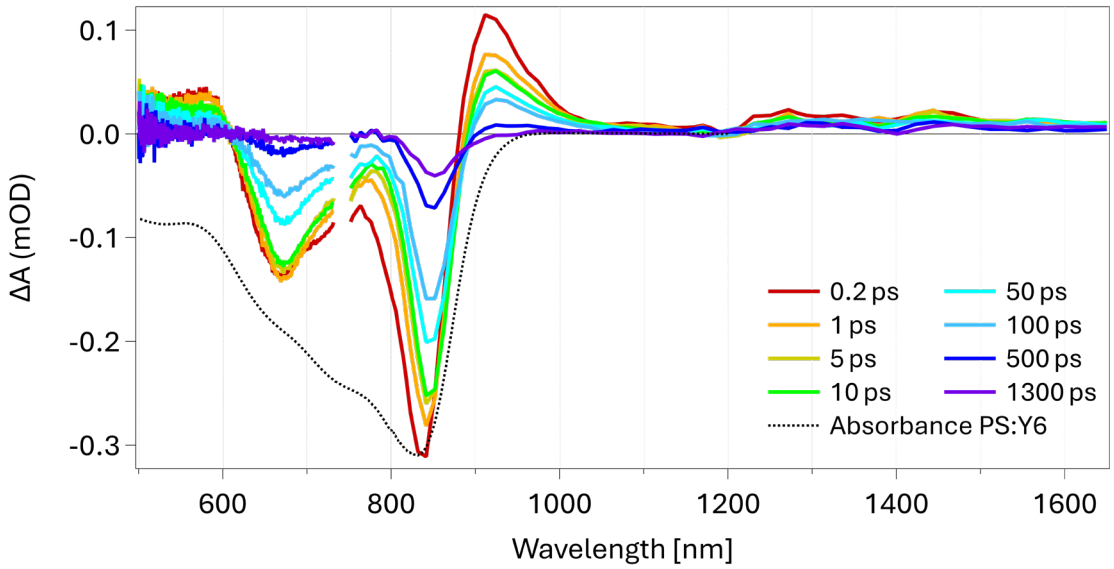

Figure S 6-2: TA spectra of a PS:Y6 thin film excited at 400 nm under linear excitation conditions ($8.8 \cdot 10^{16}$ 'Ph'·cm^{-3})for a series of pump-probe delays.

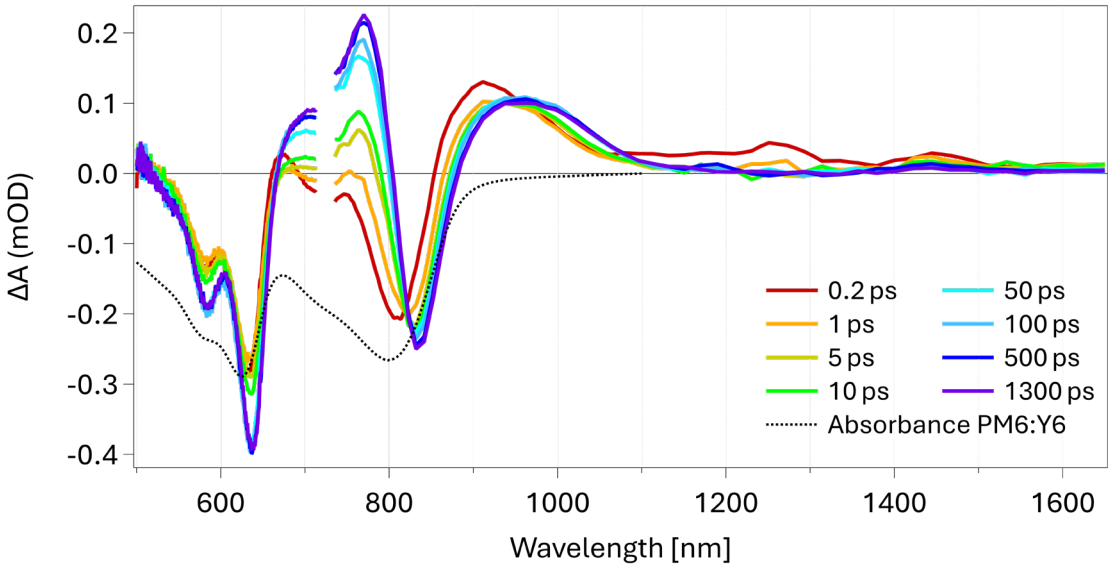

Figure S 6-3: TA spectra of a PM6:Y6 thin film excited at 400 nm under linear excitation conditions ($8.8 \cdot 10^{16}$ 'Ph'·cm^{-3}) for a series of pump-probe delays.

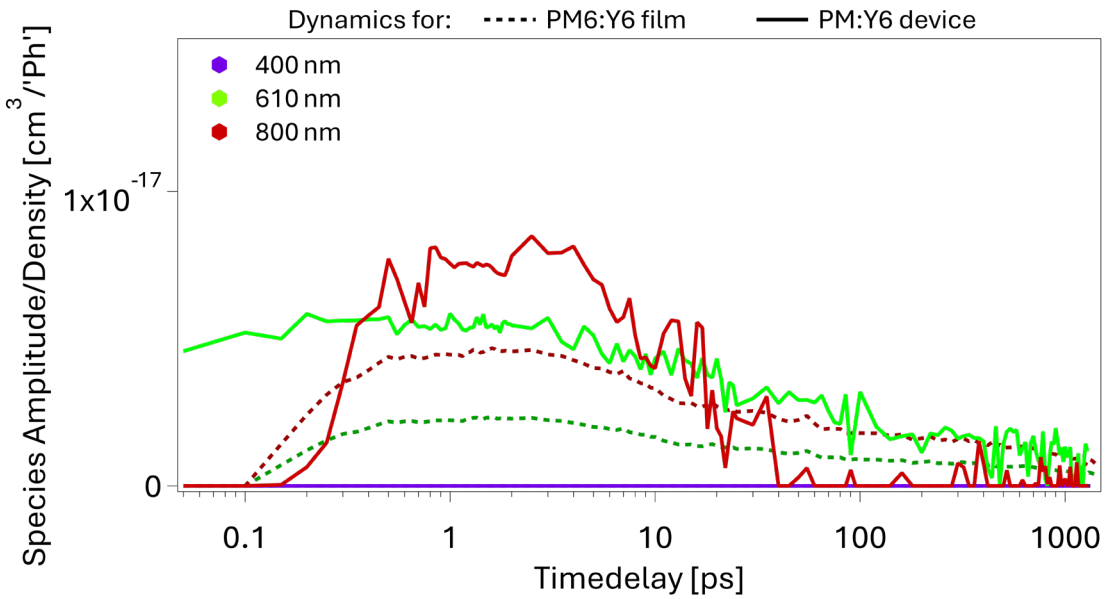

Figure S 6-4: Time-resolved relative contribution to the measured ΔA divided by the excitation density of the neat Y6 charge species in the linear excitation regime ($8.8 \cdot 10^{16}$ 'Ph'·cm^{-3}) for 400 nm (purple), 610 nm (green) and 800 nm (red) excitation present in the PM6:Y6 film (dashed lines) and device (full lines) and obtained using MCR.

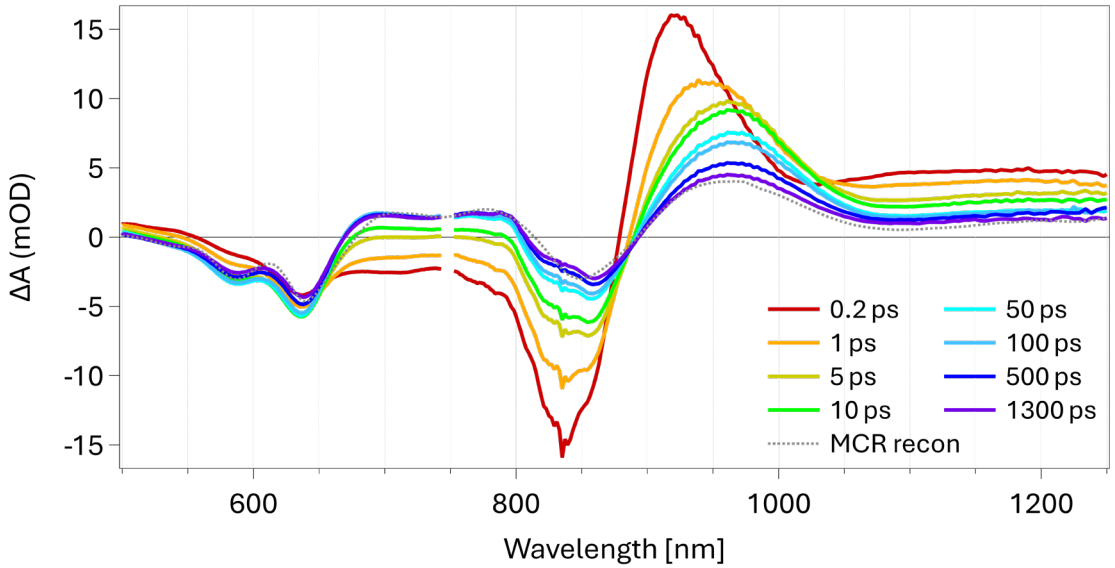

Figure S 6-5: TA spectra of a PM6:Y6 device excited at 800 nm under nonlinear excitation conditions ($3.2 \cdot 10^{18}$ 'Ph'·cm^{-3}) for a series of pump-probe delays.

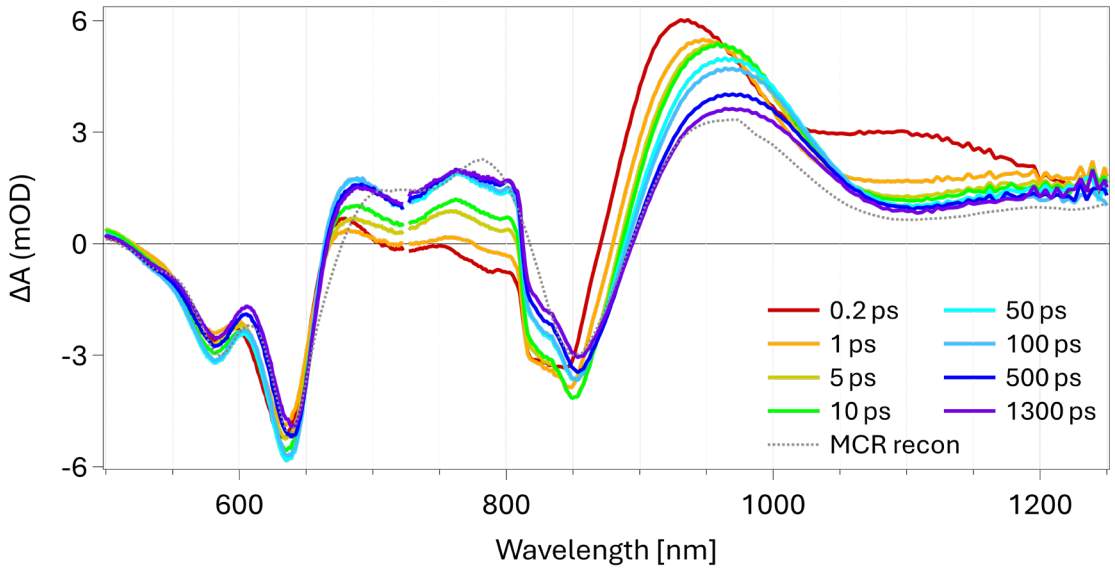

Figure S 6-6: TA spectra of a PM6:Y6 device excited at 610 nm under nonlinear excitation conditions ($3.2 \cdot 10^{18}$ 'Ph'·cm^{-3}) for a series of pump-probe delays.

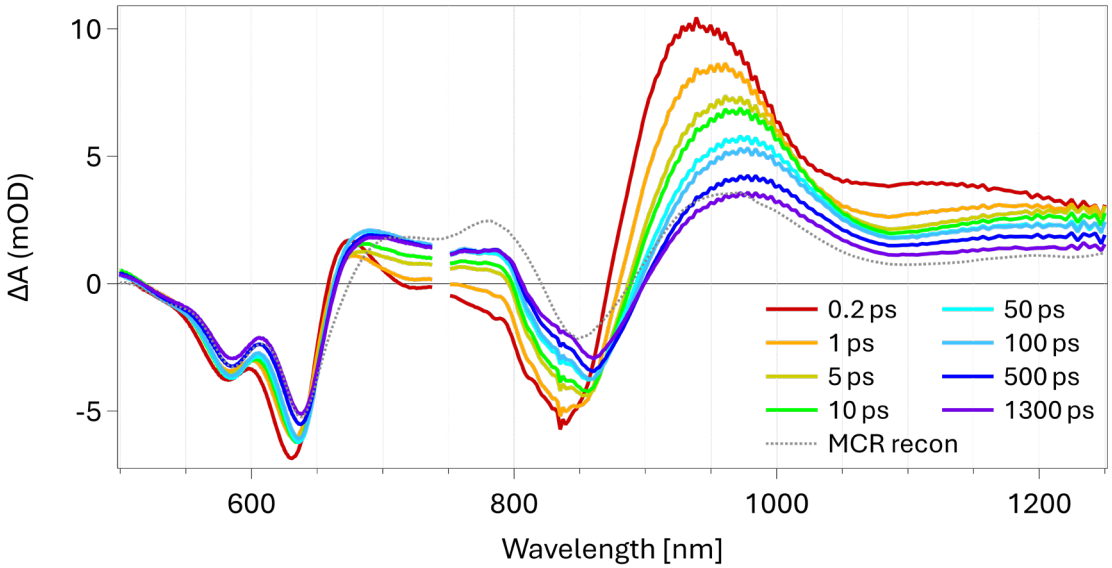

Figure S 6-7: TA spectra of a PM6:Y6 device excited at 400 nm under nonlinear excitation conditions ($3.2 \cdot 10^{18}$ 'Ph'·cm^{-3}) for a series of pump-probe delays.

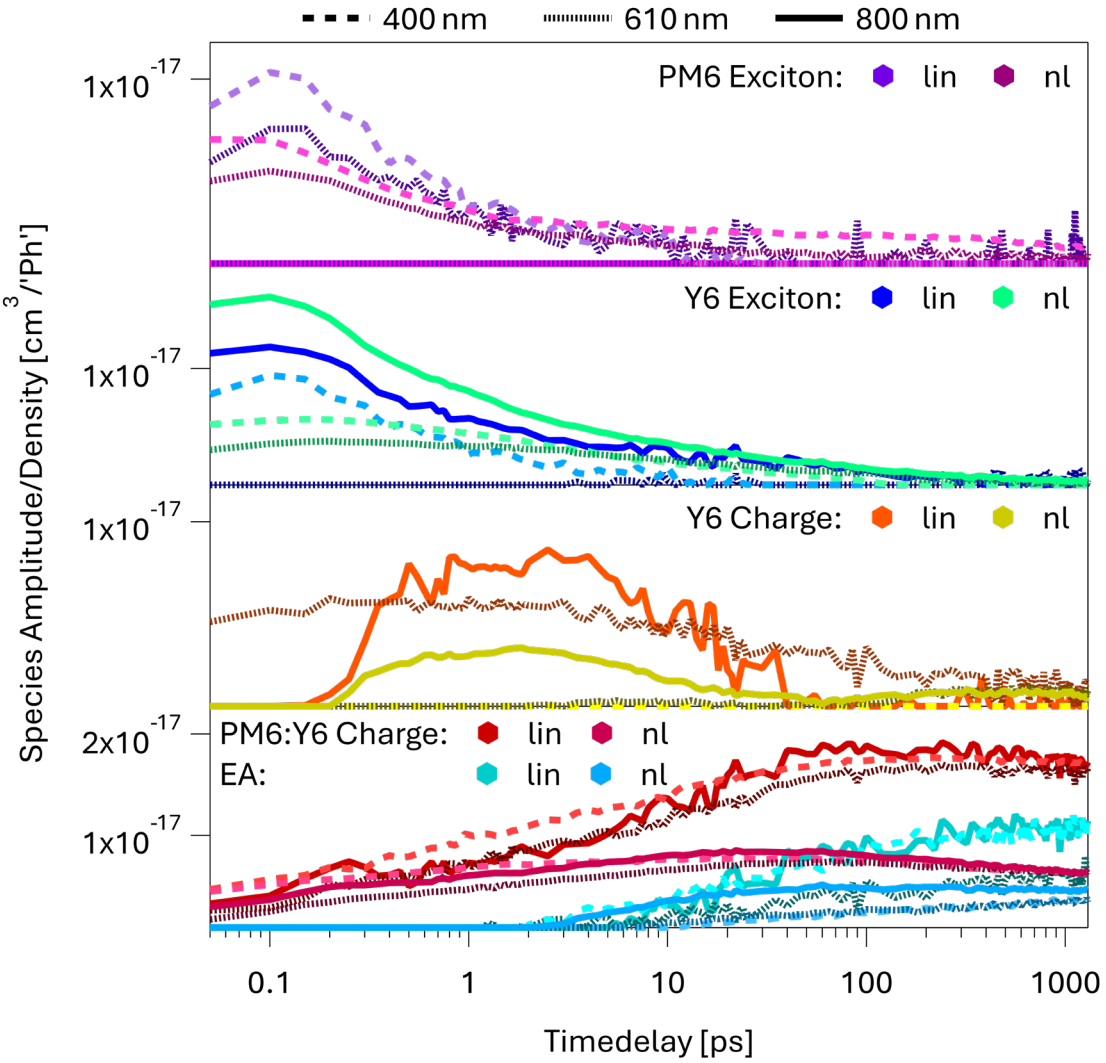

Figure S 6-8: Time-resolved relative contribution to the measured ΔA divided by the excitation density of each species in the linear ($8.8 \cdot 10^{16}$ 'Ph'·cm^{-3}) and in the nonlinear ($3.2 \cdot 10^{18}$ 'Ph'·cm^{-3}) excitation regime: singlet PM6 exciton (purple), singlet Y6 exciton (blue), neat Y6 charge (orange), PM6:Y6 charge (red) and the directional electroabsorption signal (turquoise), present in a PM6:Y6 device and obtained using MCR.

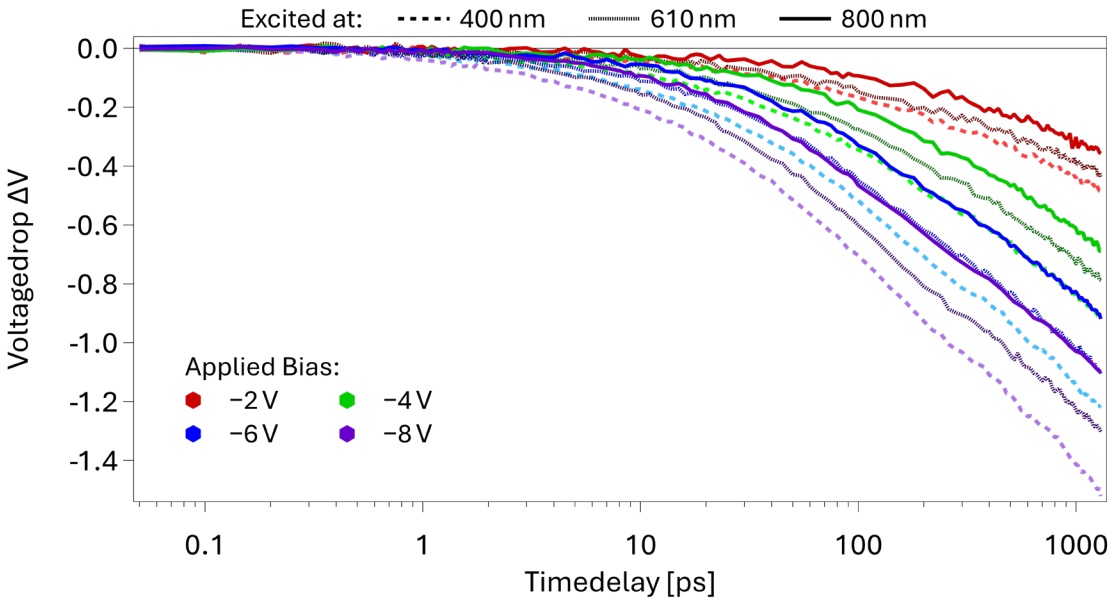

Figure S 6-9: Voltagedrop curves of the PM6:Y6 device excited under 400, 610 and 800 nm excitation at various applied external biases before normalisation.

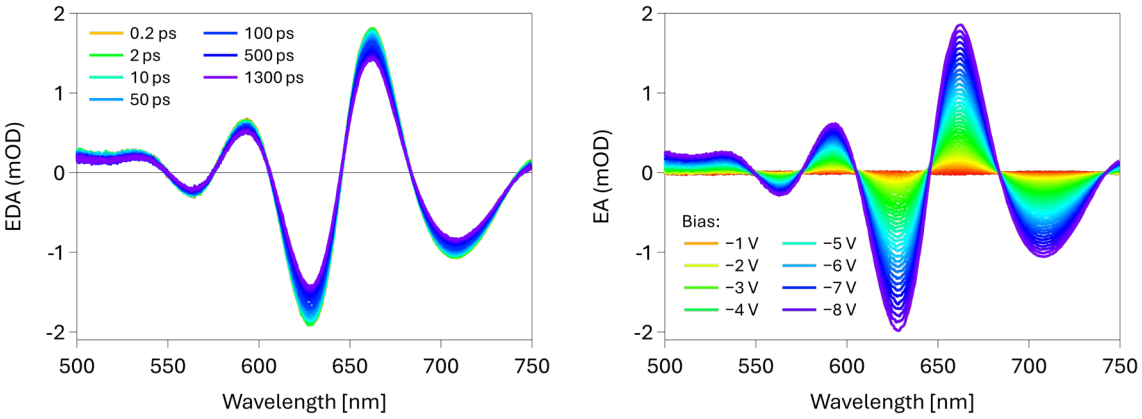

Figure S 6-10: Time-resolved EDA spectra of the PM6:Y6 device (l.) and field-dependent EA spectra of the PM6:Y6 device (r.).

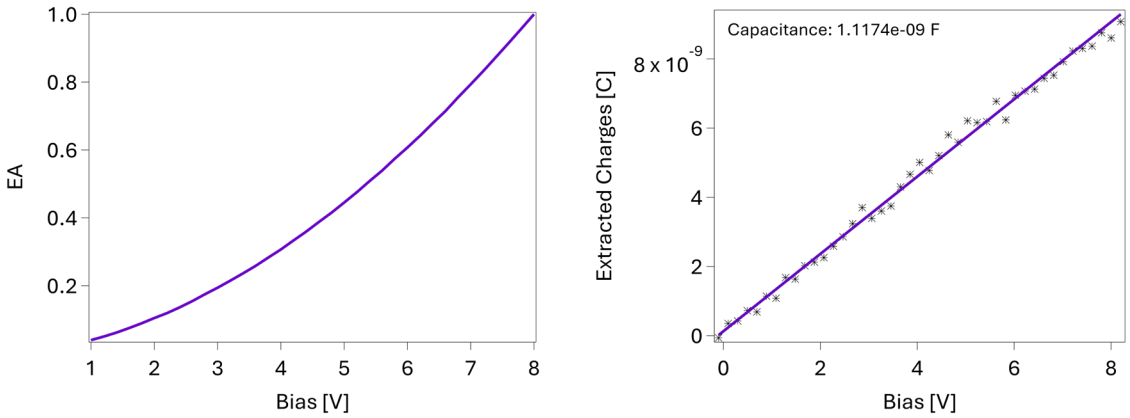

Figure S 6-11: Normalised field-dependence fit (l.) and extracted capacitance of the PM6:Y6 device (r.).

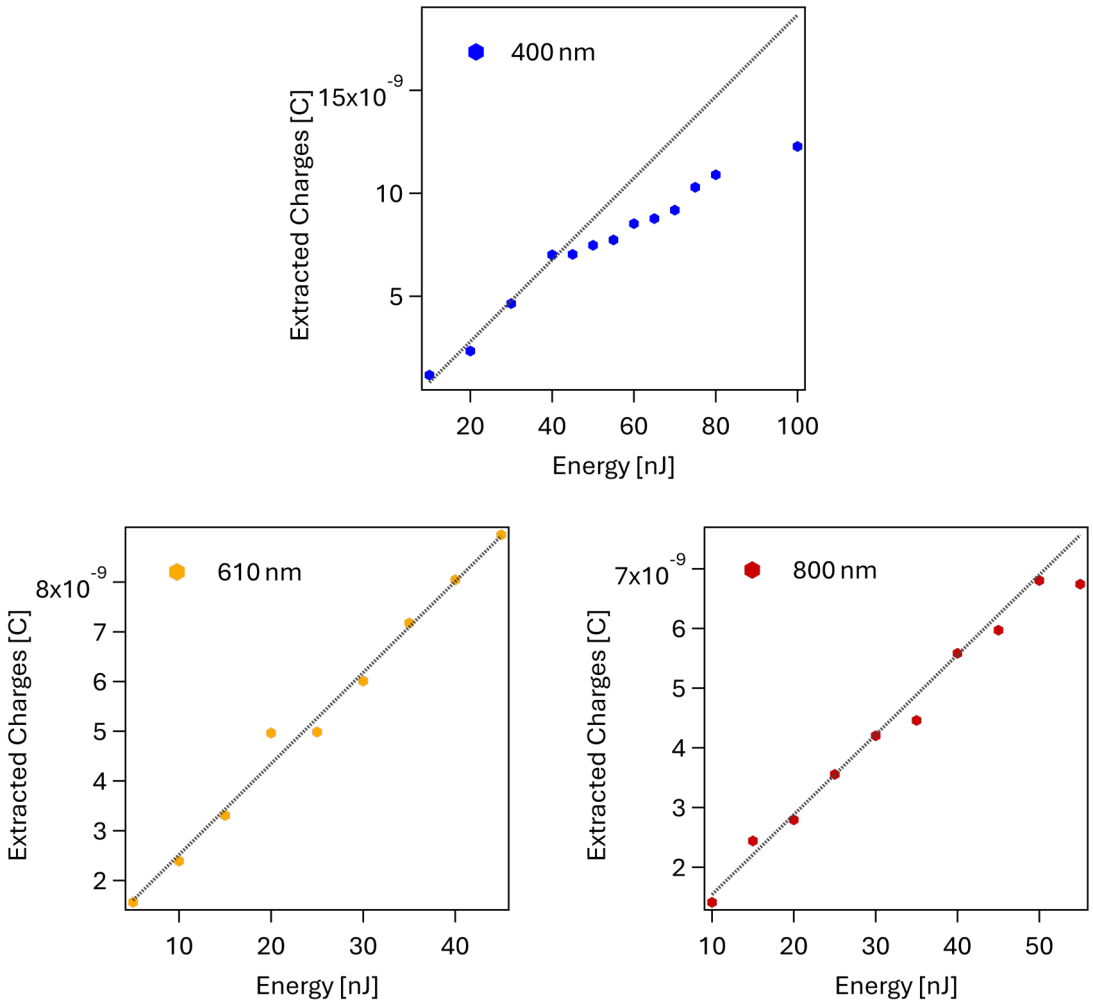

Figure S 6-12: Fluence dependence of extracted charges. EDA experiments of PM6:Y6 were performed in the linear device response. Here, the extacted charges were linearly correlated to the pump beam energy: 30 nJ at 400 nm (top), 15 nJ at 610 nm (bottom left) and 20 nJ at 800 nm (bottom right).

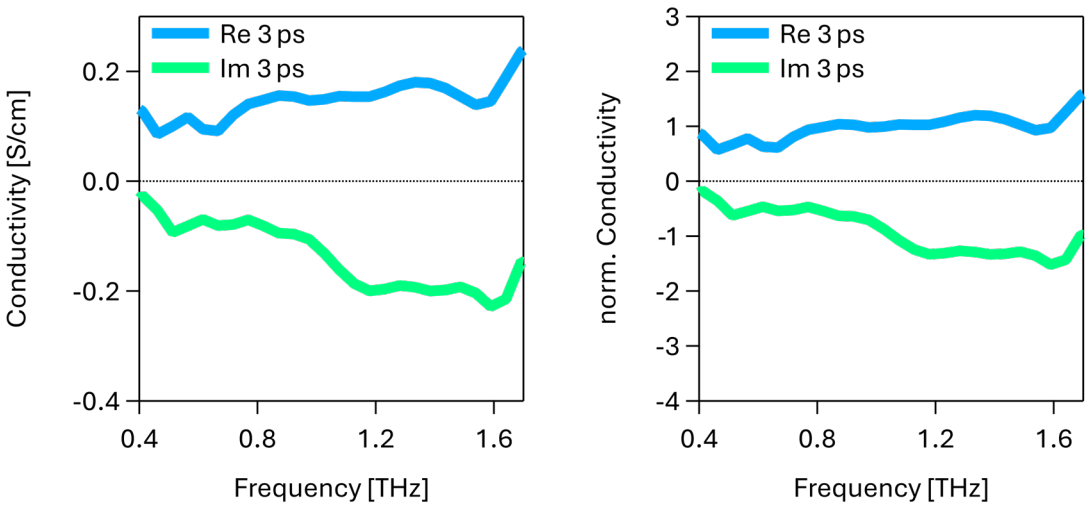

Figure S 6-13: Non-normalised (left) and normalised (right) THz conductivity of a PM6:Y6 thick film under 610 nm excitation with the real part (blue) and imaginary part (green) at 3 ps after excitation.

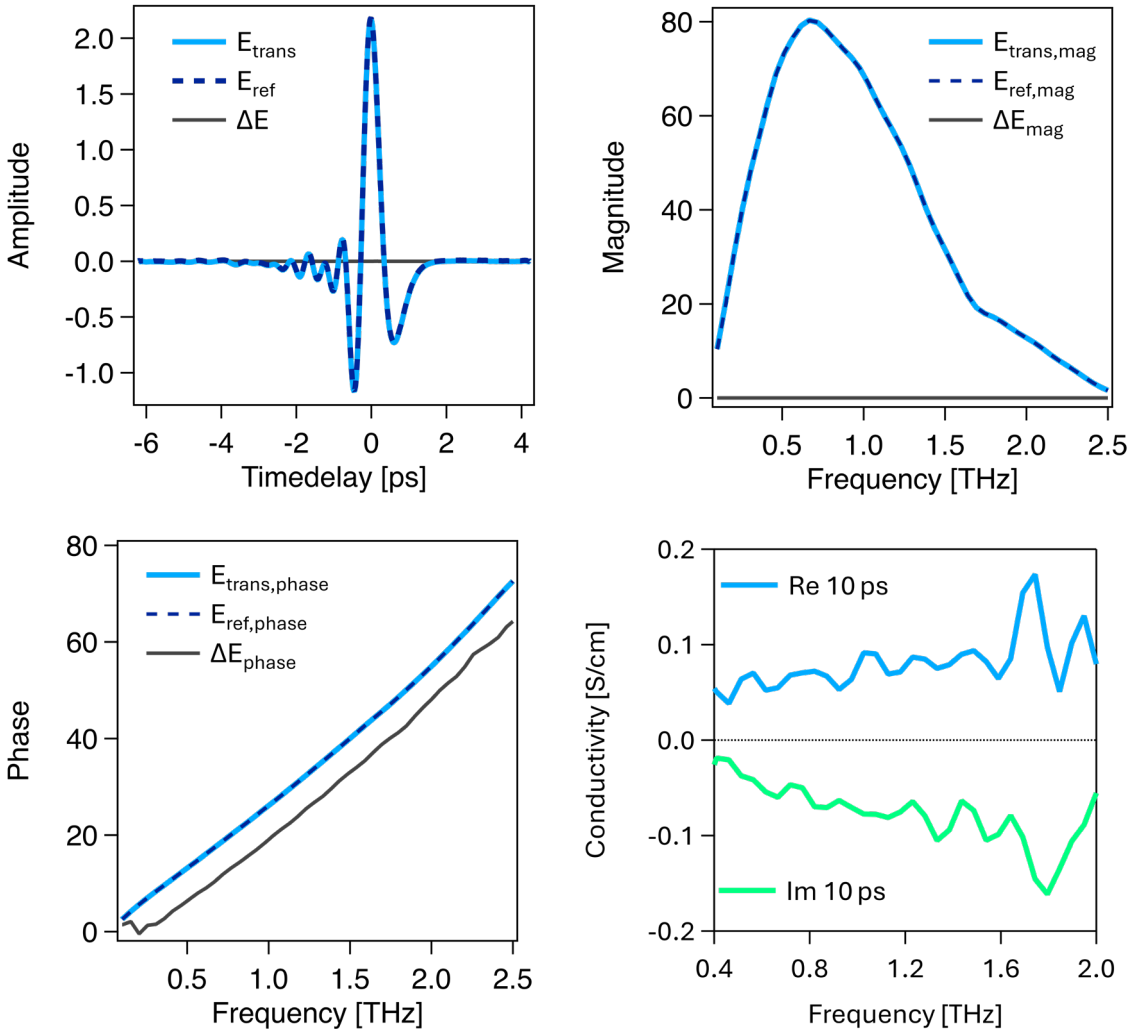

Figure S 6-14: Time-domain THz response of the 1 µm thick PM6:Y6 film with pump (E_{trans}), without pump (E_{ref}) and the resulting pump-induced change (ΔE). The magnitude panel shows the frequency-resolved amplitude of the same fields and indicates how strongly each THz frequency contributes to the waveform after transmission through the sample stack. The phase panel shows the spectral phase and reports the relative timing of the frequency components. A linear increase reflects an overall delay introduced by substrate and film, while curvature indicates dispersion. The conductivity panel shows the complex photoconductivity retrieved at the stated delay from the complex transmission change using the thin-film inversion. The real part shows the in-phase photoconductive response. The imaginary part shows the out-of-phase response and is sensitive to partial localisation and backscattering.

Table S 6-1: Time constants of the evolution of excited state species in in the PS:Y6 film at 800 nm, 610 nm & 400 nm obtained via multiexponential fits of MCR dynamics.

	Species	τ_1 [ps]	τ_2 [ps]	τ_3 [ps]
800 nm	Y6 Ex	0.05	32.6	230.9
	Y6 Ch	0.05	32.6	230.9
610 nm	Y6 Ex	0.07	29.1	230.3
	Y6 Ch	0.07	29.1	230.3
400 nm	Y6 Ex	0.93	115.6	–
	Y6 Ch	0.16	1.6	204.5
	Y6 Tr	496.1	–	–

Table S 6-2: Time constants of the evolution of excited state species in in the PM6:Y6 film at 800 nm, 610 nm & 400 nm obtained via multiexponential fits of MCR dynamics.

	Species	τ_1 [ps]	τ_2 [ps]	τ_3 [ps]
800 nm	Y6 Ex	0.03	0.3	14.9
	Y6 Ch	0.2	13.1	634.2
	PM6:Y6 Ch	1.1	24.9	–
	Y6 Tr	7780.3	–	–
610 nm	PM Ex	0.1	0.5	16.5
	Y6 Ex	0.03	0.3	14.9
	Y6 Ch	0.2	13.1	634.9
	PM6:Y6 Ch	1.2	27.6	2942.5
	Y6 Tr	7780.3	–	–
400 nm	PM6 Ex	0.03	1.2 (20 %)	36.0
	Y6 Ex	0.03	1.4	54.1
	PM6:Y6 Ch	2.5	40.7	–
	Y6 Tr	496.1	–	–

Table S 6-3: Time constants of the evolution of excited state species in in the PM6:Y6 device at 800 nm, 610 nm & 400 nm obtained via multiexponential fits of MCR dynamics.

	Species	τ_1 [ps]	τ_2 [ps]	τ_3 [ps]
800 nm	Y6 Ex	0.7	73.8	–
	Y6 Ch	0.3	1.5	15.9
	PM6:Y6 Ch	0.7	13.0	–
	EA	27.3	236.2	–
610 nm	PM Ex	0.01	0.5	16.6
	Y6 Ch	0.03	18.6	352.2
	PM6:Y6 Ch	0.8	21.7	–
	EA	24.8	353.0	–
400 nm	PM6 Ex	0.02	0.4	7.1
	Y6 Ex	0.01	0.4	6.3
	PM6:Y6 Ch	0.7	14.9	–
	EA	14.6	168.5	–

Table S 6-4: Time constants of the evolution of excited state species in in the PM6:Y6 device at 800 nm, 610 nm & 400 nm under nonlinear excitation conditions obtained via multiexponential fits of MCR dynamics.

	Species	τ_1 [ps]	τ_2 [ps]	τ_3 [ps]
800 nm	Y6 Ex	0.8	35.4	–
	Y6 Ch	0.4	8.1	36.9
	PM6:Y6 Ch	0.2)	5.1	404.5
	EA	5.9	20.0	1299.4
610 nm	PM Ex	0.5	12.1	–
	Y6 Ex	6.6	130.1	–
	Y6 Ch	1.9	19.4	–
	PM6:Y6 Ch	0.3	7.4	522.7
	EA	23.6	649.2	–
400 nm	PM6 Ex	0.6	309.6	–
	Y6 Ex	2.5	47.9	–
	PM6:Y6 Ch	0.4	5.7	323.3
	EA	51.2	965.8	–

Table S 6-5: Charge separation time constants of the voltagedrop curves at every applied bias, obtained via EDA spectroscopy of the PM6:Y6 device.

Excitation wavelength	External bias	τ_1 [ps]	τ_2 [ps]
800 nm	2 V	909.1	61.2
	4 V	949.3	81.7
	6 V	821.7	77.7
	8 V	651.6	60.0
610 nm	2 V	807.2	49.2
	4 V	697.6	52.1
	6 V	641.7	55.0
	8 V	576.0	49.7
400 nm	2 V	724.0	43.7
	4 V	680.7	47.9
	6 V	644.3	47.4
	8 V	593.9	38.7

Table S 6-6: Capacitance and extracted charges of the PM6:Y6 device under 400 nm, 610 nm and 800 nm excitation. Values are extracted from electrical measurements via an oscilloscope, performed in association with EDA.

	400 nm	610 nm	800 nm
Capacitance [F]	$1.12 \cdot 10^{-9}$		
tot. Charges at −2 V [C]	$3.43 \cdot 10^{-9}$	$2.85 \cdot 10^{-9}$	$2.45 \cdot 10^{-9}$
tot. Charges at −4 V [C]	$3.68 \cdot 10^{-9}$	$3.06 \cdot 10^{-9}$	$2.57 \cdot 10^{-9}$
tot. Charges at −6 V [C]	$3.80 \cdot 10^{-8}$	$3.17 \cdot 10^{-8}$	$2.63 \cdot 10^{-9}$
tot. Charges at −8 V [C]	$3.92 \cdot 10^{-8}$	$3.24 \cdot 10^{-8}$	$2.70 \cdot 10^{-9}$

Chapter 7

Conclusion & Outlook

Conclusion

This thesis addressed how excitation energy, electric fields and device architecture influence ultrafast mechanisms influencing photoinduced processes and the subsequent formation, separation and extraction of charge carriers in organic semiconducting systems. For this purpose, two systems were investigated that follow fundamentally different conceptual approaches. For the single component small-molecule DCV2-5T, the absence of a donor–acceptor interface means that charges form rapidly but at the same time makes them vulnerable to ultrafast recombination. The performance of DCV2-5T is thus time-critical and rather limited by incomplete extraction than the charge generation rate. In the PM6:Y6 blend, the crucial factor a is early access to delocalised acceptor domains and domain connectivity. While the scope was on their ultrafast behaviour, which was examined by a variety of spectroscopic techniques such as TA, EDA and THz, the obtained results were complemented with experiments beyond those timescales.

Excess energy accelerates and enhances early-time charge formation in both systems. In DCV2-5T, however, this advantage is tied to certain conditions. Faster formation is of little use if extraction cannot keep pace. The same excess energy also accelerates losses if charges are not extracted quickly enough. In PM6:Y6, outcomes are controlled by how quickly excited states access delocalised Y6 aggregates. Direct excitation of aggregated Y6 yields the most persistent populations, in contrast to when occurring in less favourable regions. The associated limitations can be mitigated by migration towards more delocalised aggregated domains, as long as they are in reach of the exciton. Here, excess-energy excitation exhibits an advantage when forming higher-lying excited states, which can exhibit a higher probability of reaching an aggregated Y6 region prior to charge transfer, arising from a higher delocalisation of the higher-lying exciton. Excess energy increases the probability and speed of that access but is not mandatory. At high excitation densities, the advantage of excess energy diminishes due to the saturation of the reachable sites and additional nonlinear losses.

A directional electric field and the device architecture supported charge formation and stabilisation in both systems. In DCV2-5T the internal field and the contact energetics set the barrier for charge extraction. Using transport layers increased the total charge

yield, but with a simultaneous retardation of the extraction processes. The strong field-dependence suggests that DCV2-5T devices could benefit from electrodes with a greater workfunction difference, particularly at lower excitation wavelengths. In contrast, the built-in potential in the PM6:Y6 device was sufficient for stabilising longer-lived charges populations, while the bias-dependence remained relatively low due to the already high efficiency of the PM6:Y6 blend. Nevertheless, charges from less favourable region benefit more from stronger electric fields in both systems due to a greater number of rescuable chargers present, which would otherwise recombine before separation.

Outlook

The present findings set a robust foundation for understanding ultrafast photophysics in organic semiconductors but also suggest directions for further research to resolve outstanding questions and optimise device performance. Based on the PS:Y6 observations during chapter 6, aggregate-resolved excitation studies of charge carrier behaviour could be a promising continuation, especially when performed in devices. With systematically diluted systems and controlled processing conditions, the formation of unaggregated Y6 and of specific aggregate populations could be favoured, allowing the determination of their individual influences on the charge formation and extraction behaviour on ultrafast timescales as functions of incident photon energy and internal field strength.

To further determine the role of CT states in limiting charge extraction efficiency and how this impacts energy- and bias-dependent behaviour, another approach of quantifying and identifying extraction losses could be realised by introducing a low-energy push pulse into the EDA setup. By tuning both the wavelength and the delayed arrival of the push pulse, intermediate states can be selectively re-excited. This enables a time-resolved mapping of dissociation thresholds and barriers, to evaluate whether the limiting factors are predominantly intrinsic to the material or of peripheral origin.

Although excitation with excess photon energy can promote more rapid initial charge generation, it was shown that such carriers are intrinsically less stable and more vulnerable to recombination when they are not stabilised by favourable morphological or energetic environments. To convert this potential into lasting device performance, it will be critical to identify and optimise the conditions that would allow excess-energy pathways to lead to efficient charge extraction before losses occur. This may involve developing materials with enhanced carrier delocalisation, hindering recombination and accelerate carrier movement in devices, allowing an efficiency improvement also in less favourable excitation regimes.

This thesis also revealed significant field dependence of the device performance, especially for single-component systems like DCV2-5T. A systematic optimisation of interfacial energetic alignment and transport-layer stacks could benefit from a simultaneous utilisation of ultrafast methods in order to connect modifications directly to excited-states behaviour on shorter timescales, without being limited to steady-state results exclusively. While field-induced processes can increase the device efficiency, reducing the reliance on extraction fields should be targeted to achieve minimal losses and to extend the operational flexibility and efficiency, especially but not solely for single-component devices.

Finally, it would be promising to extend the accessible time window of ultrafast spectroscopy into the microsecond regime using e.g. an electronic delay of the pump-pulse arrival. This would provide a direct time-resolved link between excited-state behaviour during the earliest times and the results observed in the steady-state. Especially tracking charge separation and extraction behaviour at longer time scales would offer detailed insights into the relation between device efficiency and dynamical behaviour of charge carriers.

Bibliography

[1] Morse, G. *et al*. Organic Photovoltaics in IoT, Architecture, and Wearables. *Material Matters* 12, 101-117 (**2017**).

[2] Ebner, M. *et al*. Regenerated cellulose fiber solar cell. *Flexible and Printed Electronics* 2, doi:10.1088/2058-8585/aa5707 (**2017**).

[3] Li, Y. *et al*. High Efficiency Near-Infrared and Semitransparent Non-Fullerene Acceptor Organic Photovoltaic Cells. *J Am Chem Soc* 139, 17114-17119, doi:10.1021/jacs.7b11278 (**2017**).

[4] van Tartwijk, G. Heliatek. *Our technology: Organic photovoltaics (OPV)*, <https://www.heliatek.com/en/technology/opv/> (accessed: 24 Jan 2025).

[5] Dracula Technologies. *Total Cost of Ownership of Organic Photovoltaics versus Battery-powered sensors*, <https://dracula-technologies.com/> (accessed: 04 Feb 2025).

[6] soleos. *10 Key Insights into Organic Photovoltaics: The Future of Solar Energy*, <https://www.soleosenergy.com/10-insights-of-organic-photovoltaics-future/> (**2024**, accessed: 04 Feb 2025).

[7] epishine. *Innovating for a Sustainable Future with Organic Solar Cells*, <https://www.epishine.com/solution> (accessed: 04 Feb 2025).

[8] Jain, P., Raina, G., Sinha, S., Malik, P. & Mathur, S. Agrovoltaics: Step towards sustainable energy-food combination. *Bioresource Technology Reports* 15, 100766, doi:10.1016/j.biteb.2021.100766 (**2021**).

[9] Brooks, A. E. in *Future Energy* pp. 383-404 (**2014**), 978-0-08-099424-6.

[10] Hatton, R. A. in *A Comprehensive Guide to Solar Energy Systems* (eds Trevor M. Letcher & Vasilis M. Fthenakis) pp. 255-277 (Academic Press, **2018**), 9780128114797.

[11] Tress, W. *Organic Solar Cells*. Vol. 208 (Springer, **2014**), 978-3-319-10096-8, 978-3-319-10097-5.

[12] Schulz, S. & Czycholl, G. Tight-binding model for semiconductor nanostructures - art. no. 165317. *Physical Review B* 72, doi:ARTN 165317, 10.1103/PhysRevB.72.165317 (**2005**).

[13] Griffiths, D. J. & Schroeter, D. F. *Introduction to Quantum Mechanics*. 3 edn, (Cambridge University Press, **2018**), 9781316995433, 9781107189638.

[14] Holleman, A. F., Wiberg, N. & Wiberg, E. *Lehrbuch der Anorganischen Chemie*. 114, 361-371 (De Gruyter, **2007**), 9783110206845.

[15] Slater, J. C. & Koster, G. F. Simplified Lcao Method for the Periodic Potential Problem. *Physical Review* 94, 1498-1524, doi:DOI 10.1103/PhysRev.94.1498 (**1954**).

[16] Bässler, H. & Köhler, A. *Electronic Processes in Organic Semiconductors*. (**2015**), 9783527685172.

[17] Trovatello, C. *et al*. The ultrafast onset of exciton formation in 2D semiconductors. *Nat Commun* 11, 5277, doi:10.1038/s41467-020-18835-5 (**2020**).

[18] Dickinson, F. *Photochemistry and Photophysics* <https://chemfd.github.io/Photochemistry_2/> (**2022**, accessed: 27 Feb 2025).

[19] Yu, P. Y. Thermalization of Excitons. *Progress in Solid State Chemistry* 18, 201-257, doi:Doi 10.1016/0079-6786(88)90003-9 (**1988**).
[20] Atkins, P. W. & Friedman, R. S. *Molecular quantum mechanics*. 4th edn, 573 (Oxford University Press, **2005**), 0-19-927-498-3.
[21] Clark, J. Chemistry LibreTexts. *The Beer-Lambert Law*, <https://chem.libretexts.org/@go/page/3747> (accessed: 28 Feb 2025).
[22] Hilborn, R. C. Einstein coefficients, cross sections, f values, dipole moments, and all that. *American Journal of Physics* 50, 982-986, doi:10.1119/1.12937 (**1982**).
[23] Saleh, B. E. A. & Teich, M. C. *Fundamentals of Photonics*. 3rd edn, (Wiley, **2019**), 978-1-119-50687-4.
[24] Mitroy, J., Safronova, M. S. & Clark, C. W. Theory and applications of atomic and ionic polarizabilities. *Journal of Physics B-Atomic Molecular and Optical Physics* 43, doi:Artn 202001, 10.1088/0953-4075/43/20/202001 (**2010**).
[25] Kira, M. & Koch, S. W. Many-body correlations and excitonic effects in semiconductor spectroscopy. *Progress in Quantum Electronics* 30, 155-296, doi:10.1016/j.pquantelec.2006.12.002 (**2006**).
[26] Kasten, F. & Young, A. T. Revised optical air mass tables and approximation formula. *Appl Opt* 28, 4735-4738, doi:10.1364/AO.28.004735 (**1989**).
[27] Laue, E. G. The measurement of solar spectral irradiance at different terrestrial elevations. *Solar Energy* 13, 43-57, doi:10.1016/0038-092x(70)90006-x (**1970**).
[28] Honsberg, C. & Bowden, S. *Photovoltaics Education*, <www.pveducation.org> (**2019**, accessed: 29 Mar 2025).
[29] Hestand, N. J. & Spano, F. C. Expanded Theory of H- and J-Molecular Aggregates: The Effects of Vibronic Coupling and Intermolecular Charge Transfer. *Chem Rev* 118, 7069-7163, doi:10.1021/acs.chemrev.7b00581 (**2018**).
[30] Haus, J. W. in *Fundamentals and Applications of Nanophotonics* pp. 341-395 (**2016**), 9781782424642.
[31] Qin, D., Chen, J. & Lu, N. A Novel Density of States (DOS) for Disordered Organic Semiconductors. *Micromachines (Basel)* 14, doi:10.3390/mi14071361 (**2023**).
[32] Boyd, R. W. *Nonlinear Optics*. 4 edn, (Academic Press, **2020**), 978-0-12-811002-7.
[33] Rumi, M. & Perry, J. W. Two-photon absorption: an overview of measurements and principles. *Advances in Optics and Photonics* 2, 451-518, doi:10.1364/Aop.2.000451 (**2010**).
[34] Samuel, I. D. W. *et al*. Photoluminescence in poly(3-hexylthiophene). *Optical Probes of Conjugated Polymers* 3145, 163-170, doi:Doi 10.1117/12.279277 (**1997**).
[35] Mikhnenko, O. V., Blom, P. W. M. & Nguyen, T.-Q. Exciton diffusion in organic semiconductors. *Energy & Environmental Science* 8, 1867-1888, doi:10.1039/c5ee00925a (**2015**).
[36] Giannini, S. *et al*. Exciton transport in molecular organic semiconductors boosted by transient quantum delocalization. *Nat Commun* 13, 2755, doi:10.1038/s41467-022-30308-5 (**2022**).
[37] Chang, C.-W. Chemistry LibreTexts. *Dexter Energy Transfer*, <https://chem.libretexts.org/@go/page/2011> (accessed: 22 Apr 2025).

[38] Riley, D. B., Meredith, P., Armin, A. & Sandberg, O. J. Role of Exciton Diffusion and Lifetime in Organic Solar Cells with a Low Energy Offset. *J Phys Chem Lett* 13, 4402-4409, doi:10.1021/acs.jpclett.2c00791 (**2022**).

[39] Zhu, L. *et al*. Efficient Organic Solar Cell with 16.88% Efficiency Enabled by Refined Acceptor Crystallization and Morphology with Improved Charge Transfer and Transport Properties. *Advanced Energy Materials* 10, doi:10.1002/aenm.201904234 (**2020**).

[40] Zhu, W. *et al*. Crystallography, Morphology, Electronic Structure, and Transport in Non-Fullerene/Non-Indacenodithienothiophene Polymer:Y6 Solar Cells. *J Am Chem Soc* 142, 14532-14547, doi:10.1021/jacs.0c05560 (**2020**).

[41] Jiang, K. *et al*. Pseudo-bilayer architecture enables high-performance organic solar cells with enhanced exciton diffusion length. *Nat Commun* 12, 468, doi:10.1038/s41467-020-20791-z (**2021**).

[42] Zhou, G. Q. *et al*. Spontaneous carrier generation and low recombination in high-efficiency non-fullerene solar cells. *Energy & Environmental Science* 15, 3483-3493, doi:10.1039/d2ee01327d (**2022**).

[43] Firdaus, Y. *et al*. Long-range exciton diffusion in molecular non-fullerene acceptors. *Nat Commun* 11, 5220, doi:10.1038/s41467-020-19029-9 (**2020**).

[44] Shoaee, S. *et al*. What We have Learnt from PM6:Y6. *Adv Mater* 36, e2302005, doi:10.1002/adma.202302005 (**2024**).

[45] Einstein, A. Über die von der molekularkinetischen Theorie der Wärme geforderte Bewegung von in ruhenden Flüssigkeiten suspendierten Teilchen. *Annalen der Physik* 322, 549-560, doi:10.1002/andp.19053220806 (**2006**).

[46] Pope, M. & Swenberg, C. *Electronic Processes in Organic Crystals and Polymers*. 2 edn, (Oxford University Press, **1999**), 0-19-512963-6.

[47] Bässler, H. Charge Transport in Disordered Organic Photoconductors a Monte Carlo Simulation Study. *physica status solidi (b)* 175, 15-56, doi:10.1002/pssb.2221750102 (**2006**).

[48] Mikhnenko, O. V. *et al*. Trap-limited exciton diffusion in organic semiconductors. *Adv Mater* 26, 1912-1917, doi:10.1002/adma.201304162 (**2014**).

[49] Sneyd, A. J., Beljonne, D. & Rao, A. A New Frontier in Exciton Transport: Transient Delocalization. *J Phys Chem Lett* 13, 6820-6830, doi:10.1021/acs.jpclett.2c01133 (**2022**).

[50] Bakulin, A. A. *et al*. The role of driving energy and delocalized States for charge separation in organic semiconductors. *Science* 335, 1340-1344, doi:10.1126/science.1217745 (**2012**).

[51] May, V. & Kühn, O. in *Charge and Energy Transfer Dynamics in Molecular Systems* pp. 309-433 (Wiley-VCH, **2011**), 9783527407323, 9783527633791.

[52] Kashani, S., Wang, Z., Risko, C. & Ade, H. Relating reorganization energies, exciton diffusion length and non-radiative recombination to the room temperature UV-vis absorption spectra of NF-SMA. *Mater Horiz* 10, 443-453, doi:10.1039/d2mh01228f (**2023**).

[53] Atkins, P. W. & De Paula, J. *Atkins' Physical Chemistry*. 9th edn, 839-842 (Oxford University Press, **2010**), 9780199543373; 0199543372.

[54] Gasparini, N. *et al*. Adjusting the energy of interfacial states in organic photovoltaics for maximum efficiency. *Nat Commun* 12, 1772, doi:10.1038/s41467-021-22032-3 (**2021**).

[55] Samuel, I. D. & Turnbull, G. A. Organic semiconductor lasers. *Chem Rev* 107, 1272-1295, doi:10.1021/cr050152i (**2007**).
[56] Tregnago, G. *Photophysics and applications of organic semiconductors*, University College London, (**2015**).
[57] Englman, R. & Jortner, J. The energy gap law for radiationless transitions in large molecules. *Molecular Physics* 18, 145-164, doi:10.1080/00268977000100171 (**1970**).
[58] Beljonne, D., Curutchet, C., Scholes, G. D. & Silbey, R. J. Beyond Forster resonance energy transfer in biological and nanoscale systems. *J Phys Chem B* 113, 6583-6599, doi:10.1021/jp900708f (**2009**).
[59] Würfel, P. & Würfel, U. *Physics of Solar Cells*. 3 edn, (Wiley-VCH, **2016**), 978-3-527-41312-6.
[60] Wu, J. *et al*. A Comparison of Charge Carrier Dynamics in Organic and Perovskite Solar Cells. *Adv Mater* 34, e2101833, doi:10.1002/adma.202101833 (**2022**).
[61] Coehoorn, R., Zhang, L., Bobbert, P. A. & van Eersel, H. Effect of polaron diffusion on exciton-polaron quenching in disordered organic semiconductors. *Physical Review B* 95, doi:10.1103/PhysRevB.95.134202 (**2017**).
[62] Clarke, T. M. & Durrant, J. R. Charge photogeneration in organic solar cells. *Chem Rev* 110, 6736-6767, doi:10.1021/cr900271s (**2010**).
[63] Grüne, J. *et al*. Triplet Excitons and Associated Efficiency - Limiting Pathways in Organic Solar Cell Blends Based on (Non -) Halogenated PBDB - T and Y - Series. *Advanced Functional Materials* 33, doi:10.1002/adfm.202212640 (**2023**).
[64] Gillett, A. J. *et al*. The role of charge recombination to triplet excitons in organic solar cells. *Nature* 597, 666-671, doi:10.1038/s41586-021-03840-5 (**2021**).
[65] Liu, Q. & Vandewal, K. Understanding and Suppressing Non-Radiative Recombination Losses in Non-Fullerene Organic Solar Cells. *Adv Mater* 35, e2302452, doi:10.1002/adma.202302452 (**2023**).
[66] Smith, M. B. & Michl, J. Singlet fission. *Chem Rev* 110, 6891-6936, doi:10.1021/cr1002613 (**2010**).
[67] Baldo, M. A. *et al*. Highly efficient phosphorescent emission from organic electroluminescent devices. *Nature* 395, 151-154, doi:Doi 10.1038/25954 (**1998**).
[68] Reineke, S., Walzer, K. & Leo, K. Triplet-exciton quenching in organic phosphorescent light-emitting diodes with Ir-based emitters. *Physical Review B* 75, doi:ARTN 125328, 10.1103/PhysRevB.75.125328 (**2007**).
[69] Tamura, H. & Burghardt, I. Ultrafast charge separation in organic photovoltaics enhanced by charge delocalization and vibronically hot exciton dissociation. *J Am Chem Soc* 135, 16364-16367, doi:10.1021/ja4093874 (**2013**).
[70] Perdigon-Toro, L. *et al*. Barrierless Free Charge Generation in the High-Performance PM6:Y6 Bulk Heterojunction Non-Fullerene Solar Cell. *Adv Mater* 32, e1906763, doi:10.1002/adma.201906763 (**2020**).
[71] Karuthedath, S. *et al*. Intrinsic efficiency limits in low-bandgap non-fullerene acceptor organic solar cells. *Nat Mater* 20, 378-384, doi:10.1038/s41563-020-00835-x (**2021**).

[72] Zhong, Y. *et al*. Sub-picosecond charge-transfer at near-zero driving force in polymer:non-fullerene acceptor blends and bilayers. *Nat Commun* 11, 833, doi:10.1038/s41467-020-14549-w (**2020**).
[73] Perdigón-Toro, L. *et al*. Excitons Dominate the Emission from PM6:Y6 Solar Cells, but This Does Not Help the Open-Circuit Voltage of the Device. *ACS Energy Letters* 6, 557-564, doi:10.1021/acsenergylett.0c02572 (**2021**).
[74] Shuai, Z., Li, W., Ren, J., Jiang, Y. & Geng, H. Applying Marcus theory to describe the carrier transports in organic semiconductors: Limitations and beyond. *J Chem Phys* 153, 080902, doi:10.1063/5.0018312 (**2020**).
[75] Lowrie, W. *et al*. Organic photovoltaics: The current challenges. *J Chem Phys* 158, 110901, doi:10.1063/5.0139457 (**2023**).
[76] Karki, A. *et al*. The role of bulk and interfacial morphology in charge generation, recombination, and extraction in non-fullerene acceptor organic solar cells. *Energy & Environmental Science* 13, 3679-3692, doi:10.1039/d0ee01896a (**2020**).
[77] Toropin, A. V., Nikitenko, V. R., Korolev, N. A. & Prezhdo, O. V. Disorder and Photogeneration Efficiency in Organic Semiconductors. *J Phys Chem Lett* 14, 7892-7896, doi:10.1021/acs.jpclett.3c02120 (**2023**).
[78] Giannini, S. *et al*. On the role of charge transfer excitations in non-fullerene acceptors for organic photovoltaics. *Materials Today* 80, 308-326, doi:10.1016/j.mattod.2024.09.009 (**2024**).
[79] Shi, Y. *et al*. Small reorganization energy acceptors enable low energy losses in non-fullerene organic solar cells. *Nat Commun* 13, 3256, doi:10.1038/s41467-022-30927-y (**2022**).
[80] Qian, D. P. *et al*. Correlating the Hybridization of Local-Exciton and Charge-Transfer States with Charge Generation in Organic Solar Cells. *Advanced Energy Materials* 13, doi:10.1002/aenm.202301026 (**2023**).
[81] Zhang, G. *et al*. Delocalization of exciton and electron wavefunction in non-fullerene acceptor molecules enables efficient organic solar cells. *Nat Commun* 11, 3943, doi:10.1038/s41467-020-17867-1 (**2020**).
[82] Zarrabi, N., Sandberg, O. J., Meredith, P. & Armin, A. Subgap Absorption in Organic Semiconductors. *J Phys Chem Lett* 14, 3174-3185, doi:10.1021/acs.jpclett.3c00021 (**2023**).
[83] Zhao, W. *et al*. Molecular Optimization Enables over 13% Efficiency in Organic Solar Cells. *J Am Chem Soc* 139, 7148-7151, doi:10.1021/jacs.7b02677 (**2017**).
[84] Yuan, J. *et al*. Single-Junction Organic Solar Cell with over 15% Efficiency Using Fused-Ring Acceptor with Electron-Deficient Core. *Joule* 3, 1140-1151, doi:10.1016/j.joule.2019.01.004 (**2019**).
[85] Liu, Q. *et al*. Electron-donating amine-interlayer induced n-type doping of polymer:nonfullerene blends for efficient narrowband near-infrared photo-detection. *Nat Commun* 13, 5194, doi:10.1038/s41467-022-32845-5 (**2022**).
[86] Classen, A. *et al*. The role of exciton lifetime for charge generation in organic solar cells at negligible energy-level offsets. *Nature Energy* 5, 711-719, doi:10.1038/s41560-020-00684-7 (**2020**).
[87] Hood, S. N. & Kassal, I. Entropy and Disorder Enable Charge Separation in Organic Solar Cells. *J Phys Chem Lett* 7, 4495-4500, doi:10.1021/acs.jpclett.6b02178 (**2016**).

[88] Pratik, S. M., Kupgan, G., Brédas, J.-L. & Coropceanu, V. Analysis of the charge generation and recombination processes in the PM6:Y6 organic solar cell. *Energy & Environmental Science* 18, 841-852, doi:10.1039/d4ee03815k (**2025**).

[89] Giannini, S. & Blumberger, J. Charge Transport in Organic Semiconductors: The Perspective from Nonadiabatic Molecular Dynamics. *Acc Chem Res* 55, 819-830, doi:10.1021/acs.accounts.1c00675 (**2022**).

[90] Rijal, K. *et al*. Endothermic Charge Separation Occurs Spontaneously in Non-Fullerene Acceptor/Polymer Bulk Heterojunction. *Adv Mater* 36, e2400578, doi:10.1002/adma.202400578 (**2024**).

[91] Price, M. B. *et al*. Free charge photogeneration in a single component high photovoltaic efficiency organic semiconductor. *Nat Commun* 13, 2827, doi:10.1038/s41467-022-30127-8 (**2022**).

[92] Fu, Y. *et al*. Molecular orientation-dependent energetic shifts in solution-processed non-fullerene acceptors and their impact on organic photovoltaic performance. *Nat Commun* 14, 1870, doi:10.1038/s41467-023-37234-0 (**2023**).

[93] Bertrandie, J. *et al*. The Energy Level Conundrum of Organic Semiconductors in Solar Cells. *Adv Mater* 34, e2202575, doi:10.1002/adma.202202575 (**2022**).

[94] Koster, L. J. A., Mihailetchi, V. D., Ramaker, R. & Blom, P. W. M. Light intensity dependence of open-circuit voltage of polymer:fullerene solar cells -: art. no. 123509. *Applied Physics Letters* 86, doi:Artn 123509, 10.1063/1.1889240 (**2005**).

[95] Vandewal, K. Interfacial Charge Transfer States in Condensed Phase Systems. *Annu Rev Phys Chem* 67, 113-133, doi:10.1146/annurev-physchem-040215-112144 (**2016**).

[96] Jones, M. L., Chakrabarti, B. & Groves, C. Monte Carlo Simulation of Geminate Pair Recombination Dynamics in Organic Photovoltaic Devices: Multi-Exponential, Field-Dependent Kinetics and Its Interpretation. *Journal of Physical Chemistry C* 118, 85-91, doi:10.1021/jp408063f (**2014**).

[97] Li, X. *et al*. Mapping the energy level alignment at donor/acceptor interfaces in non-fullerene organic solar cells. *Nat Commun* 13, 2046, doi:10.1038/s41467-022-29702-w (**2022**).

[98] Wilken, S. *et al*. Experimentally Calibrated Kinetic Monte Carlo Model Reproduces Organic Solar Cell Current-Voltage Curve. *Solar Rrl* 4, doi:ARTN 2000029, 10.1002/solr.202000029 (**2020**).

[99] Pranav, M. *et al*. Anticorrelated photoluminescence and free charge generation proves field-assisted exciton dissociation in low-offset PM6:Y5 organic solar cells. *Apl Materials* 11, doi:Artn 061111, 10.1063/5.0151580 (**2023**).

[100] Hustings, J. *et al*. Charge-transfer states in photosynthesis and organic solar cells. *Frontiers in Photonics* 3, doi:10.3389/fphot.2022.1050189 (**2022**).

[101] Zhang, Y., Lang, Y. W. & Li, G. Recent advances of non-fullerene organic solar cells: From materials and morphology to devices and applications. *Ecomat* 5, doi:ARTN e12281, 10.1002/eom2.12281 (**2023**).

[102] Xiao, X. *et al*. Strategies to achieve efficiencies of over 19% for organic solar cells. *Cell Reports Physical Science* 6, doi:10.1016/j.xcrp.2024.102390 (**2025**).

[103] Willson, J. T., Liu, W., Balzer, D. & Kassal, I. Jumping Kinetic Monte Carlo: Fast and Accurate Simulations of Partially Delocalized Charge Transport in Organic Semiconductors. *J Phys Chem Lett* 14, 3757-3764, doi:10.1021/acs.jpclett.3c00388 (**2023**).

[104] Gao, Z. R. *et al*. Ferroelectricity of the Orthorhombic and Tetragonal MAPbBr(3) Single Crystal. *J Phys Chem Lett* 10, 2522-2527, doi:10.1021/acs.jpclett.9b00776 (**2019**).

[105] Fratini, S., Mayou, D. & Ciuchi, S. The Transient Localization Scenario for Charge Transport in Crystalline Organic Materials. *Advanced Functional Materials* 26, 2292-2315, doi:10.1002/adfm.201502386 (**2016**).

[106] Liu, B. *et al*. Efficient and stable organic solar cells enabled by multicomponent photoactive layer based on one-pot polymerization. *Nat Commun* 14, 967, doi:10.1038/s41467-023-36413-3 (**2023**).

[107] Fratini, S. & Ciuchi, S. Bandlike motion and mobility saturation in organic molecular semiconductors. *Phys Rev Lett* 103, 266601, doi:10.1103/PhysRevLett.103.266601 (**2009**).

[108] Yao, N. *et al*. Efficient Charge Transport Enables High Efficiency in Dilute Donor Organic Solar Cells. *J Phys Chem Lett* 12, 5039-5044, doi:10.1021/acs.jpclett.1c01219 (**2021**).

[109] Ye, L. *et al*. Surpassing 10% Efficiency Benchmark for Nonfullerene Organic Solar Cells by Scalable Coating in Air from Single Nonhalogenated Solvent. *Adv Mater* 30, doi:10.1002/adma.201705485 (**2018**).

[110] Arkhipov, V. I., Heremans, P., Emelianova, E. V. & Bässler, H. Effect of doping on the density-of-states distribution and carrier hopping in disordered organic semiconductors -: art. no. 045214. *Physical Review B* 71, doi:ARTN 045214, 10.1103/PhysRevB.71.045214 (**2005**).

[111] Jasiūnas, R. *et al*. Thermally Activated Reverse Electron Transfer Limits Carrier Generation Efficiency in PM6:Y6 Non‐Fullerene Organic Solar Cells. *Solar RRL* 6, doi:10.1002/solr.202100963 (**2022**).

[112] Jungbluth, A. *et al*. Limiting factors for charge generation in low-offset fullerene-based organic solar cells. *Nat Commun* 15, 5488, doi:10.1038/s41467-024-49432-5 (**2024**).

[113] Wu, Y. *et al*. Reduced bimolecular charge recombination in efficient organic solar cells comprising non-fullerene acceptors. *Sci Rep* 13, 4717, doi:10.1038/s41598-023-31929-6 (**2023**).

[114] Zeiske, S. *et al*. Direct observation of trap-assisted recombination in organic photovoltaic devices. *Nat Commun* 12, 3603, doi:10.1038/s41467-021-23870-x (**2021**).

[115] Shoaee, S. *et al*. Decoding Charge Recombination through Charge Generation in Organic Solar Cells. *Solar Rrl* 3, doi:ARTN 1900184, 10.1002/solr.201900184 (**2019**).

[116] He, S. J. & Lu, Z. H. Ultralow-voltage Auger-electron-stimulated organic light-emitting diodes. *Journal of Photonics for Energy* 6, doi:Artn 036001, 10.1117/1.Jpe.6.036001 (**2016**).

[117] Staub, F., Rau, U. & Kirchartz, T. Statistics of the Auger Recombination of Electrons and Holes via Defect Levels in the Band Gap-Application to Lead-

Halide Perovskites. *ACS Omega* 3, 8009-8016, doi:10.1021/acsomega.8b00962 (**2018**).
[118] Baek, D., Lee, J. & Choi, B. Diffusion length and resistivity distribution characteristics of silicon wafer by photoluminescence. *Materials Research Bulletin* 58, 157-163, doi:10.1016/j.materresbull.2014.03.002 (**2014**).
[119] Shockley, W. & Queisser, H. J. Detailed Balance Limit of Efficiency ofp-nJunction Solar Cells. *Journal of Applied Physics* 32, 510-519, doi:10.1063/1.1736034 (**1961**).
[120] Hall, R. N. Silicon photovoltaic cells. *Solid-State Electronics* 24, 595-616, doi:10.1016/0038-1101(81)90188-x (**1981**).
[121] Blakers, A., Zin, N., McIntosh, K. R. & Fong, K. High Efficiency Silicon Solar Cells. *Pv Asia Pacific Conference 2012* 33, 1-10, doi:10.1016/j.egypro.2013.05.033 (**2013**).
[122] Ehrler, B. *et al*. Photovoltaics Reaching for the Shockley-Queisser Limit. *Acs Energy Letters* 5, 3029-3033, doi:10.1021/acsenergylett.0c01790 (**2020**).
[123] Płaczek-Popko, E. Top PV market solar cells 2016. *Opto-Electronics Review* 25, 55-64, doi:10.1016/j.opelre.2017.03.002 (**2017**).
[124] Sundaram, S., Shanks, K. & Upadhyaya, H. in *A Comprehensive Guide to Solar Energy Systems* pp. 361-370 (**2018**), 9780128114797.
[125] Louwen, A., van Sark, W., Schropp, R. & Faaij, A. A cost roadmap for silicon heterojunction solar cells. *Solar Energy Materials and Solar Cells* 147, 295-314, doi:10.1016/j.solmat.2015.12.026 (**2016**).
[126] Ranjan, S., Balaji, S., Panella, R. A. & Ydstie, B. E. Silicon solar cell production. *Computers & Chemical Engineering* 35, 1439-1453, doi:10.1016/j.compchemeng.2011.04.017 (**2011**).
[127] Fthenakis, V. M. & Kim, H. C. Photovoltaics: Life-cycle analyses. *Solar Energy* 85, 1609-1628, doi:10.1016/j.solener.2009.10.002 (**2011**).
[128] Green, M. A. *et al*. Solar cell efficiency tables (Version 58). *Progress in Photovoltaics* 29, 657-667, doi:10.1002/pip.3444 (**2021**).
[129] Green, M. A. Commercial progress and challenges for photovoltaics. *Nature Energy* 1, doi:Artn 15015, 10.1038/Nenergy.2015.15 (**2016**).
[130] Rabaia, M. K. H. *et al*. Environmental impacts of solar energy systems: A review. *Sci Total Environ* 754, 141989, doi:10.1016/j.scitotenv.2020.141989 (**2021**).
[131] Popovich, V., Janssen, M., Benett, I. J. & Richardson, I. Breakage issues in silicon solar wafers and cells. *Photovoltaics International* 12, 49-57 (**2011**).
[132] Liu, W. *et al*. Flexible solar cells based on foldable silicon wafers with blunted edges. *Nature* 617, 717-723, doi:10.1038/s41586-023-05921-z (**2023**).
[133] Russo, J., Ray, W. & Litz, M. S. Low light illumination study on commercially available homojunction photovoltaic cells. *Applied Energy* 191, 10-21, doi:10.1016/j.apenergy.2017.01.029 (**2017**).
[134] Chiang, C. K. *et al*. Electrical-Conductivity in Doped Polyacetylene. *Physical Review Letters* 39, 1098-1101, doi:DOI 10.1103/PhysRevLett.39.1098 (**1977**).
[135] Heeger, A. J. Semiconducting and Metallic Polymers: The Fourth Generation of Polymeric Materials. *The Journal of Physical Chemistry B* 105, 8475-8491, doi:10.1021/jp011611w (**2001**).
[136] Tang, C. W. & Vanslyke, S. A. Organic Electroluminescent Diodes. *Applied Physics Letters* 51, 913-915, doi:Doi 10.1063/1.98799 (**1987**).

[137] Tang, C. W. Two-layer organic photovoltaic cell. *Applied Physics Letters* 48, 183-185, doi:10.1063/1.96937 (**1986**).
[138] Burroughes, J. H. *et al*. Light-emitting diodes based on conjugated polymers. *Nature* 347, 539-541, doi:10.1038/347539a0 (**1990**).
[139] Reineke, S. *et al*. White organic light-emitting diodes with fluorescent tube efficiency. *Nature* 459, 234-238, doi:10.1038/nature08003 (**2009**).
[140] Nakayama, K. I. *et al*. Single-Component Organic Solar Cells Based on Intramolecular Charge Transfer Photoabsorption. *Materials (Basel)* 14, doi:10.3390/ma14051200 (**2021**).
[141] Bonasera, A., Giuliano, G., Arrabito, G. & Pignataro, B. Tackling Performance Challenges in Organic Photovoltaics: An Overview about Compatibilizers. *Molecules* 25, doi:10.3390/molecules25092200 (**2020**).
[142] Zhang, H. J., Yu, K. Y., Wu, Z. H. & Zhu, Y. F. Ultrathin triphenylamine-perylene diimide polymer with D-A structure for photocatalytic oxidation of -heterocycles using ambient air. *Ecomat* 4, doi:ARTN e12215, 10.1002/eom2.12215 (**2022**).
[143] Solak, E. K. & Irmak, E. Advances in organic photovoltaic cells: a comprehensive review of materials, technologies, and performance. *RSC Adv* 13, 12244-12269, doi:10.1039/d3ra01454a (**2023**).
[144] Ren, H., Chen, J. D., Li, Y. Q. & Tang, J. X. Recent Progress in Organic Photodetectors and their Applications. *Adv Sci (Weinh)* 8, 2002418, doi:10.1002/advs.202002418 (**2020**).
[145] Weng, K. *et al*. Optimized active layer morphology toward efficient and polymer batch insensitive organic solar cells. *Nat Commun* 11, 2855, doi:10.1038/s41467-020-16621-x (**2020**).
[146] Milani, E. A., Piralaee, M., Ahmadi, S. & Asgari, A. The role of structural parameters on efficiency and transparency of semi-transparent non-fullerene organic solar cell. *Sci Rep* 12, 14928, doi:10.1038/s41598-022-19346-7 (**2022**).
[147] Paci, B. *et al*. Semitransparent Organic Photovoltaic Devices: Interface/Bulk Properties and Stability Issues. *Nanomaterials (Basel)* 14, 269, doi:10.3390/nano14030269 (**2024**).
[148] Shan, T., Hou, X., Yin, X. & Guo, X. Organic photodiodes: device engineering and applications. *Front Optoelectron* 15, 49, doi:10.1007/s12200-022-00049-w (**2022**).
[149] Park, J. H., Lee, T. W., Chin, B. D., Wang, D. H. & Park, O. O. Roles of interlayers in efficient organic photovoltaic devices. *Macromol Rapid Commun* 31, 2095-2108, doi:10.1002/marc.201000310 (**2010**).
[150] Page, Z. A., Liu, Y., Duzhko, V. V., Russell, T. P. & Emrick, T. Fulleropyrrolidine interlayers: tailoring electrodes to raise organic solar cell efficiency. *Science* 346, 441-444, doi:10.1126/science.1255826 (**2014**).
[151] Chaopaknam, J. *et al*. Tin(II) thiocyanate Sn(SCN) as an ultrathin anode interlayer in organic photovoltaics. *Applied Physics Letters* 119, doi:Artn 063301, 10.1063/5.0055649 (**2021**).
[152] Annabi Milani, E., Piralaee, M. & Asgari, A. Improving efficiency of semitransparent organic solar cells by constructing semitransparent microcavity. *Sci Rep* 13, 9508, doi:10.1038/s41598-023-36488-4 (**2023**).

[153] Valle, B. *et al*. Spectral aspects of cavity tuned absorption in organic photovoltaic films. *Opt Express* 20 Suppl 6, A954-963, doi:10.1364/OE.20.00A954 (**2012**).
[154] Zhao, W. C. *et al*. Vacuum-assisted annealing method for high efficiency printable large-area polymer solar cell modules. *Journal of Materials Chemistry C* 7, 3206-3211, doi:10.1039/c8tc06513f (**2019**).
[155] Hofstetter, Y. J. *et al*. Vacuum-Induced Degradation of 2D Perovskites. *Front Chem* 8, 66, doi:10.3389/fchem.2020.00066 (**2020**).
[156] Chang, Y. M. *et al*. Top-illuminated organic solar cells fabricated by vacuum-free and all-solution processes. *Solar Energy Materials and Solar Cells* 109, 91-96, doi:10.1016/j.solmat.2012.09.020 (**2013**).
[157] Tong, J. H. *et al*. Vacuum-free and metal electrode-free organic tandem solar cells. *Applied Physics Letters* 106, doi:Artn 053306, 10.1063/1.4907864 (**2015**).

[158] Jean, J., Wang, A. N. & Bulovic, V. In situ vapor-deposited parylene substrates for ultra-thin, lightweight organic solar cells. *Organic Electronics* 31, 120-126, doi:10.1016/j.orgel.2016.01.022 (**2016**).
[159] Lu, Q. *et al*. A Review on Encapsulation Technology from Organic Light Emitting Diodes to Organic and Perovskite Solar Cells. *Advanced Functional Materials* 31, doi:ARTN 2100151, 10.1002/adfm.202100151 (**2021**).

[160] Wang, Y. *et al*. Encapsulation and Stability Testing of Perovskite Solar Cells for Real Life Applications. *ACS Mater Au* 2, 215-236, doi:10.1021/acsmaterialsau.1c00045 (**2022**).
[161] Gielen, S. *et al*. Intrinsic Detectivity Limits of Organic Near-Infrared Photodetectors. *Adv Mater* 32, e2003818, doi:10.1002/adma.202003818 (**2020**).
[162] Zou, J. T., Zhang, S. & Tang, X. Recent Advances in Organic Photodetectors. *Photonics* 11, doi:ARTN 1014, 10.3390/photonics11111014 (**2024**).

[163] Ollearo, R. *et al*. Ultralow dark current in near-infrared perovskite photodiodes by reducing charge injection and interfacial charge generation. *Nat Commun* 12, 7277, doi:10.1038/s41467-021-27565-1 (**2021**).
[164] Liu, X. *et al*. A high dielectric constant non-fullerene acceptor for efficient bulk-heterojunction organic solar cells. *Journal of Materials Chemistry A* 6, 395-403, doi:10.1039/c7ta10136h (**2018**).
[165] Causa, M. *et al*. The fate of electron-hole pairs in polymer:fullerene blends for organic photovoltaics. *Nat Commun* 7, 12556, doi:10.1038/ncomms12556 (**2016**).
[166] Kippelen, B. & Brédas, J. L. Organic photovoltaics. *Energy & Environmental Science* 2, 251-261, doi:10.1039/b812502n (**2009**).
[167] Deibel, C. & Dyakonov, V. Polymer-fullerene bulk heterojunction solar cells. *Reports on Progress in Physics* 73, doi:Artn 096401, 10.1088/0034-4885/73/9/096401 (**2010**).

[168] Physics LibreTexts. *10.6 RC Circuits*, <https://phys.libretexts.org/@go/page/4411> (**2024**, accessed: 20 Feb 2025).
[169] Wetzelaer, G. J. A. H., Koster, L. J. A. & Blom, P. W. M. in *Organic Photovoltaics* pp. 343-376 (**2014**), 9783527332250, 9783527656912.

[170] O'Kane, M. & Ward, F. Ossila. *The AM1.5 Spectrum* <https://www.ossila.com/pages/standard-solar-spectrum> (accessed: 11 Feb 2025).
[171] Sze, S. M. & Ng, K. K. *Physics of Semiconductor Devices*. (**2006**), 9780471143239, 9780470068328.
[172] Wolf, M. & Rauschenbach, H. Series resistance effects on solar cell measurements. *Advanced Energy Conversion* 3, 455-479, doi:10.1016/0365-1789(63)90063-8 (**1963**).
[173] Green, M. A. Solar-Cell Fill Factors - General Graph and Empirical Expressions. *Solid-State Electronics* 24, 788-789, doi:Doi 10.1016/0038-1101(81)90062-9 (**1981**).
[174] OSI Optoelectronics. *Photodiode Characteristics and Application*, <https://www.osioptoelectronics.com/knowledgebase> (accessed: 11 Feb 2025).
[175] Bao, C. *et al*. Low-Noise and Large-Linear-Dynamic-Range Photodetectors Based on Hybrid-Perovskite Thin-Single-Crystals. *Adv Mater* 29, doi:10.1002/adma.201703209 (**2017**).
[176] Sariciftci, N. S., Smilowitz, L., Heeger, A. J. & Wudl, F. Photoinduced Electron Transfer from a Conducting Polymer to Buckminsterfullerene. *Science* 258, 1474-1476, doi:doi:10.1126/science.258.5087.1474 (**1992**).
[177] Yu, G., Gao, J., Hummelen, J. C., Wudl, F. & Heeger, A. J. Polymer Photovoltaic Cells: Enhanced Efficiencies via a Network of Internal Donor-Acceptor Heterojunctions. *Science* 270, 1789-1791, doi:10.1126/science.270.5243.1789 (**1995**).
[178] Nielsen, C. B., Holliday, S., Chen, H. Y., Cryer, S. J. & McCulloch, I. Non-fullerene electron acceptors for use in organic solar cells. *Acc Chem Res* 48, 2803-2812, doi:10.1021/acs.accounts.5b00199 (**2015**).
[179] Wang, J., Yao, H., Xu, Y., Ma, L. & Hou, J. Recent progress in reducing voltage loss in organic photovoltaic cells. *Materials Chemistry Frontiers* 5, 709-722, doi:10.1039/d0qm00581a (**2021**).
[180] Franskevych, D. *et al*. Fullerene C(60) Penetration into Leukemic Cells and Its Photoinduced Cytotoxic Effects. *Nanoscale Res Lett* 12, 40, doi:10.1186/s11671-016-1819-5 (**2017**).
[181] Li, S. X. *et al*. A spirobifluorene and diketopyrrolopyrrole moieties based non-fullerene acceptor for efficient and thermally stable polymer solar cells with high open-circuit voltage. *Energy & Environmental Science* 9, 604-610, doi:10.1039/c5ee03481g (**2016**).
[182] Xu, Y., Yao, H. F., Zhang, T., Ma, L. J. & Hou, J. H. A Thiazole-Based Polymer Donor for Efficient Organic Solar Cells. *Transactions of Tianjin University* 28, 398-405, doi:10.1007/s12209-022-00319-w (**2022**).
[183] Sun, C. *et al*. A low cost and high performance polymer donor material for polymer solar cells. *Nat Commun* 9, 743, doi:10.1038/s41467-018-03207-x (**2018**).
[184] Scharber, M. C. & Sariciftci, N. S. Low Band Gap Conjugated Semiconducting Polymers. *Advanced Materials Technologies* 6, doi:ARTN 2000857, 10.1002/admt.202000857 (**2021**).
[185] Deshmukh, A. P. *et al*. Bridging the gap between H- and J-aggregates: Classification and supramolecular tunability for excitonic band structures in

two-dimensional molecular aggregates. *Chemical Physics Reviews* 3, doi:Artn 021401, 10.1063/5.0094451 (**2022**).

[186] Zojer, E., Taucher, T. C. & Hofmann, O. T. The Impact of Dipolar Layers on the Electronic Properties of Organic/Inorganic Hybrid Interfaces. *Advanced Materials Interfaces* 6, doi:ARTN 1900581, 10.1002/admi.201900581 (**2019**).

[187] Zhang, J. L. *et al*. Non -covalent interaction controlled 2D organic semiconductor films: Molecular self -assembly, electronic and optical properties, and electronic devices. *Surface Science Reports* 75, doi:ARTN 100481, 10.1016/j.surfrep.2020.100481 (**2020**).

[188] Kroh, D. *et al*. Identifying the Signatures of Intermolecular Interactions in Blends of PM6 with Y6 and N4 Using Absorption Spectroscopy. *Advanced Functional Materials* 32, doi:ARTN 2205711, 10.1002/adfm.202205711 (**2022**).

[189] Spano, F. C. The spectral signatures of Frenkel polarons in H- and J-aggregates. *Acc Chem Res* 43, 429-439, doi:10.1021/ar900233v (**2010**).

[190] Kupgan, G., Chen, X. K. & Brédas, J. L. Molecular packing of non-fullerene acceptors for organic solar cells: Distinctive local morphology in Y6 vs. ITIC derivatives. *Materials Today Advances* 11, doi:ARTN 100154, 10.1016/j.mtadv.2021.100154 (**2021**).

[191] Chen, Z. *et al*. Asymmetric Self-Assembled Monolayer as Hole Transport Layer Enables Binary Organic Solar Cells Based on PM6: Y6 with Over 19% Efficiency. *CCS Chemistry* 7, 507-518, doi:10.31635/ccschem.024.202404707 (**2025**).

[192] Dong, Y. *et al*. Activationless Charge Transfer Drives Photocurrent Generation in Organic Photovoltaic Blends Independent of Energetic Offset. *J Am Chem Soc* 146, 33579-33586, doi:10.1021/jacs.4c11114 (**2024**).

[193] Mahadevan, S. *et al*. Assessing intra- and inter-molecular charge transfer excitations in non-fullerene acceptors using electroabsorption spectroscopy. *Nat Commun* 15, 2393, doi:10.1038/s41467-024-46462-x (**2024**).

[194] Eisner, F. D. *et al*. Hybridization of Local Exciton and Charge-Transfer States Reduces Nonradiative Voltage Losses in Organic Solar Cells. *J Am Chem Soc* 141, 6362-6374, doi:10.1021/jacs.9b01465 (**2019**).

[195] Sayner, T., Ruseckas, A., Harwell, J. R. & Samuel, I. D. W. Exciton Diffusion to Low Energy Sites of the Acceptor Drives Charge Photogeneration in D18:Y6 Solar Cells. *J Phys Chem C Nanomater Interfaces* 128, 19319-19328, doi:10.1021/acs.jpcc.4c06706 (**2024**).

[196] Bolzonello, L. *et al*. Photocurrent-Detected 2D Electronic Spectroscopy Reveals Ultrafast Hole Transfer in Operating PM6/Y6 Organic Solar Cells. *J Phys Chem Lett* 12, 3983-3988, doi:10.1021/acs.jpclett.1c00822 (**2021**).

[197] Pranav, M. *et al*. On the critical competition between singlet exciton decay and free charge generation in non-fullerene based organic solar cells with low energetic offsets. *Energy Environ Sci* 17, 6676-6697, doi:10.1039/d4ee01409j (**2024**).

[198] Nikolis, V. C. *et al*. Field Effect versus Driving Force: Charge Generation in Small-Molecule Organic Solar Cells. *Advanced Energy Materials* 10, doi:ARTN 2002124, 10.1002/aenm.202002124 (**2020**).

[199] Dong, Y. *et al*. Orientation dependent molecular electrostatics drives efficient charge generation in homojunction organic solar cells. *Nat Commun* 11, 4617, doi:10.1038/s41467-020-18439-z (**2020**).
[200] Rana, A. *et al*. Octupole moment driven free charge generation in partially chlorinated subphthalocyanine for planar heterojunction organic photodetectors. *Nat Commun* 15, 5058, doi:10.1038/s41467-024-49169-1 (**2024**).
[201] Fitzner, R. *et al*. Dicyanovinyl-Substituted Oligothiophenes: Structure-Property Relationships and Application in Vacuum-Processed Small-Molecule Organic Solar Cells. *Advanced Functional Materials* 21, 897-910, doi:10.1002/adfm.201001639 (**2011**).
[202] Fitzner, R. *et al*. Correlation of pi-conjugated oligomer structure with film morphology and organic solar cell performance. *J Am Chem Soc* 134, 11064-11067, doi:10.1021/ja302320c (**2012**).
[203] Meerheim, R., Körner, C. & Leo, K. Highly efficient organic multi-junction solar cells with a thiophene based donor material. *Applied Physics Letters* 105, doi:Artn 063306, 10.1063/1.4893012 (**2014**).
[204] Meerheim, R., Körner, C., Oesen, B. & Leo, K. 10.4% Efficient triple organic solar cells containing near infrared absorbers. *Applied Physics Letters* 108, doi:10.1063/1.4943653 (**2016**).
[205] Tamai, Y., Murata, Y., Natsuda, S. i. & Sakamoto, Y. How to Interpret Transient Absorption Data?: An Overview of Case Studies for Application to Organic Solar Cells. *Advanced Energy Materials* 14, doi:10.1002/aenm.202301890 (**2023**).
[206] Hänisch, C. *Simojio Simulation Tool*, <https://github.com/simoji-dev/simojio> (accessed: 13 Feb 2025).
[207] Byrnes, S. J. Multilayer optical calculations. *physics.comp-ph* (**2016**).
[208] Burkhard, G. F., Hoke, E. T. & McGehee, M. D. Accounting for interference, scattering, and electrode absorption to make accurate internal quantum efficiency measurements in organic and other thin solar cells. *Adv Mater* 22, 3293-3297, doi:10.1002/adma.201000883 (**2010**).
[209] Kniepert, J. *et al*. Reliability of charge carrier recombination data determined with charge extraction methods. *Journal of Applied Physics* 126, doi:Artn 205501, 10.1063/1.5129037 (**2019**).
[210] Hußner, M., Deibel, C. & MacKenzie, R. C. I. The physical meaning of time-delayed collection field transients from disordered devices. *Journal of Applied Physics* 135, doi:10.1063/5.0187323 (**2024**).
[211] Kumar, A. *et al*. Transient absorption spectroscopy based on uncompressed hollow core fiber white light proves pre-association between a radical ion photocatalyst and substrate. *J Chem Phys* 158, 144201, doi:10.1063/5.0142225 (**2023**).
[212] Feng, Y., Vinogradov, I. & Ge, N. H. General noise suppression scheme with reference detection in heterodyne nonlinear spectroscopy. *Opt Express* 25, 26262-26279, doi:10.1364/OE.25.026262 (**2017**).
[213] Lanzani, G. *Photophysics of Molecular Materials: From Single Molecules to Single Crystals*. 583 (Wiley - VCH, **2005**), 9783527607327.

[214] Banerji, N. Sub-picosecond delocalization in the excited state of conjugated homopolymers and donor-acceptor copolymers. *Journal of Materials Chemistry C* 1, 3052-3066, doi:10.1039/c3tc00005b (**2013**).
[215] de Juan, A., Jaumot, J. & Tauler, R. Multivariate Curve Resolution (MCR). Solving the mixture analysis problem. *Anal. Methods* 6, 4964-4976, doi:10.1039/c4ay00571f (**2014**).
[216] Camp, C. H., Jr. pyMCR: A Python Library for MultivariateCurve Resolution Analysis with Alternating Regression (MCR-AR). *J Res Natl Inst Stand Technol* 124, 1-10, doi:10.6028/jres.124.018 (**2019**).
[217] de Sa Pereira, D., Menelaou, C., Danos, A., Marian, C. & Monkman, A. P. Electroabsorption Spectroscopy as a Tool for Probing Charge Transfer and State Mixing in Thermally Activated Delayed Fluorescence Emitters. *J Phys Chem Lett* 10, 3205-3211, doi:10.1021/acs.jpclett.9b00999 (**2019**).
[218] Wan, P. *et al*. Direct Observation of the Charge Transfer States from a Non-Fullerene Organic Solar Cell with a Small Driving Force. *J Phys Chem Lett* 12, 10595-10602, doi:10.1021/acs.jpclett.1c03365 (**2021**).
[219] Liu, T., Foo, Y., Zapien, J. A., Li, M. & Tsang, S. W. A generalized Stark effect electromodulation model for extracting excitonic properties in organic semiconductors. *Nat Commun* 10, 5089, doi:10.1038/s41467-019-13081-w (**2019**).
[220] Liptay, W. Elektrochromie - Solvatochromie. *Angewandte Chemie* 6, 12 (**1969**).
[221] Hörmann, U. *et al*. Stark effect of hybrid charge transfer states at planar ZnO/organic interfaces. *Physical Review B* 98, doi:10.1103/PhysRevB.98.155312 (**2018**).
[222] Devizis, A. *et al*. Dissociation of Charge Transfer States and Carrier Separation in Bilayer Organic Solar Cells: A Time-Resolved Electroabsorption Spectroscopy Study. *J Am Chem Soc* 137, 8192-8198, doi:10.1021/jacs.5b03682 (**2015**).
[223] Johnston, M. B. *et al*. Low-energy vibrational modes in phenylene oligomers studied by THz time-domain spectroscopy. *Chemical Physics Letters* 377, 256-262, doi:10.1016/S0009-2614(03)01136-9 (**2003**).
[224] Krauspe, P. *et al*. Terahertz short-range mobilities in neat and intermixed regions of polymer: fullerene blends with controlled phase morphology. *Journal of Materials Chemistry A* 6, 22301-22309, doi:10.1039/c8ta08061e (**2018**).
[225] Krauspe, P., Banerji, N. & Réhault, J. Effective detection of weak terahertz pulses in electro-optic sampling at kilohertz repetition rate. *Journal of the Optical Society of America B* 37, doi:10.1364/josab.37.000127 (**2019**).
[226] Wolansky, J. *et al*. Sensitive Self-Driven Single-Component Organic Photodetector Based on Vapor-Deposited Small Molecules. *Adv Mater* 36, e2402834, doi:10.1002/adma.202402834 (**2024**).
[227] Zhang, T. Y. *et al*. High-Performance Filterless Blue Narrowband Organic Photodetectors. *Advanced Functional Materials* 34, doi:10.1002/adfm.202308719 (**2024**).
[228] Ma, X. *et al*. Identification of the Origin of Ultralow Dark Currents in Organic Photodiodes. *Adv Mater* 35, e2209598, doi:10.1002/adma.202209598 (**2023**).
[229] Thorlabs. *Calibrated Si Photodiode*, <https://www.thorlabs.com/newgrouppage9.cfm?objectgroup_id=2822> (accessed: 21 Jun 2025).

[230] Roncali, J. Single-Material Organic Solar Cells Based on Small Molecule Homojunctions: An Outdated Concept or a New Challenge for the Chemistry and Physics of Organic Photovoltaics? *Advanced Energy Materials* 11, doi:ARTN 2102987, 10.1002/aenm.202102987 (**2021**).

[231] Marin - Beloqui, J. M. *et al*. Triplet - Charge Annihilation in a Small Molecule Donor: Acceptor Blend as a Major Loss Mechanism in Organic Photovoltaics. *Advanced Energy Materials* 11, doi:10.1002/aenm.202100539 (**2021**).

[232] Dandrade, B. *et al*. Relationship between the ionization and oxidation potentials of molecular organic semiconductors. *Organic Electronics* 6, 11-20, doi:10.1016/j.orgel.2005.01.002 (**2005**).

[233] Schwarze, M. *et al*. Analyzing the n-Doping Mechanism of an Air-Stable Small-Molecule Precursor. *ACS Appl Mater Interfaces* 10, 1340-1346, doi:10.1021/acsami.7b14034 (**2018**).

[234] MacKenzie, R. C. I., Göritz, A., Greedy, S., von Hauff, E. & Nelson, J. Theory of Stark spectroscopy transients from thin film organic semiconducting devices. *Physical Review B* 89, doi:10.1103/PhysRevB.89.195307 (**2014**).

[235] Tsokkou, D. *et al*. Ultrafast Charge Transfer Dynamics at the Origin of Photoconductivity in Doped Organic Solids. *J Phys Chem C Nanomater Interfaces* 125, 7086-7096, doi:10.1021/acs.jpcc.1c01990 (**2021**).

[236] Jasinskas, V., Franckevicius, M., Gelzinis, A., Chmeliov, J. & Gulbinas, V. Direct Tracking of Charge Carrier Drift and Extraction from Perovskite Solar Cells by Means of Transient Electroabsorption Spectroscopy. *ACS Appl Electron Mater* 5, 317-326, doi:10.1021/acsaelm.2c01346 (**2023**).

[237] Sahoo, S., Dhar, R., Dutta, S. & Bhattacharyya, J. Investigation of internal fields in organic semiconductors in the presence of traps. *Journal of Applied Physics* 130, doi:Artn 085702, 10.1063/5.0058515 (**2021**).

[238] de Juan, A. & Tauler, R. Multivariate Curve Resolution: 50 years addressing the mixture analysis problem - A review. *Anal Chim Acta* 1145, 59-78, doi:10.1016/j.aca.2020.10.051 (**2021**).

[239] Maimaris, M. *et al*. Sub-10-fs observation of bound exciton formation in organic optoelectronic devices. *Nat Commun* 13, 4949, doi:10.1038/s41467-022-32478-8 (**2022**).

[240] Garratt, D. *et al*. Direct observation of ultrafast exciton localization in an organic semiconductor with soft X-ray transient absorption spectroscopy. *Nat Commun* 13, 3414, doi:10.1038/s41467-022-31008-w (**2022**).

[241] Rao, A. & Friend, R. H. Harnessing singlet exciton fission to break the Shockley-Queisser limit. *Nature Reviews Materials* 2, doi:ARTN 17063, 10.1038/natrevmats.2017.63 (**2017**).

[242] Bogner, L. *et al*. Electronic structure and excited state dynamics in a dicyanovinyl-substituted oligothiophene on Au(111). *Phys Chem Chem Phys* 17, 27118-27126, doi:10.1039/c5cp04084a (**2015**).

[243] Bublitz, G. U. & Boxer, S. G. Stark spectroscopy: applications in chemistry, biology, and materials science. *Annu Rev Phys Chem* 48, 213-242, doi:10.1146/annurev.physchem.48.1.213 (**1997**).

[244] Wurfel, U., Neher, D., Spies, A. & Albrecht, S. Impact of charge transport on current-voltage characteristics and power-conversion efficiency of organic solar cells. *Nat Commun* 6, 6951, doi:10.1038/ncomms7951 (**2015**).
[245] Yuan, J. *et al.* Enabling low voltage losses and high photocurrent in fullerene-free organic photovoltaics. *Nat Commun* 10, 570, doi:10.1038/s41467-019-08386-9 (**2019**).
[246] Liu, Q. *et al.* 18% Efficiency organic solar cells. *Sci Bull (Beijing)* 65, 272-275, doi:10.1016/j.scib.2020.01.001 (**2020**).
[247] Zhao, X. J. *et al.* Exploring the impact of fabrication parameters in organic solar cells with PM6:Y6 using machine learning. *Aip Advances* 14, doi:Artn 065325, 10.1063/5.0201580 (**2024**).
[248] Clarke, A. J. *et al.* Non-fullerene acceptor photostability and its impact on organic solar cell lifetime. *Cell Reports Physical Science* 2, doi:ARTN 100498, 10.1016/j.xcrp.2021.100498 (**2021**).
[249] Lee, T. H., Hillman, S. A. J., Gonzalez - Carrero, S., Difilippo, A. & Durrant, J. R. Long - Lived Charges in Y6:PM6 Bulk - Heterojunction Photoanodes with a Polymer Overlayer Improve Photoelectrocatalytic Performance. *Advanced Energy Materials* 13, doi:10.1002/aenm.202300400 (**2023**).
[250] Harris, R., Chang, C. Y., Guo, J., Ivov Gonev, H. & Clarke, T. M. Modulating Polaron Behavior in PM6 Blends with Nonfullerene and Fullerene Acceptors: The Importance of Singlet Energy Transfer. *Advanced Materials Interfaces* 12, doi:10.1002/admi.202400779 (**2024**).
[251] Privitera, A. *et al.* Geminate and Nongeminate Pathways for Triplet Exciton Formation in Organic Solar Cells. *Advanced Energy Materials* 12, doi:10.1002/aenm.202103944 (**2022**).
[252] Hume, P. A., Price, M. B. & Hodgkiss, J. M. New Avenues for Organic Solar Cells Using Intrinsically Charge-Generating Materials. *JACS Au* 4, 1295-1302, doi:10.1021/jacsau.4c00046 (**2024**).
[253] Yallum, K. M. *Spectroscopic Investigation of Non-Fullerene Acceptors* PhD thesis, University of Bern, (**2023**).
[254] Kirchmeyer, S. & Reuter, K. Scientific importance, properties and growing applications of poly(3,4-ethylenedioxythiophene). *Journal of Materials Chemistry* 15, doi:10.1039/b417803n (**2005**).
[255] Fortunato, E., Ginley, D., Hosono, H. & Paine, D. C. Transparent Conducting Oxides for Photovoltaics. *MRS Bulletin* 32, 242-247, doi:10.1557/mrs2007.29 (**2011**).
[256] Yao, J. *et al.* Cathode engineering with perylene-diimide interlayer enabling over 17% efficiency single-junction organic solar cells. *Nat Commun* 11, 2726, doi:10.1038/s41467-020-16509-w (**2020**).
[257] Murugan, P., Ravindran, E., Sangeetha, V., Liu, S. Y. & Jung, J. W. Perylene-diimide for organic solar cells: current scenario and prospects in molecular geometric, functionalization, and optoelectronic properties. *Journal of Materials Chemistry A* 11, 26393-26425, doi:10.1039/d3ta04925f (**2023**).
[258] Zang, Y. *et al.* Optical modeling of microcavity strategy for highly efficient ITO-free organic solar cells with varied photoactive layers. *Optical Materials* 132, doi:ARTN 112772, 10.1016/j.optmat.2022.112772 (**2022**).

[259] Gelinas, S. *et al*. Ultrafast long-range charge separation in organic semiconductor photovoltaic diodes. *Science* 343, 512-516, doi:10.1126/science.1246249 (**2014**).
[260] Bassler, H. & Kohler, A. Charge transport in organic semiconductors. *Top Curr Chem* 312, 1-65, doi:10.1007/128_2011_218 (**2012**).
[261] Natsuda, S. *et al*. Cascaded energy landscape as a key driver for slow yet efficient charge separation with small energy offset in organic solar cells. *Energy & Environmental Science* 15, 1545-1555, doi:10.1039/d1ee03565g (**2022**).